UNIVERSITÀ DEGLI STUDI DI NAPOLI FEDERICO II

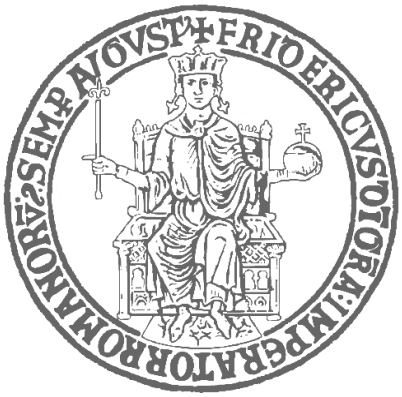

DEPARTMENT OF PHYSICS ETTORE PANCINI

THESIS FOR DEGREE OF DOCTORAL OF PHILOSOPHY

MULTISCALE OXIDATIVE CHEMISTRY OF CARBONACEOUS EMISSIONS:

INVESTIGATION OF RADICAL PATHWAYS AFFECTING SOOT AND SECONDARY ORGANIC AEROSOL FORMATION

Supervisors

Prof. Andrea D'Anna

Prof. Salvatore Amoruso

Scientific Committee

Dr. Lubna Dada

Prof. Olli Sippula

Prof. Denis Petitprez

PhD Candidate

Alessia Pignatelli

XXXVIII PhD Cycle - Scientific Sector: PHYS-06/A

ITINERIS

Resume

Atmospheric aerosols impact both climate and human health, but despite their key role, the chemical pathways driving their formation and atmospheric evolution remain only partially understood. Atmospheric aerosols can be released by biogenic sources, such as vegetation and volcanic eruptions, or by anthropogenic activities, including combustion and industrial processes. Carbonaceous emissions from combustion represent a major anthropogenic source of both primary particles, such as soot, and gaseous precursors involved in secondary organic aerosol formation (SOA).

This thesis investigates the oxidative chemistry of carbonaceous emissions from various sources, with particular focus on anthropogenic combustion emissions. A multiple-angled approach was adopted here, aiming at clarifying the role of radical pathways in soot formation, isolating the impact of atmospheric aging on primary organic aerosol (POA) and SOA formation and evolution, and monitoring the interactions of anthropogenic emissions with other pre-emitted compounds.

The work is organized in three work packages, addressing combustion-scale processes, laboratory-based atmospheric aging, and atmospherically relevant conditions.

The key findings of this thesis highlighted the possibility of using dopants to inject into different combustion systems to alter the formation of soot and, more generally, the release of harmful compounds. The introduction of ozone in a methane-air system proved to alter the chemistry of the system by impacting on the formation mechanism of π-radicals, critical intermediates in soot formation.

Furthermore, the monitoring of atmospheric aging of emissions released by ethylene-air flames are here presented. Atmospheric aging was performed using an oxidation flow reactor that mimics OH-induced oxidation. Mass spectrometric analysis and particle-size distribution measurements highlighted several differences in the composition and structure of primary and secondary organic aerosols.

Finally, atmospheric evolution of anthropogenic emissions, coupled with their interactions with biogenic compounds, was investigated. The experiments were conducted at CLOUD, CERN facility under controlled conditions mimicking forested, suburban, and highly polluted environments. These experiments focused on deciphering the role of RO_2 in atmospheric reactive pathways and, remarkably, on understanding the impact of different precursors on RO_2 structure and RO_2-RO_2 interactions.

Acknowledgements

This PhD research was financially supported by the ITINERIS – Italian Integrated Environmental Research Infrastructures System, funded by the European Union – Next Generation EU, within the framework of the PNRR, Mission 4 “Education and Research”, Component 2 “From research to business”, Investment 3.1 “Fund for the realisation of an integrated system of research and innovation infrastructures”.

Table of Contents

List of Figures

List of Tables

List of Abbreviations

AFM – Atomic Force Microscopy
AIM – Aerosol Instrument Manager
AMS – Aerosol Mass Spectrometer
AP – α-Pinene
AP-RO_2 – α-Pinene Peroxy Radicals
ArHC – Aromatic Hydrocarbons
AVOC – Anthropogenic Volatile Organic Compounds

BPR – Bicyclic Peroxy Radicals
BVOC – Biogenic Volatile Organic Compounds

CLOUD – Cosmics Leaving OUtdoor Droplets
CPC – Condensation Particle Counter
CS – Condensation Sink

DMA – Differential Mobility Analyzer
DOFR™ – Dekati® Oxidation Flow Reactor
DR – Dilution Ratio

ELVOC – Extremely Low-Volatility Organic Compounds

HACA – Hydrogen-Abstraction–C_2H_2-Addition
HCCI – Homogeneous Charge Compression Ignition
HOM – Highly Oxygenated Organic Molecules
HOA – Hydrocarbon-Like Organic Aerosol
HORUS – Hydroxyl Radical Measurement Unit based on Fluorescence Spectroscopy
HR – High Resolution
HR-MS – High-Resolution Mass Spectra
HR-ToF-AMS – High-Resolution Time-of-Flight Aerosol Mass Spectrometer

I.D. – Inner Diameter
IP – Isoprene
IP-RO_2 – Isoprene Peroxy Radicals

LIF – Laser-Induced Fluorescence
LVOC – Low-Volatility Organic Compounds
LTOF – Long Time-of-Flight

NPT- Naphtalene
NPT-RO2- Naphtalene Peroxy Radicals
NPF – New Particle Formation
NOx – Nitrogen Oxides

OFR – Oxidation Flow Reactor
OOA – Oxygenated Organic Aerosol

PAC – Plasma-Assisted Combustion
PAH – Polycyclic Aromatic Hydrocarbons
PM – Particulate Matter
POA – Primary Organic Aerosol
POZ – Primary Ozonide

PR – Production rate
PSD – Particle Size Distribution
PTR-MS – Proton Transfer Reaction Mass Spectrometry

QCH_4 – Methane Flow Rate
QPA – Primary Air Flow

RO_2 – Organic Peroxy Radicals
RP – Resolving Power
RRMS – Root Mean Square Surface Roughness
RSR – Resonantly Stabilized Aromatic π-Radicals

SA – Secondary Aerosol
SFTOF – Surface-Field Time-of-Flight
SI – Spark Ignition
SMPS – Scanning Mobility Particle Sizer
SOA – Secondary Organic Aerosol
SOx – Sulfur Oxides
SOZ – Secondary Ozonide

TMB – Trimethylbenzene
TMB-RO_2 – Trimethylbenzene Peroxy Radicals
TOL-RO_2 – Toluene Peroxy Radicals
TPD – Thermophoretic Particle Densitometry

ULVOC – Ultra-Low Volatility Organic Compounds
UMR – Unit Mass Resolution
UV – Ultraviolet
UVC – Ultraviolet C

VBS – Volatility Basis Set
VOC – Volatile Organic Compounds

Z – Height above the burner
h – Particle height
rBASE – Basal radius
$\langle h \rangle_g$ – Geometric mean height
$\sigma_g(h)$ – Geometric standard deviation
m/z – Mass-to-Charge Ratio

1. Introduction

Atmospheric aerosols play a key role in both climate and human health (Seinfeld & Pandis, 2016; WHO (World Meteorological Organization), 2016). Technically, the term *aerosol* refers to a suspension of either liquid or fine solid particles in a gaseous medium (Hinds, 1999; Putaud et al., 2010; Seinfeld, 1989).

Their ubiquitous presence in the atmosphere makes it essential to investigate the chemical and physical mechanisms governing their formation and evolution in the atmosphere to mitigate anthropogenic impact on our planet. From a climatic perspective, aerosols influence the Earth's radiation budget through multiple pathways. Firstly, they can directly affect the surface-atmosphere radiation by scattering and absorbing the incoming solar and the outgoing terrestrial radiation (Ångström, 1962; McCormick & Ludwig, 1967). Moreover, once released or formed in the atmosphere, aerosol particles can indirectly affect cloud microphysical properties, lifetime and precipitation efficiency by acting as cloud condensation and ice nuclei (Lohmann & Feichter, 2005; Ramanathan et al., 2001). Finally, the aerosol capability to absorb radiation can induce semidirect effects by altering the atmospheric thermal structure and surface energy balance through the induced alteration in the number and characteristics of formed clouds (Johnson et al., 2004). From a health point of view, long-term exposure to aerosol pollution can induce adverse effects on lungs, cardiovascular and nervous systems leading to severe pathologies with severe consequences (Cohen et al., 2017; Lelieveld et al., 2015; Pope & Dockery, 2006). In general, aerosol particles exhibit a broad range of possible chemical structures, shapes and properties and their impact on the atmosphere and on our health can vary accordingly. Aerosols size usually ranges from 0.01 to 1000 μm and based on their aerodynamic diameter, they can be classified into (J. Dong et al., 2020; Riabova, 2025):

- PM10-2.5 (coarse particulate matter), showing a diameter between 2.5 μm and 10 μm.
- PM2.5 (fine particulate matter), with aerodynamic diameters smaller than 2.5 μm.
- PM0.1 (ultrafine particulate matter), referring to particles <0.1 μm. This class of particles falls within the nanoscale range as defined by the European regulatory frameworks, where nanoparticles diameters range between 1 and 100nm, Accordingly, in atmospheric chemistry, nanoparticles are commonly considered dimensionally equivalent to ultrafine particles (Rauscher et al., 2023).

In literature, aerosols can not only be characterized based on their size but also according to their emission source. In this framework, it is possible to distinguish primary aerosols (PA), directly released by from natural or anthropogenic activities, and secondary aerosols (SA), which are formed in the atmosphere through gas-to-particle conversion mechanisms (Saraswati, 2022). These latter processes mainly involve gaseous by-products of combustion, including volatile organic compounds (VOC), ammonia (NH_3), sulphur oxides (SO_x) and nitrogen oxides (NO_x) (Krupa, 1997; Riabova, 2025).

PA originate from a wide variety of natural sources, such as volcanic eruptions, wind-blown dust and sea spray as well as from anthropogenic activities, mainly comprehending industrial processes and combustion systems (Charlson et al., 1992; Liora et al., 2015). A typical example of primary aerosols emitted by combustion processes is soot, which exhibits a hierarchical structure. It is composed of primary carbonaceous spherules with diameters typically ranging from 1 to 50 nm, which can aggregate to form fractal like agglomerates exhibiting an overall size ranging from tens of nanometers up to the micrometer scale (W. Li et al., 2024; Pang et al., 2023; Schwarz et al., 2008). Among the various PM size classes, soot has a strong impact on both the environment and human health: it exhibits strong scattering properties and the ability to affect earth-system energy balance (Buseck & Pósfai, 1999; Ramanathan & Carmichael, 2008), coupled with harmful effects to those directly or indirectly exposed to it (Avino, 2022; Niranjan & Thakur, 2017). Moreover, once emitted, primary particles can undergo atmospheric aging with oxidants, e.g. OH, O_3 and NO_3, leading to an alteration in the particle composition,

volatility, hygroscopicity and optical properties. Atmospheric aging can thus enhance their role in SA formation or, more in general, modifying their role in terms of environmental and health impact (Ng et al., 2011; Zhang et al., 2023).

Based on their geographical location and environmental conditions, aerosols chemical composition can largely vary, although it is broadly established that organic material represents between 30% and 50% of the atmospheric particles mass, originating from organic gaseous precursors (Jacobson et al., 2000). Indeed, although atmospheric aerosol can be composed of inorganic elements including, sulphates, nitrates, ammonium salts and elemental carbon, the organic component usually represents a relevant contribution (Jimenez et al., 2009a). Within this framework, it is possible to specifically discriminate between primary organic aerosols (POA) and secondary organic aerosols (SOA).

To reduce the global aerosol emissions, it is extremely important to investigate PA emission sources of primary aerosols to mitigate their release. However, while controlling already-formed particles can be a first strategy to reduce atmospheric alterations, a complementary approach involves regulating the emissions of gaseous precursors responsible of the formation of secondary organic aerosols.

Among the most relevant organic precursors, volatile organic carbons (VOCs) play an essential role in the formation and evolution of atmospheric aerosols (Atkinson, 2000; Atkinson & Arey, 2003; Kroll & Seinfeld, 2008; Ziemann & Atkinson, 2012). VOCs can be either released from biogenic sources (BVOCs), including plants and trees (Fall, 1999; Liora et al., 2015; L. Wang et al., 2024), or from anthropogenic activities (AVOCs), such as vehicle exhausts, industrial processes and domestic combustion (Friedrich & Obermeier, 1999a; L. Huang et al., 2023). In this context, fossil fuel combustion and biomass burning have been identified as accounting for approximatively 85% of airborne respirable particle in the environment, in addition to NO_x and SO_x releases (International Energy Agency (IEA), 2016). Beyond direct emissions of primary particles, such as soot and particulate matter across a wide spectrum of sizes, combustion processes are also responsible for the release of gaseous compounds actively participating in gas-to-particle formation mechanisms. These include VOCs and intermediate-volatility organic compounds (IVOCs), encompassing species such as polycyclic aromatic hydrocarbons (PAH), known to be great contributors to SOA formation (Hallquist et al., 2009; Sengupta et al., 2023).

Regardless of their source, once released in the environment, both BVOCs and AVOCs are likely to undergo oxidation by hydroxyl radicals (OH), ozone molecules (O_3) and nitrate radicals (NO_3), leading to the formation of organic peroxy radicals (RO_2) (Berndt et al., 2018; Goldman et al., 2021). Subsequent reactions of different RO_2 can lead to the formation of increasingly functionalized and less volatile compounds, either monomers or dimers, that actively contribute to SOA formation (Atkinson & Arey, 2003; Donahue et al., 2006; Thoma et al., 2025).

Due to the variety of chemical species and the number of variables affecting atmospheric interactions, deciphering the key pathways driving the formation and evolution of primary and secondary particles becomes particularly challenging. Despite significant advances in understanding aerosol formation and transformation mechanisms, the complexity of the system continues to pose major challenges. Key knowledge gaps remain mainly regarding the transformation of gas-phase precursors, their evolution and their contribution to secondary aerosols.

Among the main unveiled open questions, it is possible to mention:

- Can anthropogenic emissions from combustion systems, including gaseous precursors (like AVOCs) as well as particulate matter such as soot, be reduced? Is it possible to alter the chemistry of combustion through the use of strategic solutions, such as dopant molecules, to develop cleaner technologies?

- How does atmospheric aging impact and drive AVOCs transformations? Can we identify some key reactive pathways and variables driving the formation of secondary aerosols from gas-phase precursors in addition to the evolution of primary particles already emitted?
- How do AVOCs evolve in the presence of pre-emitted compounds? Do BVOCs or other pre-released species affect their atmospheric evolution?

To address these questions, three dedicated Work Packages (WPs) were developed.

For the WP1, the investigation of emissions released in combustion systems, such as methane (CH_4)/air flames and ethylene (C_2H_4)/air flames, was performed. Specific chemical dopants were introduced into each flame to investigate their potential in reducing harmful emissions and soot formation. The selected dopants for CH_4 and C_2H_4 flames were ozone and ethanol, respectively. In this thesis, only the ozone-doped flame studies have been reported, showing promising results in terms of soot reduction and chemical alteration of the released particles.

WP2 focuses on the investigation of primary and secondary organic aerosols released by an ethylene/air combustion system. Both physical and chemical characterizations of emitted gases and particles were performed through the analysis particle size distribution functions and mass spectrometry. The role of atmospheric aging was studied using a dedicated atmospheric aging reactor able to mimic the main atmospheric-relevant oxidation mechanisms.

WP3 explores the fate of anthropogenic emissions in the atmosphere, analysing their key oxidation pathways and their interaction with biogenic compounds. This chapter was conducted at the Cosmics Leaving Outdoor Droplets (CLOUD) facility at CERN, Geneva. A set of controlled scenarios was developed to simulate three representative environments: a forest, characterized by only BVOCs, a suburban scenario, with mixed AVOCs and BVOCs, and a highly polluted environment, where AVOCs chemistry prevails.

Overall, the analysis of these three WPs aims to provide a comprehensive investigation of AVOC emissions: from their production and possible technological mitigation strategies to their atmospheric aging simulated in a laboratory-scale environment, and finally to their evolution in an atmospheric relevant scenario.

1.1 Research Schedule

The PhD research was conducted over a three-year program. Each year was focused on a different work package (WP) investigating the topics mentioned in the introduction. Literature review preceded every experimental campaign, coupled with the data analysis. Two papers have been published and a third one is in the draft form:

- Paper I (WP1): *The effect of ozone on soot formation in partially premixed laminar methane/air flames,* Authors: A. Pignatelli, L. Basta, P. Minutolo, F. Sasso, J. W. Martin, F. Picca, A. D'Anna. Journal: Fuel, Volume 373, 2024, 13234. Status: published.
- Paper II (WP2): *A laboratory study of secondary organic aerosol formation in an oxidation flow reactor,* Authors: F. Sasso, F. Picca, A. Pignatelli, M. Commodo, P. Minutolo, A. D'Anna Journal: Fuel, Volume 367, 1 July 2024, 131491. Status: published.
- Paper III (WP3): *RO_2 Radical Interactions and Their Role in Secondary Organic Aerosol and Dimer Formation*. Status: To be Submitted.

As part of the PhD programme, in parallel with the experimental investigations, various activities were conducted, as listed in the table as Further Tasks. In particular, to enrich my knowledge I took part in the following lectures:

- ❖ Mitigation of the Environmental Impact of Chemical Processes for Energy Production (Module I and Module II) released by University of Naples Federico II.
- ❖ EPR/Scattering for Nanomaterials released by University of Naples Federico II.
- ❖ How to boost your PhD released by University of Naples Federico II.
- ❖ Statistical Methods for Data Analysis released by University of Naples Federico II.
- ❖ Tropospheric Chemistry released by ETH, Zurich.

I presented parts of the research of these years in the following conferences:

- Joint Meeting of the Italian and Belgian Sections of the combustion Institute, Firenze 2023. Oral Presentation: *Effect Of Ethanol Addition On Ethylene-Air Flame On The Primary And Secondary Particle Size Distribution* (Best Oral Presentation Award).
- ETH Nanoparticles Conference, Zurich 2023, Oral Presentation: *Formation, Growth, and Photochemical Aging of Laboratory Generated Nanoparticles.*
- EAC 2023, Malaga, Poster Presentation: *A preliminary study of secondary aerosol formation in an oxidation flow reactor at different aging times.*
- START Gaef Conferece, Wien 2024, Oral Presentation: *Effects of Ethanol addition on ethylene-air flame-generated aerosols.*
- 46th meeting of the Italian Section of the combustion institute, Bari 2024, Oral Presentation: *The Effect Of Ozone On Soot Formation In Partially Premixed Laminar Methane/Air Flames.*
- EAC 2025, Lecce, Oral Presentation: *Decoding the Synergistic Effects of Anthropogenic and Biogenic Emissions on New Particle Formation: Insights from CERN CLOUD chamber.*

In 2023, I participated to the AGORA Aerosol Training School in Granada, Spain where the data analysis of a field campaign reporting wildfire emissions in South of Spain was performed.

In September 2023, I passed the Italian State Exam for the practicing of Engineering Profession (Industrial Engineering, Section A).

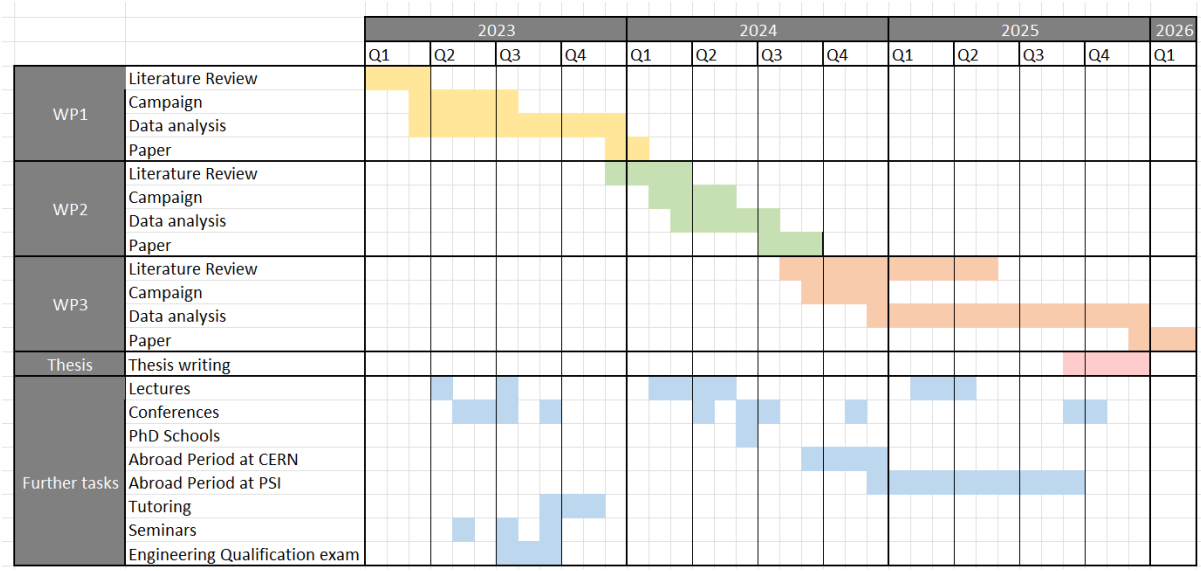

PhD Scheduling Table

1.2 References

Ångström, A. (1962). Atmospheric turbidity, global illumination and planetary albedo of the earth. Tellus, 14(4), 435–450. https://doi.org/10.3402/TELLUSA.V14I4.9570

Atkinson, R. (2000). Atmospheric chemistry of VOCs and NOx. Atmospheric Environment, 34(12–14), 2063–2101. https://doi.org/10.1016/S1352-2310(99)00460-4

Atkinson, R., & Arey, J. (2003). Atmospheric Degradation of Volatile Organic Compounds. Chemical Reviews, 103(12), 4605–4638. https://doi.org/10.1021/CR0206420

Avino, P., & Avino, P. (2022). Black Carbon in Atmosphere: Instrumentation, Chemical-Physical Behavior, Human Health Implications. Atmosphere 2022, Vol. 13, 13(12). https://doi.org/10.3390/ATMOS13122087

Berndt, T., Scholz, W., Mentler, B., Fischer, L., Herrmann, H., Kulmala, M., & Hansel, A. (2018). Accretion Product Formation from Self- and Cross-Reactions of RO2 Radicals in the Atmosphere. Angewandte Chemie - International Edition, 57(14), 3820–3824. https://doi.org/10.1002/ANIE.201710989

Buseck, P. R., & Pósfai, M. (1999). Airborne minerals and related aerosol particles: Effects on climate and the environment. Proceedings of the National Academy of Sciences of the United States of America, 96(7), 3372–3379. https://doi.org/10.1073/PNAS.96.7.3372;REQUESTEDJOURNAL:JOURNAL:PNAS;CTYPE:STRING:JOURNAL

Charlson, R. J., Schwartz, S. E., Hales, J. M., Cess, R. D., Coakley, J. A., Hansen, J. E., & Hofmann, D. J. (1992). Climate Forcing by Anthropogenic Aerosols. Science, 255(5043), 423–430. https://doi.org/10.1126/SCIENCE.255.5043.423

Cohen, A. J., Brauer, M., Burnett, R., Anderson, H. R., Frostad, J., Estep, K., Balakrishnan, K., Brunekreef, B., Dandona, L., Dandona, R., Feigin, V., Freedman, G., Hubbell, B., Jobling, A., Kan, H., Knibbs, L., Liu, Y., Martin, R., Morawska, L., … Forouzanfar, M. H. (2017). Estimates and 25-year trends of the global burden of disease attributable to ambient air pollution: an analysis of data from the Global Burden of Diseases Study 2015. The Lancet, 389(10082), 1907–1918. https://doi.org/10.1016/S0140-6736(17)30505-6

Donahue, N. M., Robinson, A. L., Stanier, C. O., & Pandis, S. N. (2006). Coupled Partitioning, Dilution, and Chemical Aging of Semivolatile Organics. Environmental Science and Technology, 40(8), 2635–2643. https://doi.org/10.1021/ES052297C

Dong, J., Chi, Y., Ephraim, A., Nzihou, A., & Millán, L. M. R. (2020). Particulate matter. Handbook on Characterization of Biomass, Biowaste and Related By-Products, 1267–1306. https://doi.org/10.1007/978-3-030-35020-8_14/FIGURES/20

Fall, R. (1999). Biogenic Emissions of Volatile Organic Compounds from Higher Plants. Reactive Hydrocarbons in the Atmosphere, 41–96. https://doi.org/10.1016/B978-012346240-4/50003-5

Friedrich, R., & Obermeier, A. (1999). Anthropogenic Emissions of Volatile Organic Compounds. Reactive Hydrocarbons in the Atmosphere, 1–39. https://doi.org/10.1016/B978-012346240-4/50002-3

Goldman, M. J., Green, W. H., & Kroll, J. H. (2021). Chemistry of Simple Organic Peroxy Radicals under Atmospheric through Combustion Conditions: Role of Temperature, Pressure, and NOx Level. The Journal of Physical Chemistry A, 125(48), 10303–10314. https://doi.org/10.1021/ACS.JPCA.1C07203

Hallquist, M., Wenger, J. C., Baltensperger, U., Rudich, Y., Simpson, D., Claeys, M., Dommen, J., Donahue, N. M., George, C., Goldstein, A. H., Hamilton, J. F., Herrmann, H., Hoffmann, T., Iinuma, Y., Jang, M., Jenkin, M. E., Jimenez, J. L., Kiendler-Scharr, A., Maenhaut, W., … Wildt, J. (2009). The formation, properties and impact of secondary organic aerosol: Current and emerging issues. Atmospheric Chemistry and Physics, 9(14), 5155–5236. https://doi.org/10.5194/ACP-9-5155-2009

Huang, L., Zhao, B., Wang, S., Chang, X., Klimont, Z., Huang, G., Zheng, H., & Hao, J. (2023). Global Anthropogenic Emissions of Full-Volatility Organic Compounds. Environmental Science & Technology, 57(43), 16435–16445. https://doi.org/10.1021/ACS.EST.3C04106

International Energy Agency (IEA). (2016). Weo-2016 Special Report Energy and Air Pollution.

Jacobson, M. C., Hansson, H. C., Noone, K. J., & Charlson, R. J. (2000). Organic atmospheric aerosols: Review and state of the science. Reviews of Geophysics, 38(2), 267–294. https://doi.org/10.1029/1998RG000045;ISSUE:ISSUE:DOI

Jimenez, J. L., Canagaratna, M. R., Donahue, N. M., Prevot, A. S. H., Zhang, Q., Kroll, J. H., DeCarlo, P. F., Allan, J. D., Coe, H., Ng, N. L., Aiken, A. C., Docherty, K. S., Ulbrich, I. M., Grieshop, A. P., Robinson, A. L., Duplissy, J., Smith, J. D., Wilson, K. R., Lanz, V. A., … Worsnop, D. R. (2009). Evolution of organic aerosols in the atmosphere. Science, 326(5959), 1525–1529. https://doi.org/10.1126/SCIENCE.1180353

Johnson, B. T., Shine, K. P., & Forster, P. M. (2004). The semi-direct aerosol effect: Impact of absorbing aerosols on marine stratocumulus. Quarterly Journal of the Royal Meteorological Society, 130(599 PART B), 1407–1422. https://doi.org/10.1256/QJ.03.61;ISSUE:ISSUE:DOI

Kroll, J. H., & Seinfeld, J. H. (2008). Chemistry of secondary organic aerosol: Formation and evolution of low-volatility organics in the atmosphere. Atmospheric Environment, 42(16), 3593–3624. https://doi.org/10.1016/J.ATMOSENV.2008.01.003

Krupa, S. V. . (1997). Air pollution, people, and plants : an introduction. 197. https://books.google.com/books/about/Air_Pollution_People_and_Plants.html?hl=it&id=3bNmQgAACAAJ

Lelieveld, J., Evans, J. S., Fnais, M., Giannadaki, D., & Pozzer, A. (2015). The contribution of outdoor air pollution sources to premature mortality on a global scale. Nature 2015 525:7569, 525(7569), 367–371. https://doi.org/10.1038/nature15371

Li, W., Riemer, N., Xu, L., Wang, Y., Adachi, K., Shi, Z., Zhang, D., Zheng, Z., & Laskin, A. (2024). Microphysical properties of atmospheric soot and organic particles: measurements, modeling, and impacts. Npj Climate and Atmospheric Science 2024 7:1, 7(1), 65-. https://doi.org/10.1038/s41612-024-00610-8

Liora, N., Markakis, K., Poupkou, A., Giannaros, T. M., & Melas, D. (2015). The natural emissions model (NEMO): Description, application and model evaluation. Atmospheric Environment, 122, 493–504. https://doi.org/10.1016/J.ATMOSENV.2015.10.014

Lohmann, U., & Feichter, J. (2005). Global indirect aerosol effects: A review. Atmospheric Chemistry and Physics, 5(3), 715–737. https://doi.org/10.5194/ACP-5-715-2005

McCormick, R. A., & Ludwig, J. H. (1967). Climate modification by atmospheric aerosols. Science, 156(3780), 1358–1359. https://doi.org/10.1126/SCIENCE.156.3780.1358;JOURNAL:JOURNAL:SCIENCE;WGROUP:STRING:PUBLICATION

Ng, N. L., Canagaratna, M. R., Jimenez, J. L., Chhabra, P. S., Seinfeld, J. H., & Worsnop, D. R. (2011). Changes in organic aerosol composition with aging inferred from aerosol mass spectra. Atmospheric Chemistry and Physics, 11(13), 6465–6474. https://doi.org/10.5194/ACP-11-6465-2011

Niranjan, R., & Thakur, A. K. (2017). The Toxicological Mechanisms of Environmental Soot (Black Carbon) and Carbon Black: Focus on Oxidative Stress and Inflammatory Pathways. Frontiers in Immunology, 8(JUN), 763. https://doi.org/10.3389/FIMMU.2017.00763

Pang, Y., Chen, M., Wang, Y., Chen, X., Teng, X., Kong, S., Zheng, Z., & Li, W. (2023). Morphology and Fractal Dimension of Size-Resolved Soot Particles Emitted From Combustion Sources. Journal of Geophysical Research: Atmospheres, 128(6), e2022JD037711. https://doi.org/10.1029/2022JD037711;WGROUP:STRING:PUBLICATION

Pope, C. A., & Dockery, D. W. (2006). Health effects of fine particulate air pollution: Lines that connect. Journal of the Air and Waste Management Association, 56(6), 709–742. https://doi.org/10.1080/10473289.2006.10464485;WGROUP:STRING:PUBLICATION

Putaud, J. P., Van Dingenen, R., Alastuey, A., Bauer, H., Birmili, W., Cyrys, J., Flentje, H., Fuzzi, S., Gehrig, R., Hansson, H. C., Harrison, R. M., Herrmann, H., Hitzenberger, R., Hüglin, C., Jones, A. M., Kasper-Giebl, A., Kiss, G., Kousa, A., Kuhlbusch, T. A. J., … Raes, F. (2010). A European aerosol phenomenology – 3: Physical and chemical characteristics of particulate matter from 60 rural, urban, and kerbside sites across Europe. Atmospheric Environment, 44(10), 1308–1320. https://doi.org/10.1016/J.ATMOSENV.2009.12.011

Ramanathan, V., & Carmichael, G. (2008). Global and regional climate changes due to black carbon. Nature Geoscience 2008 1:4, 1(4), 221–227. https://doi.org/10.1038/ngeo156

Ramanathan, V., Crutzen, P. J., Lelieveld, J., Mitra, A. P., Althausen, D., Anderson, J., Andreae, M. O., Cantrell, W., Cass, G. R., Chung, C. E., Clarke, A. D., Coakley, J. A., Collins, W. D., Conant, W. C., Dulac, F., Heintzenberg, J., Heymsfield, A. J., Holben, B., Howell, S., … Valero, F. P. J. (2001). Indian Ocean Experiment: An integrated analysis of the climate forcing and effects of the great Indo-Asian haze. Journal of Geophysical Research Atmospheres, 106(D22), 28371–28398. https://doi.org/10.1029/2001JD900133;ISSUE:ISSUE:DOI

Riabova, S. A. (2025). Aerosol Pollution of the Atmosphere (Review): Part 1. Sources, Chemical Composition, and Quantity of Natural Primary Aerosol Particles and Their Impact on Human Health. Izvestiya, Atmospheric and Oceanic Physics 2025 61:2, 61(2), 174–196. https://doi.org/10.1134/S0001433825700380

Saraswati. (2022). Characterization of Primary and Secondary Airborne Particulates. Airborne Particulate Matter: Source, Chemistry and Health, 103–129. https://doi.org/10.1007/978-981-16-5387-2_6

Schwarz, J. P., Gao, R. S., Spackman, J. R., Watts, L. A., Thomson, D. S., Fahey, D. W., Ryerson, T. B., Peischl, J., Holloway, J. S., Trainer, M., Frost, G. J., Baynard, T., Lack, D. A., de Gouw, J. A., Warneke, C., & Del Negro, L. A. (2008). Measurement of the mixing state, mass, and optical size of individual black carbon particles in urban and biomass burning emissions. Geophysical Research Letters, 35(13), 13810. https://doi.org/10.1029/2008GL033968;CTYPE:STRING:JOURNAL

Seinfeld, J. H. ., & Pandis, S. N. . (2016). Atmospheric chemistry and physics : from air pollution to climate change. 1120.
https://books.google.com/books/about/Atmospheric_Chemistry_and_Physics.html?hl=it&id=n_RmCgAAQBAJ

Sengupta, D., Samburova, V., Bhattarai, C., Moosmüller, H., & Khlystov, A. (2023). Emission factors for polycyclic aromatic hydrocarbons from laboratory biomass-burning and their chemical transformations during aging in an oxidation flow reactor. Science of The Total Environment, 870, 161857. https://doi.org/10.1016/J.SCITOTENV.2023.161857

Thoma, M., Bachmeier, F., Knauf, K., David, J., Simon, M., & Vogel, A. L. (2025). Seasonal analysis of organic aerosol composition resolves anthropogenic and biogenic sources at a rural background station in central Europe. Environmental Science: Atmospheres, 5(6), 703–713. https://doi.org/10.1039/D4EA00163J

Wang, L., Lun, X., Wang, Q., & Wu, J. (2024). Biogenic volatile organic compounds emissions, atmospheric chemistry, and environmental implications: a review. Environmental Chemistry Letters 2024 22:6, 22(6), 3033–3058. https://doi.org/10.1007/S10311-024-01785-5

WHO (World Meteorological Organization). (2016). Ambient air pollution: A global assessment of exposure and burden of disease.

Zhang, Y., Cheng, M., Gao, J., & Li, J. (2023). Review of the influencing factors of secondary organic aerosol formation and aging mechanism based on photochemical smog chamber simulation methods. Journal of Environmental Sciences, 123, 545–559. https://doi.org/10.1016/J.JES.2022.10.033

Ziemann, P. J., & Atkinson, R. (2012). Kinetics, products, and mechanisms of secondary organic aerosol formation. Chemical Society Reviews, 41(19), 6582–6605. https://doi.org/10.1039/C2CS35122F

2. WP1: The effect of ozone on soot formation in partially premixed laminar methane/air flames

2.1 Chapter Summary

The harmful impacts of soot on the environment and human health are well documented, and combustion processes figure among the major sources of atmospheric soot. For this reason, considerable efforts have been made to develop technological strategies and methodologies to reduce flame-released emissions. Among them, the use of dopants has shown great potential for altering combustion chemistry and limiting soot emissions.

This study investigates the impact of ozone addition on soot production in partially laminar methane–air flames at two equivalence ratios (Φ = 11.9 and Φ = 7.6), doped with 500 ppm and 570 ppm of O_3, respectively. Once formed in flame, soot particles were collected along the flame centerline at different heights above the burner to capture their evolution at different oxidation stages. The characterization of their size, morphology and chemical structure was performed through differential mobility analysis, atomic force microscopy (AFM), and Raman spectroscopy. At the same time, flame temperatures were assessed via thermophoretic particle densitometry (TPD).

Results showed that ozone addition decreased both soot number concentration and average particle size. In particular, particles released by doped flames exhibited flatter height profiles, attributable to reduced cross-linking within the aromatic network. Raman spectroscopy revealed a shift towards larger aromatic structures, whereas flame temperature did not show any alteration after the addition of the dopant molecule. This result suggested that the observed modification may arise from chemical rather than thermal effects. These findings support the hypothesis that ozone enhances the concentration of reactive oxygen atoms in the post-flame region, which readily interact with aromatic π-radicals, key intermediates in soot formation.

2.2 Introduction

The harmful effects of soot inhalation and its atmospheric-induced alterations are well established. As regulations become increasingly stringent, the development of economically and environmentally sustainable technologies has become central to the transition towards a cleaner future.

Among the technological approaches aimed at reducing pollutant emissions and improving combustion efficiency, plasma-assisted combustion (PAC) represents a prominent example. This technique exhibits strong potential in terms of combustion efficiency and flame control, and simultaneous reduction in NO_x emissions and particulate matter release (Cha et al., 2005; Lee et al., 2013). Plasma-flame coupling naturally generates a variety of reactive species including free electrons, ions, active radicals and excited molecules, all of which play an active role in flame chemistry. These species can enhance fuel oxidation, by shortening ignition delay times and accelerating flame propagation (Lacoste, 2023). Despite challenges such as flame stabilization under high-pressure conditions, the overall advantages of PAC and the positive effects of long-lifetime excited molecules in flame have highlighted the potentialities of doped combustion systems as strategic systems for emissions reduction.

Dopants influence the combustion chemistry by altering the reactive pathways and eventually suppressing the formation of potentially harmful compounds. Several studies have shown that the injection in the flame of excited long-lifetime molecules can positively impact on the flame stabilization and uniformity (Sun et al., 2019). Among the most promising active species, ozone (O_3) stands out.

Within the combustion framework, studies by Ombrello et al. and Ying et al. examined the impact of ozone addition on different combustion systems by measuring flame temperature, soot formation tendency, and other physicochemical alterations (Ombrello et al., 2010; Ying et al., 2023a).

Reactive molecules, including ozone, are expected to interfere with soot formation by altering the complex network of chemical reactions driving particle formation and growth from gaseous precursors. Within this context, polycyclic aromatic hydrocarbons (PAHs) are recognized to be key intermediates in soot formation, and eventually altering their formation pathways may translate into alterations in the subsequently generated soot structure. Given the variety of possible PAHs that may form, understanding their formation mechanisms may be particularly challenging. In this framework, a significant breakthrough in PAHs chemistry has been the identification and characterization of resonantly stabilized aromatic π-radicals (RSRs) as key intermediates in PAHs and, consequently, in soot nucleation and growth (Lieske et al., 2023). Despite their acknowledged importance, details about RSRs chemical behaviour in flame and their involvement in soot formation, remain only partially understood. The role of aromatic π-radicals with localized π-electrons on zig-zag edges in particle inception process was first suggested by Wang et al., who proposed possible mechanisms linking RSRs and soot formation (H. Wang, 2011). More recently, some mass spectrometry results presented by Johansson et al. highlighted the role of radical-chain propagation mechanisms in promoting the aromatic growth (Johansson et al., 2018). These latter investigations supported the existence of molecular clustering pathways driven by radical-chain reactions of π-radicals, which promote the formation of covalently bound complexes (Johansson et al., 2018). Schenk et al. also proved the presence of RSRs in different flame-extracted gas-phase samples (Schenk et al., 2015). Based on mass spectrometry results, they proposed a mechanism involving hydrogen removal from saturated -CH_2 groups in PAHs containing five-membered rings. This abstraction would explain the formation of stable radical structures, i.e. RSRs, in concentrations comparable to their parent closed shell molecule. This finding has also been confirmed by Faccinetto et al. whose AFM results pointed out the tendency of sp^3 carbons in methyl groups (-CH_3) to lose one hydrogen, forming methylene groups (-CH_2) and corresponding RSRs (Faccinetto et al., 2020). The role of π-radicals was ultimately confirmed by Martin et al., who advocated the radicals-dominant contribution in early soot nanoparticles formation and inception. Using non-contact AFM together with electron paramagnetic resonance, they confirmed the presence of π-radicals in soot extracted from laminar premixed flames (Martin et al., 2021). Their observation of localized π-electrons on non-hexagonal rings explained the presence of ground-state triplet diradicals on certain Kekulè-type aromatic soot precursors, implying the availability of unpaired electrons requiring little or no activation energy. As a result, these radicals can readily promote the formation of larger and more stable aromatic structures, which may subsequently act as early-stage precursors in soot formation (Martin et al., 2021).

Ozone has been identified as a possible interfering molecule affecting RSRs formation and consequently soot generation.

In this WP1, an investigation of the effects of ozone on a methane/air diffusion flame was performed. The main goal was to clarify its impact on π-radicals and, consequently, on PAHs formation and soot generation. Diffusion flames are of interest in many industrial applications, being involved in several combustion devices. Methane, as well as ethylene, is a key hydrocarbon that was chosen since its simple structure may reduce the uncertainties related to the investigation of ozone-linked reactivity.

The analysis explores the chemical, physical, and morphological characteristics of two main combustion systems with two different equivalence ratios, Φ=11.9 and 7.6, each examined with and without ozone injection. Diagnostic techniques employed in the current investigations include temperature monitoring, particle-size distribution analysis, atomic force microscopy, and Raman spectroscopy. The synergistic application of these instrumental techniques was aimed at accurately characterizing the structural and functional properties of the released soot. Details about the ozone chemistry in flame, the

expected outcomes, and the discussion of the experimental results is presented in the following paragraphs.

2.2.1 Chemistry of the System

Flame Chemistry

Controlled combustion is a topic of interest for both laboratorial investigation and industrial processes. Based on the combustion setup, it is possible to classify flames into premixed and non-premixed (diffusion) ones. In premixed systems, the fuel and the oxidizer flows are mixed before reaching the combustion zone, whereas in diffusion flames, the feeding of the two compounds is separated. In this last case, both the mixing and the subsequent combustion happen within the combustion chamber. Premixed flames usually exhibit higher propagation rates compared to diffusion ones since the propagation starts upon ignition whereas in diffusion systems there is a delay between flame ignition and initiation.

Diffusion flames are broadly implemented for modern technological purposes, such as in diesel vehicles or jet engines, as for research aims. Local mixing uniformities are frequent to occur within diffusion flames, hence they usually exhibit a more consistent soot production. A schematic representation of a one-dimensional diffusion flame is reported in Figure 1.

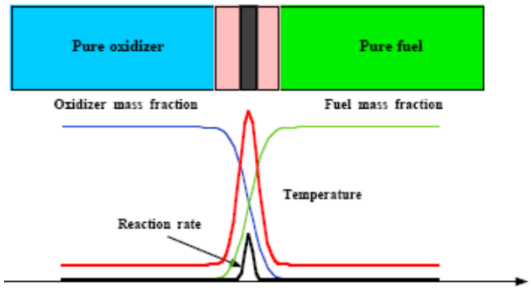

Figure 1: Schematic of a diffusion flame

Some key parameters are traditionally adopted to characterize combustion systems, like unburnt gas velocity and fuel-to-air ratio, also known as equivalence ratio.

The equivalence ratio is a dimensionless parameter that correlates the actual amount of fuel and oxidizer adopted in a combustion process to the quantities required to achieve a complete combustion (McAllister et al., 2011), as reported in Equation 1:

$$\Phi = \frac{\left[\frac{m_{fuel}}{m_{ox}}\right]_{real}}{\left[\frac{m_{fuel}}{m_{ox}}\right]_{stoic}} \quad \text{(Eq. 1)}$$

In this formulation, m_{fuel} and m_{ox} represent the flows of fuel and oxidizer injected within the system, respectively.

Based on this value, it is possible to classify the flames into:

- Lean flames achieved whenever the $\Phi<1$. In this case there is an excess of oxidizer compared to the fuel amount.
- Stoichiometric flames, when $\Phi=1$. Ideally in this case, the amount of oxidizer fuelled in the system ensures the completion of fuel combustion.
- Rich flames, whenever $\Phi>1$ so the oxidizer present in the system is not sufficient to complete the combustion. (Melton et al., 2000).

Effects of ozone on flame properties

Ozone is characterized by a long lifetime and strong oxidizing properties. It presents a multifaced role, since it can impact ignition acceleration, flame propagation enhancement and stabilization. Its long-lived character makes it easy to be transported with relatively low losses. Moreover, its production does not require additional storage of fluids or gases since it can be easily obtained from oxygen, a primary oxidizer in the great majority of combustion systems. Several studies indicate that adding O_3 to flames strongly affects soot formation and particle release (Iamcheerangkoon et al., 2025; Scribano et al., 2022; Ying & Liu, 2023). Nevertheless, the specific mechanisms by which ozone influences flame chemistry are still poorly understood.

Speculations about the impact of ozone injection within the flame were proposed by Ying et al. (Ying et al., 2023b). The study reports the impact of ozone on the formation and evolution of soot in an inverse diffusion ethylene flame, reporting how it can promote the formation of free radicals and active substances, which increase soot formation and agglomeration. Higher ozone levels lead to larger primary particle diameters, enhanced agglomeration, increased oxygen content on the soot surface and a lower sp^2/sp^3 ratio, indicating greater oxygen reactivity of the generated soot.

The thermal and kinetic effects of ozone introduction on flame propagation in a laminar non-premixed propane flame were investigated by Ombrello et al. (Ombrello et al., 2010). An enhancement in the flame propagation speed by 8% was registered after the dopant introduction.

The reason behind this result could be attributed to the decomposition reaction that leads to the formation of bimolecular (O_2) and atomic (O) oxygen. Evidence shows that this reaction may occur already in the pre-heating stage. Ombrello et al. proposed also an additional pathway involving H atom with the following pathway:

$$O_3 + H \rightarrow O_2 + OH \qquad (R1)$$

This reaction, together with other involved mechanisms, contributes to the formation of water molecules and to additional heat release. These two factors may explain the registered flame speed increment in ozone-doped systems. Furthermore, the released OH may also interact with fuel molecules and fuel-derived fragments, leading to an additional release of water molecules and heat, which increase the local temperature and consequently the flame propagation rate.

Alterations of the burning velocities after ozone injections were also registered for methane premixed flames by Wang et al. (Z. H. Wang et al., 2012). In this latter study, the analysis of the dopant impact on methane/air flames with equivalence ratios equal to 0.6, 1.0 and 1.45, is proposed. As for the previous cases, an increase in the burning velocity was registered, probably due to the presence of O_3 in the pre-flame zone enhancing the formation of intermediates species like HO_2, H_2O and CH_2O. Furthermore, based on the burning conditions, O_3 molecules seem to impact on the concentration of active radicals like H, O and OH. In particular, in lean and rich combustion conditions O_3 molecules double the concentrations of these active radicals, whereas no significant changes were observed in stoichiometric conditions.

Temperature increases in the pre-heat and combustion zone were registered after O_3 introduction, by both Ombrello et al. (Ombrello et al., 2010), and Wang et al. (Z. H. Wang et al., 2012).

Similar results were also observed for ethylene-fuelled combustion, H_2/CO experiments, n-heptane, iso-octane and other fuels (Foucher et al., 2013; Masurier et al., 2015; Y. Zhang et al., 2016).

Particularly relevant for real-life applications is the study proposed by Foucher et al. where the investigation of the effects of ozone on HCCI (homogeneous charge compression ignition) combustion on n-heptane is presented (Foucher et al., 2013). This study shows how ozone decomposition can trigger a sequence of reactions leading to an earlier oxidation of the fuel in the ozone-doped systems.

Consistently with the previously discussed experiments, ozone-seeded conditions increase the OH-radicals production, thereby advancing the reaction time. Similar results were also observed for iso-octane fuelled HCCI (Masurier et al., 2015).

Finally, ozone seems to affect not only flame temperature, burning velocity, and ignition delay time of hydrocarbon flames but also the flammability limit. Researchers have shown that the ozone addition noticeably impacts the combustion process by expanding the flammability limits of the system. The kinetic studies confirm the impact of ozone molecules on chain branching reactions and on the increase of active radicals in the system (Y. Zhang et al., 2016).

Despite these macro-effects caused by the introduction of ozone in flame, the understanding of the main chemical mechanisms affected by the O_3-molecule addition remains extremely challenging. Details related to the chemical modification caused by the addition of ozone in flame are reported below.

Effects of Ozone on Flame Chemistry

Ozone chemistry represents a fascinating topic which has mainly been explored by atmospheric scientists and only recently became of attention to the combustion community. This paragraph aims to summarize the main mechanisms involving ozone within combustion systems.

Decomposition

Ozone role in flame mainly proceeds through decomposition reactions occurring already in the pre-heating zone of the flame and promoting early fuel oxidation. The decomposition reaction is reported below:

$$O_3 + M = O_2 + O + M \quad \text{(R2)}$$

M denotes the so-called third-body reactant, representing the ensemble of the collision species. The reaction rate can be described by a modified Arrhenius equation in the form of:

$$k = AT^n e^{-\frac{Ea}{RT}} \quad \text{(Eq. 2)}$$

where A is the pre-exponential factor, T is the temperature and n is its dimensionless exponent, E_a corresponds to the activation energy and R is the universal gas constant.

Since 1950s, numerous studies have been carried out to constrain the range of possible reaction rates as a function of temperature and pressure, thereby improving the accuracy of kinetic and chemical models. The effect of various species implemented as third-body compounds has been studied, such as nitrogen molecules (N_2), argon (Ar), carbon dioxide (CO_2) or even Kripton (Kr) (Benson & Axworthy, 1957; Endo et al., 2002; Peukert et al., 2013). At its low-pressure limit, the decomposition reaction exhibits bimolecular behaviour, whereas at high-pressure limit it approaches a unimolecular character.

2.2.2 Ozone Reaction with Radicals

Understanding the behaviour of ozone with radicals is extremely important since, radicalic elements are ubiquitous components of all the combustion systems. In this context, the key reactions are reported in the following equations (Sun et al., 2019):

$$O_3 + H = O_2 + OH \quad (R3)$$

$$O_3 + H = HO_2 + O \quad (R4)$$

$$O_3 + OH = O_2 + HO_2 \quad (R5)$$

$$O_3 + HO_2 = O_2 + O_2 + OH \quad \text{(R6)}$$

$$O_3 + O = O_2 + O_2 \quad \text{(R7)}$$

Despite R3 was firstly investigated in the early 1960s, only subsequent studies focused the reaction rate-temperature correlation, using both an experimental and theoretical approach (Clyne & Monkhouse, 1977; DeMore et al., 1997; Phillips & Schiff, 1962). This reaction is a critical step which explains the presence of OH radicals in the early stage of combustion (Yelugoti & Wang, 2022).

Studies conducted at ambient temperature on reaction R4 were proposed by Phillips et al. (Phillips & Schiff, 1962). Followed by investigations on its temperature dependency (DeMore et al., 1997; Shaw, 1977; Yu & Varandas, 1997). Fewer studies were conducted for reactions R5, R6 and R7 and mainly in narrow temperature intervals, exhibiting reaction rate values within the range of 10^{10}-10^{11} $cm^3molec^{-1}s^{-1}$, for temperature ranges from 200 to 500 K, and between $5x10^8$ and $2x10^9$ $cm^3molec^{-1}s^{-1}$ for temperature range from 100 up to 2000 $cm^3molec^{-1}s^{-1}$ for R5 and R6, respectively (Atkinson, Baulch, Cox, Hampson, et al., 1997; Ju et al., 2007; Shaw, 1977).

2.2.3 Ozone Reactions with hydrocarbons

Ozone interactions with hydrocarbons can strongly vary based on the saturated or unsaturated structure of the investigated compound. Reactions with unsaturated hydrocarbons, mainly alkenes, tend to be relevantly fast. In these pathways, the first step is usually an exothermic cycloaddition of ozone to the alkene species, generally referred to as *ozonolysis reaction*. This step can be schematically reported as

$$O_3 + Fuel = Products + Heat$$

The reaction rate ranges of alkanes and alkenes can vary by several orders of magnitudes. For instance, at 300K the reaction between methane (CH_4) and O_3 shows a k approximately of 0.99 $cm^3/mol*s$ (Schubert & Pease, 2002), whereas the reaction of ethylene (C_2H_4) with O_3 presents a reaction rate of 1.12×10^6 $cm^3/mol*s$ (DeMore et al., 1997). In order to evidence the differences registered for the two classes of compounds, some examples of selected alkenes and alkanes reaction rates are reported in Table 1.

Table 1: Reaction Rates of key Alkanes and Alkenes with Ozone

	Chemical Formula	Compound	K [$cm^3/mol\ s$]	Reference
Alkanes	CH_4	Methane	0.99	(Schubert & Pease, 2002)
	C_2H_6	Ethane	8.95	(Morrissey & Schubert, 1963)
	C_3H_8	Propane	4.17	(Morrissey & Schubert, 1963)
Alkenes	C_2H_4	Ethylene	$1.12x10^6$	(DeMore et al., 1997)
	C_3H_6	Propylene	$6.29x10^6$	(Atkinson, Baulch, Cox, Crowley, et al., 1997)

The recorded difference in terms of reaction rates of the two groups of compounds is mainly attributed to their molecular structure. In this context, an interesting example may be represented by trans-2-butene (trans-2-C_4H_8), cis-2-butene (cis-2-C_4H_8), iso-C_4H_8 and 1-butene (1-C_4H_8), which show the same chemical formula but reaction rates equal to $1.43x10^8$, $7.77x10^7$, $6.68x10^6$ and $5.82x10^6$ $cm^3molec^{-1}s^{-1}$ (Wegener et al., 2007).

Reactions with alkanes have been investigated since XIIX century (Dillemuth et al., 2002). For instance, the interactions between methane molecules and ozone at room temperature were investigated already

in 1998 by Otto et al. (Otto, 1898). Later investigations highlighted the impact of temperature on ozone reactivity (Blair & Wheeler, 1922) and identified the initial steps of ozone-driven attack to hydrocarbons (Briner & Carceller, 1935). Subsequently, Kleimenov et al. correlated the appearance of oxygenated products at high temperature to ozone decomposition (Kleimenov N.A. & Nalbandyan A. B., 1958). This study first theorized the importance of the preliminary ozone decomposition and of the subsequent attack of the atomic oxygen to the hydrocarbon molecule, summarizing the reaction mechanism as follows:

$$O_3 \rightarrow O_2 + O \quad \text{(R8)}$$

$$RH + O \rightarrow R + OH + other\ products \quad \text{(R9)}$$

Concerning alkenes reacting with ozone, a complete ozonolysis mechanism was proposed by Criegee in 1975 (Criegee, 1975). The first step involves a 1,3-dipolar cycloaddition of O_3 to the alkene. During this stage the double carbon-carbon bond is cleaved upon reaction with O_3, leading to the formation of a five-membered cyclic structure. This intermediate is known as primary ozonide (POZ) which is usually unstable under atmospheric conditions, tending to decomposition. The POZ decomposition results in the formation of a carbonyl compound and a carbonyl oxide, defined as *Criegee intermediate*, which results in an excited state. A schematic of a generic alkene ozonolysis is reported in Figure 2 (Tobias & Ziemann, 2001).

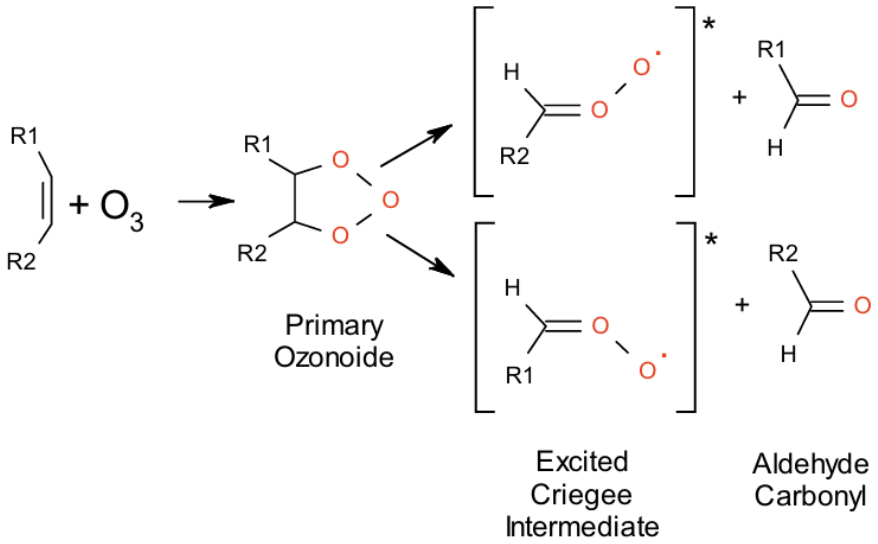

Figure 2: Initial Steps of an Alkene Ozonolysis

In the gas phase, about 50% of *Criegee intermediates* are stabilized through collisions, while the other 50% undergo decomposition or react with other hydrocarbon species (Anglada et al., 1999; Neeb et al., 1998). Anglada et al. reported the simplest *Criegee intermediate*, linked to the ethylene (C_2H_4) chemistry (Anglada et al., 1999). For ethylene, CH_2O is the carbonyl compound and CH_2OO* is the excited *Criegee intermediate*, which can eventually be stabilized by collision. Because of its instability, the detection of *Criegee intermediates* is extremely challenging, even if it has been performed using photoionization time-of-flight mass spectrometer (Taatjes et al., 2008) or chemical ionization mass spectrometer (Berndt et al., 2017). Due to their complexity, the reaction pathways following the POZ decomposition are still unclear. Subsequent studies performed by Criegee, suggested that the *Criegee intermediate* and the carbonyl compound may undergo recombination reactions, leading to secondary ozonide (SOZ) formation. Other studies suggested a unimolecular decomposition of the *Criegee intermediate* consisting in various potential pathways accurately described by Anglada et al. (Anglada et al., 1999) .The first channel, also named "ester channel", involves a first isomerization to dioxirane and a consequent decomposition into H_2O+CO or H_2+CO_2 or 2H+CO. The "hydroperoxide channel" is the second possible

pathways which consists in one hydrogen atom migration and it involves a tautomerization of the carbonyl oxides to the hydroperoxide which can eventually decompose into OH molecules- The third and last pathway is the oxygen-atom channel, which involves the splitting off of O_3(P) (Anglada et al., 1999; Sun et al., 2019). Strong influences of the pressure on the relative branching ratios of *Criegee intermediate* decomposition have been registered (Olzmann et al., 1997).

Chemistry involving the *Criegee intermediates* is also strongly present in the atmosphere, mainly for the chemistry of some monoterpenes. More details about this process will be discussed in the following chapters.

2.3 Experimental Setup

In this study, a co-flow partially premixed methane/air laminar flame is studied using an atmospheric-pressure, axisymmetric burner analogous to the experimental systems adopted by McEnally et al. and DeFalco et al. (De Falco et al., 2018; McEnally & Pfefferle, 1999).

The fuel and primary air mixture reaches the flame zone through an uncooled vertical tube with an inner diameter (I.D.) of approximately 1.2cm. In the current investigation, a distinction between primary and secondary air is introduced: primary air refers to the flow required to achieve complete combustion whereas secondary air corresponds to the additional air flow supplied to the combustion zone to stabilize the flame. Secondary air is supplied through an annular region formed by a concentric tube with inner diameter of 10.8cm. Flame stabilization is further achieved by reducing the air anulus with a 5.5cm I.D. ring positioned at the burner exit. A scheme of the burner is reported in Figure 3.

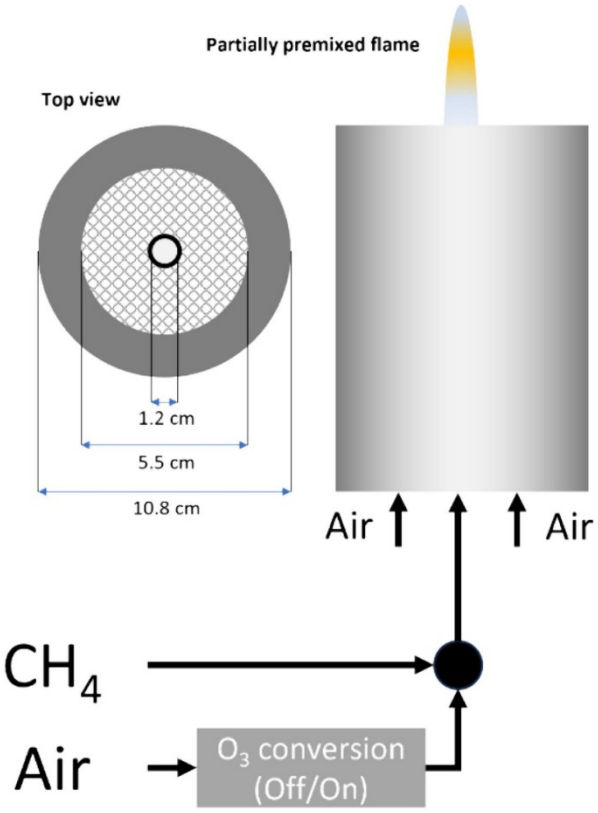

Figure 3: Schematic of the co-flow partially premixed burner setup. Ozone from the UV lamp is fed into the premixing air without changing the equivalence ratio by converting a fraction of O_2 into O_3.

The amount of primary air sent to the combustion zone is regulated by Bronkhorst-designed mass flow controllers (models F-201AV and F-201CV), whose calibration is performed with a primary flow calibrator from Gilian (model Gilibrator-2), aiming to correlate the nominal flowrate values to the real

oxidizer and fuel flowrates. An ES-2600 ASA-manufactured flowmeter is used to control secondary air flow.

Based on the primary air, two equivalence ratios are investigated, equal to 11.9 and 7.6, respectively. Details about the specific fluxes and the experimental conditions are reported in Table 2. For each flame, doped and un-doped conditions are investigated, resulting in four flames analysed in total.

Table 2: Investigated Experimental Conditions. O_3 is the ozone concentration injected in the flame, Q_{CH4}, Q_{PA} and Q_{SA} are the volumetric flowrates of methane, primary and secondary air respectively.

Flame	Φ	O_3 [ppm]±10ppm	Q_{CH4} [l/min] ±0.01 l/min	Q_{PA} [l/min] ±0.01 l/min	Q_{SA} [Nl/min] ±0.01 Nl/min
Φ7.6	7.6	0	0.40	0.50	4000
Φ7.6$_{O3}$	7.6	570	0.40	0.50	4000
Φ11.9	11.9	0	0.40	0.32	4000
Φ11.9$_{O3}$	11.9	500	0.40	0.32	4000

Similar studies investigating the effects of ozone on methane/air lean flames have been proposed by Wang et al. and Ombrello et al. (Ombrello et al., 2010; Z. Wang et al., 2007). These investigations primarily focused on lean combustion regimes, with equivalence ratios ranging from 0.6 to 1.2. Conversely, the present study aims to explore the impact of ozone molecules on rich flames, characterized by an enhanced soot production. In this case, Φ values of 7.6 and 11.9 were selected to investigate soot formation in two different rich systems. Conversely, lower equivalence ratios would result in limited soot formation, potentially compromising the efficacy of diagnostic techniques such as Raman spectroscopy. On the other hand, excessively high equivalence ratios would increase soot loading and decrease oxygen content, hindering the ability to isolate the effects of ozone on early soot formation.

As reported in Table 2, the two equivalence ratios of 11.9 and 7.6, were obtained by keeping a constant fuel flowrate (Q_{CH4}) for both flames while varying only primary air flow (Q_{PA}). Secondary air flow was kept constant for all the experimental setups.

In the doped flame, a fixed amount of ozone was injected into the system at concentrations of 500 ppm and 570 ppm for Φ11.9 and Φ7.6, respectively. The ozone flux was generated using the Model 1001 Ozone Generator released by Jelight Company Inc. This technology consists in an electropolished stainless steel cell containing internal UV lamp, deputed to the ozone formation. Ozone concentration was monitored using a Model205 Dual Beam Ozone Monitor by 2B Technologies. In literature, ozone concentrations ranging from 10ppm to 1000ppm are typically employed to mimic realistic conditions as those that can be encountered in internal combustion engines (Foucher et al., 2013; Salahi & Gharehghani, 2019). Laboratory-scale experiments tend to explore wider ozone concentration ranges, reaching values between 2750ppm and 5500 in Ying et al. work (Ying et al., 2023b) and 100ppm-5000ppm in Cheng et al. (Cheng & Scribano, 2024). In the present study, the applied ozone concentrations were mainly dictated by two main limiting factors. The first one is related to the ozone generator: the selected model could only achieve an oxygen-to-ozone conversion efficiency of 0.25% on the inlet oxygen. The other limiting condition is linked to the need to stabilize the flame by using the selected air-flow conditions. Nonetheless, the selected conditions fall within the range of ozone concentrations implemented in other studies (Cheng & Scribano, 2024; Foucher et al., 2013; Salahi & Gharehghani, 2019).

For both Φ11.9 and Φ7.6, fuel and primary air mixture were convoyed to the burner with a velocity of 11.8cm/s and 13.2cm/s, respectively, and no significant changes in the total inlet velocity were registered after the ozone addition.

A Canon EOS 1100D digital camera was used to capture flame images. Consistent acquisition parameters were applied across all the combustion conditions: resolution equal to 1920 x 1030 pixels, a focal length of 18mm, ISO set to 100, exposure time of 4 seconds and a diaphragm aperture of f/22.

An R-type thermocouple (Pt/Pt-13%Rh) with a spherical junction of 300μm diameter was adopted for thermophoretic particle densitometry (TPD). This technique was first used to estimate the particle volume fraction in flames using thermocouple signals (Eisner & Rosner, 1985; McEnally et al., 1997). In the present study, a fast-insertion procedure was employed for TPD measurements (Kent & Wagner, 1984). A significant risk in these temperature measurements within sooting-flames is related to the thermocouple coating by soot particles. This phenomenon has been documented by Basile et al. and Abed et al. (Abid et al., 2008; Basile et al., 2002). The adoption of fast-injection methods for TPD measurements overcomes this problem. Temperature measurements were corrected for radiation losses, following the procedure recorded by McEnally et al. (McEnally et al., 1997). Based on this methodology, a balance equation considering both the gas and the junction temperature can be formulated as follows (McEnally et al., 1997):

$$\varepsilon_j \sigma {T_j}^4 = \left(\frac{k_{g0} Nu_j}{2d_j}\right)\left({T_g}^2 - {T_j}^2\right) \quad \text{(Eq. 3)}$$

In this formulation, the prevailing junction emissivity is expressed as ε_j, σ is the Stefan-Boltzmann constant, Nu_j represents the Nusselt number of the junction, d_j is the prevailing junction diameter. The constant k_{g0} is assumed to be equal to the ratio of k_g over T_g, where kg is the gas thermal conductivity and T_g is the temperature of the gas. T_j is the junction temperature. Overall, the left side of the equation represents the radiation heat loss per unit area, whereas the righten side is the convection heat gain per unit area.

The physical characteristics of the particles released by the different flames were investigated through particle size distribution (PSD) functions analysis, registered by differential mobility analyzer (DMA) system. The DMA included an electrostatic aerosol classifier Vienna–type DMA (TapCon 3/150, size range of 1–40 nm), a TSI-released X-ray diffusion charging source (Model 3088), and a Faraday cup electrometer. The X-ray source was positioned at the entrance of the TapCon3/150 DMA. The soot sampling occurred through a horizontal stainless steel tubular probe, with outer diameter of 1cm and an orifice (inner diameter of 0.2mm, thickness of 0.5mm) positioned downward at the flame centreline. A dilution of the sampled flow was performed using gaseous nitrogen in a dilution ratio of 1:3000. The goal of this procedure is to prevent particle aggregation and quench any further chemical process within the probe tube (Commodo et al., 2015; Zhao et al., 2003). The samples were collected at different heights (Z) along the flame centerline, ranging from 34 to 49mm. This technique contributed to the monitoring of the particles evolution by analyzing them at different stages of the aging process.

The particle size analysis was coupled with thermophoretic samplings, aiming to characterize the released particles morphologically. These further samplings were performed through rapid insertions of atomically flat mica substrates held by TEM grid holders. A pneumatic fast actuator enabled sample collection within the combustion region at different heights. The thermophoretic samples deposited on freshly cleaved mica substrates were analysed by atomic force microscopy (AFM) with 10ms insertions at Zs equal to 34, 37 and 43mm.

The morphological properties of the released particles were analysed using a Scanning Probe Microscope NTEGRA Prima (NT-MDT), operated in semi-contact mode in air. Supersharp silicon probes (SSS-NCHR, from NANOSENSORS) were employed, featuring a nominal tip radius of 2 nm, a spring

constant of 42 N/m, and a resonant frequency of 285 kHz. The image processing was performed using Gwyddion software (Nečas & Klapetek, 2011).

For Raman spectroscopy analysis, thermophoretic sample collection was performed by repeatedly inserting the samples for 30ms per flame. The Raman spectra of soot particles deposited on 3mm sections of silver filters were acquired using a Horiba XploRA Raman microscope system, equipped with a 50× objective (NA 0.9, Olympus). The excitation source was a dual-frequency Nd:YAG laser with λ = 532 nm. The choice of key parameters, including laser beam power, exposure time, and diffraction grating, was optimized to achieve optimal resolution and to avoid structural changes due to thermal decomposition. Raman spectra were recorded with a laser beam power attenuated by 10%, equal to 1.2 mW. A diffraction grating with 1200 grooves/mm was picked, and each spectrum was acquired over five cycles, each lasting 60 seconds. For each sample, 10 randomly selected spots were averaged to obtain a statistically significant Raman spectra. After the acquisition, all spectra were baseline-corrected and normalized to the G-peak at approximately 1600 cm^{-1}.

2.4 Results

2.4.1 RGB Image Analysis

Images of partially premixed methane/air flames at equivalence ratios of Φ = 11.9 and Φ = 7.6 have been collected under both doped and undoped conditions using a Canon EOS 1100D digital camera. The pictures are reported in Figure 4. In green, the heights at which the samples for further analysis have been extracted are highlighted.

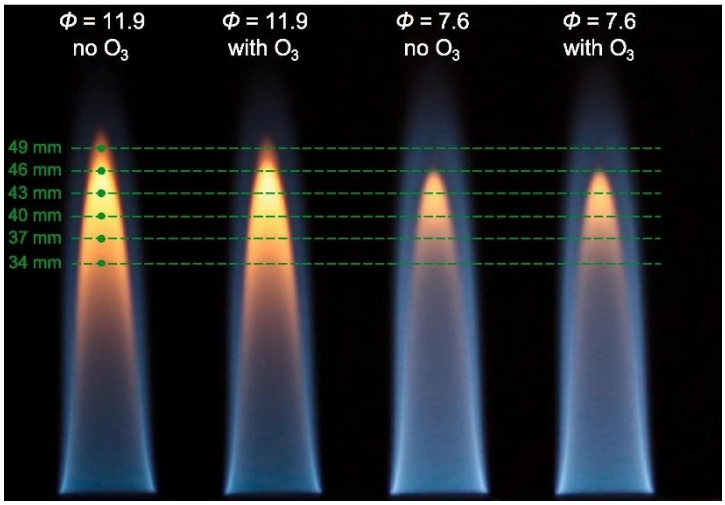

Figure 4: Pictures of partially premixed methane/air flames at two equivalence ratios, i.e., Φ = 11.9 and Φ = 7.6, without and with ozone introduction. Green-dashed lines refer to the sampling positions above the burner exit.

The ozone addition is barely detectable to the naked eye, whereas changes in flame luminosity are recorded by high-resolution camera imaging. After O_3 introduction, the acquisitions show a slight decrease of the overall flame luminosity, especially in the upper part of the combustion system. Details about the luminosity differences have been detected through a preliminary quantitative RGB analysis. Due to the flame axial-symmetry, the RGB signals were extracted along the flame axis, and the analysis was performed through the open-source software Gwyddion.

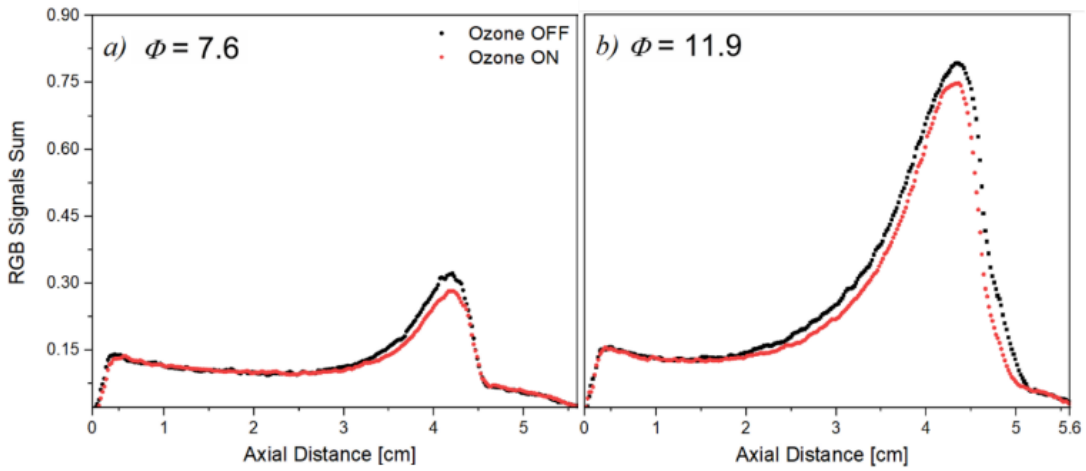

Figure 5: RGB Signals Sum vs. the axial distance (height above the burner) of (a) Φ = 7.6 and (b) Φ = 11.9. The black curves represent the ozone-free condition, and the red curves the ozonized flames.

Figure 5 presents the axial profiles of the RGB signals for each flame in ozone-free and ozone-doped conditions. The reduction in the sum of the RGB signals after O_3 injection is accurately captured by the curves. The effects of the introduction of the dopant are not only observable in terms of RGB sum but also by looking at the RED channel itself. The RED component of the RGB signal can indeed be associated with a soot-induced coloration (H. W. Huang & Zhang, 2010).

The values, normalized to the full-scale value of the colour channel, are reported in Table 3. Along the entire flame centreline, Φ7.6 flame presents a similar intensity decrease in the signals; on the other hand, the exhibited intensity difference registered for the Φ11.9 flame appears to be higher at Z=43mm and Z=34mm compared to Z=37mm.

Table 3: Normalized intensity signals recorded from the RED channel of the digital images for the different flame conditions, at the height positions selected for the sampling.

	Normalized RED Intensity		**RED Intensity Percentage Decrease**	**Normalized RED Intensity**		**RED Intensity Percentage Decrease**
	Φ=7.6	**Φ=7.6 with O_3**		**Φ=11.9**	**Φ=11.9 with O_3**	
Z=34 mm	0.153	0.147	3.7%	0.644	0.595	7.6%
Z=37 mm	0.375	0.361	3.9%	0.903	0.868	3.9%
Z=43 mm	0.012	0.011	3.3%	0.782	0.705	9.8%

2.4.2 Temperature Profiles

The temperature profiles of the analysed combustion conditions are reported in Figure 6. As for the proposed RGB analysis, the profiles were collected along the central axis of the flames, Φ11.9 and Φ7.6, in doped and undoped conditions. From the curves, it is possible to highlight that no significant temperature change can be observed after the introduction of ozone molecules in the system. The low ozone concentrations adopted in this study may explain the low sensitivity of the flame temperature to the dopant introduction. As previously mentioned, the influence of ozone on flame temperature is accurately documented in literature but its effect on temperature becomes significant only at high ozone concentrations (Ying et al., 2023b). Indeed, as reported by Cheng et al., ozone addition in low concentrations has a negligible or absent effect on flame temperature at atmospheric pressure (Cheng & Scribano, 2024).

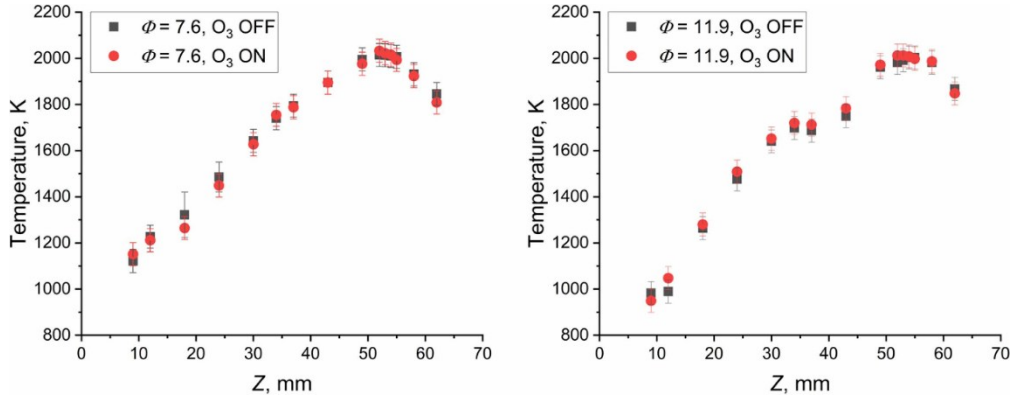

Figure 6: Temperature profiles for Φ=7.6 (left pane) and Φ=11.9 (right panel), with and without ozone.

2.4.3 Particle Size Distribution Curves

The particle size distribution functions were collected from the flame exhaust at two flame tip positions, Z=49 mm and Z=46 mm. For each of the investigated combustion conditions, the resulting PSDs curves are reported in Figure 7.

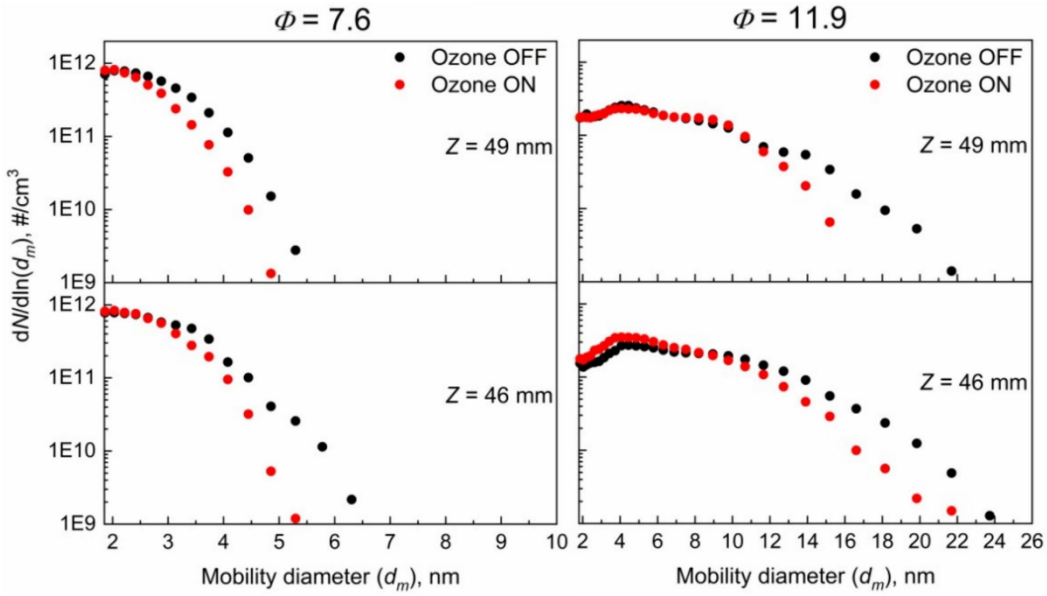

Figure 7: Particle size distribution functions collected at the centreline for Φ=7.6 (left panel) and Φ=11.9 (right panel) with and without ozone.

For both doped and undoped conditions, the flame Φ7.6 results in a monomodal distribution, whereas the Φ11.9 function shows a clear bimodal trend. Despite their different equivalence ratio, each flame shows a decrease in the particle number in the upper part of the flame, consequent to the dopant addition. This result may be explained either by greater reactivity of the generated soot toward oxidation after O_3 injection, or by lower soot concentration or nucleation due to ozone introduction.

2.4.4 Atomic Force Microscopy Analysis

Semi-contact atomic force microscopy (AFM) was used to investigate the morphology of soot particles at Z values of 43 mm, 37 mm, and 34 mm. The collection of particles (or clusters of particles) via rapid substrate insertions into the flame enabled direct and effective analysis of the sampled materials. Figure 8 shows the AFM results for each flame at various heights. Coherent with the expectations, at the same Z, Φ11.9 shows larger particles than those formed at Φ7.6. This result can be readily explained by the smaller amount of premixed air in the Φ11.9 flame. Furthermore, the reduction of the equivalent ratio

impacts also on the surface coverage and the collected volume of the particles, key parameters to consider in AFM analysis.

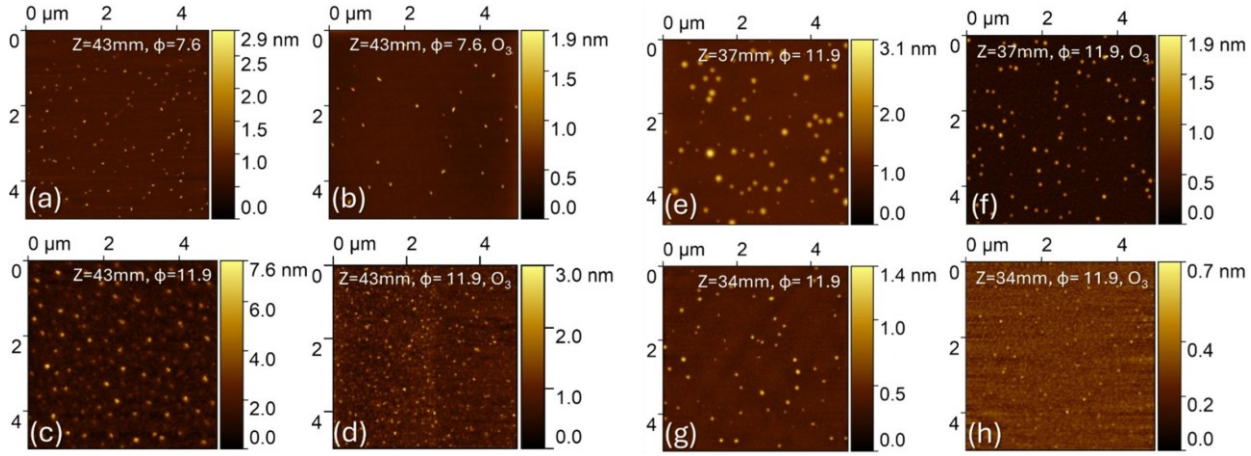

Figure 8: AFM semi-contact images of 5 μm × 5 μm areas acquired on samples with soot particles sampled in flames with (a-b) Φ = 7.6 at Z = 43 mm, and Φ = 11.9 at (c-d) Z = 43 mm, (e-f) Z = 37 mm, and (g-h) Z = 34 mm. The left panels show images of particles sampled without ozone while the right panels show images of samples collected with ozone addition.

At Z=43 mm, the Φ11.9 flame shows a coverage of 5.9% and a total volume of $1.38x10^{-3}$ μm^3 whereas 1.16% coverage and a $0.12x10^{-3}$ μm^3 are registered for Φ7.6. Accordingly, at the same quota, the surface roughness (RRMS) is reduced in the flame with greater oxygen premixing, reaching 0.12 nm in Φ7.6 compared to a value 0.59 nm registered for Φ11.9. These results suggest that ozone introduction impacts on the collected particles by altering several properties. Indeed, for both flames, at Z=43 mm, the surface coverage is reduced after the O_3 introduction, going from 2.2% to 0.74% in doped conditions for Φ11.9 and Φ7.6, respectively. A reduction is also registered in terms of total particle volume and the surface roughness, corresponding to $0.18\times10-3$ μm^3 and an RRMS of 0.23 nm for the flame with Φ11.9 (at Z=43mm), to $0.06\times10-3$ μm^3 and an RRMS of 0.08 nm for the flame with Φ7.6.

The AFM 3D-visualization investigation provides information about the tridimensional characteristics of the released particles. A significant lower height is exhibited by the particles released by ozone-doped flames. This result is reported in Figure 9. All the pictures reported in Figure 9, present an aspect ratio (X: Y: Z) set equal to 1:1:50, aiming to highlight the differences among the various conditions.

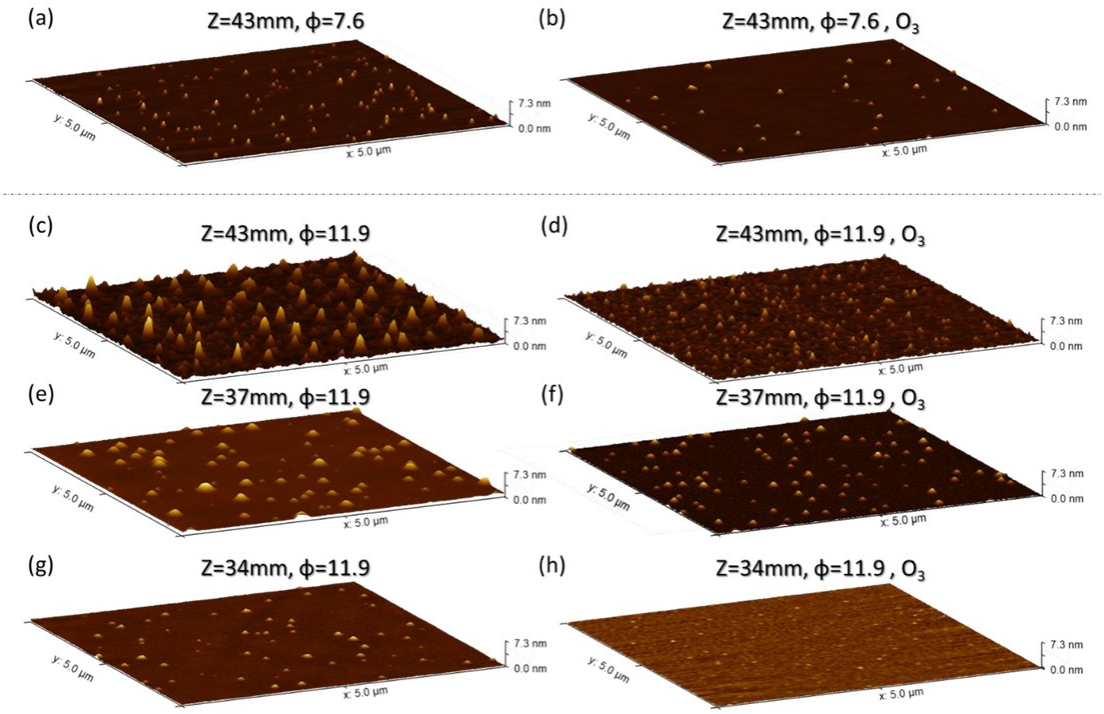

Figure 9: 3D visualization of AFM semi-contact images of 5 µm × 5 µm areas acquired on samples with particles sampled in flame Φ = 7.6 at Z = 43 mm with (a) no ozone, and (b) with ozone addition, and in flame Φ = 11.9 at Z = 43 mm with (c) no ozone, and (d) with ozone addition. The aspect ratio (X:Y:Z) is set to 1:1:50 for all the images to better visualize the height differences between the various conditions.

In agreement with previous studies, the particles deposited on the substrate present a spherical cap morphology. The assumption can be justified by the heights *(h)* being lower than the corresponding basal radius *(rBASE),* as shown by the tridimensional structures. This result is consistent with previous studies obtained with scanning probe microscopy techniques (Barone et al., 2003; Minutolo et al., 2014). The observed shape can be explained considering it as a result of the particle striking on the substrate surface during the sampling process (Veronesi et al., 2022)

Additional details about particles morphology are reported in Figure 10, where the distributions, as relative frequency, of the height and the base radius, are recorded. The measured lateral dimensions of small particles in AFM images represent a convolution of the probe geometry with the actual topography of the sample. It is worth noticing that this result is considered an overestimation of the base radius by 4 to 6nm, corresponding to two or three tip radii (Minutolo et al., 2014). Moreover, to avoid the influence of surface roughness on particle counting for the heigh distribution analysis, the smallest morphological features were excluded from the statistical dataset. With this aim, the single-layer PAHs may have been omitted from the analysis. However, the consistency of the performed analysis is guaranteed by the systematic application of the same methodology for all the flame conditions and so any potential bias related to this criterion is consistently accounted across the entire dataset.

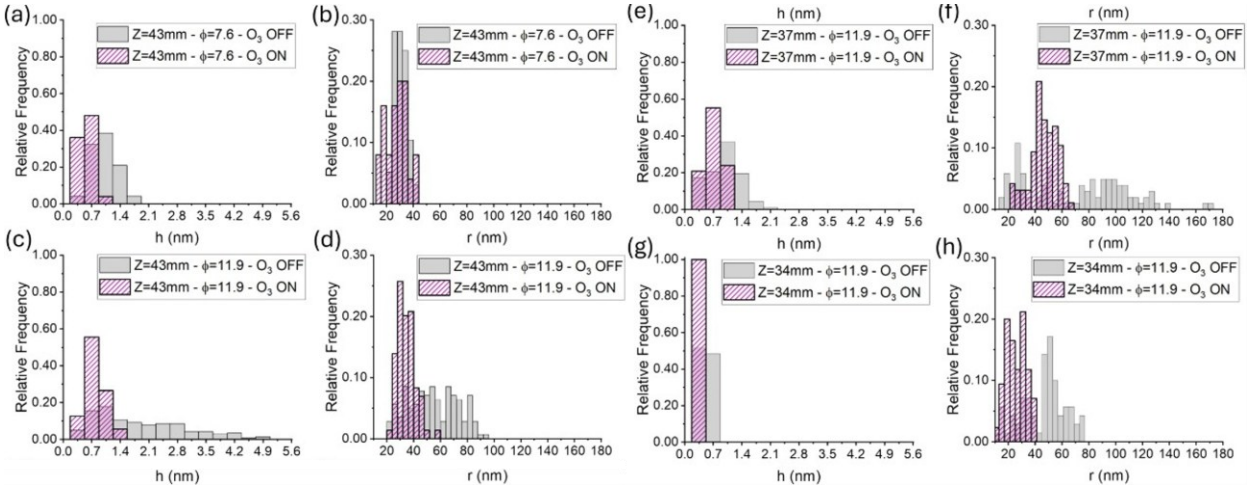

Figure 10: Relative frequency distributions of the height (h) and the base radius (rBASE) of the particles collected in the flames with (a-b) Φ = 7.6 at Z = 43 mm, and Φ = 11.9 at (c-d) Z = 43 mm, (e-f) Z = 37 mm, and (g-h) Z = 34 mm. The grey-filled bins show the distribution of the flames before ozone addition, while the purple slanted-line pattern bins show the distribution of the flames with ozone addition.

The results show a decrease in the average particles height for all the flame conditions; moreover, a narrowing of the distribution caused by the ozone addition is registered in the distribution plot of Figure 10.

At Z=43 mm, the geometric average height ($\langle h_g \rangle$) decrements from 2.0nm to 0.76nm with a geometric standard deviation ($\sigma(h)_g$) narrowing from 3.4nm to 0.32nm for Φ11.9. These values were obtained performing the fitting with a lognormal function. Analogously, at Z=43 mm, also for Φ7.6 a decrease in $\langle h_g \rangle$ is registered (from 0.95 nm to 0.46 nm) and in the same way $\sigma(h)_g$ narrows from 0.41 nm to 0.31nm. The heights of the particles collected in the doped flames are consistent with structures composed by only a few PAH layers, with bin spacing closely corresponding to the PAH interlayer distance.

Table 4: Statistical parameters of sampled soot particle characteristics obtained from AFM morphology measurements in the different flames and at different heights

	Z=43 mm		**Z=43 mm**		**Z=37 mm**		**Z=34 mm**	
Flame Conditions	**Φ7.6**	**$\Phi 7.6_{O3}$**	**Φ11.9**	**$\Phi 11.9_{O3}$**	**Φ11.9**	**$\Phi 11.9_{O3}$**	**Φ11.9**	**$\Phi 11.9_{O3}$**
RRMS [nm]	0.12	0.08	0.59	0.23	0.20	0.14	0.07	0.04
Surface Coverage	1.16%	0.74%	5.90%	2.20%	7.90%	2.70%	2.10%	0.77%
Total Particles Volume [$\cdot 10^{-3}$ μm^3]	0.12	0.06	1.38	0.18	0.9	0.22	0.12	0.02
$\langle h \rangle_g$	0.95	0.46	2.0	0.76	1.20	0.39	0.52	0.35
$\sigma(h)_g$	0.41	0.31	3.4	0.32	1.10	0.32	0.14	0.11

The smaller dimensions exhibited by particles at lower Zs may be explained considering the decrease in the overlapping and the cross-linking of PAH layers. This decrement affects both the height and the base radius of the particles, decreasing them. At Z=37 mm and 34 mm, the sampled particles released by ozonized flames are mainly monolayer molecules.

2.4.5 Raman Spectroscopy Investigation

The investigation of the chemical characteristics of the particles has mainly been performed with Raman Spectroscopy. This analysis not only provided details about the chemical information of the samples but also about the structural properties of the collected molecules. The released soot was thermophoretically collected on silver membranes and the associated Raman spectra for the different flame conditions, are reported in Figure 11.

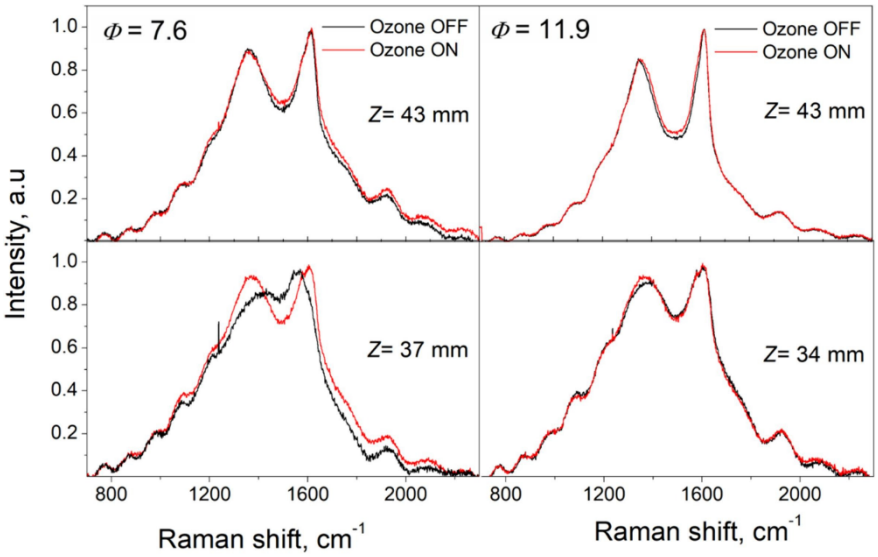

Figure 11: Raman spectra of soot collected at different flame conditions, left panel Φ=7.6 and right panel Φ=11.9

The registered values around 1600 cm^{-1} and 1340 cm^{-1}, of the G and the D band respectively, reveal the amorphous character of the sampled carbon. The sensitivity of the D and G peaks intensities is widely recognized as correlated with the size of the aromatic domains (Ferrari et al., 2004). In highly disordered or amorphous carbonaceous materials, like very small graphite crystallites typical of flame-generated soot, an increment in the D/G ratio reflects an increase in the size of the aromatic structures. Furthermore, for both Φ7.6 and Φ11.9 flames, an increase in the sampling position, Z, reveals a slightly higher D band intensity compared to the G band. This result is coherent to the expected increase in the size of the aromatic domains present in the soot structures. From the Raman spectra, the introduction of ozone within the systems seems to strongly impact on soot formed at lower *Z*, where an increment in the D/G ratio is registered. These values of the D/G ratio, indicate the presence of larger aromatic constituents present in the ozone-doped flames compared to undoped systems. This effect starts to appear at Z=34 mm for Φ11.9 and it becomes more evident at Z=37 mm for Φ7.6. This latter flame condition presents a unique Raman spectrum, that differs from all the others. In particular, a low and not well-resolved D band indicates the presence of small PAHs and the absence of graphitic character in the just nucleated soot. In general, the larger D/G ratio registered in the ozonized flames confirms the effect of O_3 as a promoter of aromatic size growth. Moreover, the deeper valley between the D and G peaks can testify the presence of a better graphitic structure formed after ozone introduction. This result may be attributed to the removal of resonantly stabilized radicals whenever ozone is added. Indeed, O_3-free flames present a high number of radicals formed by non-hexagonal defects. These radicals favour crosslinks between aromatic structures, reducing HACA (Hydrogen-Abstraction–C_2H_2-Addition) growth and producing smaller aromatic structures (Leon et al., 2021). Since from the current results, the chosen concentrations of O_3 seem not to affect the temperature of the system, the registered alteration of soot size, morphology and graphitic structure can be purely addressed to the O_3-induced chemical alteration of the system. The size changes observed after the ozone introduction are consistent with the hypothesized chemical interactions between atomic oxygen and aromatic π-radicals, resulting in a reduced clusterization of soot molecular constituents. Moreover, the interaction between atomic

oxygen and π-radicals in incipient particles can also affect particle coagulation affecting the growth and formation of larger particles. This result is supported by the hypothesis that functional groups containing oxygen might cause a lower coagulation as reported for small soot particles by Stankovich et al. and Bockhorn et al. (Bockhorn et al., 2024; Stankovich et al., 2006). In these studies, the effect of oxygen removal in particles was investigated through a reduction with hydrazine. An increase in terms of particle coagulation in both incipient soot particles (Bockhorn et al., 2024) and graphene oxide composites was registered (Stankovich et al., 2006).

In conclusion, the effect of ozone is mainly registered in lower Z positions whereas the oxidative flame regions, i.e. higher Zs, do not show structural changes associated to the presence of O_3 molecules. The main effect at higher Zs lies in a slightly increased intervalley region signal registered in the doped flame from the Raman spectra of the doped flames. In this region of the spectrum, the main contribution to the signal is represented by the amorphous carbon. Its increment can be justified by a stronger oxidation tendency in soot released by O_3-added flames. Similar effect was presented by Kelesidis et al. (Kelesidis et al., 2023), where a correlation between O_2 oxidation in mature soot and amorphous phase content increase by fragmentation was recorded.

2.5 Conclusions

The effects of the addition of ozone to a methane/air diffusion flame were discussed in this study. In the current investigation, ozone was proposed as possible dopant to reduce the production of soot. With this purpose, two premixed flames with two equivalence ratios, Φ11.9 and Φ7.6 were investigated. Each of these flames was studied in ozone-free and ozone-doped conditions. Ozone has been introduced in the combustion system, by direct conversion of part of the premixed oxygen of the air flow. Soot samples were extracted at different flame positions to investigate the impact of ozone on the entire soot evolution, from nucleation to growth stages. The investigations were conducted using thermocouple measurements, atomic force microscopy, differential mobility analysers and Raman spectroscopy. The aim of the combination of these techniques stands in the necessity of characterizing the released soot from the physical to morphological to chemical point of view. From the performed investigation it is possible to extract some key points:

- O_3 affects the particle nucleation and growth by removing the resonantly stabilized radicals. This interaction explains the reduction in terms of grown particles observed after the introduction of ozone.
- AFM results reveal a reduction in both number and site of soot particles, down to few-layers PAHs.
- Ozonized conditions present flatter particles compared to O_3-free flames, revealing lower levels of cross-linking in the aromatic networks forming the particles.
- Raman spectra exhibit higher intensity ratios of the D peak over the G one whenever ozone is added to the system. This is particularly evident at lower heights, hence for young soot particles, evidencing larger aromatic soot constituents.
- Ozonized conditions showed a lower number of aromatic cross-links enabling HACA mechanism to proceed more effectively, which results in the formation of larger aromatic species.

For the employed ozone concentrations, a clear effect of O_3 introduction on flame temperature was not registered. The similarity in the temperature profiles for doped and undoped flames reveals that the registered alterations in the soot inception and growth after O_3 addition can be mainly ascribed to chemical effects. This assumption is consistent with the role attributed in literature to atomic oxygen and aromatic π-radicals, precursors of the soot particles. Indeed, the presence of higher oxygen concentrations due to the O_3 decomposition, can result in a reduced chemical clusterization of soot molecular constituents and decreased incipient soot coagulation.

2.6 Further Steps

The effects of ozone addition to a methane/air diffusion flame were discussed in this study, with ozone proposed as a potential dopant to mitigate soot formation. The results highlighted the clear impact of the introduction of the dopant on soot formation and, this preliminary investigation could motivate further and deeper analysis.

While this study focuses on the morphological, structural and size evolution of soot particles, the observed chemical modifications strongly suggest that ozone addition may also alter the nature and reactivity of gas-phase precursors and primary aerosol emissions. This highlights the need to extend the analysis beyond soot morphology, encompassing both gaseous species and the broader aerosol population released by combustion sources. In particular, investigating how these emissions evolve under atmospheric oxidation conditions is essential to assess their contribution to primary and POA and SOA formation. This perspective naturally motivates the investigation presented in the following chapter, which addresses the chemical transformation of flame-generated emissions and their role in SOA formation.

2.7 References

Abid, A. D., Heinz, N., Tolmachoff, E. D., Phares, D. J., Campbell, C. S., & Wang, H. (2008). On evolution of particle size distribution functions of incipient soot in premixed ethylene–oxygen–argon flames. Combustion and Flame, 154(4), 775–788. https://doi.org/10.1016/J.COMBUSTFLAME.2008.06.009

Anglada, J. M., Crehuet, R., & Bofill, J. M. (1999). The Ozonolysis of Ethylene: A Theoretical Study of the Gas-Phase Reaction Mechanism. www.wiley-vch.de/home/chemistry/

Atkinson, R., Baulch, D. L., Cox, R. A., Crowley, J. N., Hampson, R. F., Hynes, R. G., Jenkin, M. E., Kerr, J. A., Rossi, M. J., & Troe, J. (1997). Summary of Evaluated Kinetic and Photochemical Data for Atmospheric Chemistry IUPAC Subcommittee on Gas Kinetic Data Evaluation for Atmospheric Chemistry. http://www.iupac-kinetic.ch.cam.ac.uk/.

Atkinson, R., Baulch, D. L., Cox, R. A., Hampson, R. F., Kerr, J. A., Rossi, M. J., & Troe, J. (1997). Evaluated Kinetic, Photochemical and Heterogeneous Data for Atmospheric Chemistry: Supplement V. IUPAC Subcommittee on Gas Kinetic Data Evaluation for. IUPAC Subcommittee on Gas Kinetic Data Evaluation for Atmospheric Chemistry Journal of Physical and Chemical Reference Data, 26, 881. https://doi.org/10.1063/1.556010

Barone, A. C., D'Alessio, A., & D'Anna, A. (2003). Morphological characterization of the early process of soot formation by atomic force microscopy. Combustion and Flame, 132(1–2), 181–187. https://doi.org/10.1016/S0010-2180(02)00434-0

Basile, G., Rolando, A., D'Alessio, A., D'Anna, A., & Minutolo, P. (2002). Coagulation and carbonization processes in slightly sooting premixed flames. Proceedings of the Combustion Institute, 29(2), 2391–2397. https://doi.org/10.1016/S1540-7489(02)80291-7

Benson, S. W., & Axworthy, A. E. (1957). Mechanism of the Gas Phase, Thermal Decomposition of Ozone. The Journal of Chemical Physics, 26(6), 1718–1726. https://doi.org/10.1063/1.1743610

Berndt, T., Herrmann, H., & Kurtén, T. (2017). Direct Probing of Criegee Intermediates from Gas-Phase Ozonolysis Using Chemical Ionization Mass Spectrometry. Journal of the American Chemical Society, 139(38), 13387–13392. https://doi.org/10.1021/JACS.7B05849

Blair, E. W., & Wheeler, T. S. (1922). The oxidation of hydrocarbons, with special reference to the production of formaldehyde. J. Soc. Chem. Ind., 41, 303–310.

Bockhorn, H., D'Anna, A., Sarofim, A. F., & Wang, H. (2024). Nanoparticles of organic carbon (NOC) formed in flames and their effect in urban atmospheres. Combustion Generated Fine Carbonaceous Particles, 205–230. https://iris.cnr.it/handle/20.500.14243/210865

Briner, E., & Carceller, J. (1935). Recherches sur le rôle de l'ozone comme catalyseur d'oxydation. VIII. Ozonation du propane et du butane. Helv. Chim. Acta, 18, 973–981.

Cha, M. S., Lee, S. M., Kim, K. T., & Chung, S. H. (2005). Soot suppression by nonthermal plasma in coflow jet diffusion flames using a dielectric barrier discharge. Combustion and Flame, 141(4), 438–447. https://doi.org/10.1016/J.COMBUSTFLAME.2005.02.002

Cheng, X., & Scribano, G. (2024). A numerical study on the laminar diffusion and premixed flames for methane–air and methane–ethanol with ozone at atmospheric and elevated pressures. Combustion and Flame, 259, 113100. https://doi.org/10.1016/J.COMBUSTFLAME.2023.113100

Clyne, M. A. A., & Monkhouse, P. B. (1977). Atomic resonance fluorescence for rate constants of rapid bimolecular reactions. Part 5—Hydrogen atom reactions; H + NO2 and H + O3. Journal of the Chemical Society, Faraday Transactions 2: Molecular and Chemical Physics, 73(2), 298–309. https://doi.org/10.1039/F29777300298

Commodo, M., De Falco, G., Bruno, A., Borriello, C., Minutolo, P., & D'Anna, A. (2015). Physicochemical evolution of nascent soot particles in a laminar premixed flame: from nucleation to early growth. Combustion and Flame, 162(10), 3854–3863. https://doi.org/10.1016/J.COMBUSTFLAME.2015.07.022

Criegee, R. (1975). Mechanism of Ozonolysis. Angewandte Chemie International Edition in English, 14(11), 745–752. https://doi.org/10.1002/ANIE.197507451

De Falco, G., Sirignano, M., Commodo, M., Merotto, L., Migliorini, F., Dondè, R., De Iuliis, S., Minutolo, P., & D'Anna, A. (2018). Experimental and numerical study of soot formation and evolution in co-flow laminar partially premixed flames. Fuel, 220, 396–402. https://doi.org/10.1016/J.FUEL.2018.02.028

DeMore, W. B., Sander, S. P., Golden, D. M., Hampson, R. F., Kurylo, M. J., Howard, C. J., Ravishankara, A. R., Kolb, C. E., & Molina, M. J. (1997). Chemical Kinetics and Photochemical Data for Use in Stratospheric Modeling.

Dillemuth, F. J., Skidmore, D. R., & Schubert, C. C. (2002). THE REACTION OF OZONE WITH METHANE. Journal of Physical Chemistry, 64(10), 1496–1499. https://doi.org/10.1021/J100839A035

Eisner, A. D., & Rosner, D. E. (1985). Experimental studies of soot particle thermophoresis in nonisothermal combustion gases using thermocouple response techniques. Combustion and Flame, 61(2), 153–166. https://doi.org/10.1016/0010-2180(85)90161-0

Endo, H., Glänzer, K., & Troe, J. (2002). Shock wave study of collisional energy transfer in the dissociation of nitrogen dioxide, nitrosyl chloride, ozone, and nitrous oxide. Journal of Physical Chemistry, 83(16), 2083–2090. https://doi.org/10.1021/J100479A007

Faccinetto, A., Irimiea, C., Minutolo, P., Commodo, M., D'Anna, A., Nuns, N., Carpentier, Y., Pirim, C., Desgroux, P., Focsa, C., & Mercier, X. (2020). Evidence on the formation of dimers of polycyclic aromatic hydrocarbons in a laminar diffusion flame. Communications Chemistry 2020 3:1, 3(1), 112-. https://doi.org/10.1038/s42004-020-00357-2

Ferrari, A. C., Robertson, J., Ferrari, A. C., & Robertson, J. (2004). Raman spectroscopy of amorphous, nanostructured, diamond–like carbon, and nanodiamond. Philosophical Transactions of the Royal Society A: Mathematical, Physical and Engineering Sciences, 362(1824), 2477–2512. https://doi.org/10.1098/RSTA.2004.1452

Foucher, F., Higelin, P., Mounam-Rousselle, C., & Dagaut, P. (2013). Influence of ozone on the combustion of n-heptane in a HCCI engine. Proceedings of the Combustion Institute, 34(2), 3005–3012. https://doi.org/10.1016/J.PROCI.2012.05.042

Huang, H. W., & Zhang, Y. (2010). Dynamic application of digital image and colour processing in characterizing flame radiation features. Measurement Science and Technology, 21(8). https://doi.org/10.1088/0957-0233/21/8/085202

Iamcheerangkoon, T., Prodkornburee, T., Chollacoop, N., Sawatmongkhon, B., Sittichompoo, S., Theinnoi, K., & Promhuad, P. (2025). Plasma-Assisted Soot Oxidation: Ozone and NO2 as Dual Oxidants for Efficient Diesel Particulate Filter Regeneration. ACS Omega, 10(45), 55008–55020. https://doi.org/10.1021/ACSOMEGA.5C09243

Johansson, K. O., Head-Gordon, M. P., Schrader, P. E., Wilson, K. R., & Michelsen, H. A. (2018). Resonance-stabilized hydrocarbon-radical chain reactions may explain soot inception and growth. Science, 361(6406), 997–1000. https://doi.org/10.1126/SCIENCE.AAT3417;PAGEGROUP:STRING:PUBLICATION

Ju, L. P., Han, K. L., & Varandas, A. J. C. (2007). Variational transition-state theory study of the atmospheric reaction OH + O3 → HO2 + O2. International Journal of Chemical Kinetics, 39(3), 148–153. https://doi.org/10.1002/KIN.20226;WGROUP:STRING:PUBLICATION

Kelesidis, G. A., Nagarkar, A., Trivanovic, U., & Pratsinis, S. E. (2023). Toward Elimination of Soot Emissions from Jet Fuel Combustion. Environmental Science and Technology, 57(28), 10276–10283. https://doi.org/10.1021/acs.est.3c01048

Kent, J. H., & Wagner, H. G. (1984). Why do Diffusion Flames Emit Smoke? Combustion Science and Technology, 41(5–6), 245–269. https://doi.org/10.1080/00102208408923834;ISSUE:ISSUE:DOI

Kleimenov N.A., & Nalbandyan A. B. (1958). “A study of low-temperature methaneoxidation initiated by oxygen atoms formed during thermal disintegration of ozone.” Dokl. Akad. Nauk SSSR, 122:3 420–423. https://www.mathnet.ru/php/archive.phtml?wshow=paper&jrnid=dan&paperid=23461&option_lang=eng

Lacoste, D. A. (2023). Flames with plasmas. Proceedings of the Combustion Institute, 39(4), 5405–5428. https://doi.org/10.1016/J.PROCI.2022.06.025

Lee, D. H., Kim, K. T., Kang, H. S., Song, Y. H., & Park, J. E. (2013). Plasma-Assisted Combustion Technology for NOx Reduction in Industrial Burners. Environmental Science and Technology, 47(19), 10964–10970. https://doi.org/10.1021/ES401513T

Leon, G., Martin, J. W., Bringley, E. J., Akroyd, J., & Kraft, M. (2021). The role of oxygenated species in the growth of graphene, fullerenes and carbonaceous particles. Carbon, 182, 203–213. https://doi.org/10.1016/J.CARBON.2021.05.052

Lieske, L. A., Commodo, M., Martin, J. W., Kaiser, K., Benekou, V., Minutolo, P., D’Anna, A., & Gross, L. (2023). Portraits of Soot Molecules Reveal Pathways to Large Aromatics, Five-/Seven-Membered Rings, and Inception through π-Radical Localization. ACS Nano, 17(14), 13563–13574. https://doi.org/10.1021/ACSNANO.3C02194

Lohmann, U., Friebel, F., Kanji, Z. A., Mahrt, F., Mensah, A. A., & Neubauer, D. (2020). Future warming exacerbated by aged-soot effect on cloud formation. Nature Geoscience 2020 13:10, 13(10), 674–680. https://doi.org/10.1038/s41561-020-0631-0

Martin, J. W., Pascazio, L., Menon, A., Akroyd, J., Kaiser, K., Schulz, F., Commodo, M., D’Anna, A., Gross, L., & Kraft, M. (2021). π-Diradical Aromatic Soot Precursors in Flames. Journal of the American Chemical Society, 143(31), 12212–12219. https://doi.org/10.1021/JACS.1C05030/SUPPL_FILE/JA1C05030_SI_005.MP4

Masurier, J. B., Foucher, F., Dayma, G., & Dagaut, P. (2015). Investigation of iso-octane combustion in a homogeneous charge compression ignition engine seeded by ozone, nitric oxide and nitrogen dioxide. Proceedings of the Combustion Institute, 35(3), 3125–3132. https://doi.org/10.1016/J.PROCI.2014.05.060

McAllister, S., Chen, J.-Y., & Fernandez-Pello, A. C. (2011). Fundamentals of Combustion Processes. https://doi.org/10.1007/978-1-4419-7943-8

McEnally, C. S., Köylü, Ü. Ö., Pfefferle, L. D., & Rosner, D. E. (1997). Soot volume fraction and temperature measurements in laminar nonpremixed flames using thermocouples. Combustion and Flame, 109(4), 701–720. https://doi.org/10.1016/S0010-2180(97)00054-0

McEnally, C. S., & Pfefferle, L. D. (1999). Experimental study of nonfuel hydrocarbon concentrations in coflowing partially premixed methane/air flames. Combustion and Flame, 118(4), 619–632. https://doi.org/10.1016/S0010-2180(99)00017-6

Melton, T. R., Inal, F., & Senkan, S. M. (2000). The effects of equivalence ratio on the formation of polycyclic aromatic hydrocarbons and soot in premixed ethane flames. Combustion and Flame, 121(4), 671–678. https://doi.org/10.1016/S0010-2180(99)00180-7

Minutolo, P., Commodo, M., Santamaria, A., De Falco, G., & D’Anna, A. (2014). Characterization of flame-generated 2-D carbon nano-disks. Carbon, 68, 138–148. https://doi.org/10.1016/J.CARBON.2013.10.073

Morrissey, R. J., & Schubert, C. C. S. J. (1963). The reactions of ozone with propane and ethane. Combustion and Flame, 7, 263–268. https://doi.org/10.1016/0010-2180(63)90191-3

Nečas, D., & Klapetek, P. (2011). Gwyddion: an open-source software for SPM data analysis. Central European Journal of Physics 2011 10:1, 10(1), 181–188. https://doi.org/10.2478/S11534-011-0096-2

Neeb, P., Horie, O., & Moortgat, G. K. (1998). The Ethene−Ozone Reaction in the Gas Phase. Journal of Physical Chemistry A, 102(34), 6778–6785. https://doi.org/10.1021/JP981264Z

Niranjan, R., & Thakur, A. K. (2017). The Toxicological Mechanisms of Environmental Soot (Black Carbon) and Carbon Black: Focus on Oxidative Stress and Inflammatory Pathways. Frontiers in Immunology, 8(JUN), 763. https://doi.org/10.3389/FIMMU.2017.00763

Olzmann, M., Kraka, E., Cremer, D., Gutbrod, R., & Andersson, S. (1997). Energetics, kinetics, and product distributions of the reactions of ozone with ethene and 2,3-dimethyl-2-butene. Journal of Physical Chemistry A, 101(49), 9421–9429. https://doi.org/10.1021/JP971663E

Ombrello, T., Won, S. H., Ju, Y., & Williams, S. (2010). Flame propagation enhancement by plasma excitation of oxygen. Part I: Effects of O3. Combustion and Flame, 157(10), 1906–1915. https://doi.org/10.1016/J.COMBUSTFLAME.2010.02.005

Otto, M. (1898). Ozone. Annales de Chimie et de Physique, 13(7), 77–144.

Peukert, S. L., Sivaramakrishnan, R., & Michael, J. V. (2013). High Temperature Shock Tube Studies on the Thermal Decomposition of O3 and the Reaction of Dimethyl Carbonate with O-Atoms. Journal of Physical Chemistry A, 117(18), 3729–3738. https://doi.org/10.1021/JP400613P

Phillips, L. F., & Schiff, H. I. (1962). Mass Spectrometric Studies of Atomic Reactions. III. Reactions of Hydrogen Atoms with Nitrogen Dioxide and with Ozone. The Journal of Chemical Physics, 37(6), 1233–1238. https://doi.org/10.1063/1.1733270

Rauscher, H., Kestens, V., Rasmussen, K., Linsinger, T., & Stefaniak, E. (2023). Guidance on the implementation of the Commission Recommendation 2022/C 229/01 on the definition of nanomaterial. https://doi.org/10.2760/237496

Salahi, M. M., & Gharehghani, A. (2019). Control of combustion phasing and operating range extension of natural gas PCCI engines using ozone species. Energy Conversion and Management, 199, 112000. https://doi.org/10.1016/J.ENCONMAN.2019.112000

Schenk, M., Hansen, N., Vieker, H., Beyer, A., Gölzhäuser, A., & Kohse-Höinghaus, K. (2015). PAH formation and soot morphology in flames of C4 fuels. Proceedings of the Combustion Institute, 35(2), 1761–1769. https://doi.org/10.1016/J.PROCI.2014.06.139

Schubert, C. C., & Pease, R. N. (2002). The Oxidation of Lower Paraffin Hydrocarbons. I. Room Temperature Reaction of Methane, Propane, n-Butane and Isobutane with Ozonized Oxygen1. Journal of the American Chemical Society, 78(10), 2044–2048. https://doi.org/10.1021/JA01591A006

Scribano, G., Cheng, X., & Tran, M. V. (2022). Numerical study on the effects of ozone addition on the development of laminar premixed flames and emissions for methane and propane in a co-flow configuration. Energy, 243, 122744. https://doi.org/10.1016/J.ENERGY.2021.122744

Shaw, R. (1977). Estimation of rate constants as a function of temperature for the reactions W + XYZ = WX + YZ, where W, X, Y, and Z are H or O atoms. International Journal of Chemical Kinetics, 9(6), 929–941. https://doi.org/10.1002/KIN.550090608

Stankovich, S., Dikin, D. A., Dommett, G. H. B., Kohlhaas, K. M., Zimney, E. J., Stach, E. A., Piner, R. D., Nguyen, S. B. T., & Ruoff, R. S. (2006). Graphene-based composite materials. Nature, 442(7100), 282–286. https://doi.org/10.1038/NATURE04969

Sun, W., Gao, X., Wu, B., & Ombrello, T. (2019). The effect of ozone addition on combustion: Kinetics and dynamics. Progress in Energy and Combustion Science, 73, 1–25. https://doi.org/10.1016/J.PECS.2019.02.002

Taatjes, C. A., Meloni, G., Selby, T. M., Trevitt, A. J., Osborn, D. L., Percival, C. J., & Shallcross, D. E. (2008). Direct Observation of the Gas-Phase Criegee Intermediate (CH2OO). Journal of the American Chemical Society, 130(36), 11883–11885. https://doi.org/10.1021/JA804165Q

Tobias, H. J., & Ziemann, P. J. (2001). Kinetics of the Gas-Phase Reactions of Alcohols, Aldehydes, Carboxylic Acids, and Water with the C13 Stabilized Criegee Intermediate Formed from Ozonolysis of 1-Tetradecene. Journal of Physical Chemistry A, 105(25), 6129–6135. https://doi.org/10.1021/JP004631R

Veronesi, S., Commodo, M., Basta, L., De Falco, G., Minutolo, P., Kateris, N., Wang, H., D'Anna, A., & Heun, S. (2022). Morphology and electronic properties of incipient soot by scanning tunneling microscopy and spectroscopy. Combustion and Flame, 243, 111980. https://doi.org/10.1016/J.COMBUSTFLAME.2021.111980

Wang, H. (2011). Formation of nascent soot and other condensed-phase materials in flames. Proceedings of the Combustion Institute, 33(1), 41–67. https://doi.org/10.1016/J.PROCI.2010.09.009

Wang, Z. H., Yang, L., Li, B., Li, Z. S., Sun, Z. W., Aldén, M., Cen, K. F., & Konnov, A. A. (2012). Investigation of combustion enhancement by ozone additive in CH4/air flames using direct laminar burning velocity measurements and kinetic simulations. Combustion and Flame, 159(1), 120–129. https://doi.org/10.1016/J.COMBUSTFLAME.2011.06.017

Wang, Z., Zhou, J., Zhu, Y., Wen, Z., Liu, J., & Cen, K. (2007). Simultaneous removal of NOx, SO2 and Hg in nitrogen flow in a narrow reactor by ozone injection: Experimental results. Fuel Processing Technology, 88(8), 817–823. https://doi.org/10.1016/J.FUPROC.2007.04.001

Wegener, R., Brauers, T., Koppmann, R., Bares, S. R., Rohrer, F., Tillman, R., Wahner, A., Hansel, A., & Wisthaler, A. (2007). Simulation chamber investigation of the reactions of ozone with short-chained alkenes. Journal of Geophysical Research: Atmospheres, 112(D13), 13301. https://doi.org/10.1029/2006JD007531

Yelugoti, S. R., & Wang, W. C. (2022). The effect of ozone addition on the combustion characteristics of hydrogen-jet fuel. Combustion and Flame, 245, 112337. https://doi.org/10.1016/J.COMBUSTFLAME.2022.112337

Ying, Y., & Liu, D. (2023). Formation and Evolution of Soot in Ethylene Inverse Diffusion Flames in Ozone Atmosphere. Nanomaterials (Basel, Switzerland), 13(5). https://doi.org/10.3390/NANO13050816

Ying, Y., Liu, D., Ying, Y., & Liu, D. (2023a). Formation and Evolution of Soot in Ethylene Inverse Diffusion Flames in Ozone Atmosphere. Nanomaterials 2023, Vol. 13, 13(5). https://doi.org/10.3390/NANO13050816

Ying, Y., Liu, D., Ying, Y., & Liu, D. (2023b). Formation and Evolution of Soot in Ethylene Inverse Diffusion Flames in Ozone Atmosphere. Nanomaterials 2023, Vol. 13, 13(5). https://doi.org/10.3390/NANO13050816

Yu, H. G., & Varandas, A. J. C. (1997). Dynamics of H(D) + O3 reactions on a double many-body expansion potential-energy surface for ground state HO3. Journal of the Chemical Society, Faraday Transactions, 93(16), 2651–2656. https://doi.org/10.1039/A700762K

Zhang, Y., Zhu, M., Zhang, Z., Shang, R., & Zhang, D. (2016). Ozone effect on the flammability limit and near-limit combustion of syngas/air flames with N2, CO2, and H2O dilutions. Fuel, 186, 414–421. https://doi.org/10.1016/J.FUEL.2016.08.094

Zhao, B., Yang, Z., Wang, J., Johnston, M. V., & Wang, H. (2003). Analysis of soot nanoparticles in a laminar premixed ethylene flame by scanning mobility particle sizer. Aerosol Science and Technology, 37(8), 611–620. https://doi.org/10.1080/02786820300908;ISSUE:ISSUE:DOI

3. WP2: A laboratory study of secondary organic aerosol formation in an oxidation flow reactor

3.1 Chapter Summary

Secondary organic aerosol (SOA) covers a key role in atmospheric composition and the presence of this class of particles presents harmful implications for the environment and human health. Despite decades of research, the main mechanisms driving the gas-to-particle processes and, more specifically, the SOA formation remain an active area of investigation, due to their inherent complexity and the high number of influencing parameters. This study aims to clarify the chemical steps leading to SOA generation, resulting from the oxidation of gaseous precursors gases and nanoparticles released by a premixed, fuel-rich ethylene-air laminar flame. Combustion processes are indeed essential contributors to secondary aerosol thereby understanding the mechanisms driving aerosol formation from flame-related sources represents a key step toward clarifying atmospheric composition.

Flame exhaust gases and particles from the described flame are convoyed into an oxidation flow reactor that mimics the atmospheric photooxidative environment. Particle size distributions are measured using a scanning mobility particle sizer, while the chemical composition of both primary and secondary aerosols is analysed with a high-resolution time-of-flight aerosol mass spectrometer.

Comparison of fresh (primary) and oxidized (secondary) emissions reveals a clear particle growth upon photooxidation and marked modifications in aerosol chemical profiles. These changes include the depletion of hydrocarbon-like species and an enhancement of oxygenated compounds, consistent with the typical evolution of SOA.

3.2 Introduction

Anthropogenic activities have a direct impact on the composition of atmospheric aerosol (Daellenbach et al., 2019). Combustion processes, and more specifically on-road and off-road vehicles emissions, significantly affect air quality in urban and sub-urban areas by releasing gaseous precursors and particles across a wide range of sizes (Hooftman et al., 2018). These processes contribute not only to POA emissions, i.e., the one directly released by the source, but also SOA formation through the atmospheric oxidation of volatile and semi-volatile organic compounds (Takegawa et al., 2006; Q. Zhang et al., 2007).

In ambient air, SOA can account for approximately 60–95% of the total organic aerosol fraction and numerous literature studies investigated its formation through atmospheric oxidation of gas-phase organic compounds released by both biogenic and anthropogenic activities (Gentner et al., 2017; Tkacik et al., 2014). Understanding the formation pathways and transformation mechanisms of SOA is a critical step to improve the current atmospheric models and for developing effective air quality control strategies. In this scenario, a detailed characterization of laboratory-scale combustion systems represents a powerful tool for an accurate identification of the key precursors and subsequent formation of aerosols under reproducible conditions. Moreover, it improves the understanding of the main oxidative processes happening in the atmosphere, by separating the contribution of each chemical pathway and physical mechanism. Indeed, due to the infinite number of reactions occurring in the atmosphere, the comprehension and characterization of the main reactive pathways bringing to the formation of fuel-combustion-derived-SOA remains limited (Bahreini et al., 2012; Chirico et al., 2010; Pieber et al., 2018; Timonen et al., 2017). Atmospheric oxidation processes mainly involve O_3, nitrate (NO_3) and hydroxyl radicals (OH) and their action contributes either to further gas-phase reactions or to partition of oxidation products into the condensed phase (Srivastava et al., 2022).

The characterization of emissions from anthropogenic sources and more specifically from combustion systems is extremely challenging due to the high reactivity of the involved compounds and short timescale of the processes. Currently, the investigation of SOA formation pathways usually involves in-situ methods mainly based on the use of atmospheric chambers or oxidation flow reactors.

Smog chambers are large, enclosed reactors largely implemented to investigate chemical processes under controlled conditions (Carter & Atkinson, 1996; Paulsen et al., 2005). Typically, they consist of inert volumes, usually constituted by Teflon or glass chambers, where trace gases and particles are injected and subsequently exposed to known oxidants e.g., OH, O_3, NO_3 radicals) and radiation sources that mimic solar irradiation (Takekawa et al., 2003; J. Wang et al., 2011). Due to their large volumes and long residence times, smog chambers are particularly suitable to perform gas-phase chemistry and SOA formation investigations under near-atmospheric conditions. However, these systems also present some limitations mainly related to wall losses of gaseous and particles, and to the need for extended experimental times, which may hinder their applicability to rapidly evolving emission sources (Krechmer et al., 2016; Matsunaga & Ziemann, 2010). Additional key drawbacks include their large volumes and the limited portability, which restrict their use in experiments targeting fast-changing emissions such as combustion releases (Chu et al., 2022). As a consequence, smog chambers were not considered the most suitable option for the present investigation.

To address these limitations, an oxidation flow reactor (OFR) was implemented. OFRs represent a mature technology particularly effective for the characterization of organic aerosol (OA) heterogeneous oxidation (Cao et al., 2020; Z. Peng & Jimenez, 2020). OFRs offer multiple advantages over traditional atmospheric chambers, including enhanced portability and higher suitability for lab-scale environments, reduced wall losses, shorter residence time and higher oxidation degrees (Simonen et al., 2017a). Since the dynamics of the atmospheric processes occurring in the OFR are extremely fast, the short residence time represents a great advantage for a detailed characterization (Ortega et al., 2016). Moreover, OFRs have higher oxidation rates and allow accurate measurements of emissions released by constantly changing sources, like combustion systems (Platt et al., 2013; Simonen et al., 2017a). These features make OFRs particularly effective for simulating atmospheric aging processes in laboratorial environments.

In atmospheric chemistry, the most common OFR configurations are OFR185 and OFR254. This terminology has been proposed by Li et al. in 2015 (R. Li et al., 2015) and it refers to the UV radiation wavelength of low-pressure mercury (Hg) lamps emitting at 185 nm or 254 nm, respectively (Z. Peng & Jimenez, 2020). The wavelength represents the photochemistry initiator, and different values can directly influence the OH radicals formation mechanisms. In OFR185, OH radicals are primarily produced by H_2O photolysis, whereas in OFR254 configuration, the OH radicals production occurs via the photolysis of externally supplied O_3.

For this study, an OFR254 was employed to generate SOA through the oxidation of premixed ethylene-air flame products. Ethylene was selected as the target fuel since it is an intermediate product in the combustion of many hydrocarbons, thereby its behaviour in flame can be representative of more complex hydrocarbon-based fuels. Together with methane, ethylene can efficiently serve as model compound for studying the combustion of aliphatic hydrocarbons (Turns, 2012). In literature, different methodologies have been used to characterize SOA, generally categorized into top-down and bottom-up approaches. Top-down methods typically rely on ambient measurements and large-scale models to infer SOA characteristics and sources (Hallquist et al., 2009a; Jimenez et al., 2009b). Conversely, bottom-up approaches aim to replicate SOA formation under controlled conditions, using environmental or oxidation chambers (Kroll & Seinfeld, 2008; Ng et al., 2007). This foster approach is also adopted in the current investigation.

Experiments were conducted at laboratory level under combustion-rich conditions. The reason behind this choice relies on the intent of investigating non-ideal combustion systems, which more closely

resemble real-world combustion devices, such as on-road and off-road vehicles, industrial furnaces, residential heating appliances, and power plants. Indeed, even in clean combustion apparatuses, local non-idealities can be encountered, resulting in areas with higher concentration density of undesired compounds. These regional inhomogeneities could impact the aerosol formation dynamics, leading to the generation of particles spanning a broad size range, from few nanometres up to several microns.

In this study, a laminar premixed combustion system was implemented. Some key input parameters mentioned in this work include flame temperature, equivalence ratio and residence time in flame, and they will be discussed in the following paragraphs.

Movable tubular probes enabled the sampling of the exhaust at different heights above the burner (Hs). The height above the burner serves as a proxy of the residence time in flame, allowing the characterization of molecules at different stages of the formation and growth process. Different residence time exhausts were collected and convoyed to the oxidation flow reactor, specifically designed to simulate atmospheric-relevant conditions. The chemical and physical characterization of the sampled compounds was performed using a Scanning Mobility Particle Sizer (SMPS) and High-Resolution-Time-Of-Flight- Aerosol Mass Spectrometer (HR-ToF-AMS). These instruments allowed for the monitoring of the evolution of particle size distributions (PSDs) in the flame, the investigation of the nucleation of new particles and the analysis of the chemical composition under atmospheric-relevant conditions.

3.2.1 Chemistry of the System

Flame Chemistry

The combustion system implemented in this study is a laminar premixed ethylene-air flame. Premixed systems are employed in many heating appliances, spark-ignition (SI) engines and stationary gas turbines (Duva et al., 2021; Glassman et al., 2014). They are mainly constituted by two combustion regions:

- A preheat zone, characterized by an unsignificant heat release.
- A reaction zone, where the chemical energy is released.
  The reaction zone by itself can be further divided into a so-called “thin region”, smaller than a millimetre where the reactivity is dominated by fuel molecules destruction and bimolecular reactions releasing CO, and a “wide region” of several millimetres where radical recombination reactions occur leading to the final burnout of CO and the release of CO_2. The structure of a one-dimensional premixed laminar flame is reported in Figure 12.

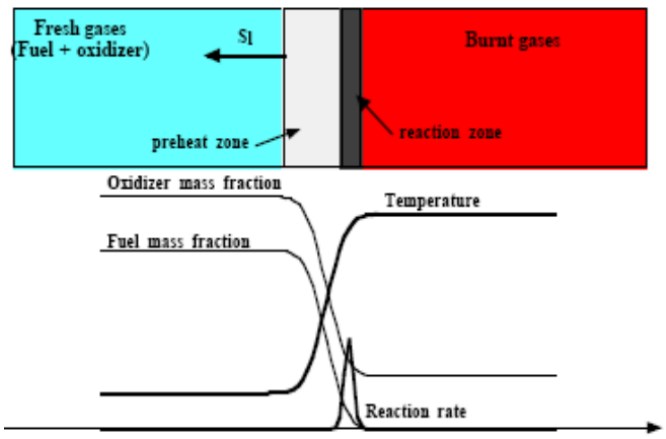

Figure 12: 1D Scheme of a premixed laminar flame

As for diffusion flames, the introduction of the equivalence ratio classifies the flames into lean systems ($\Phi<1$, fuel in quantitative defect compared to the oxidant), and rich ones ($\Phi>1$, fuel in quantitative excess compared to the oxidant).

Based on the type of flame, it is possible to predict the expected structure and composition of the generated soot. Rich-soot premixed laminar flames tend to release core shell structured soot, with an aromatic core composed by PAHs with dimensions ranging from pyrene to ovalene and an aliphatic shell. Due to the higher temperatures of these combustion systems, the early stages of the flame are responsible for the formation of the aromatic core, whereas the aliphatic shells form later in areas where the temperature starts decreasing (Ishiguro et al., 1997; Jenei et al., 2018; Kholghy et al., 2016; La Rocca et al., 2013).

In this study, the oxidation of flame exhaust was performed using OH-driven oxidation, mimicking real-atmospheric chemistry. Details about the OH reactive pathways are reported below.

OH Oxidative Chemistry

In the atmosphere, diurnal oxidative chemistry is dominated by OH radicals, being the most ubiquitous oxidative radical in terms of concentration. OH contributes to the so-called atmospheric self-cleaning processes (Levy, 1971) and it plays a key role in O_3 production and secondary aerosols formation (Hallquist et al., 2009b; Z. Peng et al., 2015; Volkamer et al., 2006). In real atmosphere, OH radicals usually have very short lifetime, typically lower than one second. Since OFRs reactors are designed to mimic atmospheric processes, OH radicals are expected to behave in the reactor as they do in the real atmosphere. Peng et al. proposed a schematic representation of the main O_x-HO_x photolytic processes occurring in the OFR254 reactors (Z. Peng et al., 2015). This reactive network, reported in Figure 13, is based on the model presented by Li et al. for the radical chemistry (R. Li et al., 2015).

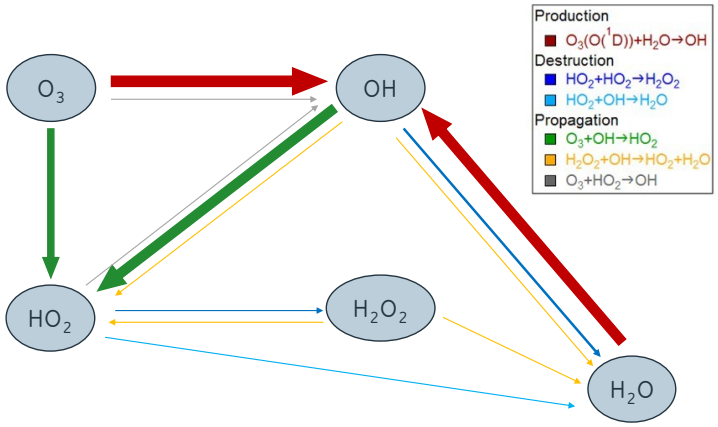

Figure 13: Ox-HOx Cycle within an OFR254 Reactor adapted from Peng et al. (Peng et al., 2022). The reactive pathways are derived from the model proposed by Li et al. (R. Li et al., 2015) while the arrow thickness is based on the relative contribution inferred from OFR254 results reported by Peng et al. (Peng et al., 2022).

The proposed reaction mechanisms are based on some input parameters: medium water mixing ratio (1%), medium photon flux ($1.4 * 10^{15}$ photons cm^{-2} s^{-1} at 254 nm) and absent external OH reactivity (Z. Peng et al., 2015).

The concentration values of O_3, OH and HO_2 adopted in Peng's analysis are higher than atmospheric ones, coherently to the values reached in OFR systems. One of the main observations reported in this study focuses on the high efficiency of the HO_x conversion mainly through the reactions:

$$O_3 + OH \rightarrow HO_2 + O_2 \quad \text{(R10)}$$

$$O_3 + HO_2 \rightarrow OH + 2O_2 \quad \text{(R11)}$$

It has been registered that the interconversion OH-HO_2, does not predominate over the primary production and final destruction, hence the primary HO_x produced quickly goes to form H_2O or H_2O_2. Furthermore, it has been observed that compared to OFR185, higher conversion rates are recorded for OFR254, due to the more efficient OH formation from injected O_3. This source reaction reflects the

atmospheric process that leads to the release of OH molecules. Indeed, in the atmosphere, OH radicals govern daytime chemistry, being mainly produced by O_3-photolysis. Other minor OH sources include: the photolysis of nitrous acid (HONO), hydrogen peroxide (H_2O_2) or peroxy-methane (CH_3OOH), the reaction of nitrogen monoxide (NO) with the hydroperoxy radical (HO_2) or the reaction of alkenes with ozone, but their contribution is limited.

Once produced, OH radicals react with many compounds present in the atmosphere, starting from volatile organic compounds. The main reactive mechanism involving VOC and OH is characterized by a hydrogen abstraction from the VOC molecule operated by the OH radical, followed by the production of an organic radical (R), which will likely react with an O_2 molecule to form a peroxyradical (RO_2) (Z. Peng et al., 2021). It has been revealed that peroxides not only have a key role in flame systems (Goldman et al., 2021) but also in atmospheric processes (Day et al., 2022). Understanding the role of RO_2 is crucial to clarifying the mechanisms driving dimers formation and particle generation. More details about the dimer formation mechanisms and OH reaction pathways will be discussed in the next chapters.

3.3 Experimental Setup

The scheme of the experimental setup implemented in the current investigation is shown in Figure 14. The setup consists of several key components:

- A combustion apparatus serving as a source of flame-generated products
- A set of pipelines and mass flows ensuring the gas flow through the system.
- A sampling probe system surrounded by thermally cooled lines.
- A manometer and pressure valve to regulate the flow and pressure of the flow entering the reactor, followed by an exhaust discharge.
- An ozone generator for oxidant supply.
- A Dekati® Oxidation Flow reactor (DOFR™) for atmospheric aging.
- An auxiliary exhaust line to prevent overflows from entering the detection instruments.
- A final sampling line leading to the detection instruments.

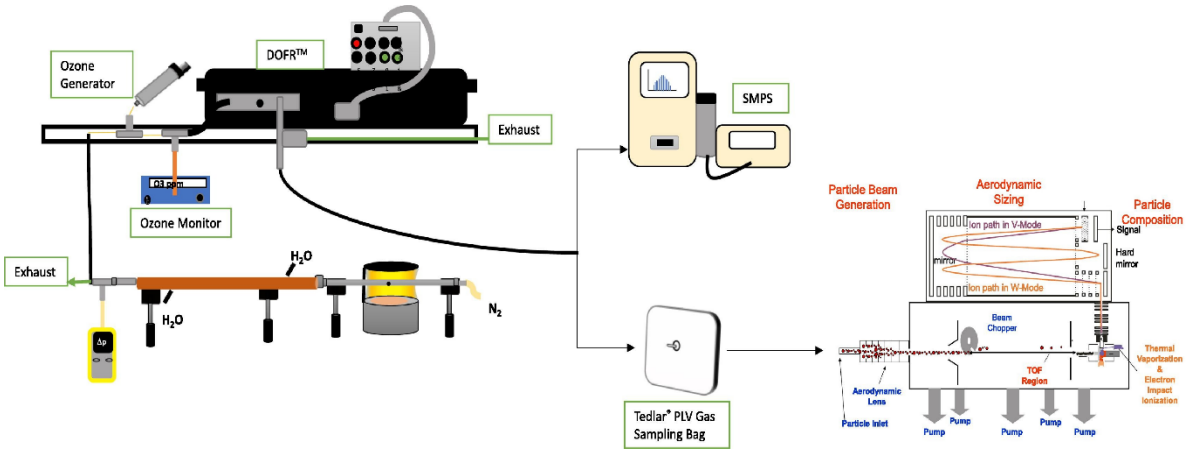

Figure 14: Experimental Setup

3.3.1 Combustion Apparatus and Exhaust Extraction

The atmospheric pressure laminar premixed ethylene-air flame implemented in this study operates under fuel-rich conditions. The employed water-cooled sintered steel McKenna Flat Flame porous burner with a 6cm plug diameter is shown in Figure 15. The cold inlet gases (ethylene and air) are sent to the burner at a velocity of 9.8 cm/s, generating a flame with an equivalence ratio (Φ) equal to 2.01.

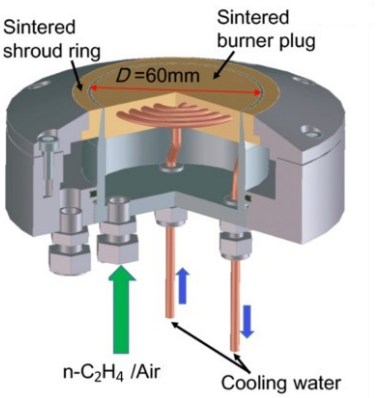

Figure 15: McKenna Burner Schematic. Figure adapted from Jiang et al. (Jiang et al., 2021)

The extraction of the flame products proceeds through turbulent flow tubular dilution probes consisting of a tube with 1cm outer diameter and orifices of different internal diameters based on the performed analysis. The sampling is performed by positioning the probe horizontally, along the flame centerline at different heights above the burner (Z). For this work, three heights were investigated: 8, 10, and 14 mm. These quotas are representative of three distinct stages of the soot formation process. Z=8 mm corresponds to the particle nucleation zone, Z=10 mm to the early particle growth region, and Z=14 mm to the maturation/decarbonization zone (Sabbah et al., 2021). The sampled mixture was immediately diluted with gaseous nitrogen (N_2), aiming to minimize particle aggregation and to quench chemical reactions. The importance of implementing a dilution flow was initially proposed by Zhao et al. (B. Zhao et al., 2003) and consequently consolidated in other works (Sabbah et al., 2021). In the present study, the amount of N_2 involved ensures a dilution ratio (DR) of $1:3x10^3$, enabling the reach of critical dilution conditions (Zhao et al., 2003) above which particle losses are no longer measurable. This condition allows to minimize the artefacts related to coagulation and wall losses, ensuring that the registered particle concentrations are representative of the emitted aerosol.

3.3.2 Ozone Generator and Oxidation Flow Reactor

Once released by the flame, the gaseous and particle phases are conveyed into an Oxidation Flow Reactor designed by Dekati® (DOFR™), which enables the oxidation process via ozone generated OH radicals (Kuittinen, McCaffery, Peng, et al., 2021; Kuittinen, McCaffery, Zimmerman, et al., 2021; Simonen et al., 2019). The DOFR™ reactor is equipped with a cylindrical quartz vessel with a 3.3 L volume (52 cm x 9 cm inner diameter) enclosed by two constant power ozone-free low-pressure mercury lamps emitting 245 nm UV light. A picture of the DOFR™ system is reported in Figure 16:

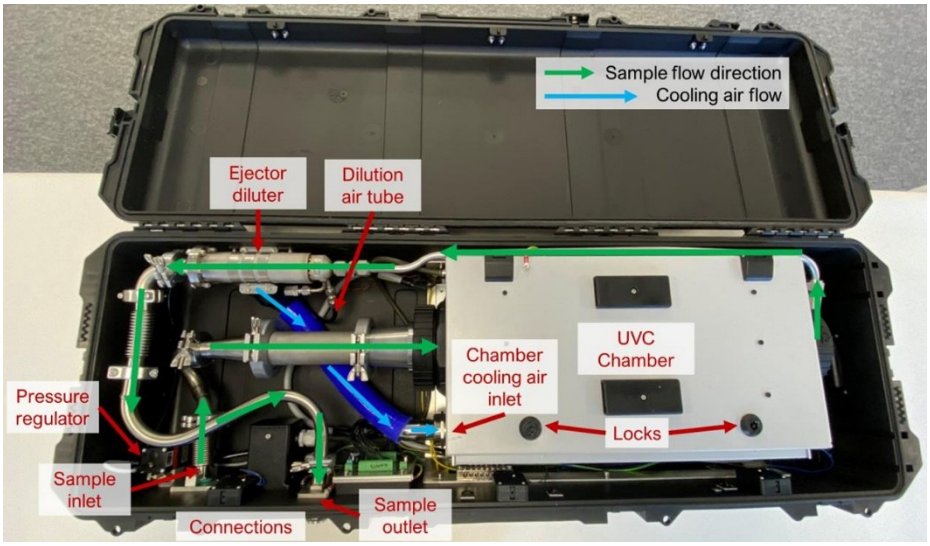

Figure 16: Schematic of Dekati Oxidation Flow Reactor (Dekati Ltd., 2022)

Once introduced within the instrument system, the sampled flow is conveyed along a dedicated pathway and driven to the UVC chamber, as illustrated in Figure 16. Inside this chamber, a cylindrical quartz reactor surrounded by two sets of UV lamps is installed. This configuration ensures to reach laminar flow conditions within the reactor. Moreover, placing the UV lights outside the reactor volume limits particle–wall interactions and associated surface-related artefacts, without altering the intrinsic surface-to-volume ratio (Simonen et al., 2017b). The UV lamps are positioned externally to the cylindrical quartz reactor to preserve laminar flow and reduce wall interactions, while ensuring that the emitted radiation is ozone-free. The system is equipped with an internal cooling unit to dissipate heat generated by the UV lamps and an integrated ejector diluter to regulate the sample flow and to dilute the sample for downstream measurement instruments.

The UV lamp assembly consists of 12 lamps with adjustable intensity, allowing precise control of OH radical production and enabling the simulation of different equivalent atmospheric aging times. The lamps emit radiation at 254 nm, which photolyses ozone introduced into the reactor, leading to the formation of excited oxygen atoms, $O(^1D)$. These atoms subsequently react with water vapour present in the sampled air, producing hydroxyl (OH) radicals, as schematized in Figure 17.

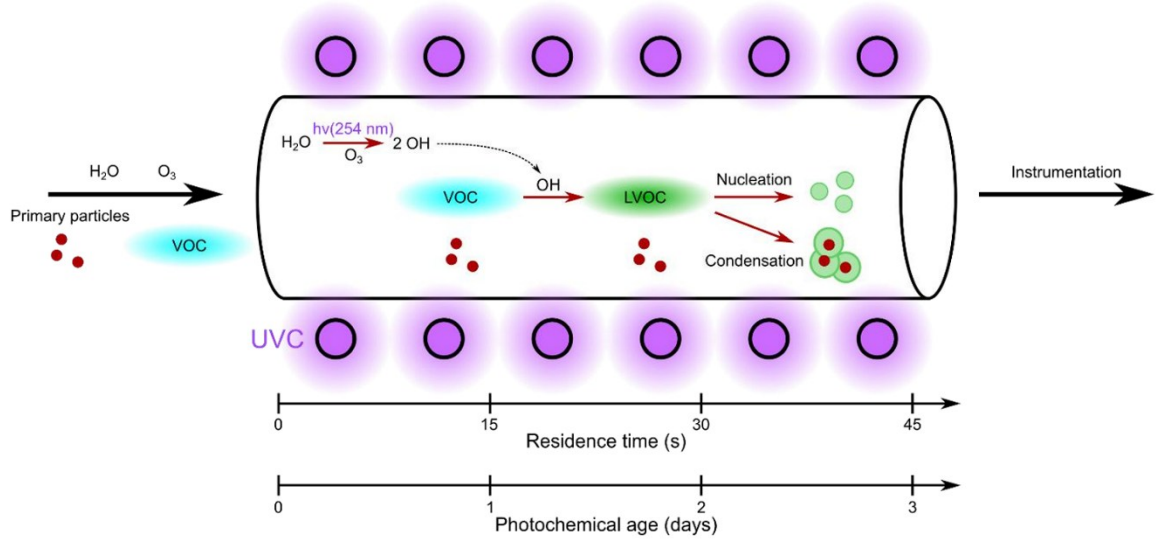

Figure 17: Internal Scheme of DOFR Reactive Zone. Figure adapted from Arffman et al. (Arffman et al., 2022)

For the OH generation, the ozone flow is provided by an external ozone generator, Model 1000 designed by Jelight Company Inc. This instrument consists of an electropolished stainless steel cell, and it generates ozone molecules from air-oxygen photolysis by applying 185 nm UV radiation. Ozone levels are monitored right before the reactor by the 205 Dual Beam Ozone Monitor -2B Technologies. The adjustment of ozone concentrations is performed through the regulation of the air flowrate entering the lamp.

By regulating ozone and water molecules concentration, it is possible to mimic atmospheric residence time in a range spanning from few hours up to some days. The estimation of the corresponding residence time based on these two concentrations can be achieved by using the DOFR™ calibration sheet provided by Dekati®. Indeed, the equivalent aging time is a function of the ozone concentration, which is actually correlated to the relative humidity (RH). The DOFR™ calibration sheet points out three main RH levels: 30%, 50%, and 75%, as reported in Figure 18. No significant differences in the aging times at low ozone concentrations are observed for the different RH levels. Conversely, the aging time discrepancies among different RH values become more relevant for higher O_3 concentrations. For instance, considering an ozone concentration of 75 ppm, the equivalent aging times for RH are 30%, 50%, and 75% correspond to 14, 22, and 38 days, respectively. At a fixed inlet ozone flux, it is possible to regulate the OH concentration by adjusting the number of lamps involved in each experiment. This datasheet is obtained considering 6UV lamps on a total of 12UV lamps.

Another commonly used parameter to describe oxidation time in literature is the OH exposure (OH_{exp}). OH_{exp} quantifies the cumulative dose of hydroxyl radicals to which chemical compounds are exposed during a reaction. The average atmospheric OH concentration over a typical day (24 hours) is approximately $1.5 \cdot 10^6$ molecules/cm^3. Consequently, one day of oxidation corresponds to an OH_{exp} of $1.3 \cdot 10^{11}$ molecules/cm^3·s

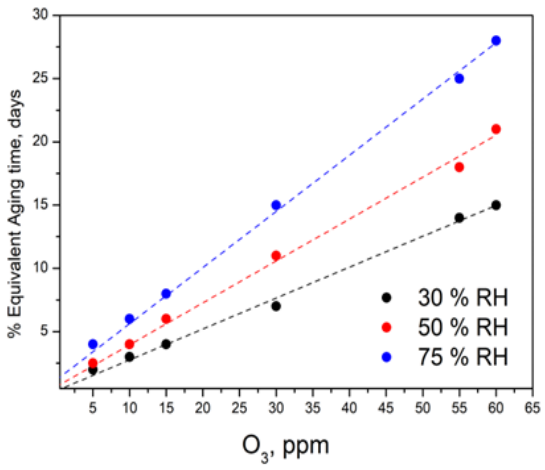

Figure 18: Equivalent aging time in DOFRTM as a function of ozone concentration and relative

3.3.3 Detection System

Since the aim of the study is to gain a clearer picture of the main oxidation mechanisms leading to secondary aerosol formation from primary emissions, the released compounds are characterized by both before and after the aging process. This approach facilitates the isolation of OH-driven processes.

Physical and chemical characterizations of the combustion exhausts are performed through online and offline measurements of the unaged and aged compounds based on particle size distribution function (PSDs) analysis coupled with mass spectrometry results. PSDs are collected using a scanning mobility particle size analyzer, whereas mass spectra are collected with an HR-ToF-AMS.

Online Measurements

PSDs represent an extremely powerful tool to characterize flame-generated particles. Several studies pointed out the correlation of PSDs with Φ, residence time (Sgro et al., 2003), flame temperature (Abid et al., 2008) and fuel chemistry (Echavarria et al., 2011).

The samples are collected at the exit of the DOFR™, with a horizontally positioned probe, and diluted with gaseous nitrogen. The probe used for the PSDs investigation is a turbulent flow tubular dilution probe with an outer diameter of 1cm and an orifice characterized by an internal diameter of 0.2 mm and 0.5 mm thickness. As previously mentioned, the aim of the N_2 dilution is to prevent particle coagulation and to quench chemical reactions, avoiding further reactivity and growth within the sampling line. The flow, composed of gaseous and particle phases, is then sent to an Advanced Aerosol Soft X-ray Neutralizer, model TSI 3088. The implementation of the neutralizer aims to achieve Fuchs' stable charge distribution (Reischl et al., 1996).

Subsequently, the sampled flow is conveyed into a cylindrical electrostatic classifier for differential mobility analysis (DMA), model TSI 3085, and to a Condensation Particles Counter (CPC), model TSI 3776. PSDs analysis is performed using the TSI aerosol instrument manager software (AIM), through which the adjustments by multiple charges and wall-diffusion particle losses were implemented. By following the procedure, a post-processing analysis is performed so to correct the data by the total sampling efficiency (M. He & Dhaniyala, 2013; Wiedensohler et al., 2012).

PSDs were collected for two sets of samples representing primary and secondary exhausts. Whenever primary exhaust was measured, the ozone was not injected into the system and the lamps within the DOFR™ were off. PSDs for secondary aerosol refer to the condition where ozone was injected, and DOFR™ lamps were on, so OH radicals were present.

Offline Measurements

The chemical composition of the flame products was analyzed with an HR-ToF-AMS by Aerodyne Research. Inc. For logistical reasons, this analysis was performed offline by collecting the samples within 5 L Tedlar® PLV Gas Sampling bags. A similar collection system was already adopted in the investigation by Cereceda et al., which revealed a peculiar suitability of Tedlar sampling bags for gas sampling and combustion emissions collection (Cereceda-Balic et al., 2017). Once collected in the bags, the samples were stored for ~20 min, corresponding to the minimum time required to physically reach the HR-ToF-AMS location. During this time span, they were kept in the dark to minimize additional chemical processing and prevent further photo-oxidation reactions.

The bags were consequently connected to the aerosol mass spectrometer and analyzed. HR-ToF-AMS was equipped with a PM2.5 aerodynamic lens able to efficiently detect particles of about 100nm (Xu et al., 2016).

For this reason, a turbulent flow tubular dilution probe with 2.5 mm orifice diameter was used for this analysis. Indeed, using a larger orifice diameter compared to PSDs analysis is related to the dynamic lens efficiency of the AMS, which is higher for 100nm particles. Based on the 2.5 mm orifice, a dilution ratio (DR) equal to 1:21 was chosen to ensure proper particles detection. Indeed, this value is high enough to maintain the quenching flame requirements and the reactivity stop, but at the same time, it is low enough to allow particle coagulation.

The Tedlar® bags were positioned at the outlet of the DOFR™. The samples were then sent to the HR-ToF-AMS passing through the PM2.5 aerodynamic lenses and being focused into a narrow beam impacting a resistively heated (ca. 600 °C) capture vaporizer, to allow the evaporation of non-refractory particle species. An ionization of a 70-eV electron beam is applied to the resulting vapors, which are finally conveyed into the mass spectrometer. The HR-ToF-AMS is also equipped with a Soot Particle AMS (SP-AMS), enabling the detection of refractory particle classes such as Black Carbon and metals. For the

HR-ToF-AMS an operational flow rate of 0.085 L/min was applied. The HR-ToF-AMS was set to V-mode with the SP-AMS Laser turned ON. The system was calibrated for inlet flow, ionization efficiency (IE), and particle sizing following the AMS protocols (Allan et al., 2003; Drewnick et al., 2015; Jayne et al., 2000).

The acquired data were analyzed with the ToF-AMS analysis toolkit Squirrel 1.65/PIKA 1.25 by Aerodyne Research Inc, accurately described by DeCarlo et al. (DeCarlo et al., 2006). AMS acquisition data process allows to evaluate Unit Mass Resolution (UMR) spectra up to a chosen mass-to-charge ratio (m/z), fixed at 1100 in this study. Moreover, it simultaneously analyzes the signals between 12 and 120 m/z with a mass resolving power up to 2500 (high-resolution region). This analysis allowed to perform an accurate chemical characterization of the main flame products components, cross matching this information with the PSDs physical details. A tracers investigation based on the identification of the main indicators of POA and SOA was performed. Triangular plots and Van Krevelen diagrams were investigated, aiming to properly highlight the effect of a simulated atmospheric oxidation environment on flame products.

3.4 Results

3.4.1 Particle Size Distribution Functions

The particle size distribution functions measured online at the exhaust of the DOFR$_{TM}$ are reported in Figure 19. The measurements have been performed considering two ozone concentrations, 0 and 5 ppm targeting at simulating different aging times.

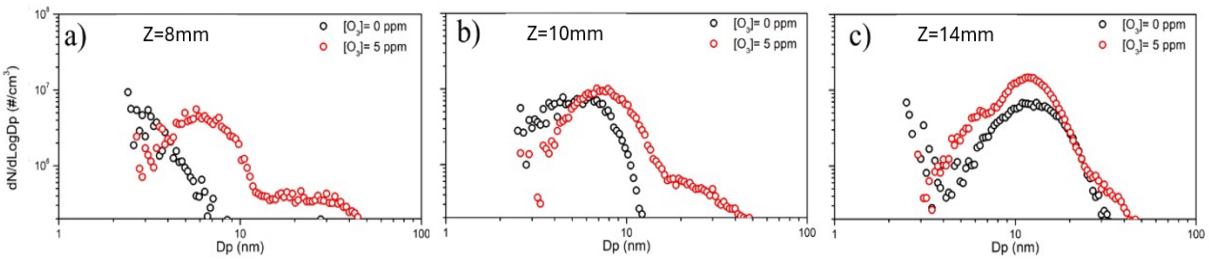

Figure 19: Particle Size Distribution Functions

Based on the plot reported in Figure 18, for the chosen RH, an ozone concentration of 5 ppm corresponds to two days of atmospheric aging. According to the implemented ozone concentration, the aerosol flow will be referred to as primary organic and secondary organic aerosols for O_3=0 ppm and 5 ppm, respectively. By looking at the plots Figure 19a, it is worth noticing that the particles released at 8 mm show a smaller size than those generated at Z=10 mm, resulting in a unimodal size distribution function. The 8 mm quota represents the so-called early zone of the post-flame region, and the mode corresponding to this region includes first detectable particles and incipient soot. For each of the subplots, some differences can be pointed out by comparing aged conditions (red curves) to unaged ones (black curves). Already at Z=8 mm, OH triggers some photo-oxidation reactions resulting in the formation of new and larger particles revealed by the presence of two additional modes centered at about 8 nm and 30 nm, respectively. A similar behaviour is also observed at 10 mm, where a slight increase in the particle mode centred at about 8 nm is recorded. At this height, PSDs start exhibiting a bimodal shape with particles bigger than 15 nm, as reported in Figure 19b. At Z=14 mm, Figure 19c, the effect of the induced photo-oxidation is more pronounced. A slight indication of an additional contribution at intermediate particle sizes around 6 nm in diameter, can be noticed and may be further explored in future studies.

Considering the cubic dependence of the particle mass/volume on particle diameter, it is possible to infer that the mass of the carbon materials collected at these flame locations is mainly composed by

primary soot particles, although a remarkable number of incipient soot particles is registered by the bimodality at quotas higher that 8 mm (Commodo et al., 2019; Schulz et al., 2019). The effect of the higher residence times, i.e., at increased Zs, impacts on the particle growth processes, especially coagulation and coalescence, and on the surface mass addition, as confirmed by the PSDs modes.

The differences in the aging process on particles collected at different heights above the burner can be noticed from Figure 20. In this plot, the effect of the photo-oxidation on incomplete combustion products at different residence times, and so at different maturation stages, is observed. The presence of a new particle mode is mainly detectable at 14 mm, and it could be attributed to soot particle oxidation-induced fragmentation (Echavarria et al., 2011; Sirignano et al., 2013).

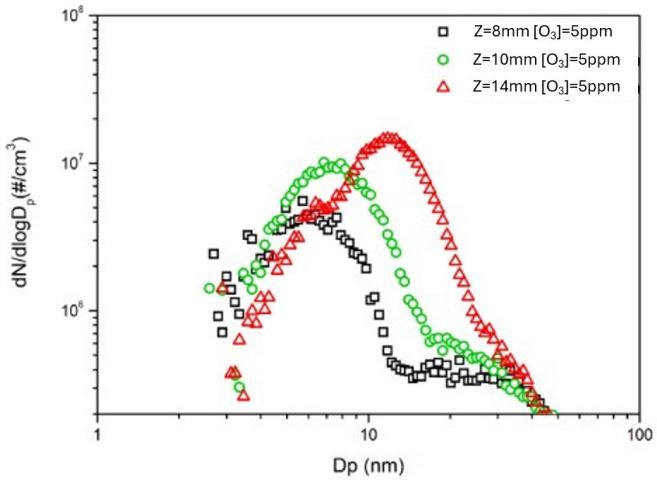

Figure 20: Particle size distribution functions of SOA at different heights above the burner

3.4.2 Mass Spectrometry Core Findings

Unit Mass Resolution (UMR) AMS Profiles

The analysis of the incomplete combustion products is enriched by the mass spectra investigation. No separation of the gaseous and particle phases was performed; hence, the reported spectra are related to the entire exhausts. As for PSDs investigation, the spectra analysis of the exhaust was collected at three heights above the burner, Z= 8 mm, 10 mm, 14 mm, with two different ozone concentrations, O_3=0 and 5 ppm.

The mass-to-charge (m/z) range covered by the spectrometer analysis goes from 100 to 1100 m/z. Despite the distribution of the molecular masses spanning the entire range, a higher peak intensity has been observed within the range 100-600 m/z. The presence of medium-sized polycyclic aromatic hydrocarbons (PAHs), dimensionally spanning from coronene to ovalene, is detected. Other studies have already highlighted the consistent contribution of PAHs of moderate size to nascent soot for similar flame conditions (Commodo et al., 2019; Schulz et al., 2019). Furthermore, mainly at Z=14 mm, some peaks attributed to pure carbon species (C_x), i.e., fullerenes structures have been registered. Similar results from analogous experimental conditions were also registered by Sabbah et al. (Sabbah et al., 2021).

A preliminary analysis of the spectra immediately pointed out the impact of the photo-oxidation processes on the collected samples: the variation of the ozone concentration directly causes a PAHs peaks reduction or even complete annihilation. For each Zs, the peaks in the m/z range from 300 to 500 tend to reduce once photo-oxidation is activated. This can be explained considering the key participation of the compounds associated with this range of m/z to oxidative processes. An additional peak reduction in the m/z range 700-1000 was detected mainly for higher Zs. At the same time, an overall remarkable signal increase has been registered in the oxidizing conditions, indicating potential nucleation of new

particles. Indeed, under oxidizing conditions, a total ion signal increase of 12%, 17% and 18%, is estimated for Z=8 mm, 10 mm, and 14 mm, respectively.

High Resolution (HR) AMS profiles

The investigation of the mass spectra within a lower mass range was performed using the high-resolution tool. An accurate investigation of the organic spectra within this region can furnish precious information about the effects of photooxidation (DeCarlo et al., 2006; L. Y. He et al., 2010; Ng et al., 2011). The implementation of a 70-eV electron impact ionization technique results in the fragmentation of many input species (Aiken et al., 2007). For each of the collected samples, most of the signals (approximately between 82 and 90%) fall within the m/z region ranging from 12 to 120, ensuring a higher precision in the examination of the aerosol elemental composition. High-resolution mass spectra (HR-MS) were processed using a fitting procedure implemented in the PIKA software, allowing the separation of fragment ions within the m/z range 12-120 with a mass resolving power up to 2500, where the resolving power (RP) is defined as (DeCarlo et al., 2006):

$$RP = \frac{\left(\frac{m}{z}\right)_{nominal}}{\Delta m} \qquad \text{(Eq. 4)}$$

This ratio correlates to the nominal mass-to-charge over the full width at half maximum, Δm. The higher the resolving power (RP), the better the mass spectrometer can separate ions with very similar mass-to-charge ratios, reducing peak overlap and allowing more precise identification of individual species.

The mass spectra at different Zs are reported in Figure 21. For each Z, the lower panel reports the spectra of non-oxidized samples (O_3=0 ppm) whereas the upper one represents the oxidized spectra (O_3=5 ppm).

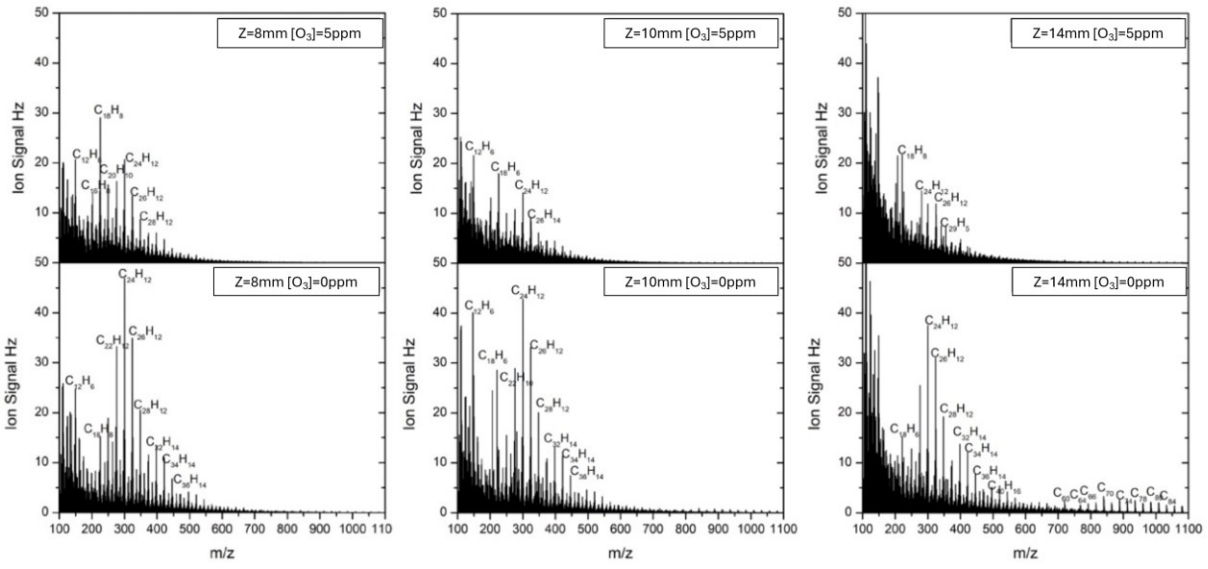

Figure 21: Mass spectra of the unburned gas at different heights above the burner (Z = 8, 10, and 14 mm, from left to right). The upper panels correspond to experiments conducted in the presence of ozone at a concentration of 5 ppm, while the lower panels show spectra obtained without oxidation. The main peaks are annotated with the chemical species contributing to the corresponding signals.

Based on their molecular composition, the detected molecules have been classified in seven families: C_x, CH, CHO_1, CHO_{gt1}, CHN, CHO_1N, and $CHO_{gt1}N$ (where O_{gt1} stands for number of oxygen atoms greater than one). The selection of these families in the HR analysis was guided by the main species expected to form during combustion processes. Furthermore, tracking these compound classes offered initial insights into the molecular groups most affected by photooxidation. In order to obtain a clear analysis of the organic fractions, the $C_2H_4^+$ ion was excluded from the fitting procedure due to the inability of the

software to accurately distinguish his contribution from N_2. Indeed, $C_2H_4^+$ and N_2 present a similar mass-to-charge ratio equal to 28.03130 vs 28.00615, respectively. The relative contribution of each family on the total signal is summarized in pie chart, Figure 22. A minor contribution arises from the CHON and $CHO_{gr1}N$ families: in both oxidized and unoxidized spectra, the combined contribution of these two molecular classes accounts for less than 5%.

Coherently with the expected results, the CH family exhibits the highest contribution. The increase in the CH fraction with height above the burner is consistent with the decreasing ethylene concentration (not accounted for in the ion fitting procedure) at higher positions. Accordingly, as the height above the burner increases, other species within the same family become more dominant. A similar upward trend with Z is recorded for the C_x family, extending over a broader m/z range. Analogous results were reported also by Sabbah et al., where the most intense C_x peaks with high m/z values are attributed to fullerenes. (Sabbah et al., 2021). This conclusion is supported by previous studies conducted by Dobbins et al. and Homann et al. (Dobbins et al., 1998; Homann, 1998). Dobbins registered the presence of various carbon clusters and PAH molecules using laser direct imaging (LDI) with a single-step 266nm laser at an irradiance of 1–20 MW/cm^3. Homann, on the other hand, performed online analyses of premixed low-pressure flames, enabling the detection of several fullerenes.

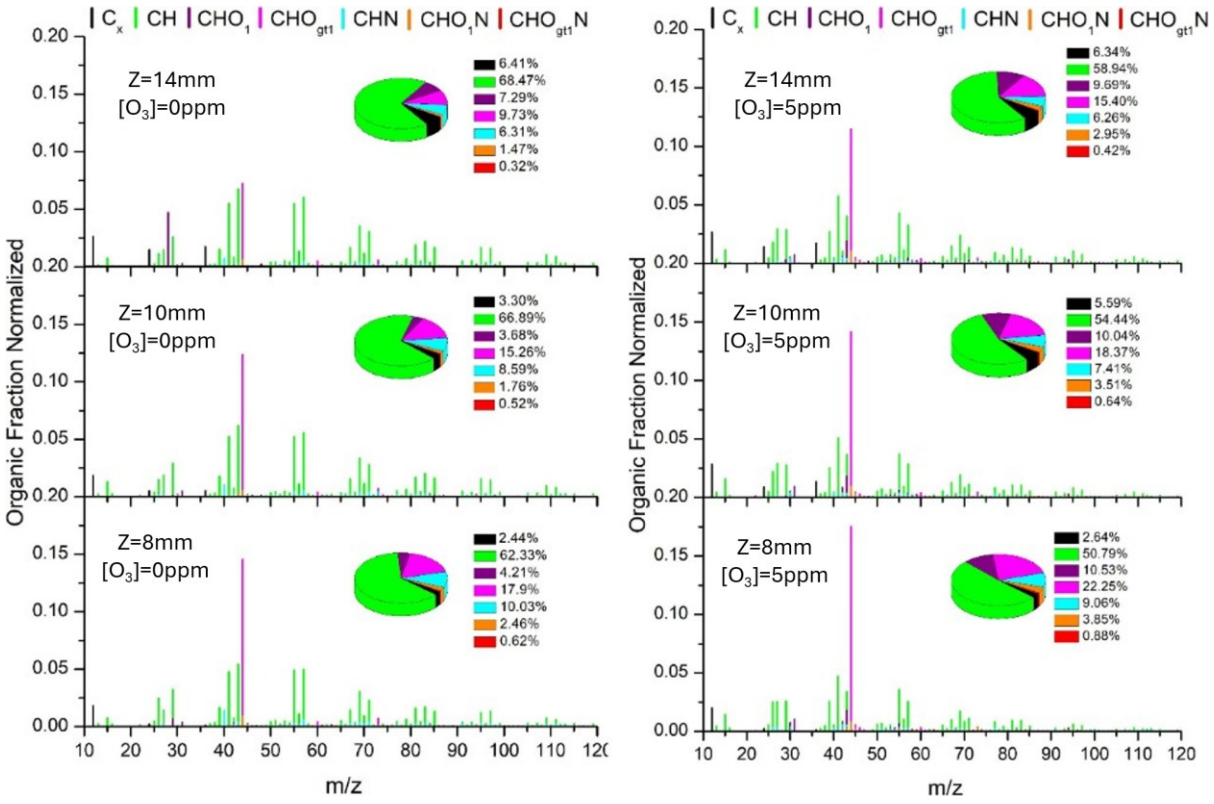

Figure 22: Pie Chart representing the main chemistry families for each condition with correlated high resolution mass spectra profiles. On the left panels, the acquisition for samples at no-oxidation conditions (POA); on the right, the acquisition for samples at 5 ppm ozone concentration (SOA).

Fullerenes exhibit three-dimensional closed-cage structures, and in-flame online detection has shown that their carbon atom count varies depending on the flame conditions. All the aforementioned experiments identified fullerene molecules containing more than 50 carbon atoms. Considering the structure of the investigated molecules, at lower Zs, planar aromatic structures are expected to dominate, either in form of peri-condensed molecules or less compact configurations (with higher hydrogen content compared to peri-condensed PAHs) or even as structures containing pentagonal rings. Sabbah et al. detected also many π radicals mainly in the form of odd C# and odd H# (Sabbah et al., 2021). By increasing the H, the conversion of the large PAHs into fullerene-like structures is

hypothesized, involving intermediate large HC clusters coherently with the decarbonization process in which a series of dehydrogenations and isomerizations are induced by thermal processing. The effects of photo-oxidation can mainly be observed by looking at the CHO and CHO_{gt1} families, whose contribution to the total composition increases after the ozone injection. Under shorter residence times in flame, i.e. lower heights above the burner, a higher concentration of oxygenated compounds is recorded, probably related to the higher tendency to form highly reactive species.

To clearly highlight the effects induced by photooxidation, the differential high-resolution ion signals between SOA (O_3=5 ppm) and POA (O_3=0 ppm) was calculated and shown in Figure 23.

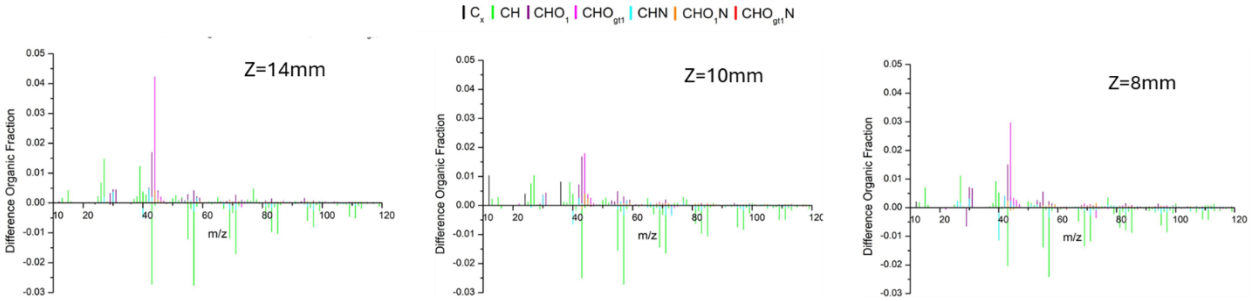

Figure 23: Differences in the HR-MS signals of ions between SOA and POA. Each POA and SOA contribution was first normalized to the respective total organic signal. Subsequently, the difference between the two normalized signals was calculated.

All the species contributing more to the POA show a negative signal; conversely, positive signals correspond to SOA-contributing species. The main families affected by photooxidations are CHO and CHO_{gt1}, represented in purple and magenta, respectively. For each height above the burner, the strongest increase induced by photooxidation is observed for m/z ratios ranging from 43 to 47. These m/z values are associated with specific fragments by the HR analysis: $C_2H_3O^+$ (43.01839 m/z), CO_2^+ (43.98938 m/z), CHO_2+ (44.99760 m/z), $CH_2O_2^+$ (46.00548 m/z) and $CH_3O_2^+$ (47.01330 m/z). In the CH family, reported in green, the strongest decrement involves the m/z ratios equal to 43, 55, 57, 69, 71, 83, 85. This trend does not seem to be affected by the burner-to-probe distance. Again, the HR analysis allows to associate these m/z to the specific fragment contribution: $C_3H_7^+$ (43.05470 m/z), $C_4H_7^+$ (55.05030 m/z), $C_4H_9^+$ (57.07043 m/z), $C_5H_9^+$ (69. 07043 m/z), $C_5H_{11}^+$ (71.08606 m/z), $C_6H_{11}^+$ (83.08606 m/z), $C_6H_{13}^+$ (85.10172 m/z). In general, an increase of the oxidized species and a decrease in the hydrocarbon-like structures are registered after photooxidation. These results are coherent with other works available in literature (Heringa et al., 2012; Q. Zhang et al., 2005a; Zhu et al., 2021).

Tracers Investigation

Among the most representative mass-to-charge signals, m/z 43 fragment can be associated to either saturated hydrocarbons in the form of $C_3H_7^+$ or to oxidized carbonyl containing compounds such as aldehydes or ketones in the form of $C_2H_3O^+$ or CH_3CO^+ (Alfarra et al., 2004, 2006). Great importance is also acquired by the m/z 44, corresponding to CO_2^+ fragment: in many laboratory experiments, it tends to increase accordingly to the mass fragment 18 (H_2O^+) from decarboxylation of oxo- and di-carboxylic acids as well as highly oxidized compounds. This crossmatch of increments between m/z 18 and 44 has been observed for AMS experiments involving di- and poly carboxylic acids and humic-like substances, where it can be associated to the thermal breakdown of the carboxylic acid group on the vaporizer (Alfarra et al., 2004). The m/z=44 signal has been proven to be correlated with SOA formation: smog chamber experiments registered a progressive increase of m/z=44 when SOA generation arises. Moreover, a linear increase of m/z 44 relative intensity with oxygen-to-carbon ratio is detected for a broad range of inorganic molecules (Q. Zhang et al., 2005a). These observations indicated the existence of a correlation between m/z 44 and the oxygenated organic compounds contained in the aerosols (Alfarra et al., 2006; Bahreini et al., 2005). Furthermore, experiments investigating wood burning products revealed a strong contribution of the m/z44 to the total organic mass. This finding justifies the

use of m/z44 as oxygenated organic aerosols (OOA) marker, rising from both secondary organic aerosol sources but also primary ones (Alfarra et al., 2007). Mass-to-charge ratios of 43 and 44 can be adopted as tracers for hydrocarbon-like and oxygenated organic aerosols (HOA and OOA) compounds, respectively. In the present study, at Z = 8 mm, CO_2^+ ion represents the largest peak at 17.5% of the HR-MS. The contributions of the main tracers have been reported in Table 5 and 6 for HOA and OOA, respectively.

Table 5: Mass-to-charge ratios of the main HOA tracers reported as organic fraction normalized signals

HOA m/z	Fragment	Z=8 mm		Z=10 mm		Z=14 mm	
		0 ppm	5 ppm	0 ppm	5 ppm	0 ppm	5 ppm
57	$C_4H_9^+$	0.0572	0.0329	0.0621	0.0354	0.0658	0.0397
67	$C_5H_7^+$	0.0178	0.0129	0.0181	0.0156	0.0195	0.0173
69	$C_5H_9^+$	0.0345	0.0219	0.0374	0.0234	0.0394	0.0270
71	$C_5H_{11}^+$	0.0280	0.0163	0.0333	0.0170	0.0345	0.0186
81	$C_6H_9^+$	0.0189	0.0123	0.0195	0.0130	0.0209	0.0153
83	$C_6H_{11}^+$	0.0215	0.0140	0.0241	0.0143	0.0251	0.0154
85	$C_6H_{13}^+$	0.0142	0.0079	0.0177	0.0082	0.0201	0.0100
95	$C_7H_{11}^+$	0.0158	0.0087	0.0174	0.0098	0.0184	0.0122
97	$C_7H_{13}^+$	0.0163	0.0076	0.0178	0.0085	0.0193	0.0099

Table 6: Mass-to-charge ratios of the main OOA tracers reported as organic fraction normalized signals.

OOA m/z	Fragment	Z=8 mm		Z=10 mm		Z=14 mm	
		0 ppm	5 ppm	0 ppm	5 ppm	0 ppm	5 ppm
15	CH_3^+	0.0075	0.0145	0.0129	0.0157	0.0073	0.0115
31	CH_3O^+	0.0035	0.0104	0.0051	0.0095	0.0027	0.0073
44	CO_2^+	0.0179	0.0279	0.0141	0.0281	0.0120	0.0249
45	CO_2H^+	0.0060	0.0096	0.0041	0.0088	0.0023	0.0089
53	C_3HO^+	0.0065	0.0106	0.0063	0.0099	0.0064	0.0098

The registered values refer to the organic fraction normalized reported in Figure 24. The choice of the fragments to analyze has been pursued by considering the most-likely species formed in flame, based on literature analysis (Alfarra et al., 2006; Q. Zhang et al., 2005a). A notable decrease is registered for HOA tracers after photooxidation processes, especially for m/z equal to 57, 67, 69, 71, 81, 83, 85, 95, 97. M/z57 usually represents a major peak in the hydrocarbon-related spectra, and it is typically associated with combustion exhausts (Goetz et al., 2022).

Mass-to-charge ratios equal to 67, 81, 95 can be associated to the $C_nH_{2n-3}^+$ sequence, arising from cycloalkanes; m/z equal to 69, 83 97 can instead be correlated to $C_nH_{2n-1}^+$ sequence, typical of alkenes formed from H_2 neutral loss of alkyl fragments and/or alkenes; whereas m/z=57, 71, 85 are particularly relevant for saturated and normal branched alkenes considering the $C_nH_{2n+1}^+$ sequence (Alfarra et al., 2004; Tobias et al., 2001; Q. Zhang et al., 2005b). For each height above the burner, the signal of the pre-listed m/z decreases after photooxidation. In Figure 24, the relative abundances of some selected m/z (15, 44, 85 and 97) have been recorded.

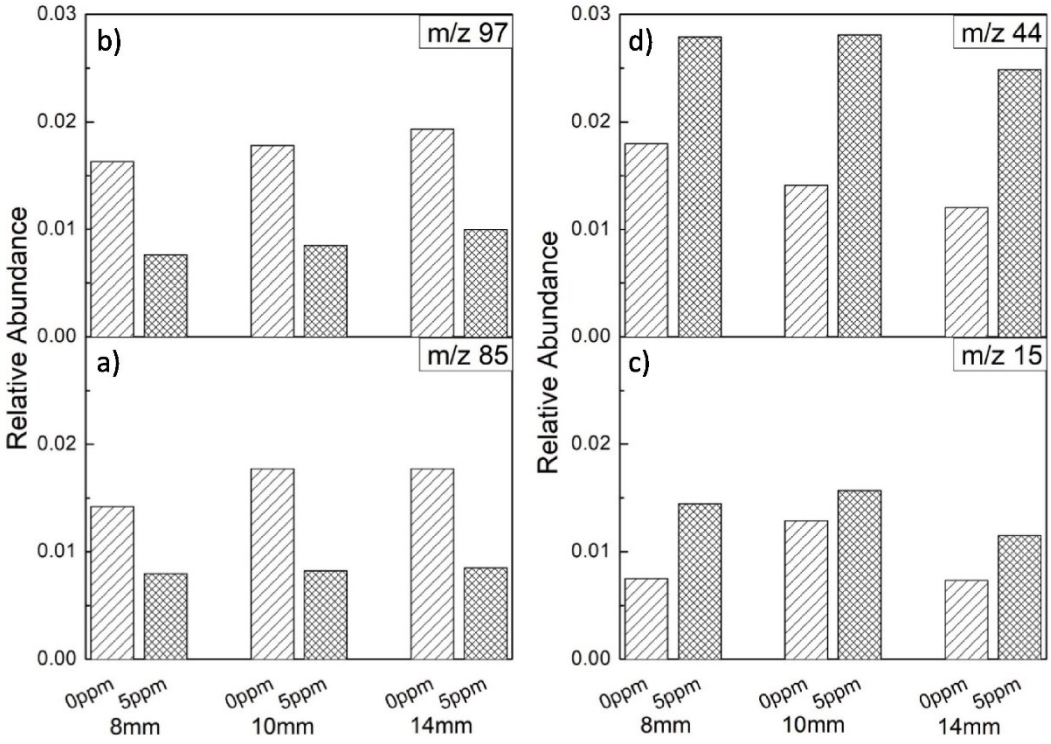

Figure 24: Relative Abundance of different m/z ratios for different m/z ratios

These mass-to-charge ratios have been chosen not only for their representativity of the HOA and OOA compounds but also due to the evident effect of photooxidation on their signal intensity. In general, HOA component is dominated by the hydrocarbon ion series $C_nH^+2_{n+1}$ and $C_nH^+_{2n-1}$, i.e. m/z equal to 27, 29, 41, 43, 55, 57 etc. Mass-to-charge ratios equal to 85 and 97 have been considered as representative of HOA (hence of POA). These two m/z can be associated to $C_6H_{13}^+$ and $C_7H_{13}^+$, respectively. Their hydrocarbon-like structure is particularly affected by oxidative conditions, explaining the variation of their signal going from 0 ppm to 5 ppm of ozone. The oxidation-related decrease of their signal is observed for each height above the burner.

As HOA, also OOA tracers, used as SOA indicators, have been affected by the photooxidation, especially m/z equal to 15, 17, 18, 31, 44, 45, 53. Conversely but coherently to HOA, for each height above the burner, an increase in OOA tracer signal was registered after ozone introduction. Mass-to-charge ratio equal to 15 can be associated to methyl radical presence, CH_3^+, mainly released by the fragmentation of aromatic-like structures associated to increased oxidative conditions (Q. Zhang et al., 2005b; Zhu et al., 2021). As previously described, m/z 44 is a marker of samples oxidation levels (Ng et al., 2011). Both m/z equal to 15 and 44 show a signal increase for higher heights above the burner.

Triangular Plots

A zoom-in in the oxidation effect on the samples was performed by investigating the so called f43 and f44 fractions. The values f44 and f43 are defined as the ratios of m/z44 and m/z43 to total signal in the component spectrum, respectively (Ng et al., 2011). By plotting the f44 against f43, the so called "triangular plots" can be obtained. As previously described, f43 is an indicator of the saturated carbonyl group, although it can also be related to other species whereas f44 is associated to the thermal decarboxylation of oxo-, di-, and poly-carboxylic acids (Aiken et al., 2007; Alfarra et al., 2006). Implementing f43 vs f44 plot in this study, represents a useful way to efficiently compare the samples before and after the exposure to O_3 and DOFR™ UV lamps, aiming to isolate the effects of the photooxygenation processes on the collected samples. The intensity of f43 and f44 fractions, can reveal the presence of oxygen containing functional groups. The expression "triangular plot" refers to the triangular shape within the plot area bordered by the blue and red dashed lines, visible in Figure 25.

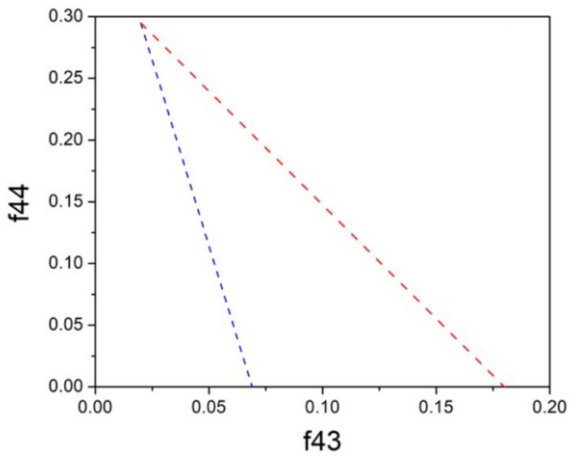

Figure 25: Triangular plot f43 vs f44. The red and blue dotted lines delimit the area within the atmospheric data usually fall (Ng et al., 2010)

For both laboratory and atmospheric studies, this area within the two lines has been used as standardized region for comparing and characterizing any OOA component recorded by mass spectrometry (Ng et al., 2010). The blue line has a slope and an intercept equal to -6.0204 and 0.4154, whereas the red one -1.8438 and 0.3319, respectively, valid for $0.069 \leq x \leq 0.18$, and $y \leq 0.29$ (Ng et al., 2010). Triangular plots provide several information about the OOA volatility: usually, semi-volatile (SV) OOA tends to fall in the lower half of the triangle, while low volatile (LV) OOA components tend to concentrate in the upper half of the triangle. Actually, f43 and f44 by themselves can represent semi-volatile OOA and low volatile OOA, respectively, as reported by previous studies (Jimenez et al., 2009c; Lambe et al., 2011). SV-OOA represent less oxidized and photochemically younger organics and the differences in terms of f43 for this class of compounds can be attributed to different sources and chemical pathways.

In the present study, under non-oxidation conditions, a decrease in f44 and an opposite increase in f43 are registered for higher residence times, i.e. heights above the burner. This result aligns with the data shown in Figure 22 and it suggests that higher residence times impact on the hydrocarbon species by increasing their fraction. A similar trend is observed whenever ozone is injected, but in this case higher values of f44 are registered. This result confirms the occurrence of an oxidation process that impacts on the formation of organic oxygenated carboxylic species. Analogous differences from non-oxidative to oxidative conditions, in the f43 values are not registered. This observation aligns with the results registered by Figure 22, there the photooxidation seems to promote oxygenated compounds by simultaneously reducing hydrocarbon-like species.

The triangular plots for the collected sample are reported in Figure 26.

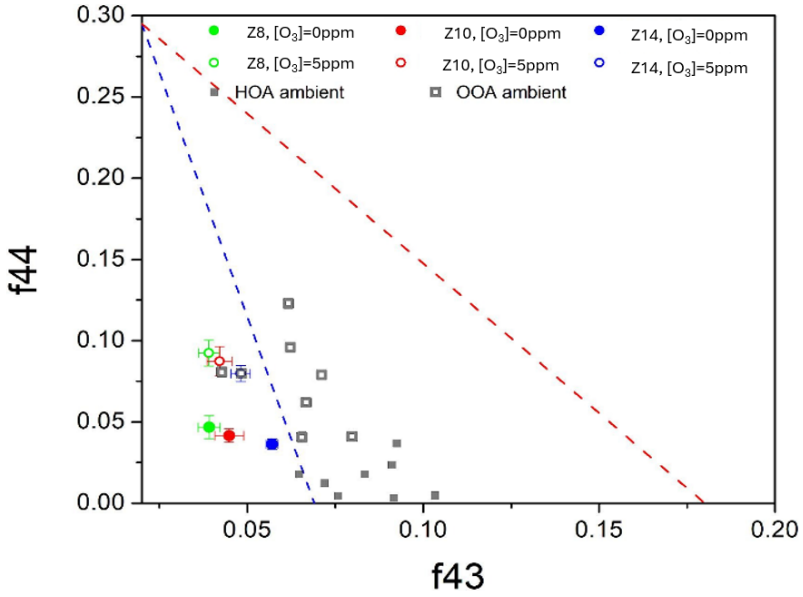

Figure 26: Triangular Plots for POA (O_3=0 ppm) and SOA (O_3=5 ppm). The reference HOA and OOA ambient data refer to the studies of Ng et al. (Ng et al., 2010, 2011).

As a comparison, the data provided by Ng et al. for HOA and OOA are reported on the plot in grey colour (Ng et al., 2010, 2011). The dataset investigated by Ng et al., is determined through a multivariate factor analysis of the dataset in the unit mass resolution (UMR) of the Northern Hemisphere. In the plot, the filled dots represent the POA (non-oxidized condition with O_3 = 0 ppm) collected at Z = 8, 10, 14 mm represented in green, red, and blue, respectively.

The empty dots represent the oxidated condition (SOA generated with O_3 = 5 ppm), having the same colour legend adopted for POA, to separate the various Zs. The location of the oxidized products on the plot appears to be consistent with the environmental OOA reference data produced by Ng et al. Furthermore, under unoxidized conditions, lower f44 values are registered compared to oxidized samples. This result is coherent with the gap observed between reference HOA and OOA values.

OA composition is affected by several variables, going from physical mixing to condensation/evaporation effects, to photochemical transformation. Due to the variety of all the possible effects, the characterization of the OA composition is extremely challenging. The evolution of total OA composition can not only be performed through the f44 vs f43 diagram but also using the Van Krevelen plots, reporting H:C vs O:C (Van Krevelen, 1950). These plots are produced by performing an elemental analysis of the high-resolution mass spectra, based on the studies developed by Aiken et al. (Aiken et al., 2007, 2008) and consequently improved by Canagaratna et al. (Canagaratna et al., 2015). A correlation between f44 vs f43 and Van Krevelen plots was found by Ng et al. (Ng et al., 2011); in particular, the triangle region characteristic of the f44 vs f43 was calculated through the application of a specific parametrization method correlating the f44 and f43 to O:C and H:C respectively (Aiken et al., 2007; Ng et al., 2011). From this parametrization, it is possible to transpose the triangular region of the f44 vs f43 plot on the Van Krevelen diagram: this correspondence is reported in Figure 27.

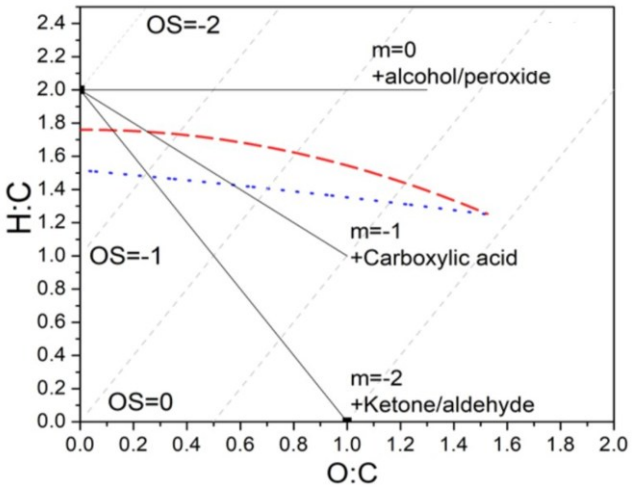

Figure 27: Van Krevelen Plot. Blue and red dotted lines delimit the region of the plot where atmospheric data usually fall.

The black lines with different slopes (m) are representative of three key functional groups: ketone/aldehydes (m = -2), carboxylic acids (m = -1) and alcohol/peroxides (m = 0). Dashed lines have been used to report different oxidation states (OS_c), which represents an ideal metric to quantify the oxidation degree of organic species in the atmosphere. By literature, oxidation state can be defined as the charge a carbon atom would take if lost all the electrons in bond with more electronegative atoms but gain all the electrons in bond with less electronegative atoms (Kroll et al., 2011a).In oxidizing environments, even if the oxidation state of single molecules may change differently, the average oxidation state of the carbon (OS_c) must increase. In the atmosphere, an increase in OS_c can be related to the formation of carbon-to-oxygen (or other electronegative elements) bonds and/or to the breaking of carbon-to-hydrogen (or other electropositive elements) bonds. According to the definition of Kroll et al., OS_c can be calculated with the following equation (Kroll et al., 2011a):

$$OS_c = 2\frac{O}{C} - \frac{H}{C} \qquad \text{(Eq. 5)}$$

The Van Krevelen plots for the three-residence times in flame are reported in Figure 28 for POA and SOA compounds. All the experimental conditions, the effect of the oxidative conditions is registered as increase in the O:C ratio followed by a reduction in the H:C. This result is coherent with the expectations of having a higher OOA contribution in a more oxidative environment, i.e. when O_3 is added to the system.

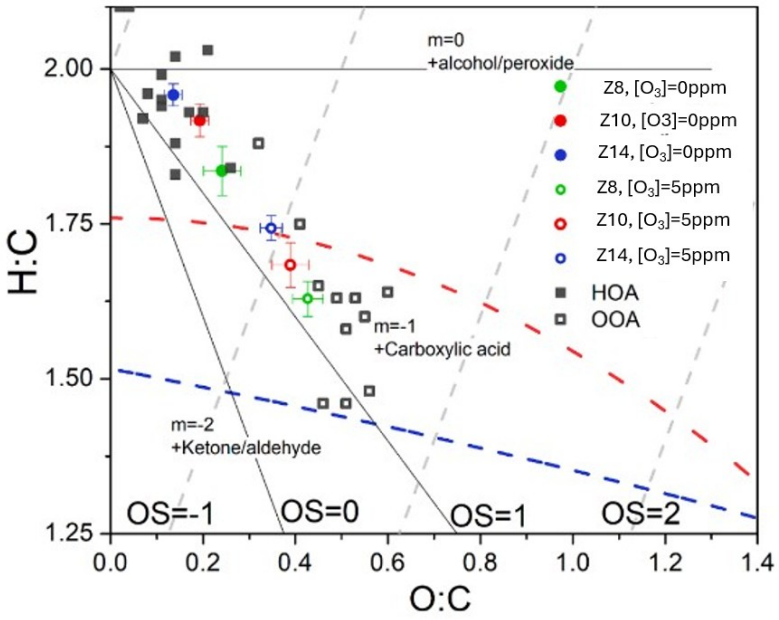

Figure 28: Van Krevelen plots for POA (O_3=0 ppm) and SOA (O_3=5 ppm) at the three-residence times in flame. Gray squares represent the reference ambient data of HOA (filled) and OOA (empty) from Canagaratna et al. (Canagaratna et al., 2015)

The observed variations in terms of oxidation state, result to be coherent with previous findings about aromatic precursors and with OA observed transformations under photochemical conditions (Lambe et al., 2011; Ng et al., 2011). The collected data rely within the region defined by the dashed lines, resulting in an oxidation state approximately around -0.5. Previous studies showed the consistency of this slope with specific chemical transformations mainly involving the formation of acid groups.

In general, the slope range can be directly correlated to the chemical transformation and, more specifically to presence of specific functional groups, registered in the experiment. For instance, if the functional group addition happens on a CH_2 unit without proceeding by the C-C bond breakage, a -0.5 slope can be attributed either to three OH-groups addition and one (C=O) unit or to the addition of two OH and one COOH group. Under low-NOx environments, the formation of peroxides can also be recorded and in this case the slope can be explained by considering the addition of one OOH unit, one OH group and one C=O group or eventually by the addition of one OOH and one COOH (Surratt et al., 2006). Furthermore, hydroperoxides react with aldehydes, and with ketones as well under acidic conditions, forming peroxyhemialcetals and peroxyacetals, respectively. This alternative pathway can also explain the addition of a carbonyl group. Briefly, several laboratory and field data measurements show that the net OOA aging mechanism reactions involve both COOH and OH/OOH functional groups addition. Moreover, a -0.5 slope could also be explained considering the addition of a COOH group to the C-C bond cleavage site; for instance, the replacement of -CH_3 group with -COOH unit in correspondence of a C-C bond breakage site with no oxygen losses due to fragmentation, will result in a -0.5 slope on the Van Krevelen diagram (Decarlo et al., 2010; Docherty et al., 2011; Ng et al., 2011; X. Wang et al., 2010).

3.4 Conclusions

The current study aims to investigate the impact of photooxidation on combustion-released aerosols. Both gaseous and particle phases generated by the ethylene-air flame are physically and chemically characterized by using particle size distribution functions (PSDs) and mass spectra analysis. Samples are collected with movable probes at different heights above the burner, allowing the examination of products released at different residence times within the flame. POA and SOA are studied under two different aging conditions, equal to O_3=0 ppm and O_3=5 ppm, respectively. The involved O3 concentration aims to replicate a SOA obtained after approximately two days of atmospheric aging. The

aging process was performed by using an oxidation flow reactor (Dekati® DOFR™) equipped with UV lamps in order to photolyze the injected O_3 by producing OH radicals.

PSDs analysis highlighted the formation of new and larger particles after the ozone introduction. Moreover, at higher residence times in the flame, i.e. Z = 14 mm, an additional mode with intermediate particles size equal to 6nm is registered and purely attributed to photooxidation.

The chemical characterization of the system unveiled significant changes in SOA and POA, marked by the variation of some crucial peaks assigned to tracer markers. The use of a high-resolution analysis ranging in the m/z interval from 10 to 120 is performed. This investigation highlights the key contribution of CH-like hydrocarbon species to total POA with a less significant contribution of CHO_{gt1} and CHO families. After the aging process, the results show a strong increase in the oxygenated carbon compounds, key components of secondary aerosols. On the other hand, after O_3 injection, the contribution of CH family appears to be reduced. C_x species, traditionally associated to fullerenes, show an increasing trend following the residence time in flame but no strong correlation with the oxidative process. Moreover, for both SOA and POA samples, nitrogenous species, whenever present, do not seem to crucially contribute to the system. Triangular plots and Van Krevelen diagrams are used as efficient tools to validate oxidation-related trends. In conclusion, photooxidation seems to promote the formation of oxygenated compounds and the reduction of hydrocarbon-like species. This result strongly agrees with atmospheric studies due to the correlation between oxidated conditions and carboxylic acids contribution.

3.5 Further Steps

These findings highlight the key role of photooxidation in shaping both the physical and chemical properties of combustion-generated aerosols, promoting oxygenated species while reducing hydrocarbon-like contributions. Building on this mechanistic understanding, it becomes clear that further online analyses are needed to fully capture the dynamic evolution of particles and their precursors. Motivated by these results, the subsequent study extends the investigation to atmospheric conditions, focusing on the interactions between biogenic and anthropogenic RO_2 radicals and their influence on secondary organic aerosol formation, dimer production, and new particle formation. This approach allows us to bridge the insights gained from controlled flame experiments with the complex radical-driven processes occurring in the real atmosphere.

3.6 References

Abid, A. D., Heinz, N., Tolmachoff, E. D., Phares, D. J., Campbell, C. S., & Wang, H. (2008). On evolution of particle size distribution functions of incipient soot in premixed ethylene–oxygen–argon flames. Combustion and Flame, 154(4), 775–788. https://doi.org/10.1016/J.COMBUSTFLAME.2008.06.009

Aiken, A. C., DeCarlo, P. F., & Jimenez, J. L. (2007). Elemental Analysis of Organic Species with Electron Ionization High-Resolution Mass Spectrometry. Analytical Chemistry, 79(21), 8350–8358. https://doi.org/10.1021/AC071150W

Aiken, A. C., Decarlo, P. F., Kroll, J. H., Worsnop, D. R., Huffman, J. A., Docherty, K. S., Ulbrich, I. M., Mohr, C., Kimmel, J. R., Sueper, D., Sun, Y., Zhang, Q., Trimborn, A., Northway, M., Ziemann, P. J., Canagaratna, M. R., Onasch, T. B., Alfarra, M. R., Prevot, A. S. H., … Jimenez, J. L. (2008). O/C and OM/OC Ratios of Primary, Secondary, and Ambient Organic Aerosols with High-Resolution Time-of-Flight Aerosol Mass Spectrometry. Environmental Science and Technology, 42(12), 4478–4485. https://doi.org/10.1021/ES703009Q

Alfarra, M. R., Coe, H., Allan, J. D., Bower, K. N., Boudries, H., Canagaratna, M. R., Jimenez, J. L., Jayne, J. T., Garforth, A. A., Li, S. M., & Worsnop, D. R. (2004). Characterization of urban and rural organic particulate in the Lower Fraser Valley using two Aerodyne Aerosol Mass Spectrometers. Atmospheric Environment, 38(34), 5745–5758. https://doi.org/10.1016/J.ATMOSENV.2004.01.054

Alfarra, M. R., Paulsen, D., Gysel, M., Garforth, A. A., Dommen, J., Prévôt, A. S. H., Worsnop, D. R., Baltensperger, U., & Coe, H. (2006). A mass spectrometric study of secondary organic aerosols formed from the photooxidation of anthropogenic and biogenic precursors in a reaction chamber. Atmospheric Chemistry and Physics, 6(12), 5279–5293. https://doi.org/10.5194/ACP-6-5279-2006

Alfarra, M. R., Prevot, A. S. H., Szidat, S., Sandradewi, J., Weimer, S., Lanz, V. A., Schreiber, D., Mohr, M., & Baltensperger, U. (2007). Identification of the Mass Spectral Signature of Organic Aerosols from Wood Burning Emissions. Environmental Science and Technology, 41(16), 5770–5777. https://doi.org/10.1021/ES062289B

Allan, J. D., Jimenez, J. L., Williams, P. I., Rami Alfarra, M., Bower, K. N., Jayne, J. T., Coe, H., Worsnop, D. R., Jimenez, J. L., Williams, P. I., Alfarra, M. R., Bower, K. N., Jayne, J. T., Coe, H., & Worsnop, D. R. (2003). Quantitative sampling using an Aerodyne aerosol mass spectrometer 1. Techniques of data interpretation and error analysis. Journal of Geophysical Research: Atmospheres, 108(D3), 4090. https://doi.org/10.1029/2002JD002358

Arffman, A., Laakkonen E., Nikka M., Luntta E., (2022). Oxidation Flow Reactor characterisation and applications. [Poster], IAC 2022, Dekati Ltd. Retrieved from https://dekati.com/wp-content/uploads/arffman_iac2022_poster.pdf

Bahreini, R., Keywood, M. D., Ng, N. L., Varutbangkul, V., Gao, S., Flagan, R. C., Seinfeld, J. H., Worsnop, D. R., & Jimenez, J. L. (2005). Measurements of secondary organic aerosol from oxidation of cycloalkenes, terpenes, and m-xylene using an Aerodyne aerosol mass spectrometer. Environmental Science & Technology, 39(15), 5674–5688. https://doi.org/10.1021/ES048061A

Bahreini, R., Middlebrook, A. M., De Gouw, J. A., Warneke, C., Trainer, M., Brock, C. A., Stark, H., Brown, S. S., Dube, W. P., Gilman, J. B., Hall, K., Holloway, J. S., Kuster, W. C., Perring, A. E., Prevot, A. S. H., Schwarz, J. P., Spackman, J. R., Szidat, S., Wagner, N. L., … Parrish, D. D. (2012). Gasoline emissions dominate over diesel in formation of secondary organic aerosol mass. Geophysical Research Letters, 39(6), 6805. https://doi.org/10.1029/2011GL050718;REQUESTEDJOURNAL:JOURNAL:19448007;WGROUP:STRING:PUBLICATION

Canagaratna, M. R., Jimenez, J. L., Kroll, J. H., Chen, Q., Kessler, S. H., Massoli, P., Hildebrandt Ruiz, L., Fortner, E., Williams, L. R., Wilson, K. R., Surratt, J. D., Donahue, N. M., Jayne, J. T., & Worsnop, D. R. (2015). Elemental ratio measurements of organic compounds using aerosol mass spectrometry: Characterization, improved calibration, and implications. Atmospheric Chemistry and Physics, 15(1), 253–272. https://doi.org/10.5194/ACP-15-253-2015

Cao, J., Wang, Q., Li, L., Zhang, Y., Tian, J., Chen, L. W. A., Ho, S. S. H., Wang, X., Chow, J. C., & Watson, J. G. (2020). Evaluation of the Oxidation Flow Reactor for particulate matter emission limit certification. Atmospheric Environment, 224, 117086. https://doi.org/10.1016/J.ATMOSENV.2019.117086

Carter, W. P. L., & Atkinson, R. (1996). Development and evaluation of a detailed mechanism for the atmospheric reactions of isoprene and NOx. International Journal of Chemical Kinetics, 28(7), 497–530. https://doi.org/https://doi.org/10.1002/(SICI)1097-4601(1996)28:7<497::AID-KIN4>3.0.CO;2-Q

Cereceda-Balic, F., Toledo, M., Vidal, V., Guerrero, F., Diaz-Robles, L. A., Petit-Breuilh, X., & Lapuerta, M. (2017). Emission factors for PM2.5, CO, CO2, NOx, SO2 and particle size distributions from the combustion of wood species using a new controlled combustion chamber 3CE. Science of The Total Environment, 584–585, 901–910. https://doi.org/10.1016/J.SCITOTENV.2017.01.136

Chirico, R., Decarlo, P. F., Heringa, M. F., Tritscher, T., Richter, R., Prévôt, A. S. H., Dommen, J., Weingartner, E., Wehrle, G., Gysel, M., Laborde, M., & Baltensperger, U. (2010). Impact of aftertreatment devices on primary emissions and secondary organic aerosol formation potential from in-use diesel vehicles: Results from smog chamber experiments. Atmospheric Chemistry and Physics, 10(23), 11545–11563. https://doi.org/10.5194/ACP-10-11545-2010

Chu, B. J., Chen, T., Liu, Y., Ma, Q., Mu, Y., Wang, Y., Ma, J., Zhang, P., Liu, J., Liu, C., Gui, H., Hu, R., Hu, B., Wang, X., Wang, Y., Liu, J., Xie, P., Chen, J., Liu, Q., … He, H. (2022). Application of smog chambers in atmospheric process studies. National Science Review, 9(2). https://doi.org/10.1093/NSR/NWAB103

Commodo, M., Kaiser, K., De Falco, G., Minutolo, P., Schulz, F., D'Anna, A., & Gross, L. (2019). On the early stages of soot formation: Molecular structure elucidation by high-resolution atomic force microscopy. Combustion and Flame, 205, 154–164. https://doi.org/10.1016/J.COMBUSTFLAME.2019.03.042

Daellenbach, K., Kourtchev, I., Vogel, A., Bruns, E., Jiang, J., Petäjä, T., Jaffrezo, J. L. L., Aksoyoglu, S., Kalberer, M., Baltensperger, U., El Haddad, I., & Prevot, S. H. (2019). Impact of anthropogenic and biogenic sources on the seasonal variation in the molecular composition of urban organic aerosols: A field and laboratory study using ultra-high-resolution mass spectrometry. Atmospheric Chemistry and Physics, 19(9), 5973–5991. https://doi.org/10.5194/ACP-19-5973-2019

Day, D. A., Fry, J. L., Kang, H. G., Krechmer, J. E., Ayres, B. R., Keehan, N. I., Thompson, S. L., Hu, W., Campuzano-Jost, P., Schroder, J. C., Stark, H., Devault, M. P., Ziemann, P. J., Zarzana, K. J., Wild, R. J., Dubè, W. P., Brown, S. S., & Jimenez, J. L. (2022). Secondary Organic Aerosol Mass Yields from NO3 Oxidation of α-Pinene and Δ-Carene: Effect of RO2 Radical Fate. The Journal of Physical Chemistry A, 126(40), 7309–7330. https://doi.org/10.1021/ACS.JPCA.2C04419

DeCarlo, P. F., Kimmel, J. R., Trimborn, A., Northway, M. J., Jayne, J. T., Aiken, A. C., Gonin, M., Fuhrer, K., Horvath, T., Docherty, K. S., Worsnop, D. R., & Jimenez, J. L. (2006). Field-Deployable, High-Resolution, Time-of-Flight Aerosol Mass Spectrometer. Analytical Chemistry, 78(24), 8281–8289. https://doi.org/10.1021/AC061249N

Decarlo, P. F., Ulbrich, I. M., Crounse, J., De Foy, B., Dunlea, E. J., Aiken, A. C., Knapp, D., Weinheimer, A. J., Campos, T., Wennberg, P. O., & Jimenez, J. L. (2010). Investigation of the sources and processing of organic aerosol over the Central Mexican Plateau from aircraft measurements during MILAGRO. Atmospheric Chemistry and Physics, 10(12), 5257–5280. https://doi.org/10.5194/ACP-10-5257-2010

Dekati Ltd. (2022). Oxidation Flow Reactor DOFRTM User Manual Ver 2.0 Dekati ®. www.dekati.com

Dobbins, R. A., Fletcher, R. A., & Chang, H. C. (1998). The evolution of soot precursor particles in a diffusion flame. Combustion and Flame, 115(3), 285–298. https://doi.org/10.1016/S0010-2180(98)00010-8

Docherty, K. S., Aiken, A. C., Huffman, J. A., Ulbrich, I. M., Decarlo, P. F., Sueper, D., Worsnop, D. R., Snyder, D. C., Peltier, R. E., Weber, R. J., Grover, B. D., Eatough, D. J., Williams, B. J., Goldstein, A. H., Ziemann, P. J., & Jimenez, J. L. (2011). The 2005 Study of Organic Aerosols at Riverside (SOAR-1): Instrumental intercomparisons and fine particle composition. Atmospheric Chemistry and Physics, 11(23), 12387–12420. https://doi.org/10.5194/ACP-11-12387-2011

Drewnick, F., Diesch, J. M., Faber, P., & Borrmann, S. (2015). Aerosol mass spectrometry: Particle-vaporizer interactions and their consequences for the measurements. Atmospheric Measurement Techniques, 8(9), 3811–3830. https://doi.org/10.5194/AMT-8-3811-2015

Duva, B. C., Wang, Y. C., Chance, L. E., & Toulson, E. (2021). Laminar flame characteristics of sequential two-stage combustion of premixed methane/air flames. Journal of Engineering for Gas Turbines and Power, 143(6). https://doi.org/10.1115/1.4048450/1087026

Echavarria, C. A., Sarofim, A. F., Lighty, J. A. S., & D'Anna, A. (2011). Evolution of soot size distribution in premixed ethylene/air and ethylene/benzene/air flames: Experimental and modeling study. Combustion and Flame, 158(1), 98–104. https://doi.org/10.1016/J.COMBUSTFLAME.2010.07.021

Gentner, D. R., Jathar, S. H., Gordon, T. D., Bahreini, R., Day, D. A., El Haddad, I., Hayes, P. L., Pieber, S. M., Platt, S. M., De Gouw, J., Goldstein, A. H., Harley, R. A., Jimenez, J. L., Prévôt, A. S. H., & Robinson, A. L. (2017). Review of Urban Secondary Organic Aerosol Formation from Gasoline and Diesel Motor Vehicle Emissions. Environmental Science and Technology, 51(3), 1074–1093. https://doi.org/10.1021/ACS.EST.6B04509

Glassman, I., Yetter, R. A., & Glumac, N. G. (2014). Combustion [M]. 293. https://books.google.com/books/about/Combustion.html?hl=it&id=lLJZAwAAQBAJ

Goetz, J. D., Giordano, M. R., Stockwell, C. E., Bhave, P. V., Puppala, P. S., Panday, A. K., Jayarathne, T., Stone, E. A., Yokelson, R. J., & Decarlo, P. F. (2022). Aerosol Mass Spectral Profiles from NAMaSTE Field-Sampled South Asian Combustion Sources. ACS Earth and Space Chemistry, 6(11), 2619–2631. https://doi.org/10.1021/ACSEARTHSPACECHEM.2C00173

Goldman, M. J., Green, W. H., & Kroll, J. H. (2021). Chemistry of Simple Organic Peroxy Radicals under Atmospheric through Combustion Conditions: Role of Temperature, Pressure, and NOx Level. The Journal of Physical Chemistry A, 125(48), 10303–10314. https://doi.org/10.1021/ACS.JPCA.1C07203

Hallquist, M., Wenger, J. C., Baltensperger, U., Rudich, Y., Simpson, D., Claeys, M., Dommen, J., Donahue, N. M., George, C., Goldstein, A. H., Hamilton, J. F., Herrmann, H., Hoffmann, T., Iinuma, Y., Jang, M., Jenkin, M. E., Jimenez, J. L., Kiendler-Scharr, A., Maenhaut, W., … Wildt, J. (2009a). The formation, properties and impact of secondary organic aerosol: Current and emerging issues. Atmospheric Chemistry and Physics, 9(14), 5155–5236. https://doi.org/10.5194/ACP-9-5155-2009

Hallquist, M., Wenger, J. C., Baltensperger, U., Rudich, Y., Simpson, D., Claeys, M., Dommen, J., Donahue, N. M., George, C., Goldstein, A. H., Hamilton, J. F., Herrmann, H., Hoffmann, T., Iinuma, Y., Jang, M., Jenkin, M. E., Jimenez, J. L., Kiendler-Scharr, A., Maenhaut, W., … Wildt, J. (2009b). The formation, properties and impact of secondary organic aerosol: Current and emerging issues. Atmospheric Chemistry and Physics, 9(14), 5155–5236. https://doi.org/10.5194/ACP-9-5155-2009

He, L. Y., Lin, Y., Huang, X. F., Guo, S., Xue, L., Su, Q., Hu, M., Luan, S. J., & Zhang, Y. H. (2010). Characterization of high-resolution aerosol mass spectra of primary organic aerosol emissions from Chinese cooking and biomass burning. Atmospheric Chemistry and Physics, 10(23), 11535–11543. https://doi.org/10.5194/ACP-10-11535-2010

He, M., & Dhaniyala, S. (2013). A multiple charging correction algorithm for scanning electrical mobility spectrometer data. Journal of Aerosol Science, 61, 13–26. https://doi.org/10.1016/J.JAEROSCI.2013.03.007

Heringa, M. F., Decarlo, P. F., Chirico, R., Tritscher, T., Clairotte, M., Mohr, C., Crippa, M., Slowik, J. G., Pfaffenberger, L., Dommen, J., Weingartner, E., Prévôt, A. S. H., & Baltensperger, U. (2012). A new method to discriminate secondary organic aerosols from different sources using high-resolution aerosol mass spectra. Atmospheric Chemistry and Physics, 12(4), 2189–2203. https://doi.org/10.5194/ACP-12-2189-2012

Homann, K. H. (1998). Fullerenes and Soot Formation- New Pathways to Large Particles in Flames. Angewandte Chemie (International Ed. in English), 37(18), 2434–2451. https://doi.org/10.1002/(sici)1521-3773(19981002)37:18<2434::aid-anie2434>3.0.co;2-l

Hooftman, N., Messagie, M., Van Mierlo, J., & Coosemans, T. (2018). A review of the European passenger car regulations – Real driving emissions vs local air quality. Renewable and Sustainable Energy Reviews, 86, 1–21. https://doi.org/10.1016/J.RSER.2018.01.012

Ishiguro, T., Takatori, Y., & Akihama, K. (1997). Microstructure of diesel soot particles probed by electron microscopy: First observation of inner core and outer shell. Combustion and Flame, 108(1–2), 231–234. https://doi.org/10.1016/S0010-2180(96)00206-4

Jayne, J. T., Leard, D. C., Zhang, X., Davidovits, P., Smith, K. A., Kolb, C. E., & Worsnop, D. R. (2000). Development of an aerosol mass spectrometer for size and composition analysis of submicron particles. Aerosol Science and Technology, 33(1–2), 49–70. https://doi.org/10.1080/027868200410840;JOURNAL:JOURNAL:UAST20;REQUESTEDJOURNAL:JOURNAL:UAST20;WGROUP:STRING:PUBLICATION

Jenei, I. Z., Dassenoy, F., Epicier, T., Khajeh, A., Martini, A., Uy, D., Ghaednia, H., & Gangopadhyay, A. (2018). Mechanical characterization of diesel soot nanoparticles: in situ compression in a transmission electron microscope and simulations. Nanotechnology, 29(8), 085703. https://doi.org/10.1088/1361-6528/AAA2AA

Jiang, L., Zhou, G., Huo, J., Gu, C., & Chen, X. (2021). Experimental Study on Hydrodynamic Instability Characteristics of N2-Diluted n-C4H10/Air Flat Flames. Flow, Turbulence and Combustion 2021 108:4, 108(4), 1115–1137. https://doi.org/10.1007/S10494-021-00303-9

Jimenez, J. L., Canagaratna, M. R., Donahue, N. M., Prevot, A. S. H., Zhang, Q., Kroll, J. H., DeCarlo, P. F., Allan, J. D., Coe, H., Ng, N. L., Aiken, A. C., Docherty, K. S., Ulbrich, I. M., Grieshop, A. P., Robinson, A. L., Duplissy, J., Smith, J. D., Wilson, K. R., Lanz, V. A., … Worsnop, D. R. (2009a). Evolution of organic aerosols in the atmosphere. Science, 326(5959), 1525–1529. https://doi.org/10.1126/SCIENCE.1180353;WEBSITE:WEBSITE:AAAS-SITE;ISSUE:ISSUE:DOI

Jimenez, J. L., Canagaratna, M. R., Donahue, N. M., Prevot, A. S. H., Zhang, Q., Kroll, J. H., DeCarlo, P. F., Allan, J. D., Coe, H., Ng, N. L., Aiken, A. C., Docherty, K. S., Ulbrich, I. M., Grieshop, A. P., Robinson, A. L., Duplissy, J., Smith, J. D., Wilson, K. R., Lanz, V. A., … Worsnop, D. R. (2009b). Evolution of organic aerosols in the atmosphere. Science, 326(5959), 1525–1529. https://doi.org/10.1126/SCIENCE.1180353;SUBPAGE:STRING:ABSTRACT;WEBSITE:WEBSITE:AAAS-SITE;ISSUE:ISSUE:DOI

Kholghy, M. R., Veshkini, A., & Thomson, M. J. (2016). The core–shell internal nanostructure of soot – A criterion to model soot maturity. Carbon, 100, 508–536. https://doi.org/10.1016/J.CARBON.2016.01.022

Krechmer, J. E., Pagonis, D., Ziemann, P. J., & Jimenez, J. L. (2016). Quantification of Gas-Wall Partitioning in Teflon Environmental Chambers Using Rapid Bursts of Low-Volatility Oxidized Species Generated in Situ. Environmental Science & Technology, 50(11), 5757–5765. https://doi.org/10.1021/ACS.EST.6B00606

Kroll, J. H., Donahue, N. M., Jimenez, J. L., Kessler, S. H., Canagaratna, M. R., Wilson, K. R., Altieri, K. E., Mazzoleni, L. R., Wozniak, A. S., Bluhm, H., Mysak, E. R., Smith, J. D., Kolb, C. E., & Worsnop, D. R. (2011). Carbon oxidation state as a metric for describing the chemistry of atmospheric organic aerosol. Nature Chemistry 2010 3:2, 3(2), 133–139. https://doi.org/10.1038/nchem.948

Kroll, J. H., & Seinfeld, J. H. (2008). Chemistry of secondary organic aerosol: Formation and evolution of low-volatility organics in the atmosphere. Atmospheric Environment, 42(16), 3593–3624. https://doi.org/10.1016/J.ATMOSENV.2008.01.003

Kuittinen, N., McCaffery, C., Peng, W., Zimmerman, S., Roth, P., Simonen, P., Karjalainen, P., Keskinen, J., Cocker, D. R., Durbin, T. D., Rönkkö, T., Bahreini, R., & Karavalakis, G. (2021). Effects of driving conditions on secondary aerosol formation from a GDI vehicle using an oxidation flow reactor. Environmental Pollution, 282, 117069. https://doi.org/10.1016/J.ENVPOL.2021.117069

Kuittinen, N., McCaffery, C., Zimmerman, S., Bahreini, R., Simonen, P., Karjalainen, P., Keskinen, J., Rönkkö, T., & Karavalakis, G. (2021). Using an oxidation flow reactor to understand the effects of gasoline aromatics and ethanol levels on secondary aerosol formation. Environmental Research, 200, 111453. https://doi.org/10.1016/J.ENVRES.2021.111453

La Rocca, A., Di Liberto, G., Shayler, P. J., & Fay, M. W. (2013). The nanostructure of soot-in-oil particles and agglomerates from an automotive diesel engine. Tribology International, 61, 80–87. https://doi.org/10.1016/J.TRIBOINT.2012.12.002

Lambe, A. T., Onasch, T. B., Massoli, P., Croasdale, D. R., Wright, J. P., Ahern, A. T., Williams, L. R., Worsnop, D. R., Brune, W. H., & Davidovits, P. (2011). Laboratory studies of the chemical composition and cloud condensation nuclei (CCN) activity of secondary organic aerosol (SOA) and oxidized primary organic aerosol (OPOA). Atmospheric Chemistry and Physics, 11(17), 8913–8928. https://doi.org/10.5194/ACP-11-8913-2011

Levy, H. (1971). Normal atmosphere: Large radical and formaldehyde concentrations predicted. Science, 173(3992), 141–143. https://doi.org/10.1126/SCIENCE.173.3992.141;WEBSITE:WEBSITE:AAAS-SITE;JOURNAL:JOURNAL:SCIENCE;ISSUE:ISSUE:DOI

Li, R., Palm, B. B., Ortega, A. M., Hlywiak, J., Hu, W., Peng, Z., Day, D. A., Knote, C., Brune, W. H., De Gouw, J. A., & Jimenez, J. L. (2015). Modeling the Radical Chemistry in an Oxidation Flow Reactor: Radical Formation and Recycling, Sensitivities, and the OH Exposure Estimation Equation. Journal of Physical Chemistry A, 119(19), 4418–4432. https://doi.org/10.1021/JP509534K

Matsunaga, A., & Ziemann, P. J. (2010). Gas-wall partitioning of organic compounds in a teflon film chamber and potential effects on reaction product and aerosol yield measurements. Aerosol Science and Technology, 44(10), 881–892.
https://doi.org/10.1080/02786826.2010.501044;JOURNAL:JOURNAL:UAST20;REQUESTEDJOURNAL:JOURNAL:UAST20;WGROUP:STRING:PUBLICATION

Ng, N. L., Canagaratna, M. R., Jimenez, J. L., Chhabra, P. S., Seinfeld, J. H., & Worsnop, D. R. (2011). Changes in organic aerosol composition with aging inferred from aerosol mass spectra. Atmospheric Chemistry and Physics, 11(13), 6465–6474. https://doi.org/10.5194/ACP-11-6465-2011

Ng, N. L., Canagaratna, M. R., Zhang, Q., Jimenez, J. L., Tian, J., Ulbrich, I. M., Kroll, J. H., Docherty, K. S., Chhabra, P. S., Bahreini, R., Murphy, S. M., Seinfeld, J. H., Hildebrandt, L., Donahue, N. M., Decarlo, P. F., Lanz, V. A., Prévôt, A. S. H., Dinar, E., Rudich, Y., & Worsnop, D. R. (2010). Organic aerosol components observed in Northern Hemispheric datasets from Aerosol Mass Spectrometry. Atmospheric Chemistry and Physics, 10(10), 4625–4641. https://doi.org/10.5194/ACP-10-4625-2010

Ng, N. L., Kroll, J. H., Chan, A. W. H., Chhabra, P. S., Flagan, R. C., & Seinfeld, J. H. (2007). Secondary organic aerosol formation from m-xylene, toluene, and benzene. Atmospheric Chemistry and Physics, 7(14), 3909–3922. https://doi.org/10.5194/ACP-7-3909-2007

Ortega, A. M., Hayes, P. L., Peng, Z., Palm, B. B., Hu, W., Day, D. A., Li, R., Cubison, M. J., Brune, W. H., Graus, M., Warneke, C., Gilman, J. B., Kuster, W. C., De Gouw, J., Gutiérrez-Montes, C., & Jimenez, J. L. (2016). Real-time measurements of secondary organic aerosol formation and aging from ambient air in an oxidation flow reactor in the Los Angeles area. Atmospheric Chemistry and Physics, 16(11), 7411–7433. https://doi.org/10.5194/ACP-16-7411-2016

Paulsen, D., Dommen, J., Kalberer, M., Prévôt, A. S. H., Richter, R., Sax, M., Steinbacher, M., Weingartner, E., & Baltensperger, U. (2005). Secondary Organic Aerosol Formation by Irradiation of 1,3,5-Trimethylbenzene−NOx−H2O in a New Reaction Chamber for Atmospheric Chemistry and Physics. Environmental Science and Technology, 39(8), 2668–2678. https://doi.org/10.1021/ES0489137

Peng, Z., Day, D. A., Stark, H., Li, R., Lee-Taylor, J., Palm, B. B., Brune, W. H., & Jimenez, J. L. (2015). HOx radical chemistry in oxidation flow reactors with low-pressure mercury lamps systematically examined by modeling. Atmospheric Measurement Techniques, 8(11), 4863–4890. https://doi.org/10.5194/AMT-8-4863-2015

Peng, Z., & Jimenez, J. L. (2020). Radical chemistry in oxidation flow reactors for atmospheric chemistry research. Chemical Society Reviews, 49(9), 2570–2616. https://doi.org/10.1039/C9CS00766K

Peng, Z., Lee-Taylor, J., Stark, H., Orlando, J. J., Aumont, B., & Jimenez, J. L. (2021). Evolution of OH reactivity in NO-free volatile organic compound photooxidation investigated by the fully explicit GECKO-A model. Atmospheric Chemistry and Physics, 21(19), 14649–14669. https://doi.org/10.5194/ACP-21-14649-2021

Pieber, S. M., Kumar, N. K., Klein, F., Comte, P., Bhattu, D., Dommen, J., Bruns, E. A., Kiluic, D., El Haddad, I., Keller, A., Czerwinski, J., Heeb, N., Baltensperger, U., Slowik, J. G., & Prévôt, A. S. H. (2018). Gas-phase composition and secondary organic aerosol formation from standard and particle filter-retrofitted gasoline direct injection vehicles investigated in a batch and flow reactor. Atmospheric Chemistry and Physics, 18(13), 9929–9954. https://doi.org/10.5194/ACP-18-9929-2018

Platt, S. M., El Haddad, I., Zardini, A. A., Clairotte, M., Astorga, C., Wolf, R., Slowik, J. G., Temime-Roussel, B., Marchand, N., Ježek, I., Drinovec, L., Močnik, G., Möhler, O., Richter, R., Barmet, P., Bianchi, F., Baltensperger, U., & Prévôt, A. S. H. (2013). Secondary organic aerosol formation from gasoline vehicle emissions in a new mobile environmental

reaction chamber. Atmospheric Chemistry and Physics, 13(18), 9141–9158. https://doi.org/10.5194/ACP-13-9141-2013

Reischl, G. P., Mäkelä, J. M., Karch, R., & Necid, J. (1996). Bipolar charging of ultrafine particles in the size range below 10 nm. Journal of Aerosol Science, 27(6), 931–949. https://doi.org/10.1016/0021-8502(96)00026-2

Sabbah, H., Commodo, M., Picca, F., De Falco, G., Minutolo, P., D'Anna, A., & Joblin, C. (2021). Molecular content of nascent soot: Family characterization using two-step laser desorption laser ionization mass spectrometry. Proceedings of the Combustion Institute, 38(1), 1241–1248. https://doi.org/10.1016/J.PROCI.2020.09.022

Schulz, F., Commodo, M., Kaiser, K., De Falco, G., Minutolo, P., Meyer, G., D'Anna, A., & Gross, L. (2019). Insights into incipient soot formation by atomic force microscopy. Proceedings of the Combustion Institute, 37(1), 885–892. https://doi.org/10.1016/J.PROCI.2018.06.100

Sgro, L. A., Basile, G., Barone, A. C., D'Anna, A., Minutolo, P., Borghese, A., & D'Alessio, A. (2003). Detection of combustion formed nanoparticles. Chemosphere, 51(10), 1079–1090. https://doi.org/10.1016/S0045-6535(02)00718-X

Simonen, P., Kalliokoski, J., Karjalainen, P., Rönkkö, T., Timonen, H., Saarikoski, S., Aurela, M., Bloss, M., Triantafyllopoulos, G., Kontses, A., Amanatidis, S., Dimaratos, A., Samaras, Z., Keskinen, J., Dal Maso, M., & Ntziachristos, L. (2019). Characterization of laboratory and real driving emissions of individual Euro 6 light-duty vehicles – Fresh particles and secondary aerosol formation. Environmental Pollution, 255, 113175. https://doi.org/10.1016/J.ENVPOL.2019.113175

Simonen, P., Saukko, E., Karjalainen, P., Timonen, H., Bloss, M., Aakko-Saksa, P., Rönkkö, T., Keskinen, J., & Dal Maso, M. (2017a). A new oxidation flow reactor for measuring secondary aerosol formation of rapidly changing emission sources. Atmospheric Measurement Techniques, 10(4), 1519–1537. https://doi.org/10.5194/AMT-10-1519-2017

Simonen, P., Saukko, E., Karjalainen, P., Timonen, H., Bloss, M., Aakko-Saksa, P., Rönkkö, T., Keskinen, J., & Dal Maso, M. (2017b). A new oxidation flow reactor for measuring secondary aerosol formation of rapidly changing emission sources. Atmos. Meas. Tech, 10, 1519–1537. https://doi.org/10.5194/amt-10-1519-2017

Sirignano, M., Kent, J., & D'Anna, A. (2013). Modeling Formation and Oxidation of Soot in Nonpremixed Flames. Energy and Fuels, 27(4), 2303–2315. https://doi.org/10.1021/EF400057R

Srivastava, D., Vu, T. V, Tong, S., Shi, Z., & Harrison, R. M. (2022). Formation of secondary organic aerosols from anthropogenic precursors in laboratory studies. Npj Climate and Atmospheric Science. https://doi.org/10.1038/s41612-022-00238-6

Surratt, J. D., Kroll, J. H., Kleindienst, T. E., Edney, E. O., Claeys, M., Sorooshian, A., Ng, N. L., Offenberg, J. H., Lewandowski, M., Jaoui, M., Flagan, R. C., & Seinfeld, J. H. (2006). Evidence for Organosulfates in Secondary Organic Aerosol. Environmental Science and Technology, 41(2), 517–527. https://doi.org/10.1021/ES062081Q

Takegawa, N., Miyakawa, T., Kondo, Y., Jimenez, J. L., Zhang, Q., Worsnop, D. R., & Fukuda, M. (2006). Seasonal and diurnal variations of submicron organic aerosol in Tokyo observed using the Aerodyne aerosol mass spectrometer. Journal of Geophysical Research Atmospheres, 111(11). https://doi.org/10.1029/2005JD006515

Takekawa, H., Minoura, H., & Yamazaki, S. (2003). Temperature dependence of secondary organic aerosol formation by photo-oxidation of hydrocarbons. Atmospheric Environment, 37(24), 3413–3424. https://doi.org/10.1016/S1352-2310(03)00359-5

Timonen, H., Karjalainen, P., Saukko, E., Saarikoski, S., Aakko-Saksa, P., Simonen, P., Murtonen, T., Dal Maso, M., Kuuluvainen, H., Bloss, M., Ahlberg, E., Svenningsson, B., Pagels, J., Brune, W. H., Keskinen, J., Worsnop, D. R., Hillamo, R., & Rönkkö, T. (2017). Influence of fuel ethanol content on primary emissions and secondary aerosol formation potential for a modern flex-fuel gasoline vehicle. Atmospheric Chemistry and Physics, 17(8), 5311–5329. https://doi.org/10.5194/ACP-17-5311-2017

Tkacik, D. S., Lambe, A. T., Jathar, S., Li, X., Presto, A. A., Zhao, Y., Blake, D., Meinardi, S., Jayne, J. T., Croteau, P. L., & Robinson, A. L. (2014). Secondary organic aerosol formation from in-use motor vehicle emissions using a potential

aerosol mass reactor. Environmental Science & Technology, 48(19), 11235–11242. https://doi.org/10.1021/ES502239V

Tobias, H. J., Beving, D. E., Ziemann, P. J., Sakurai, H., Zuk, M., McMurry, P. H., Zarling, D., Waytulonis, R., & Kittelson, D. B. (2001). Chemical Analysis of Diesel Engine Nanoparticles Using a Nano-DMA/Thermal Desorption Particle Beam Mass Spectrometer. Environmental Science and Technology, 35(11), 2233–2243. https://doi.org/10.1021/ES0016654

Turns, S. R. (2012). An introduction to combustion: concepts and applications. 732. https://books.google.com/books/about/An_Introduction_to_Combustion.html?hl=it&id=idM8twAACAAJ

Van Krevelen. (1950). Graphical-statistical method for the study of structure and reaction processes of coal. Fuel.

Volkamer, R., Jimenez, J. L., San Martini, F., Dzepina, K., Zhang, Q., Salcedo, D., Molina, L. T., Worsnop, D. R., & Molina, M. J. (2006). Secondary organic aerosol formation from anthropogenic air pollution: Rapid and higher than expected. Geophysical Research Letters, 33(17). https://doi.org/10.1029/2006GL026899;WGROUP:STRING:PUBLICATION

Wang, J., Doussin, J. F., Perrier, S., Perraudin, E., Katrib, Y., Pangui, E., & Picquet-Varrault, B. (2011). Design of a new multi-phase experimental simulation chamber for atmospheric photosmog, aerosol and cloud chemistry research. Atmospheric Measurement Techniques, 4(11), 2465–2494. https://doi.org/10.5194/AMT-4-2465-2011

Wang, X., Gao, S., Yang, X., Chen, H., Chen, J., Zhuang, G., Surratt, J. D., Chan, M. N., & Seinfeld, J. H. (2010). Evidence for High Molecular Weight Nitrogen-Containing Organic Salts in Urban Aerosols. Environmental Science and Technology, 44(12), 4441–4446. https://doi.org/10.1021/ES1001117

Wiedensohler, A., Birmili, W., Nowak, A., Sonntag, A., Weinhold, K., Merkel, M., Wehner, B., Tuch, T., Pfeifer, S., Fiebig, M., Fjäraa, A. M., Asmi, E., Sellegri, K., Depuy, R., Venzac, H., Villani, P., Laj, P., Aalto, P., Ogren, J. A., … Bastian, S. (2012). Atmospheric Measurement Techniques Mobility particle size spectrometers: harmonization of technical standards and data structure to facilitate high quality long-term observations of atmospheric particle number size distributions. Atmos. Meas. Tech, 5, 657–685. https://doi.org/10.5194/amt-5-657-2012

Xu, W., Croteau, P., Williams, L., Canagaratna, M., Onasch, T., Cross, E., Zhang, X., Robinson, W., Worsnop, D., & Jayne, J. (2016). Aerosol Science and Technology Laboratory characterization of an aerosol chemical speciation monitor with PM 2.5 measurement capability Laboratory characterization of an aerosol chemical speciation monitor with PM 2.5 measurement capability. https://doi.org/10.1080/02786826.2016.1241859

Zhang, Q., Jimenez, J. L., Canagaratna, M. R., Allan, J. D., Coe, H., Ulbrich, I., Alfarra, M. R., Takami, A., Middlebrook, A. M., Sun, Y. L., Dzepina, K., Dunlea, E., Docherty, K., DeCarlo, P. F., Salcedo, D., Onasch, T., Jayne, J. T., Miyoshi, T., Shimono, A., … Worsnop, D. R. (2007). Ubiquity and dominance of oxygenated species in organic aerosols in anthropogenically-influenced Northern Hemisphere midlatitudes. Geophysical Research Letters, 34(13). https://doi.org/10.1029/2007GL029979;WGROUP:STRING:PUBLICATION

Zhang, Q., Rami Alfarra, M., Worsnop, D. R., Allan, J. D., Coe, H., Canagaratna, M. R., & Jimenez, J. L. (2005a). Deconvolution and Quantification of Hydrocarbon-like and Oxygenated Organic Aerosols Based on Aerosol Mass Spectrometry. Environmental Science and Technology, 39(13), 4938–4952. https://doi.org/10.1021/ES048568L

Zhang, Q., Rami Alfarra, M., Worsnop, D. R., Allan, J. D., Coe, H., Canagaratna, M. R., & Jimenez, J. L. (2005b). Deconvolution and quantification of hydrocarbon-like and oxygenated organic aerosols based on aerosol mass spectrometry. Environmental Science & Technology, 39(13), 4938–4952. https://doi.org/10.1021/ES048568L

Zhao, B., Yang, Z., Wang, J., Johnston, M. V., & Wang, H. (2003). Analysis of soot nanoparticles in a laminar premixed ethylene flame by scanning mobility particle sizer. Aerosol Science and Technology, 37(8), 611–620. https://doi.org/10.1080/02786820300908;ISSUE:ISSUE:DOI

Zhu, W., Guo, S., Zhang, Z., Wang, H., Yu, Y., Chen, Z., Shen, R., Tan, R., Song, K., Liu, K., Tang, R., Liu, Y., Lou, S., Li, Y., Zhang, W., Zhang, Z., Shuai, S., Xu, H., Li, S., … Prévôt, A. S. H. (2021). Mass spectral characterization of secondary organic aerosol from urban cooking and vehicular sources. Atmospheric Chemistry and Physics, 21(19), 15065–15079. https://doi.org/10.5194/ACP-21-15065-2021

4. WP3:RO_2 Radical Interactions and Their Role in Secondary Organic Aerosol and Dimer Formation

4.1 Summary of the Chapter

Secondary organic aerosol (SOA) formation remains one of the least constrained processes in atmospheric chemistry, mainly due to incomplete understanding of the radical-driven mechanisms that transform gaseous precursors into low-volatility products. Among these reactive pathways, organic peroxy radicals (RO_2) play a central role in shaping SOA composition and yield through autoxidation, and bimolecular reactions, leasing to the formation of highly oxygenated organic molecules (HOMs) and dimers. Yet, major uncertainties persist regarding RO_2–RO_2 interactions, especially concerning how these interactions govern the formation of low-volatility dimeric species that efficiently contribute to new particle formation (NPF) and SOA growth.

The aim of this study is to investigate how the interactions between biogenic and anthropogenic RO_2-derived radicals affect SOA formation, with a specific focus on dimers production and contribution to NPF. Experiments were conducted in the CERN CLOUD (chamber, using α-pinene and isoprene as biogenic precursors, and trimethylbenzene, naphthalene, and toluene as representative anthropogenic VOCs. These species were injected within the chamber under controlled conditions at varying amounts to mimic forest, suburban, and urban chemical regimes.

A systematic exploration of the effects of precursor concentrations, and photooxidation conditions on RO_2 chemistry, dimer formation pathways, and their contribution to NPF and early particle growth is proposed. The results provide new insights into how mixed biogenic–anthropogenic RO_2 interactions can enhance or suppress SOA formation, improving mechanistic understanding of radical-driven aerosol production in diverse atmospheric environments.

4.2 Introduction

In the previous chapters, a chemical and morphological analysis of some chemical compounds released by anthropogenic activities, i.e., combustion systems, was presented. WP1 and WP2 studies highlighted the critical importance of clearly understanding the chemistry governing each system in order to accurately predict, and eventually mitigate, the release of harmful compounds and, more specifically, NPF and SOA production.

This chapter focuses on the gaseous precursors responsible for NPF under atmospherically relevant conditions, with particular emphasis on a key intermediate in volatile organic compounds (VOCs) daytime and nighttime chemistry: organic peroxy radicals (RO_2) (Okuljar et al., 2023; W. Peng et al., 2022; Wolfe et al., 2013; Zang et al., 2024).

Volatile organic compounds cover a broad range of chemical species with variegated chemical structures, including non-methane hydrocarbons, e.g. alkanes, alkene, aromatics, as well as oxygenated species, such as aldehydes, ketones and alcohols, and other multifunctional compounds with heteroatoms (X. Liu et al., 2025; Stanton & Tandon, 2023). In general, all these compounds are characterized by a relatively wide range of volatilities under ambient conditions yet strongly differing in composition and functional groups and, consequently, reactivity based on their chemical structure and their emission source (W. Wang et al., 2023; X. Zhang et al., 2025).

VOCs can be emitted from both anthropogenic (AVOCs) and biogenic (BVOCs) sources. BVOCs represent a major global source of VOCs and their contribution to NPF and SOA formation has been extensively investigated (W. Huang et al., 2024; Janyasuthiwong et al., 2022; Shen et al., 2024a). Although BVOC emissions may also originate from natural sources such as oceans and volcanic activity, they are

predominantly emitted by vegetation as part of plants physiological and ecological responses (Peñuelas & Staudt, 2010; Šimpraga et al., 2016). Among BVOCs, isoprene and terpenes are particularly abundant and reactive in the atmosphere (Guenther, 1995; Messina et al., 2016), with terpenoids constituting a class of compounds presenting more than 40000 identified structures, including monoterpenes (C_{10}) and sesquiterpenes (C_{15}).

Anthropogenic VOCs, by contrast, primarily originate from industrial and agricultural activities, fossil fuel combustion and solvent use (Friedrich & Obermeier, 1999b). Intuitively, urban environments are dominated by AVOCs emissions with benzene, toluene and trimethylbenzene (TMB) being among the most reactive and ubiquitous aromatic anthropogenic species (Molteni et al., 2018). Small fractions of compounds traditionally classified as BVOCs, particularly monoterpenes, can also be emitted by anthropogenic sources, such as cleaning agents and personal care products. However, their contribution is usually drastically minor compared to BVOCs emitted by vegetation (Gkatzelis et al., 2021; X. B. Li et al., 2022)

Once released into the atmosphere, both BVOCs and AVOCs are likely to undergo oxidation reactions with ozone (O_3), hydroxyl radicals (OH) or nitrate radicals (NO_3) (Finlayson-Pitts & Pitts, 2000; Wayne, 2006).

Ozone is a trace gas whose presence in the troposphere can be mainly reconducted to in situ photochemical production involving VOCs and NO_x under sunlight conditions (S. C. Liu et al., 1980) or alternatively to downward transport from the stratosphere (Roelofs & Lelieveld, 1997). These sources are counterbalanced by photochemical losses and dry deposition at the Earth's surface, resulting in ozone being ubiquitously present throughout the troposphere, with background mixing ratios of 10–40 ppbv at remote sites and values frequently exceeding 100 ppbv in polluted urban environments (Monks et al., 2015). OH is the main oxidizing agent participating in atmospheric photooxidation (Levy, 1971). OH radicals in the atmosphere can either be produced through photolytic processes, i.e. O_3 photolysis in presence of water molecules, or by non-photolytic ones, such as OH recycling in radical reaction chains (Lelieveld et al., 2016). Under atmospheric conditions, ozone photolysis represents the main OH source and its chemistry is mostly relevant during daytime (Lelieveld et al., 2016). Due to their high reactivity, i.e., lifetime shorter than one second, OH radicals react as soon as they are formed (Crutzen et al., 1999). Their concentration in the environment ranges from $1{\cdot}10^5$ to $1{\cdot}10^7$ molec/cm^3, measuring from rural to urban areas (Lu et al., 2013; Zou et al., 2025). NO_3 radicals are produced by NO_2 reaction with O_3 and during daytime this compound is usually consumed by photolysis or by reaction with NO, making its chemistry mainly relevant during nighttime (Wayne et al., 1991). NO_3 concentration ranges from $1{\cdot}10^3$ - $1{\cdot}10^5$ molec/cm^3 during daytime to, averagely, $1{\cdot}10^8$ molec/cm^3 during nighttime, exhibiting peaks up to $1{\cdot}10^{10}$ molec/cm^3 in continental areas or in regions characterized by high BVOCs emissions coupled with low NO concentrations (Atkinson, 2000; Lin et al., 2022).

Under atmospheric conditions, VOCs oxidation leads to the production of carbon-centered radicals which rapidly react with O_2 molecules, forming of peroxy radicals (RO_2) (Bianchi et al., 2019; Okuljar et al., 2023). Figure 29 shows the key generic steps of VOCs oxidation operated by atmospheric oxidants (O_3, NO_3 and OH) leading to the formation of peroxy radicals and contributing to O_3 tropospheric budget (T. Liu et al., 2022). Once formed, RO_2 can either undergo autoxidation with O_2 forming highly oxidized molecules or undergo termination reactions with RO_2, HO_2 and NO yielding various organic products. All these species actively participate in multiphase chemistry, nucleation and condensation mechanisms, driving the formation of SOA.

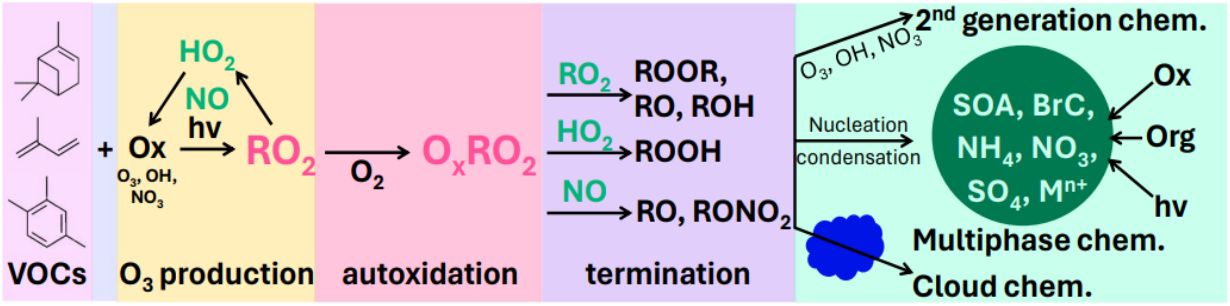

Figure 29: General Scheme of VOCs atmospheric fate. Credits to Imad El Haddad

Their high reactivity, makes RO_2 termination reactions with NO, RO_2 or HO_2 extremely fast; simultaneously RO_2 radicals may experience autoxidation reaction, which drives the formation of highly oxygen content molecules (HOMs), exhibiting a low volatility and, so, actively contributing to NPF (Berndt et al., 2016; Bianchi et al., 2019; Ehn et al., 2014; L. Wang et al., 2024; L. Xu et al., 2019a; Y. Zhao et al., 2018).

The reactive pathway followed by each given RO_2 radical is strongly affected by the chemical environment in which it is produced, the local concentrations of previously released compounds, i.e., NO, HO_2, RO_2, as well as the structure of the RO_2 itself (Nozière, 2025).

In this context, considerable efforts have been devoted to characterizing the chemical composition of the RO_2 species released by different emission sources, however major challenges remain in accurately predicting their atmospheric behaviour and interactions with previously emitted compounds. Atmospheric conditions vary widely depending on meteorology and geography, which in turn affect the reactive fate of RO_2 radicals. In urban areas, for example, elevated NO_x concentrations with strong diurnal variability significantly influence the fate of RO_2 radicals, promoting their reactions with NO_x rather than with HO_2 or other RO_2 species (Dusanter et al., 2009).

Given the complexity of fully resolving RO_2 fates across all the possible atmospheric conditions, and their diverse role in NPF and SOA production, this study focuses on a single well-defined reactive pathway: the formation of dimeric species (ROOR) via gas-phase self- and cross- RO_2–RO_2 accretion reactions. This pathway has emerged as particularly relevant for gas-to-particle mechanisms and early-stage SOA growth (Berndt et al., 2018; Lehtipalo et al., 2018), as it leads to the formation of high mass species that typically exhibit extremely low volatilities (Mayhew et al., 2025; Tomaz et al., 2021).

The efficiency of RO_2-RO_2 accretion is strongly modulated by the surrounding chemical environment. In particular, the rapid reaction of RO_2 with NO can suppress dimers formation, making ROOR formation mechanism increasingly relevant in areas with low NO levels and high BVOCs concentrations, such as remote tropical forests, including the Amazon Basin and South-east Asia (R. Xu et al., 2022).

Dimers, usually characterized by greater stability and lower volatility than monomeric species, play a crucial role in particle growth and in determining the chemical composition of newly formed aerosols (Chen et al., 2022; Kenseth et al., 2018). To better understand their role in NPF, this study examines in detail some key properties of these accretion products: their chemical composition, which affects their reactivity and contribution to SOA mass; their formation rates, which dictate how efficiently dimers can compete with other RO_2 loss pathways; and their atmospheric lifetimes, which control whether they persist long enough to participate in nucleation and growth processes.

These processes were investigated under controlled conditions within the Cosmics Leaving Outdoor Droplets (CLOUD) facility at CERN, which allows for the simulation of diverse oxidation environments with high precision.

The precursors were injected into the CLOUD reactor, a 26.1 m^3 stainless-steel chamber internally equipped with UV lamps to mimic atmospheric photo-oxidation. Extracted gas- and particle-phase species were analysed through a suite of instruments, including mass spectrometers, particle sizers, and volatility measurement systems (Kirkby et al. 2023).

To capture the variability of RO_2 chemistry across the atmosphere, the radicals generated from different VOC precursors were analysed under three representative environmental scenarios:

- Rural Scenario, representing a biogenically dominated environment, such as a forest or a remote rural region. In this case, isoprene and αpinene were injected with different biogenic ratios aiming at investigating the RO_2 chemistry typical of pristine atmospheres.
- Suburban scenario, where not only αpinene and isoprene were injected in the reactor but also trimethylbenzene as representative AVOCs, reflecting environments in which biogenic emissions coexist with moderate anthropogenic releases.
- Urban Scenario, representative of a highly polluted system, such as urban or industrialized areas in which naphthalene, trimethylbenzene and toluene were injected to probe RO_2 interactions under strong anthropogenic dominance.

The data presented for the rural and suburban scenarios were collected during an intensive campaign in 2023 (CLOUD16) whereas the experiments for urban scenario were conducted in an analogous campaign in 2016 (CLOUD12).

By comparing these controlled conditions, the study aims to clarify how the diversity of RO_2 structures and functionalities affects dimer formation pathways and, ultimately, the efficiency with which these accretion products contribute to NPF and early SOA growth.

4.2.1 Chemistry of the System

Despite the complexity of deciphering atmospheric oxidation chemistry, the aim of this work is to provide a clear picture of the key reactive pathways leading to dimers formation, with particular emphasis on the variables driving RO_2-RO_2 interactions under different atmospherically relevant conditions. Recently, Kenagy et al. investigated the contribution of some RO_2 underestimated reaction pathways and their contribution to the formation of low-volatility compounds involved in SOA formation (Hallquist et al., 2009a; Kenagy et al., 2024). These processes are illustrated in Figure 30.

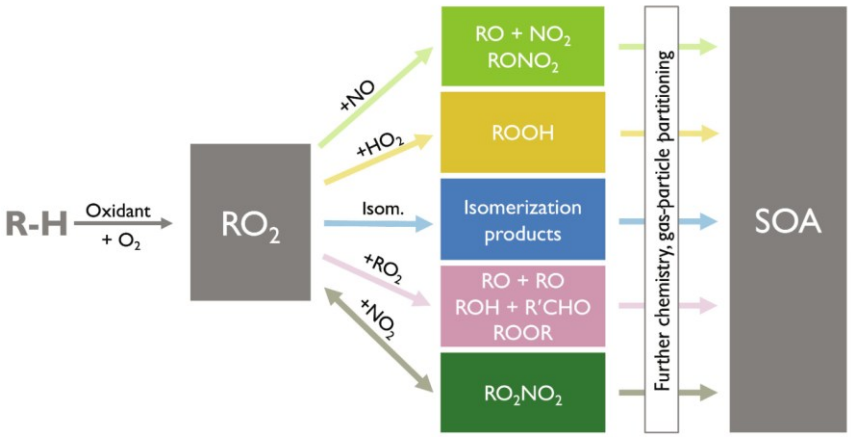

Figure 30: Schematic of RO_2 atmospheric key fates proposed by Kenagy et al. (Kenagy et al., 2024)

Once formed, peroxy radicals can undergo a variety of competing reactions, including unimolecular isomerization and bimolecular terminations with NO, HO_2 or other peroxy radicals. RO_2-RO_2

interactions can lead to multiple products, some of them are summarized in the following reactive pathways:

$$RO_2 + RO_2 \rightarrow RO + RO + O_2 \quad \text{(R12a)}$$

$$RO_2 + RO_2 \rightarrow ROH + R(-H, = O) + O_2 \quad \text{(R12b)}$$

$$RO_2 + RO_2 \rightarrow ROOR + O_2 \quad \text{(R12c)}$$

Considering the reported reactive steps, RO_2-RO_2 interactions can form either an alkoxy radical, RO (Reaction 12a) or an alcohol, ROH, in combination with a carbonyl compound, R(-H,=O) (Reaction 12b) or an accretion product in the form of ROOR (Reaction 12c). Additional compounds, such as dialkyl peroxides, can also be generated by RO_2-RO_2 interactions but they do not usually exhibit a significant contribution (Berndt et al., 2018).

This study specifically focuses on the accretion channel leading to the formation of ROOR dimers, as these products are expected to exhibit low volatilities and, thus, to contribute to SOA formation. The alternative reactive pathways arising from RO_2-RO_2 interactions, although chemically relevant, are not the primary focus of this work.

Recent studies have demonstrated that the likelihood of ROOR dimer formation is not solely controlled by external factors, such as NO_x/HO_2/RO_2 concentrations, but also by intrinsic molecular properties inherited from the precursor VOC which affects RO_2 steric accessibility, composition and reactivity towards other peroxy radicals (Berndt et al., 2018).

Therefore, a mechanistic understanding of RO_2-RO_2 accretion chemistry necessarily requires careful consideration of the parent VOC structure. On this basis, the following section focuses on the VOC precursors selected for this investigation, discussing their structural characteristics and how these features are expected to influence the formation, evolution and accretion behaviour of the corresponding RO_2 radicals and, consequently, of the formed ROOR molecule.

VOC precursors

Volatile organic compounds (VOCs) encompass a broad range of carbon-based chemicals, including saturated and unsaturated hydrocarbons, aromatics, aliphatics, as well as functionalized species such as aldehydes, ketones, alcohols, ethers, and acids (Atkinson & Arey, 2003; Seinfeld & Pandis, 2016). Their contribution to atmospheric chemistry varies depending on multiple factors, including seasonal cycles, regional emissions, and environmental conditions (Guenther, 1995; Hallquist et al., 2009a)

Biogenic VOCs

Biogenic VOCs include a wide range of carbon-based compounds ubiquitous in our atmosphere. Table 7 summarizes the major BVOC classes released by vegetation, their estimated global emissions, and primary emitting vegetation types (Laothawornkitkul et al., 2009).

Table 7: Some of the most contributing BVOC Species and their corresponding emitting plants

BVOCs Species	Estimated annual Global Emission [10^{12} g C]	Atmospheric Lifetime [days]	Compounds	Major Emitting Plants
Isoprene	412-601	0.2	Isoprene	*Populus, Salix, Platanus*
Monoterpene	33-480	0.1-0.2	α-pinene, β-pinene, limonene	*Quercus, Pinus*

Other reactive BVOCs	≈260	<1	Acetaldehyde, 2-methyl-3-buten-2-ol and hexenal family	*Grassland, Vitis and Betula*
Other Less reactive BVOCs	≈260	>1	Methanol, ethanol, formic acid, acetic acid, acetone	*Vitis, Brassica and Betula*

In this study, BVOCs investigated were isoprene (IP) and αpinene (AP), selected as representative BVOCs, due to their atmospheric abundance and their high reactivity.

Isoprene (IP) (C_5H_8) is the most abundant non-methane hydrocarbon emitted in the atmosphere, with an estimated global emission around 500 Tg a^{-1} (Bates & Jacob, 2019). It is highly reactive, with an atmospheric lifetime of approximately 1 hour (Jenkin et al., 2015; Khan et al., 2025), mainly emitted by broad-leaved evergreen trees. In the Amazon forest, median isoprene concentrations range from [0.5-2.0] ppbv at night to [2.0-6.0] ppbv during daytime whereas values lower than 2 ppbv typically characterize urban environments (Andreae et al., 2015; dos Santos et al., 2022; Wagner & Kuttler, 2014). Despite its ubiquity, isoprene chemistry is far from being completely understood during daytime, IP mainly reacts with OH radicals and its oxidation products can undergo complex oxidative cascade leading to a wide range of compounds (Wennberg et al., 2018a) exhibiting different chemical structures and volatilities (D'Ambro et al., 2017). Recent studies have demonstrated that it can actively contribute to NPF especially under low-NO_x conditions (Shen et al., 2024b). In such environments, IP oxidation leads to the formation of low-volatile, highly oxygenated compounds that can contribute to nucleation and early growth, particularly in synergy with sulphuric acid. Furthermore, many isoprene oxidation products are water-soluble and can partition into aerosol aqueous phase, promoting SOA formation through aqueous pathways (El-Sayed et al., 2018).

OH-driven oxidation of IP is responsible for the majority of daytime isoprene losses and subsequent RO_2 formation (Wennberg et al., 2018b). Ozonolysis of isoprene is usually slower than OH oxidation and only becomes relevant in highly O_3-polluted regions or in areas where the concentrations of OH is extremely low. Nighttime chemistry of isoprene is dominated by nitrate radicals (NO_3) becoming increasingly significant in polluted or semi-urban areas. NO_3 reacts with isoprene double-bong forming RO_2 radicals (Schwantes et al., 2015).

Independently from the involved oxidant, as for all the VOCs, RO_2 formation is a key step in isoprene oxidation chemistry and IP-RO_2 can subsequently undergo termination reactions with other compounds or autooxidation pathways, producing a wide range of oxygenated multifunctional compounds (Berndt et al., 2025)

αpinene (AP) ($C_{10}H_{16}$) accounts for around 34% of the total monoterpene emissions (Simon et al., 2020) and it participates in multiple oxidative pathways, readily reacting with OH, O_3 and NO_3 (Eddingsaas et al., 2012). Compared to isoprene, ozonolysis plays a more relevant role in αpinene chemistry: O_3 can indeed easily the endocyclic double bond functionality, initiating autoxidation reactions (Crounse et al., 2013). Autoxidation drives the formation of highly oxygenated RO_2 and HOMs, but the multiplicity of possible radical structures makes the chemical mapping extremely challenging. Additional AP-HOMs formation can be attributed to OH-initiated oxidation of αpinene, fastly occurring during daytime (Rolletter et al., 2019). As for isoprene, nighttime chemistry is dominated by NO_3 (Bates et al., 2021). As for IP-RO_2, also the fate of AP-RO_2 is strongly influenced by the concentrations of proximity compounds especially NO_x levels:

- High NO_x regimes, such as urban or suburban areas, enhance the formation of organonitrates limiting autoxidation steps.

- Low NO_x environments, typical of pristine forests, favor RO_2-RO_2 interactions enhancing HOM formation and high-molecular-weight accretion dimer (ROOR) generation, thus contributing to NPF.

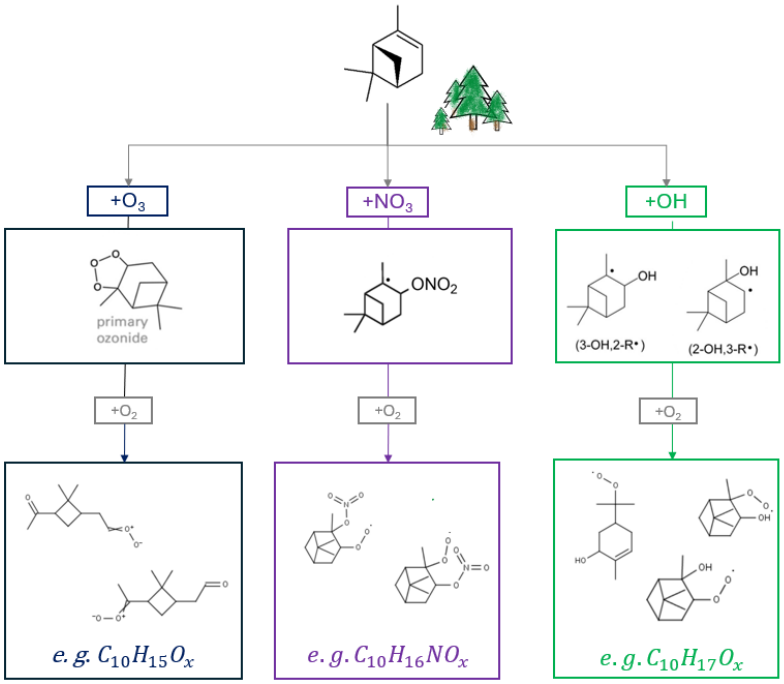

Figure 31: Simplified αpinene oxidation scheme with key atmospheric oxidation agents and some possible released RO_2

In Figure 31, a simplified schematic representation of the exemplificative classes of products formed by the main αpinene oxidation reactions under atmospheric conditions (Bates et al., 2021; Klippenstein & Elliott, 2023; L. Xu et al., 2019b). The initial oxidant attack, followed by an H-shift and an O_2 addition, brings to the formation of several species which can ultimately continue their reactive route leading to HOMs formation (Kang et al., 2025).

In this study, the first investigated scenario, also referred to as rural or pure BVOCs case, only includes αpinene and isoprene as biogenic VOC precursors. Once formed, the RO_2 from these two compounds have several possible reactive pathways to follow. A simplified scheme of the key resulting C_x classes of compounds is reported in Figure 32. The analysis focuses on the monomeric products, C_5 and C_{10} addressed to isoprene and αpinene oxidation, respectively, and on the dimers C_{20} (from AP-RO_2 self-reactions) and C_{15} (from AP-RO_2 and IP-RO_2 cross-reactions) (Dada et al., 2023; Heinritzi et al., 2023).

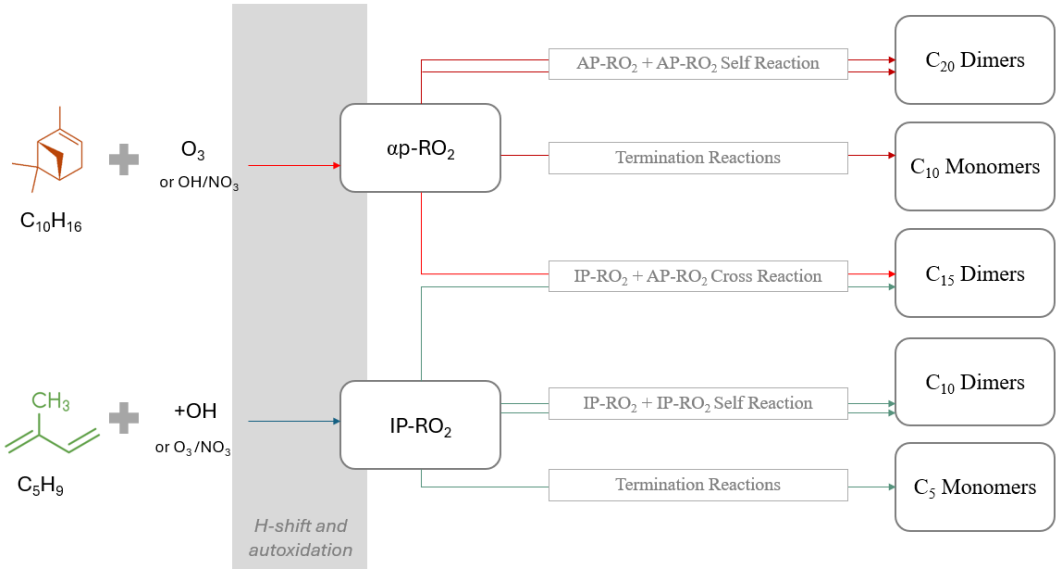

Figure 32: Simplified reactive scheme for rural scenario leading to ROOR formation

C_{10} dimers produced by IP-RO_2 self-reactions are not individually examined in this study. This choice is motivated by the observation, discussed in the following chapters, that monomer contribution generally dominates over the dimers in each investigated experimental condition. Additionally, distinguishing between C_{10}-dimers from IP oxidation and C_{10}-monomers from AP-pathways is extremely challenging. Given the complexity of these reactive pathways and the incomplete knowledge of all the chemical reactions involved, no reliable method has yet been established to clearly separate the two contributions unambiguously. Therefore, for the purpose of this study, the entire C_{10} contribution was attributed to AP monomers rather than IP dimers.

In this study, αpinene and isoprene were injected into the reactor in two biogenic ratios, corresponding to two specific concentration pairs:

- AP: IP=1.4 ppbv: 8 ppbv and
- AP: IP = 2 ppbv :4 ppbv.

The selected mixing ratios are coherent with some atmospheric-relevant concentrations reported in literature mainly for temperate vegetation areas (H. Li et al., 2021). While coniferous forests are usually characterized by an excess of monoterpenes compared to isoprene, deciduous or temperate forests tend to be dominated by isoprene-emitting species, explaining the higher levels of isoprene registered in those regions. In temperate regions, isoprene-rich forests are mainly located in central Europe, like in Germany and France as well as in the southeastern United States, where oak, poplar, and maple species are abundant. For instance, McGlynn et al. reported average daily concentrations of isoprene and αpinene ranging between [4-6] ppbv and [0-2] ppbv, respectively, representative of summertime values observed in Southeastern US forests. Tropical isoprene-rich forests are also found in the Amazon basin and in some areas of tropical Africa and Asia, often comprising high-biomass, sunlit canopies. These ecosystems are characterized by high solar radiation, warm temperatures, and species with strong isoprene-emitting capacities, resulting in atmospheric isoprene mixing ratios that typically exceed those of monoterpenes (Jones et al., 2011).

For the biogenic runs, not only αpinene and isoprene were introduced into the reactor but also NO (<1 ppbv) and SO_2 (<3 ppbv) in concentrations coherent with values typically registered in forests or remote rural areas (Andersen et al., 2021; X. Liu et al., 2022).

Anthropogenic RO_2

Key anthropogenic aromatic VOCs include benzene, naphthalene (NPT), toluene (TOL) and trimethylbenzene (TMB), and they mainly originate from industrial operations, solvent use and vehicular exhaust (Friedrich & Obermeier, 1999a; L. Huang et al., 2023). Despite their reduced global abundance compared to BVOCs, aromatic AVOCs are highly relevant for atmospheric chemistry due to their high reactivity towards the production of RO_2.

Considering the main oxidating agents, daytime AVOCs oxidation is dominated by OH radicals addition to the aromatic ring. This step generates bicyclic peroxy radicals (BPRs) rapidly transforming into a ring-opened compound or an oxygenated RO_2 species (Glowacki et al., 2009). As for biogenics, anthropogenic derived RO_2 can undergo several autoxidation steps forming HOMs and eventually contributing to NPF (Molteni et al., 2018). Moreover, particularly important for aromatics-derived HOMs is multigeneration OH oxidation, which contributes to the formation of molecules with higher oxygen content (Garmash et al., 2020). Ozonolysis does not considerably contribute to benzene-like AVOCs oxidation (Calvert et al., 2002), whereas nighttime chemistry is dominated by NO_3, especially effective on highly substituted aromatics leading to the formation of RO_2 or ring-opening products (Kumar et al., 2023).

As BVOC-RO_2, AVOC-RO_2 fate is strongly affected by the NO_x levels. In high NO_x conditions, the reaction between a peroxy radical and NO molecules prevails forming nitrates and favoring fragmentation or ring-opening mechanisms. Low NO_x levels will let reactions of RO_2 with HO_2 or other RO_2 prevail, enabling the formation of hydroperoxides and dimers.

In this investigation, two main AVOCs-related scenarios were analysed. The first one replicating Suburban concentrations, also referred to as "mixed AVOCs/BVOCs" case and the second one, aiming at reproducing a highly polluted urban scenario, referred to as "Urban" or "pure AVOCs" case. The Suburban runs differ from the pure BVOCs scenario for the addition of 1,2,4-trimethylbenzene, which is injected alongside α-pinene and isoprene.

Trimethylbenzene (C_9H_{12}) is among the most reactive aromatic AVOCs (Tsiligiannis et al., 2019). Reaction with OH radicals mainly proceeds via OH-addition to the aromatic ring, forming TMB–OH adducts. These adducts that can either undergo irreversible H-abstraction, producing phenolic compounds, or reversible O_2 addition, leading to RO_2 radicals. TMB-derived RO_2 can undergo intramolecular cyclization to form bicyclic radicals which react with O_2 generating BPRs (Y. Li & Wang, 2014). Alternatively, as for the other aromatics, TMB-RO_2 can react either with NO_x, HO_2 and RO_2 species or undergo autooxidation processes (Ponnusamy et al., 2017).

While OH-initiated oxidation is the dominant atmospheric loss pathway for TMB during daytime, NO_3-initiated oxidation may contribute under nighttime conditions, whereas ozonolysis is generally slow thus it represents a minor sink. NO_3-initiated oxidation proceeds via NO_3 addition to the aromatic ring, followed by O_2 addition and subsequent reactions leading to nitrogen-containing peroxy radicals (Tsiligiannis et al., 2019).

In the present study, for the mimicking of atmospheric concentrations typical of suburban areas, AP and IP were injected in the reactor chamber at mixing ratios of 1.4:8 ppbv and 2:4 ppbv (equal to rural runs), along with 1,2,4-TMB injections at concentrations ranging from 2.5 to 10 ppbv. These values are coherent with concentrations registered in several on-field studies located in peripherical areas of big cities (Batterman et al., 2002).

Within this framework, after the initial oxidation of the precursors, all the BVOCs-derived RO_2 and TMB-RO_2 can freely interact in the chamber, leading to the formation of different ROOR accretion products. A schematic representation of this scenario is reported in Figure 33:

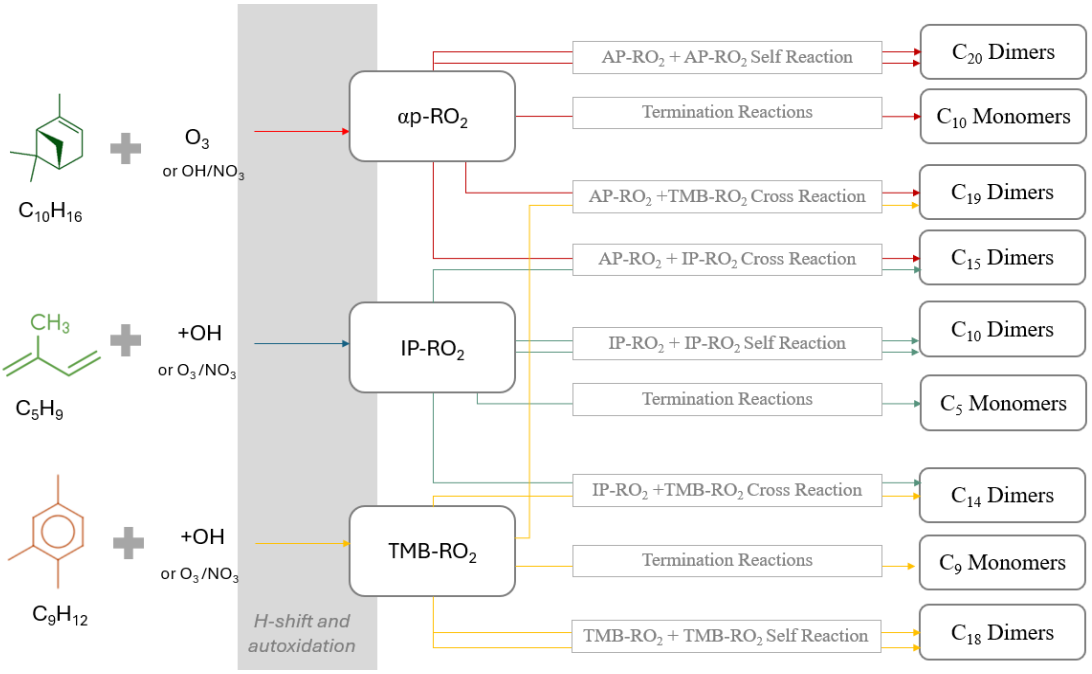

Figure 33: Scheme of the C_x classes expected to be more relevant within the suburban scenario

The last scenario investigated in this chapter involved the injection of only AVOCs, mimicking concentrations typical of highly polluted urban environments. In addition to trimethylbenzene, two other AVOCs precursors are injected into the system: naphthalene and toluene.

Naphthalene ($C_{10}H_8$), is the simplest polycyclic aromatic hydrocarbon (PAH) and it is mainly emitted by vehicle emissions. Similarly to the majority of aromatics, atmospheric oxidation of naphthalene is predominantly initiated by OH addition to the aromatic ring, followed by rapid reaction of the resulting hydroxy-substituted radical with O_2, to form a variety of peroxy radicals (Lannuque & Sartelet, 2024). Depending on the site of OH and O_2 attack, the generated RO_2 species are key intermediates in subsequent oxidation chemistry, which includes intramolecular transformation leading to bicyclic structures.

Under high NO_x conditions, naphthalene-derived RO_2 can easily undergo ring-opening via reaction with NO molecules forming alkoxy radicals (RO) (Chan et al., 2009). In low- NO_x regimes, RO_2 radicals preferentially react with HO_2, favoring the formation of ring-retaining hydroperoxides and limiting extensive fragmentation (Kautzman et al., 2010).

Toluene (C_7H_8) is one of the most abundant AVOCs in urban environments; it is mainly released by vehicular exhaust, solvent usage, industrial activities and fuel evaporation (Beauregard, 1994). As for naphthalene, toluene oxidation is usually initiated by OH-addition to one of the carbons of the aromatic ring, forming toluene-OH adducts (Z. Dong et al., 2023). These intermediates can easily react with molecular oxygen either via direct H-abstraction forming cresol or via O_2 addition, producing peroxy radicals.

Toluene derived-RO_2 can undergo bimolecular reactions with NO_x and HO_2/RO_2 forming alkoxy radicals or experience ring-closure mechanisms leading to BPRs (Wu et al., 2014). Once formed, Toluene-derived BPRs further react with NO_x, HO_2 and RO_2 producing bicyclic alkoxy radicals (BARs) and other species, including nitrates, alcohols, ketos, and peroxides (Chen et al., 2022).

The combination of the RO_2 generated molecules, leading to accretion products investigated in urban-mimicking experiments is summarized in Figure 34:

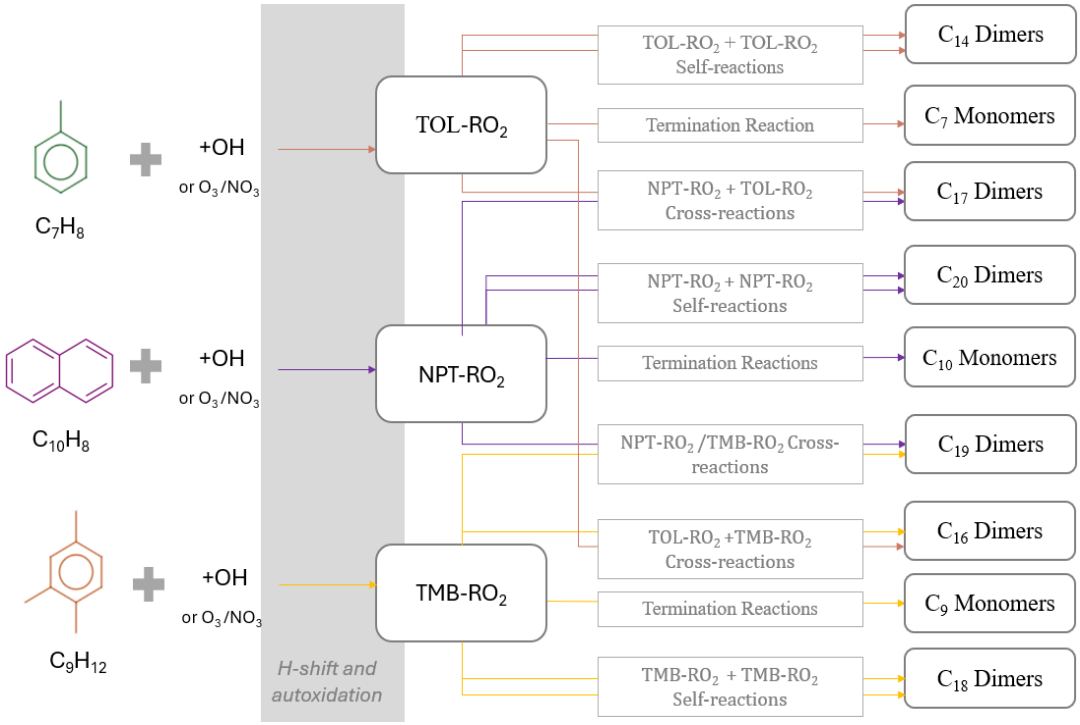

Figure 34: RO2 and ROOR formation scheme for Urban Runs

For the urban runs, concentrations injected in the chamber ranged from 4 to 8 ppbv for 1,2,4-trimethylbenzene, whereas for toluene and naphthalene 40 ppbv and 0.1-10 ppbv were introduced, respectively. Furthermore, SO_2 was also injected in the reactor in concentration around ~ 2 ppbv. These values were selected to reflect atmospherically relevant conditions characteristic of urban and polluted environments.

In particular, typical urban areas settings exhibit toluene concentrations from 1 to 50 ppbv with peaks correlated to highly trafficked or industrialized areas (Mitchell et al., 1984). Values around the order of several ppbv are recorded for aromatic compounds such as TMB in urban environments, particularly in proximity of vehicular emissions and solvent usage (Atkinson & Arey, 2003; Calvert et al., 2002a). Similarly, naphthalene injected concentrations are coherent with urban concentration of this aromatic compound (Jia et al., 2010).

In the next chapters, the analysis of monomers and dimers released under different atmospherically relevant scenarios is presented, spanning rural, suburban, and urban environments. All experiments were conducted in the CLOUD chamber. A detailed description of the experimental setup and of the CLOUD facility will be provided in the following chapters.

4.3 Experimental Setup

The CLOUD Chamber located at CERN (European Center for Nuclear research) is a cylindrical, well-controlled, stainless-steel chamber with electro-polished walls and a volume of 26.1 m^3 (Kirkby et al., 2011). The characteristics of the chamber guarantee an accurate investigation atmospheric-relevant mechanisms at molecular level with unique precision, thanks to the extremely low contamination levels kept under pptv levels (Kirkby et al., 2016). Internal fans positioned at the top and at the bottom of the reactor allow to achieve homogeneous mixing within the chamber

A schematic of the chamber is reported in Figure 35:

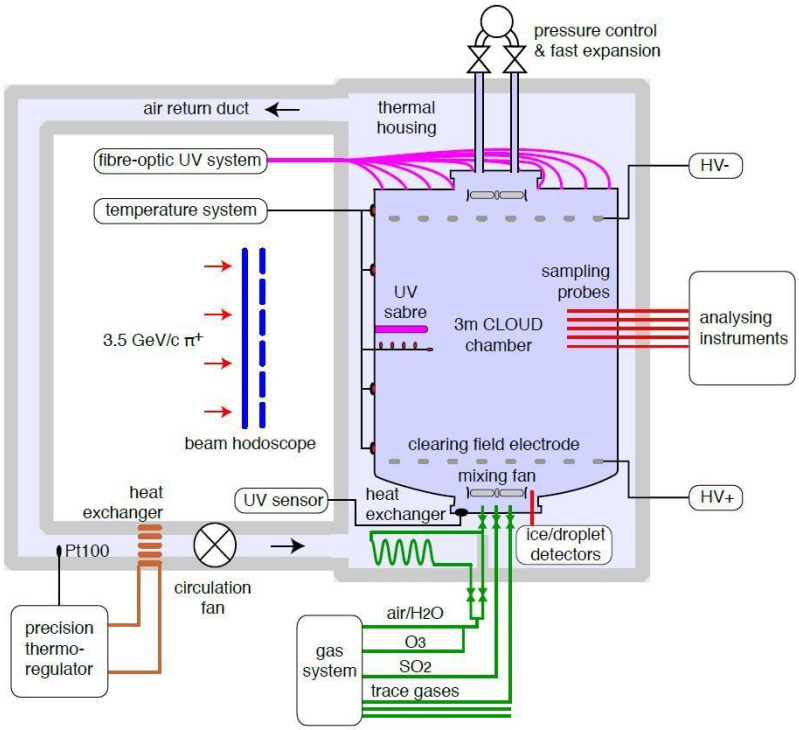

Figure 35: CLOUD Chamber

The chamber is internally equipped with UV lights, installed to mimic daytime photochemistry. In the CLOUD chamber, photolysis is initiated once precursor gases reached the target concentrations, using a 4 W KrF excimer UV laser (UVX, 248 nm) in combination with four 200 W Hamamatsu Hg–Xe lamps (UVH, 250–450 nm). The lamps were coupled to the chamber via optical fibres to provide homogeneous irradiation while minimizing thermal perturbations. OH radicals were generated from 40–100 ppbv O_3, produced by passing a fraction of the chamber air through a quartz tube irradiated with UVC lamps (<240 nm). For experiments involving NO_x, NO_2 was injected and photolyzed to NO using a 385 nm LED sabre (LS3), yielding a NO/NO_2 ratio of 0.05–0.10 and a maximum NO_2 photolysis rate of 0.0025 s^{-1}. This controlled photolytic environment enabled reproducible generation of oxidizing radicals and precise simulation of VOC oxidation and secondary aerosol formation under atmospherically relevant conditions. Based on the light condition and on the consequent induced photolysis, the experiments were divided into “light” and “night” conditions, aiming at replicating daytime and nighttime chemistry, respectively. In the light runs, photolysis was activated by turning on the UV lamps, generating OH radicals and driving photochemically initiated reactions, whereas in the night runs the lamps were kept off, allowing the investigation of dark chemistry and of all the processes that proceed without photolytic radical production. In this study the nomenclature “light” condition will refer to the set up mimicking a daily sunlight environment, whereas “dark” condition aimed at replicating night chemistry.

During the experiments, three operational modes were employed to investigate the role of ions in VOC oxidation and secondary aerosol formation: GCR runs, aiming at mimicking natural background ionization produced by galactic cosmic rays; neutral runs, in which the ion concentration is kept low to represent the absence of additional ionizing sources; and cleaning runs, where ion concentrations are minimized to establish the baseline chemistry in the absence of charged particles. The use of a pion beam from the CERN Proton Synchrotron allows the chamber to reach tropospheric-relevant ion concentrations, reproducing nucleation conditions comparable to those observed in the atmosphere. By comparing these three modes, it is possible to disentangle the specific contributions of charged particles in driving secondary aerosol formation under controlled atmospheric conditions.

The operating pressure was set at 5mbar; temperature regulation was operated thanks to an external thermal housing surrounding the reactor, showing a stability of around 0.1K. Furthermore, the reactor is equipped with internal fans ensuring an homogeneous mixing of the injected compounds.

A continuous injection of synthetic air, 79% N_2 and 21% O_2, combined with trace gases was performed within the chamber between ~340 and 360 Liters per minute for CLOUD12 and CLOUD16, respectively.

4.3.1 Detection Instruments

The chamber is equipped with a complex probes system sending the exhaust to each specific detection instrument. The data presented in the current investigations have been collected and analysed by the following instruments:

- Nitrate CI-Api-LTOF. It is a high-resolution chemical ionization mass spectrometer designed for the detection of highly oxidized and low-volatility atmospheric compounds. This instrument employs a corona discharge ion source to generate nitrate reagent ions (NO_3^-) from nitric acid, enabling highly selective ion–molecule reactions with oxidized vapors. Thanks to its long time-of-flight (LTOF) analyzer, it provides high mass accuracy and resolving power across a wide mass range extending up to ~2000 Th, allowing the simultaneous quantification of several trace species, including sulfuric acid (H_2SO_4) and HOMs. For this study, the instrument was operated in negative mode, using a soft-ionization configuration, aiming at minimizing the fragmentation and preserving the molecular integrity of the detected ions. This procedure ensures more reliable molecular assignments and improved quantification of fragile oxidized species.
- Surface-Field Time-of-Flight (SFTOF) mass spectrometry is a variant of traditional TOF-MS that utilizes a strong electric field near the sample surface to accelerate ions. In this configuration, ion transmission and temporal focusing are optimized, resulting in higher resolution spectra.
- Proton Transfer Reaction MS (PTR3). This is a proton-transfer-reaction mass spectrometer developed by Tofwerk Long-Time-Of-Flight. Compared to earlier PTR systems, it exhibits an improved sensitivity, reaching detection limits up to 10ppq and sensitivity on the order of 10000 cps per ppb, together with high mass resolution. In our experimental setup, the instrument was operated as an NH_4^+ CIMS at low collision energy, enabling the detection of VOCs emissions while limiting fragmentation. The sampling inlet is mounted coaxially with the reaction chamber, allowing a fast response time and reducing the wall losses, which is particularly relevant during the tracking of rapidly changing signals.
- Hydroxy Radical Measurement Unit Based on fluorescence Spectroscopy (HORUS). This system is a laser-induced fluorescence (LIF) instrument designed for the detection of OH and HO_2 radicals. It relies on optical excitation of the radicals and measurement of the resulting fluorescence signal, ensuring a high sensitivity and fast time resolution. HORUS system allows direct observation of OH and HO_2 within the chamber, offering reliable tracking of their temporal evolution during the experiments.
- Trace Gas Monitors:
    - Picarro CO_2/CO/CH_4/H_2O Monitor. This analyzer is based on cavity-ring-down spectroscopy and provides stable, high-precision measurements of CO_2, CO, CH_4 and water vapor. Its long-path optical cell ensures excellent sensitivity and low drift, making it suitable for tracking slow variations as well as rapid changes in trace gas concentrations during chamber experiments.
    - Picarro NH_3 Monitor. As the above monitors, it uses a cavity-ring-down spectroscopy technology optimized for ammonia, which is a challenging compound due to wall interactions. The instrument offers reliable sub-ppb detection, with a limit of detection around 0.5 ppb.

- CAPS NO_2 Monitor performed NO_2 detection via cavity attenuated phase shift spectroscopy, coupling high precision and a rapid response. It exhibits typical noise levels of approximately 10 ppt, making it well-suited for studying low-NO_x regimes and nighttime chemistry.
- CLD 780TR NO monitor. Its operation is based on a chemiluminescence detector that measures NO via its reaction with O_3. This process leads to the formation of a photon signal, proportional to NO concentrations. The instrument achieves high sensitivity, corresponding to approximately 50 ppt at a 3-second integration time and about 10 ppt at 60 seconds, making it suitable for both field studies and chamber experiments.
- Thermoscientific SO_2 monitor. The SO_2 analyser is based on pulsed UV fluorescence. It provides robust, stable measurements and is widely used to track SO_2 during oxidation experiments or when sulphur-containing precursors are introduced into the system.

- Scanning Mobility Particle Sizer for particle detection:
  - **Nano Differential Mobility Analyser (Nano-DMA),** TSI Model 3085**.** The sizes detected by this instrument range from 5nm to 60nm. It combines a differential mobility analyser with a condensation particle counter, ensuring high-resolution measurements on nucleation-mode particles and early-stage aerosol formation.
  - **Long-Range Differential Mobility Analyser (Long-DMA),** TSI Model 3061. Compared with nano-DMA, this instrument can measure aerosols ranging from 20 to 600 nm, capturing accumulation-mode aerosols and larger nucleation-mode particles. Its high size resolution and rapid scanning capability make it suitable for tracking aerosol growth dynamics and secondary organic aerosol formation.
  - **Condensation Particle Counter (CPC)**, TSI model 3776, is implemented to detect and count extremely small airborne particles, usually in the nanometer range. The particles are first exposed to a supersaturated butanol, which condenses onto them, causing the particles to grow up to optically detectable sizes. The enlarged particles are then counted using a light-scattering detector.

  - **Particle Size Magnifier (PSM)**, Model 180 from AirMoDus. PSM is adopted to enhance the growth of nanoparticles up to sizes detectable by CPC. By continuously scanning the saturator flow, this instrument allows the sizing of particles below 10 nm, being able to detect particles within the range 1-12 nm.

The experimental apparatus and measurement techniques employed in this investigation are described in the previous section. In order to interpret the acquired data and to relate the measured quantities to the physical phenomena under investigation, a mathematical formulation of the system is required.

For this purpose, the governing equations, key variables and basic assumptions employed in the data analysis are presented in the following section.

4.4 Mathematical Model and Set of Equations

This section presents the mathematical framework used to analyze the experimental data. The main variables that define the atmospheric regimes and drive RO_2 pathways in the investigated process are first introduced, particularly the parameters τ and β. The governing balance equations developed for each experimental configuration are then presented, providing the basis for the quantification of the relevant physical and chemical contributions. In addition, a simplified mathematical model used to estimate HO_2 concentrations in the CLOUD12 experiments is described. The section concludes with the correction procedures applied to account for measurement losses.

4.4.1 Definition of key Variables: β and τ

Aiming to properly characterize the system, a comprehensive set of parameters has been defined, ranging from input measurements provided by the detection instruments to specific variables describing the current system. Based on literature, two key parameters have been introduced to describe each experimental condition (Kenagy et al., 2024):

- The bimolecular lifetime, also referred to as τ_{bi}, and
- The "Branching Ratio", β.

To estimate the RO_2 lifetime, this study adopts the bimolecular lifetime (τ_{bi}) as a first diagnostic parameter. Atmospheric lifetime defines the average survival time of a specific compound, in this case RO_2, in the atmosphere by accounting for its main reactive consumption pathways. This concept was first introduced by Teng et al. in their investigation focused on isoprene oxidation in the atmosphere. Since their study was conducted under experimental conditions dominated by reactions with NO and HO_2 (Teng et al., 2017). Under these conditions, the bimolecular lifetime was defined as:

$$\tau_{bi} = \frac{1}{k_{RO2+NO}[NO]+k_{RO2+HO2}[HO_2]} \quad \text{(Eq. 6)}$$

In this expression [NO], [HO_2] and [RO_2] represent the concentrations of NO, HO_2 and RO_2 in the system, respectively, whereas k_{RO_2+NO} and $k_{RO_2+HO_2}$ represent the reaction constants for the RO_2 reactions with NO and HO_2.

The current investigation uses NO concentrations below 1.0 ppb. Considering these low NO_x levels, the RO_2-RO_2 pathway contribution becomes non-negligible, for this reason, in this investigation, the bimolecular lifetime has been reformulated as follows:

$$\tau_{bi} = \frac{1}{k_{RO_2+NO}[NO]+k_{RO_2+HO_2}[HO_2]+k_{RO_2+RO_2}[RO_2]} \quad \text{(Eq. 7)}$$

The rate constant values implemented in the calculation of the current investigation are reported in Table 8:

Table 8: Rate constant of the reactions involved in the calculation of the bimolecular lifetime

	[cm^3 $molecule^{-1}$ s^{-1}]	**Reference**
k_{RO_2+NO}	$1 \cdot 10^{-11}$	(Xiao et al., 2025)
$k_{RO_2+HO_2}$	$2.5 \cdot 10^{-11}$	
$k_{RO_2+RO_2}$	$8.8 \cdot 10^{-13}$	

The variable τ_{bi} only accounts for bimolecular reactions since the occurrence of unimolecular RO_2 isomerization, also referred to as autoxidation, results in a regeneration of RO_2 radicals and therefore does not represent a net loss term (Berndt et al., 2018; Crounse et al., 2013).

The chemical parameter β was initially introduced by Pye et al. to quantify the competition between RO_2 reactions with NO and HO_2 (Pye et al., 2010a). Considering these two reactive pathways, β can be interpreted as a branching ratio describing the relative importance of the two competing RO_2 reaction channel (Kenagy et al., 2024; Presto & Donahue, 2006; J. Zhang et al., 2006). It can be defined as:

$$\beta = \frac{k_{RO_2+NO}[NO]}{k_{RO_2+NO}[NO]+k_{RO_2+HO_2}[HO_2]} \quad \text{(Eq. 8)}$$

where the rate constant values for the reactions with NO and HO_2 are the same as those reported in Table 8.

This parameter plays a key role in secondary organic aerosol (SOA) formation, as it accounts not only for the RO_2-HO_2 reaction pathway but also for the interaction of RO_2 radicals with NO_x. On this basis, β-dependent models have been developed to properly predict SOA formation (Heald et al., 2008; Henze & Seinfeld, 2006; Pye et al., 2010b).

In the present study, the bimolecular lifetime τ_{bi} has been reformulated to include the contribution of RO_2–RO_2 termination reactions. This modification is necessary under the experimental conditions investigated here, where low NO_x levels make the RO_2–RO_2 pathway non-negligible. Including this pathway ensures that τ_{bi} accurately represents the effective lifetime of RO_2 radicals with respect to all significant bimolecular loss processes.

In contrast, the branching ratio β is intentionally left defined as in the literature, considering only the competition between RO_2 reactions with NO and HO_2. This choice is deliberate: β is not intended to quantify the total loss of RO_2, but rather to characterize the relative importance of the two major atmospheric reaction channels that govern RO_2 fate under different chemical regimes. RO_2–RO_2 reactions, while contributing to radical termination, do not influence this competition and are therefore not included in the definition of β (Presto & Donahue, 2006; Pye et al., 2010a).

4.4.2 Governing Balance Equation

As previously described, understanding RO_2-RO_2 interactions is extremely challenging since the variety of products formed depends on the chemical composition and structure of the interacting RO_2 radicals. Within this context, determining the rate coefficient of self- and cross- reactions is difficult due to the range of possible reaction pathways.

Previous studies have reported RO_2-RO_2 rate coefficients ($k_{RO_2+RO_2}$) spanning several orders of magnitude (10^{-13}–10^{-17} cm^3 $molecule^{-1}$ s^{-1}), depending on whether the radical is primary, secondary, or tertiary, with reactivity generally decreasing in the order primary > secondary > tertiary (Orlando & Tyndall, 2012; Z. Peng et al., 2019; Tyndall et al., 2001; Ziemann & Atkinson, 2012). Recently, Berndt et al. recorded relatively high values of rate constants of RO_2-RO_2 accretion reaction, showing that this pathway can compete with RO_2 reactions with NO and HO_2 (Berndt et al., 2018). Collectively, all these cited studies highlighted the broad range of possible rate constant values for RO_2-RO_2 interactions and the dependency of these k values from the multiple factors, from the radical precursors to its structure, to concentrations of pre-emitted compounds. This highlights the need for further investigations to better constrain RO_2-RO_2 kinetics and broaden the understanding of the factors controlling these reactions.

In the present study, we aim to extract effective reaction rate coefficients under the experimental conditions considered. The formation of a generic RO_2 radical from the reaction of a VOC with an oxidant (Ox) can be expressed as:

$$VOC + Ox \; \gamma_{RO_2} k_{VOC+Ox} \rightarrow \; RO_2 \quad \text{(R13)}$$

In the reaction R13, the k_{VOC+Ox} is the reaction rate coefficient and γ_{RO_2} is the yield of RO_2 radicals.

Considering the key atmospheric oxidants, O_3, OH and NO_3, it is possible to infer that, under typical tropospheric conditions, VOCs reactions with NO_3 and OH radicals present a near-unitary yield (Calvert et al., 2015; Hantschke et al., 2021) whereas the same assumption cannot be inferred for ozonolysis. Reaction of VOCs with ozone, will lead to the formation of Criegee intermediates (CI) which will further evolve into closed-shell molecules instead of RO_2 radicals, resulting in yields lower than 1 (Berndt et al., 2015). The non-unitary efficiency of this reaction is taken into account through the term γ_{RO_2} which measures the conversion yield of VOC-oxidant interactions.

The time evolution of RO_2 concentrations can be described by the following mass balance:

$$\frac{d[RO_2]}{dt} = \gamma_{RO_2} k_{VOC+Ox}[VOC][Ox] - k_{RO2+NO}[NO][RO_2] + k_{RO2+HO2}[HO_2][RO_2] + k_{RO2+RO2}[RO_2]^2$$

(Eq. 9)

In Eq. 9, [RO_2], [NO], [HO_2] [VOC] and [Ox] represent the concentrations of RO_2 radicals, NO, HO_2, VOC precursors and oxidants, respectively. The first term, highlighted in green, represents the contribution to RO_2 production from VOCs oxidation. In red, the loss term of RO_2 radicals through bimolecular termination reactions of the peroxy radical molecule with either RO_2, HO_2 or NO.

Considering the definition of the bimolecular lifetime, it is possible to simplify Eq. 9 as it follows:

$$\frac{d[RO_2]}{dt} = \gamma_{RO_2} PR - \frac{[RO_2]}{\tau_{bi}} \qquad \text{(Eq. 10)}$$

In this formulation, the term "PR" refers to the production rate, obtained as the product of the two precursor molecules interacting in the process, hence [VOC] and [Ox] and the reaction constant k_{VOC+Ox}.

Bimolecular reactions may not only represent a consumption term in RO_2 balance but also a production contribution: RO_2-RO_2 interactions can indeed generate secondary RO_2 through the production of an intermediate alkoxy radical (RO) subsequently evolving into an RO_2. In this investigation this additional contribution was not considered based on the hypothesis that primary RO_2 radicals (directly produced by VOCs oxidation) constitute the majority of the total RO_2 radicals (Jenkin et al., 2019). Assuming the steady state, the equation simplifies to:

$$[RO_2] = \tau_{bi} \gamma_{RO_2} PR \qquad \text{(Eq. 11)}$$

This equation provides a general formulation of the RO_2 concentration which can in fact be calculated specifically for each RO_2 derived by the individual VOCs injected into the chamber. In this context, the total production rate for each VOC was calculated as the sum of the contributions of each oxidation pathway. For instance, for αpinene, the total PR has been formulated as:

$$PR_{AP} = k_{AP+OH}[AP][OH] + k_{O3+AP}[AP][O_3] + k_{AP+NO3}[AP][NO_3] \qquad \text{(Eq. 12)}$$

This calculation was performed for each of the VOC involved in the investigated scenarios.

An additional mention is required regarding the oxidation pathways of the aromatic compounds considered in this study. Although under atmospheric conditions, aromatic VOCs can undergo oxidation reaction with multiple atmospheric oxidants (OH, O_3 and NO_3), their gas-phase kinetics differ significantly among these pathways. Experimental and modeling studies have shown that the OH-driven reaction of several aromatic hydrocarbons proceeds relatively rapidly with, for instance, second-order rate constants for OH+1,2,4-TMB of the order of $3 \cdot 10^{-11}$ cm^3 $molecule^{-1}$ s^{-1} at room temperature while corresponding NO_3+aromatic rate constants can reach values of the order of $1 \cdot 10^{-16}$ cm^3 $molecule^{-1}$ s^{-1} (Jenkin et al., 2003a). Considering ozonolysis, direct ozone reactions with aromatic rings are extremely slow unless specific C=C unsaturations are present in substituent groups (Calvert et al., 2002b). As a result, the contribution of NO_3- and O_3- initiated oxidation pathways to the overall degradation of the aromatics in our chamber experiments is expected to be negligible compared to OH-initiated pathways and was therefore omitted from the current chemical mechanism.

The rate constant values assumed for each precursor-oxidant couple are reported in Table 9:

Table 9: Values of rate constant for each VOC-Oxidant couple involved in the current investigation

VOC	Oxidant	PR Contribution	K values [cm^3 $molecule^{-1}$ s^{-1}]	Reference
αpinene	O_3	$k_{AP+O3}[AP][O_3]$	$8.05 \cdot 10^{-16} \cdot e^{\frac{-640}{T}}$	(Simon et al., 2020)

	OH	$k_{AP+OH}[AP][OH]$	$1.2 \cdot 10^{-11} \cdot e^{\frac{440}{T}}$	(Simon et al., 2020)
	NO_3	$k_{AP+NO3}[AP][NO_3]$	$1.19 \cdot 10^{-12} \cdot e^{\frac{490}{T}}$	(Atkinson et al., 2006)
Isoprene	O_3	$k_{IP+O3}[IP][O_3]$	$1.27 \cdot 10^{-17}$	(Yang et al., 2023)
	OH	$k_{IP+OH}[IP][OH]$	$2.7 \cdot 10^{-11} \cdot e^{\frac{390}{T}}$	(Yang et al., 2023)
	NO_3	$k_{IP+NO3}[IP][NO_3]$	$6.95 \cdot 10^{-13}$	(Suh et al., 2001)
Trimethylbenzene	OH	$k_{TMB+OH}[TMB][OH]$	$1.32 \cdot 10^{-11} \cdot e^{\frac{450}{T}}$	(Bohn & Zetzsch, 2012)
Naphtalene	OH	$k_{Napht+OH}[Napht][OH]$	$2.31 \cdot 10^{-11}$	(Phousongphouang & Arey, 2002)
Toluene	OH	$k_{Tol+OH}[Tol][OH]$	$6.16 \cdot 10^{-12}$	(Carter & Heo, 2012)

As previously discussed, once formed, RO_2 can undergo several fates. Considering the accretion reaction as key interest of this study, the reaction leading to ROOR formation can be written as:

$$RO_2 + RO_2 \; \gamma_{ROOR} k_{RO_2+RO_2} \rightarrow ROOR + O_2 \qquad \text{(R14)}$$

In this equation, γ_{ROOR} is the branching ratio leading to dimer formation and $k_{RO_2+RO_2}$is the corresponding rate coefficient.

Following the same mechanism, the ROOR concentration can be calculated as:

$$\frac{d[ROOR]}{dt} = \gamma_{ROOR} k_{RO_2+RO_2} [RO_2]^2 - \frac{[ROOR]}{\tau_{ROOR}} \qquad \text{(Eq. 13)}$$

In this formulation, [ROOR] is the concentration of the generic dimer formed in this reaction and the [RO_2] concentrations refer to the peroxy radical precursors contributing to the specific ROOR. In this case, τ_{ROOR} represents the lifetime of ROOR, taking into account the losses by dilution, wall deposition, particle condensation.

Resolving equation (13) at steady state results in the following expression of $[ROOR]$:

$$[ROOR] = \tau_{ROOR} \gamma_{ROOR} k_{RO_2+RO_2} [RO_2]^2 \qquad \text{(Eq. 14)}$$

Combining Equations (11) and (14) results in:

$$[ROOR] = \gamma_{RO_2}^2 \gamma_{ROOR} k_{RO_2+RO_2} \tau_{ROOR} \tau_{bi}^2 PR^2 = \gamma_{RO_2}^2 k_{ROOR} \tau_{ROOR} \tau_{bi}^2 PR^2 \qquad \text{(Eq. 15)}$$

In Equation (15), the accessible variables are highlighted in blue, while the unknown reaction constants are shown in green. In this formulation $\gamma_{ROOR} k_{RO_2+RO_2} = k_{ROOR}$. In our analysis, we represent the dimer concentration, [ROOR], as a function of $\tau_{bi}^2 PR^2$, and use isopleths to indicate the values of $\gamma_{RO_2}^2 \gamma_{ROOR} k_{RO_2+RO_2}$ required to reproduce the observed data. It is important to emphasize that this method does not allow a direct determination of k_{ROOR} but instead constrains the combined parameter $\gamma_{RO_2}^2 \gamma_{ROOR} k_{RO_2+RO_2}$. When the RO_2 yield, γ_{RO_2}, is known for a given VOC, k_{ROOR} can be inferred. As will be shown in the following, this approach provides meaningful constraints on the variability of dimer yields under different reaction conditions, enabling a more robust and simplified model parameterization.

4.4.3 Losses and Correction Procedures

Despite the highly controlled conditions, the CLOUD chamber is operated in continuous mode, with the synthetic air being continuously injected into the reactor and with sampling flows being sucked by the instruments. Thus, this operational model will cause some losses mainly associated either with the dilution of the species in the reactor or wall deposition. The dilution for CLOUD chamber was calculated with the formula (*Dada et al.*, 2020):

$$k_{dil} = \frac{Flow_{sinthetic\ air}}{Volume} \quad \text{(Eq. 16)}$$

Based on the operating conditions for each of the investigated campaigns, k_{dil}=0.0002 s^{-1} was calculated for CLOUD16 experiments, i.e. rural and suburban runs, corresponding to a dilution timescale of 1.4 hours, whereas k_{dil}=0.00016 s^{-1}, corresponding to a dilution time of 1.7 h, was obtained for CLOUD12 data (urban runs).

In addition to dilution, gas-phase compounds can be lost through interactions with the chamber walls. Following the approach described by Dada et al., diffusional wall losses were estimated empirically using the decay of compounds with known properties (Dada et al., 2020). Specifically, the wall loss rate constants were extrapolated from the decay of sulfuric acid monomer concentration after its photochemical production was stopped by switching off the UV lights.

Based on these assumptions, the dilution losses were calculated as:

$$k_{wall}(d_p, T) = F \cdot \left(\frac{T}{T_{ref}}\right)^{0.875} \cdot \left(\frac{d_{p,ref}}{d_p}\right) \quad \text{(Eq. 17)}$$

Where T is the operating temperature, dp is the effective molecular diameter, F is the flow, and the subscript "ref" refers to the reference conditions used. Based on this parametrization, a wall loss rate constant of k_{wall}=0.002[s^{-1}] was adopted for monomeric species, whereas k_{wall}=0.001[s^{-1}] was used for dimers. The lower wall loss rate for dimers reflects their larger effective molecular size and reduced diffusivity relative to monomers. Since the reference wall loss rate was derived from sulfuric acid monomers, a rescaling based on molecular dimensions was applied when extending the correction to larger species such as ROOR dimers.

Finally, the value of k_{loss} accounting for both these contributions was calculated as:

$$k_{loss} = k_{wall} + k_{dil} \quad \text{(Eq. 18)}$$

Additional loss involving gas-phase compounds may be associated with their partitioning onto pre-existing particles, commonly referred to as condensation sink (CS). The CS represents the rate at which condensable vapors are scavenged by particle surfaces and removed from the gas phase, and, in chamber experiments, it represents an additional contribution to the overall losses of vapors. Previous investigations in CLOUD chamber revealed that CS values can be usually lower than k_{wall} and k_{dil}(Simon et al., 2020; Xiao et al., 2025), representing a minor contribution to total losses. As a result, although CS can play a role in specific high particle loadings or haze-like conditions, reaching values up to 0.1s^{-1}, in the current investigation its contribution is expected to be dramatically lower than other losses. For this reason, the condensation sink has been neglected in the loss budget of the present study.

4.4.4 Model-Based Estimation of RO_2 and HO_2 Concentrations in Urbar Runs

One of the main parameters implemented in this study is the peroxy radical lifetime, τ_{bi}. Its calculation requires the concentrations of NO, HO_2 and RO_2. However, for the data collected during the urban campaign (CLOUD 12), no direct measurements of HO_2 and RO_2 were available.

To overcome this limitation, it has been necessary to assess the key reactive processes occurring in the reactor in order to infer the HO_2 concentration for each stage from known variables. The precursors injected for the CLOUD12 campaign were naphthalene, toluene and trimethylbenzene. Following the approach proposed by Xiao et al., the contributions of first and second generations oxidation products were separately evaluated (Xiao et al., 2025).

The reactive chain is initiated by the interaction of OH radicals with the aromatic hydrocarbons (ArHC), primarily leading to the formation of a first-generation peroxyradical (RO_2,G1) or, alternatively, of a hydrogenated molecule that generates ROH and HO_2.

$$ArHC + OH\ \gamma_{R15}k_{R1} \rightarrow\ RO_{2,G1} \quad \text{(R15)}$$

$$ArHC + OH\ \gamma_{R16}k_{R2} \rightarrow\ HO_2 + ROH \quad \text{(R16)}$$

A non-unitary branching ratio was assumed for the reactions R15 and R16. In particular, based on toluene chemistry as reported in the Master Chemical Mechanism (MCM), values of γ_{R1} =0.65, and γ_{R2} =0.28 have been implemented in the calculations (Jenkin et al., 2003; J. Zhang et al., 2021)

Then, the highly reactive RO_2 radicals can undergo termination reactions with NO, HO_2, or RO_2:

$$RO_{2,G1} + NO\ k_{RO2NO} \rightarrow\ G1NO \quad \text{(R17)}$$

$$RO_{2,G1} + RO_2\ k_{RO2} \rightarrow\ G1RO_2 \quad \text{(R18)}$$

$$RO_{2,G1} + HO_2\ k_{RO2HO2} \rightarrow\ G1HO_2 \quad \text{(R19)}$$

Similarly to first generation chemistry, second generation oxidation products can be modelled; in this case second generation RO_2 were considered as derived by first-generation RO_2 reacting with OH.

$$G1 + OH\ \gamma_{R20a}k_{G1} \rightarrow\ RO_{2,G2} \quad \text{(R20}a\text{)}$$

$$RO_{2,G2} + NO\ k_{RO2NO} \rightarrow\ G2NO \quad \text{(R21)}$$

$$RO_{2,G2} + RO_2\ k_{RO2} \rightarrow\ G2RO_2 \quad \text{(R22)}$$

$$RO_{2,G2} + HO_2\ k_{RO2HO2} \rightarrow\ G2HO_2 \quad \text{(R23)}$$

The total concentration of first-generation molecules undergoing secondary OH oxidation is referred to as G1, with $G1 = G1NO + G1RO_2 + G1HO_2$.

Based on MCM reactive mechanism of OH-driven oxidation of cresol, a branching ratio of γ_{R20} =0.7 was assumed for the second-generation RO_2 formation while the branching ratio for HO_2 formation from G1 was set to γ'_{R20} =0.3 (Bloss et al., 2005). Figure 36 summarizes the key reactive scheme described in this paragraph.

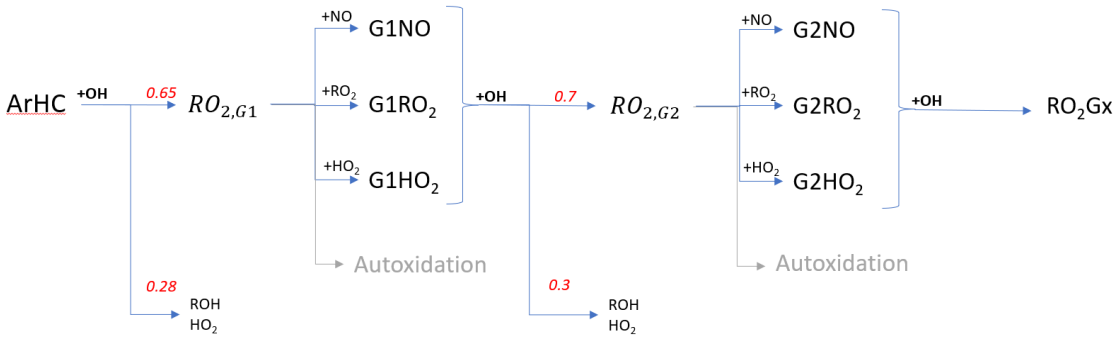

Figure 36: Schematic model of RO_2 and HO_2 Production Reactive Scheme

An additional source of HO_2 in the system arises from the reactions $O_3 + OH \rightarrow HO_2 + O_2$ and $CO + OH + O_2 \rightarrow CO_2 + HO_2$.

For the HO_2 sink, the following reactions were considered:

$$HO_2 + OH \rightarrow H_2O + O_2 \quad \text{(R24)}$$

$$HO_2 + NO \rightarrow OH + NO_2 \quad \text{(R25)}$$

$$HO_2 + RO_2 \rightarrow ROOH + O_2 \quad \text{(R26)}$$

$$HO_2 + HO_2 \rightarrow H_2O_2 + O_2 \quad \text{(R27)}$$

Where the total concentration of RO_2 is defined as: $[RO_2] = [RO_2G1] + [RO_2G2]$.

By combining all these reactive pathways into a single HO_2 balance, the evolution of $[HO_2]$ can be expressed as:

$$\frac{[dHO_2]}{dt} = \gamma_{R2} k_{NPT-OH}[NPT][OH] + \gamma_{R2}\, k_{Tol-OH}[Tol][OH] + \gamma_{R2}\, k_{TMB-OH}[TMB][OH] + k_{O3-OH}[O_3][OH] + k_{CO-OH}[CO][OH] - k_{HO2-OH}[HO_2][OH] - k_{NO-HO2}[NO][HO_2] - k_{RO2-HO2}[HO_2]([RO_2G2] + [RO_2G1]) - k_{HO2-HO2}[HO_2]^2 + \gamma_{R10} k_{OH-RO2}[OH][G1] \quad \text{(Eq. 19)}$$

$$\frac{[dRO_2G1]}{dt} = \gamma_{R1} k_{NPT-OH}[NPT][OH] + \gamma_{R1} k_{Tol-OH}[Tol][OH] + \gamma_{R1} k_{TMB-OH}[TMB][OH] - k_{RO2-RO2}[RO_2G2][RO_2G1] - k_{RO2-HO2}[RO_2G1][HO_2] - k_{NO-RO2}[NO][RO_2G1] \quad \text{(Eq. 20)}$$

For first-generation RO_2 termination reactions are expressed as:

$$\frac{[dG1NO]}{dt} = k_{NO-RO2}[NO][RO_2G1] - (k_{loss} + k_{OH-G1NO}[OH])[G1NO] \quad \text{(Eq. 21)}$$

$$\frac{[dG1HO_2]}{dt} = k_{HO2-RO2}[HO_2][RO_2G1] - (k_{loss} + k_{OH-G1NO}[OH])[G1HO_2] \quad \text{(Eq. 22)}$$

$$\frac{[dG1RO_2]}{dt} = k_{RO2-RO2}([RO_2G1] + [RO_2G2])[RO_2G1] - (k_{loss} + k_{OH-G1NO}[OH])[G1RO_2] \quad \text{(Eq.23)}$$

Second-generation RO_2 (RO_2G2), formed from further OH oxidation of first generation RO_2, evolve as:

$$\frac{[dRO_2G2]}{dt} = \gamma_{R6} k_{RO2-OH}([G1NO] + [G1HO_2] + [G1RO_2])[OH] - k_{RO2-RO2}[RO_2G2]([RO_2G2] + [RO_2G1]) - k_{RO2-HO2}[RO_2G2][HO_2] - k_{NO-RO2}[NO][RO_2G2] \quad \text{(Eq.24)}$$

With termination reactions of RO_2G2:

$$\frac{[dG2NO]}{dt} = k_{NO-RO2}[NO][RO_2G2] - k_{loss}[G2NO] \quad \text{(Eq. 25)}$$

$$\frac{[dG2HO_2]}{dt} = k_{HO2-RO2}[HO_2][RO_2G2] - k_{loss}[G2HO_2] \quad \text{(Eq. 26)}$$

$$\frac{[dG2RO_2]}{dt} = k_{RO2-RO2}([RO_2G1] + [RO_2G2])[RO_2G1] - k_{loss}[G2RO_2] \quad \text{(Eq. 27)}$$

Only HO_2 generated from first- and second- generation RO_2 were taken into account; contributions from further oxidation generations are neglected.

The rate constant values adopted in the current investigation for G1- and G2-RO_2 chemistry are reported in Table 8. The calculation of the losses was performed considering different contributions, coherently with Equation 20:

By assuming steady-state conditions for all the RO_2 and HO_2 species, it is possible to calculate the contribution of RO_2G1 and RO_2G2 and finally HO_2. Under steady-state approximation, the equations associated with these terms become: for first generation RO_2

$$[RO_2G1] = \frac{\gamma_{R1}\left(k_{Napht+OH}[Napht] + k_{Tol+OH}[Tol] + k_{TMB+OH}[TMB]\right)[OH]}{k_{RO2+RO2}([RO_2G2] + [RO_2G1]) + k_{RO2+HO2}[HO_2] + k_{NO+RO2}[NO]} \quad \text{(Eq. 28)}$$

For second generation RO_2:

$$[RO_2G2] = \frac{\gamma_{R6}(k_{RO2+OH}[G1NO] + [G1HO_2] + [G1RO_2])[OH]}{k_{RO2+RO2}([RO_2G2] + [RO_2G1]) + k_{RO2+HO2}[HO_2] + k_{NO+RO2}[NO]} \quad (Eq. 29)$$

For HO_2:

$$[HO_2] = \frac{(\gamma_{R2}k_{NPT+OH}[NPT][OH] + \gamma_{R2}k_{Tol+OH}[Tol][OH] + \gamma_{R2}k_{TMB+OH}[TMB][OH])}{\left(k_{HO_2+OH}[OH] + k_{NO+HO_2}[NO] + k_{RO_2+HO_2}([RO_2, G1] + [RO_2, G2])\right)} + \frac{k_{O_3+OH}[O_3][OH] + k_{CO+OH}[CO][OH] + \gamma_{R10}k_{OH+RO_2}[OH][G1]}{\left(k_{HO_2+OH}[OH] + k_{NO+HO_2}[NO] + k_{RO_2+HO_2}([RO_2, G1] + [RO_2, G2])\right)} \quad (Eq. 30)$$

This framework allows the calculation of HO_2 concentrations and the total RO_2, obtained as the sum of RO_2G1 and RO_2G2, under the experimental conditions of CLOUD12. This model provides then a useful tool for interpreting radical dynamics and evaluating the key parameters governing peroxy radical chemistry in the chamber experiments.

HO_2 and RO_2 model uncertainties

The quantification of the uncertainty associated with the modelled HO_2 and RO_2 concentrations, was performed through the use of a time-resolved box-model-based approach. For each experimental run, the model was driven by the measured time series of the key controlling variables, alias OH, NO, O_3 and VOCs concentrations, over the timespan of the corresponding stage. At each time step, the chemical system was integrated forward in time until steady state was reached, assuming constant input conditions over the integration window.

For each run, once computed HO_2 and RO_2 concentrations, the associated uncertainty was estimated as the standard deviation of the steady state concentration, after excluding an initial transient fraction of the time series. In this framework, the reported uncertainties represent the propagation of variability of the measured input parameters through the chemical mechanism. Therefore, this methodology provides a realistic estimation of the chemical variability affecting radical concentrations under the investigated conditions.

4.5 Results

As previously described, three key scenarios have been investigated in this study, aiming to mimic different atmospherically relevant conditions to represent a broad range of environments where RO_2-RO_2 interactions can occur. An illustrative overview of these scenarios showing the injected precursors, of OH radicals and the temperature of the set of runs, is presented in Figure 37.

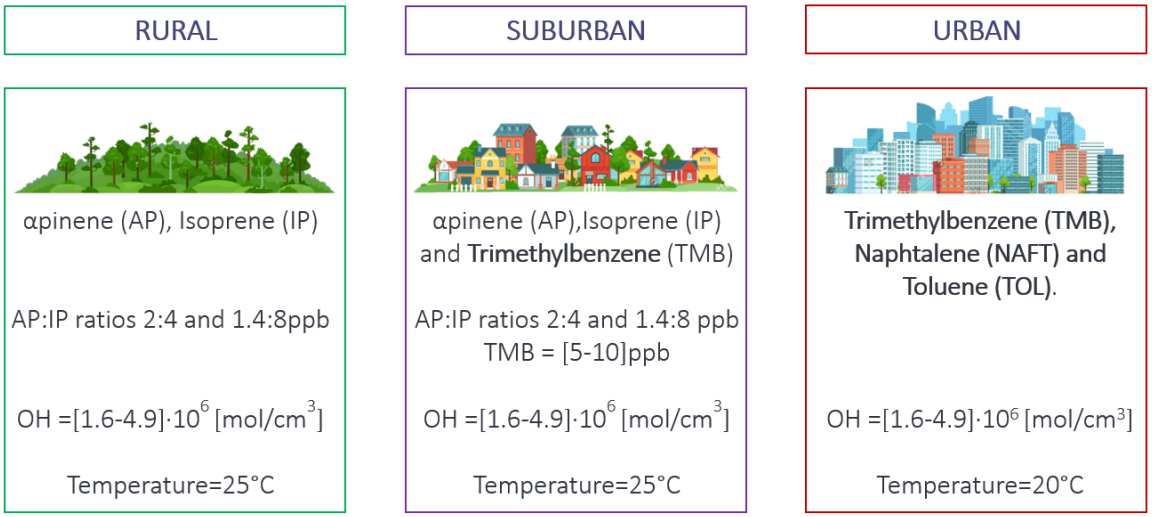

Figure 37: Illustrative scheme of the investigated scenarios discussed in this chapter

Aiming at discriminating and visualizing the key bimolecular pathways involving RO_2 radicals, a comprehensive plot reporting all the experimental conditions is shown in Figure 38. For each scenario, the corresponding values of RO_2 lifetime, τ_{bi}, and branching parameter, β, are reported. The grey shaded region refers to the global distributions of β and τ derived by GEOS-Chem simulations, based on hourly output from January and July, weighted by the isoprene + OH oxidation rate (Kenagy et al., 2024).

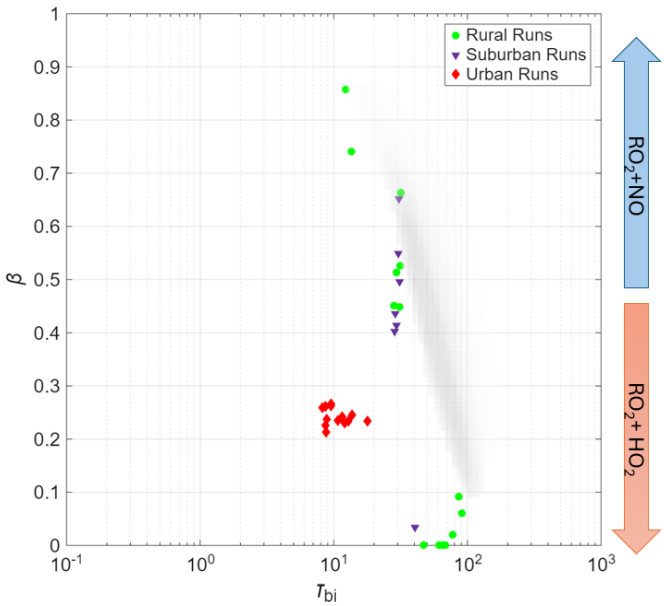

Figure 38: Positioning of the current experiments on the global distribution of τbi (expressed in seconds) and β (adimentional), with red, violet and green dots representing urban, suburban and rural runs, respectively (light conditions)

Based on the definition of β, higher values of β correspond to RO_2 radicals predominantly reacting with NO whereas lower values indicate a chemistry dominated by RO_2 reactions with HO_2. Urban runs (red dots) exhibit shorter lifetimes and lower β values. Given the low NO regime employed in the CLOUD12 experiments, this result is consistent with HO_2-driven chemistry under limited NO. Suburban runs, highlighted in purple, are positioned at intermediate lifetime and branching ratio values, whereas rural experiments exhibit a broader spread, with some points reflecting long lifetimes and HO_2-dominated chemistry and others showing greater NO influence. Despite NO concentrations being kept below 1.0 ppbv across all experimental conditions, rural runs exhibiting higher β values also showed a greater contribution of NO-driven reaction pathways, consistent with the branching ratio values.

This comparison highlights that the experimental setup captures a realistic spectrum of RO_2 lifetime and branching behaviours and that variations in NO availability, even if limited within a low range, are sufficient to shift the balance between HO_2- and NO-dominated RO_2 chemistry.

Following this general overview, the next step is to examine the results for each specific scenario in detail, going from rural to suburban and finally moving to the urban environment. By considering each set of runs separately, it is possible to identify the key processes governing the different RO_2-RO_2 interactions under atmospherically relevant conditions.

4.5.1 Rural Scenario (Pure BVOCs)

The first set of results focuses on the rural experimental runs, where only BVOCs were injected into the reactor. These conditions are characterized by low NO concentrations and long RO_2 lifetimes, providing interesting insights about HO_2-dominated chemistry. The following analysis examines the formation of RO_2 radicals originating from αpinene and isoprene oxidation, the monomeric and dimeric composition of these runs, their molecular characteristic and the impact of all these aspects on NPF.

As previously mentioned, αpinene and isoprene were injected into the system in two different biogenic ratios, corresponding to AP: IP equal to 1.4:8 ppbv and 2:4 ppbv. The temperature of the system was set at 25°C to mimic a temperate environment. Figure 39 shows the timeseries of the key input species involved in the initial oxidation steps, ranging from the BVOCs α-pinene and isoprene to the key oxidants (O_3 and OH) as the injected NO. In the analysed runs, the concentration of NO was kept lower than 1ppb, aiming at replicating remote rural areas where NO_x chemistry, typically correlated to vehicle emissions, does not prevail.

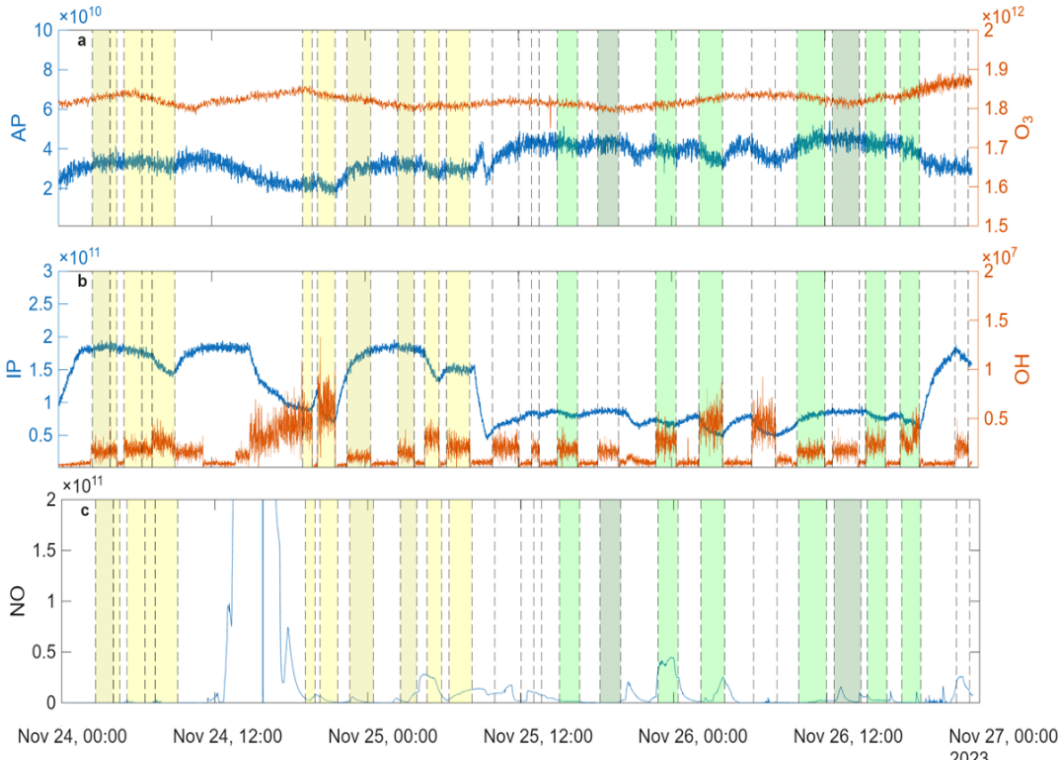

Figure 39: Timeseries of some key variables for the Rural runs. All the concentrations are reported in molec/cm³. Panel a) reports the αpinene concentration (left axis) against O_3 values (right axis). Panel b) records isoprene (left axis) against OH concentration (right axis). Panel c) reports NO concentration. The time-intervals highlighted with the colors refer to the GCR runs analysed in this experiment. Yellow runs refer to AP: IP=1.4:8 ppbv, with light and dark yellow referring to light and dark conditions. Green runs are related to AP: IP=2:4 ppbv with the same color legend for light and dark experiments.

The experiments were carried out from the 24th to the 27th of November 2023. In Figure 39, the dotted vertical lines delimit the GCR runs discussed in this section. Different colours are used to distinguish

between AP: IP ratios equal to 1.4:8 ppbv and 2:4 ppbv (yellow and green, respectively), with variations in color intensity differentiating between daytime-mimicking runs, where the lights were turned on to activate the photooxidation, and nighttime-replicating chemistry, where the lights were off.

Since this work focuses on the RO_2-RO_2 interactions leading to dimers formation, a first overview of the results in term of dimeric/monomeric composition is proposed in Figure 40. This plot illustrates a decreased monomer-to-dimer ($C_{monomers}/C_{dimers}$) ratio obtained by increasing the RO_2 lifetime. For τ_{bi}<20s, the monomer-to-dimer ratio remains high, whereas increasing τ_{bi}, the ratio stabilizes within the range 5-10, possibly indicating a relatively higher formation of dimers under longer reaction times. The NO-based colorbar indicates that the runs exhibiting higher ratio values, are those characterized by a slightly higher NO concentration, confirming that RO_2+NO chemistry influences monomers chemistry.

In order to investigate the impact of τ_{bi}, two runs with similar monomer-to-dimer ratios, identical AP: IP value and comparable OH concentrations were selected, and their composition is shown in the pie charts in Figure 40 and summarized in Table 10. The contributions of $C_{4\text{-}5}$ were assumed to be primarily associated to isoprene oxidation with C_5 reflecting isoprene-derived oxidation products and C_4 mainly originated from fragmentation. Similarly, C_9 and C_{10} were assumed to be predominantly correlated to αpinene chemistry, with C_9 mainly arising from fragmentation and C_{10} comprehending AP-oxidation products. Among the dimers, C_{15} and C_{20} were selected as key compounds, formed after the cross-interaction of AP-RO_2 and IP-RO_2 and the self-reaction of two AP-RO_2, respectively.

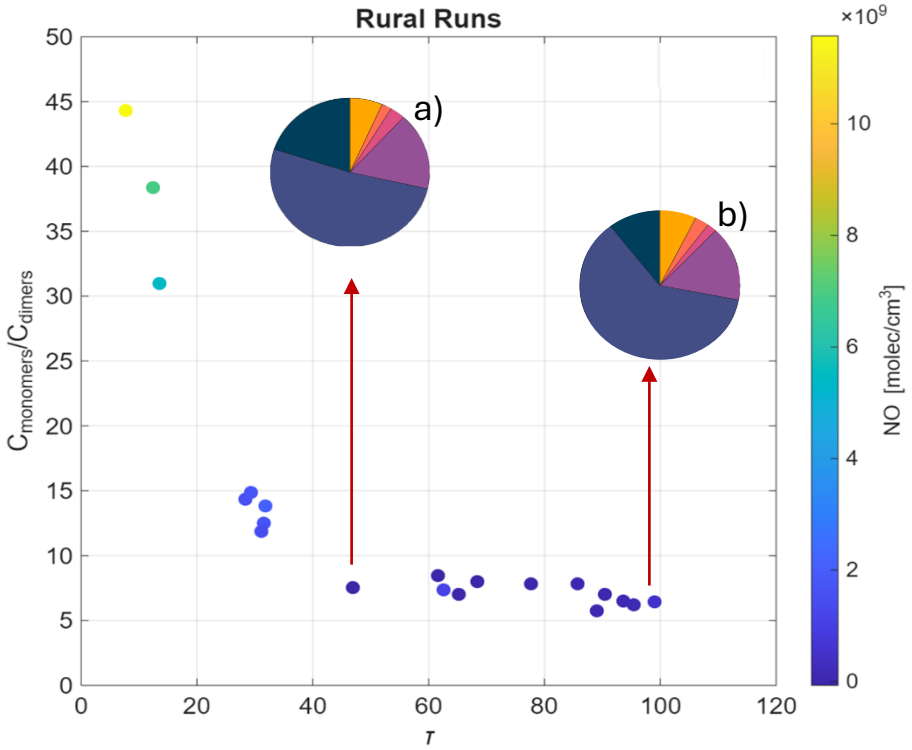

Figure 40: Monomer-to-Dimer ratio against lifetime τ_{bi} for all the investigated rural runs (light and night conditions). The colorbar reports the NO concentration in molecule/cm^3. The piecharts represent the composition of two runs presenting the same $C_{monomer}/C_{dimer}$ ratio but different τbi. Piechart a) and b) represent two runs with same AP:IP ratio (2:4 ppbv) and OH concentration of 3.45e6 and 1.96e6, respectively. The legend of the different piecharts contributions is reported in Table 10.

The trends reported in Table 10 are consistent with the definition of τ_{bi}: shorter lifetimes correspond to faster radical reactivity, with RO_2 radicals quickly consumed by NO or HO_2, limiting RO_2-RO_2 interactions and dimer formation. Conversely, longer τ_{bi} enhances the probability of RO_2-RO_2 collisions, promoting the formation of accretion products (Berndt et al., 2018; Ehn et al., 2014). However, it is worth noting that high- τ_{bi} experiments correspond to ozonolysis conditions in which OH concentrations are insufficient to oxidize IP efficiently. As a result, the contribution of AP-derived species dominated,

reinforcing the registered increase in heavier compounds (C_{20}) and the relative decrease of IP-related species ($C_{4\text{-}5}$ and C_{15}). Thus, the observed compositional shifts result from a combined effect of RO_2 lifetime and the dominant oxidant chemistry.

Table 10: Composition of Runs reported in the piecharts in Figure 40, exhibiting the same monomer-to-dimer ratio but different lifetimes

		Run a)	Run b)
	$C_{4\text{-}5}$	20.0%	10.0%
	$C_{9\text{-}10}$	51.5%	61.2%
	Others $C_{<=10}$	16.8%	15.5%
	C_{15}	3.10%	1.9%
	C_{20}	2.0%	2.9%
	Others $C_{>10}$	6.60%	7.6%

Before diving into the composition of monomers and dimers pool, it is worth noticing this is a complex system where isoprene and αpinene reactivities are not only affected by the availability of the various oxidants but also by the mutual interaction and competition of the oxidants towards the reaction with one or the other precursors. Chamber studies investigating similar conditions have strongly highlighted the non-additive oxidation behaviour of similar experimental conditions. The presence of isoprene, which rapidly reacts with OH radicals, can effectively compete with αpinene, reducing the availability of hydroxy radicals for monoterpene oxidation. This competitive scavenging of OH operated by isoprene has been shown to suppress the formation of products actively contributing to SOA formation (McFiggans et al., 2019) and to affect NPF in environments where both IP and AP are present (Schervish et al., 2024). The reason justifying these results is still under debate, and despite OH-scavenging operated by IP definitely represents one of the key processes, it cannot be considered the only one.

Detailed modelling and experimental studies indicate that this competition extends beyond simple oxidant consumption: high isoprene reactivity alters the fate of peroxy radicals (RO_2), interfering with the formation of extremely low-volatility species such as C_{20} dimers that are considered active contributors to SOA formation. More in general, it has been proven that increasing isoprene concentrations can promote competition for C_{10}-RO_2 by C_5-RO_2, resulting in a suppression of ultra-low volatile organic compounds (ULVOCs). Parallelly, extremely low volatility compounds (ELVOCs) are also reduced although to a lesser extent as the decrease in C_{20} dimers coupled with IP increase is partially compensated by the enhancement of cross-RO_2 reactions leading to the formation of C_{15} dimers. Low volatility compounds (LVOCs) are less affected than ULVOCs or ELVOCs because both C_{15} and C_{10} contribute to this volatility range (Schervish et al., 2024).

In the next paragraphs, specific details about the monomeric and dimeric composition in the investigated runs are proposed.

Monomeric Composition

The first step of the analysis focused on investigation of the monomeric products formed under each experimental condition simulating daytime chemistry. Figure 41a reports the concentration of C_5 and C_4 species, whereas Figure 41b shows C_9 and C_{10} concentrations. The runs from 1 to 7 refer to AP: IP equal to 2:4ppbv whereas runs 8-14 present AP: IP ratio of 1.4:8ppbv. The doubling in the isoprene injected concentration is reflected by the increase in its production rate reported with the dotted blue lines on the right y-axis of Figure 41a.

C_4 and C_5 are primarily associated to isoprene oxidation chemistry. Upon oxidation by O_3, OH, or NO_3, isoprene typically produces closed-shell molecules containing five carbon atoms, thus contributing to C_5 signal. Thus, these closed-shell products are not the only contributors to C_5 signal: in soft ionization

conditions, the LTOF also detects stabilized peroxy radicals, their clusters with nitrate, and highly oxygenated intermediates derived from isoprene oxidation.

The C_4 component can be interpreted as a result of the fragmentation processes occurring in the chamber. Reactions involving larger oxygenated molecules may lead to the cleavage of functional groups, often involving the loss of CH_3 complex or similar moieties, ultimately yielding four-carbon products. Alternatively, fragmentation can be explained considering possible gas-phase β-scissions of C_5-RO_2 or RO species as well as mild in-instrument fragmentation of larger oxidized molecules (Almeida et al., 2024). More advanced oxidation can further enhance C_4 formation via carbon–carbon bond scission. The synergistic effect of these processes likely explains the observed levels of C_4 species.

Coherently with the expected chemistry of the system, the C_5 signal exhibits a strong correlation with the total production rate of isoprene as well as with OH concentration, not shown in this plot. This behaviour reflects the preferential OH-driven oxidation of isoprene compared to αpinene.

An increase in OH enhances the reaction rate of isoprene, leading to higher formation of IP-RO_2 radicals and their subsequent closed-shell products, which dominate the C_5 contribution in the mass spectra.

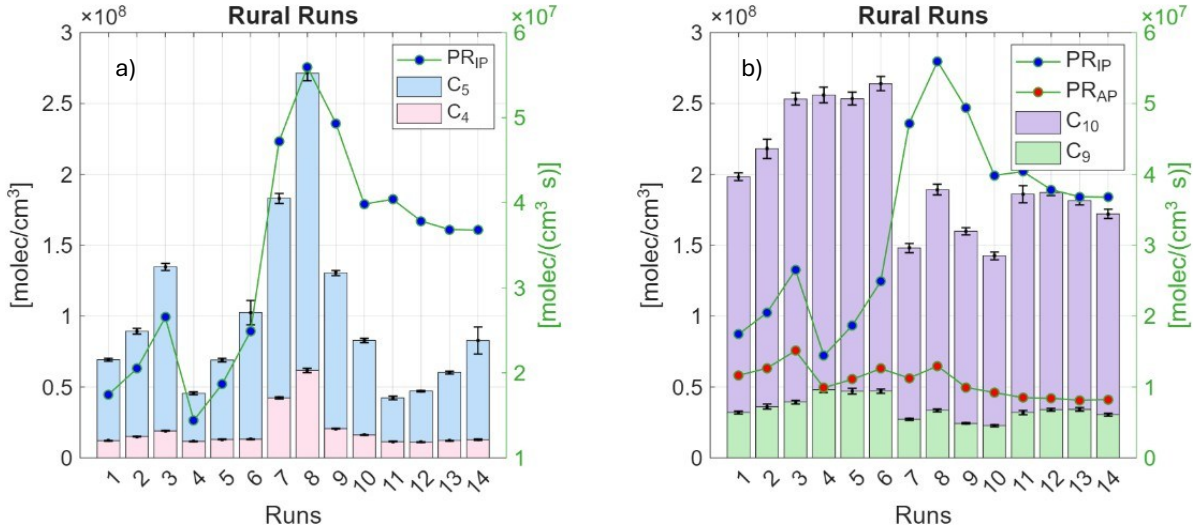

Figure 41: Concentrations of key monomeric groups. Panel a) exhibits the concentrations in molec/cm3 of C_4 and C_5 for each of the investigated runs. On the right axis the total production rate of isoprene is reported. Panel b) registers the contributions of C_9 and C_{10} for each run and the corresponding production rates of isoprene and αpinene. The runs refer to GCR light-conditions. Runs from 1 to 7 refer to AP: IP=2:4 ppbv whereas from 8 to 14, show AP: IP=1.4:8 ppbv

Conversely, when considering combined isoprene and α-pinene chemistry, identifying a clear correlation becomes more challenging. Figure 41b reports the detected concentrations of C_9 and C_{10} molecules, along with the total production rates of α-pinene and isoprene for the experiments (right axis).

The complexity in interpreting C_{10} signal stands in the fact that it is composed by two main contributions: monomers derived from α-pinene oxidation and dimers formed from isoprene. Distinguishing between these contributions is extremely difficult, as there are no apparent differences in hydrogen-to-oxygen ratios or other simple molecular markers that can unambiguously assign a molecule to one source or the other. Nevertheless, a trend with the BVOC mixing ratio is apparent: C_{10} concentrations are generally lower when the AP:IP ratio is 1.4:8 ppbv and higher when AP: IP is 2:4 ppbv. As previously mentioned, C_{10} signal may arise from both IP-RO_2 self-reactions and AP-RO_2 termination reactions. Previous studies have investigated the stability of accretion products and monomers (Heinritzi et al., 2020). More specifically, Heinritzi et al. focused on C_{15} molecules formed either via IP-RO_2 + AP-RO_2 cross-reactions or from β-caryophyllene ($C_{15}H_{24}$)-derived monomers. In their study, C_{15} accretion products were found to be more stable than the corresponding monomers. In the

present case, no separation between C_{10} monomers and dimers has been performed, but further studies will aim at distinguishing these two contributions.

In parallel, the isoprene production rate roughly doubles when the AP:IP ratio decreases to 1.4:8 ppbv, highlighting the sensitivity of isoprene oxidation to its initial abundance.

As for the C_4–C_5 case, the C_9 signal can be largely attributed to C_{10} fragmentation where fragmentation processes are analogous to those described previously.

To further explore the relationship among the output species and the controlling experimental parameters, a Spearman rank correlation analysis was performed across all experimental runs of rural scenario, reported in Figure 42. Spearman correlation evaluates monotonic relationships based on the ranked values of the variables, rather than their absolute magnitudes, and is therefore less sensitive to non-linear responses and outliers compared to linear correlation metrics such as Pearson correlation. This approach is particularly suitable for atmospheric datasets, and it has already been implemented in previous environmental studies to investigate the relationship between molecular composition, oxidant levels and precursors abundance (Seinfeld & Pandis, 2016; Zhi et al., 2021). In the present study, the Spearman analysis was complemented by the calculation of a Pearson matrix correlation, not shown in this context. The close similarity between these two correlation patterns indicates the robustness of the registered correlations, not being influenced by single extreme values.

The analysis includes the concentrations of the main products in the range C_4–C_{20}, the total production rates of isoprene and α-pinene, the effective RO_2 lifetime (τ_{bi}), and the initial concentrations of the main reactants and oxidants. Among the strongest relationship, C_4 and C_9 exhibit a strong correlation with C_5 and C_{10}, respectively, coherently with the predicted fragmentation pathways. A similarly strong correlation is observed between C_5 and OH concentration, coherent with the results reported in the bar chart Figure43, thus reflecting the dominant role of OH-initiated isoprene oxidation. A weaker, yet still positive correlation between C_4 and OH is also observed, consistent with increased fragmentation occurring under more oxidative conditions. Initial αpinene concentration exhibits a clear positive correlation with C_{20} species, in agreement with the interpretation of C_{20} as a product of αpinene RO_2 self-reactions. This relationship highlights the importance of precursor availability in controlling the formation of higher-carbon number products. Furthermore, a strong correlation is also found between C_{10} and C_{20}, suggesting a common chemical pathway linked to αpinene oxidation. While C_{10} species are primarily attributed to α-pinene-derived monomers, C_{20} species originate from the self-reaction of α-pinene RO_2 radicals, naturally coupling their formation through the same precursor pool. A positive correlation is also registered between τ_{bi} and C_{15} and C_{20}, consistent with the fact that longer RO_2 lifetimes can favour bimolecular RO_2 reactions and the formation of accretion products. The negative correlation of IP precursor concentration with C_4 and C_5 may suggest that OH represents here the limiting factor leading to the formation of $C_{4\text{-}5}$ from IP, hence an increase in the initial IP concentration will only correspond to an increment in $C_{4\text{-}5}$ group if coupled with higher OH concentrations.

The total monomer and dimer concentration is also reported considering nitrogen-free ($Mon_{N=0}$ and $Dim_{N=0}$) and nitrogen-containing compounds ($Mon_{N>0}$ and $Dim_{N>0}$). As expected, a strong correlation between nitrogen containing molecules and initial NO levels, is recorded. The production rates reported in the matrix refer to the total production rates calculated by considering the contribution of each oxidant. Furthermore, a strong positive correlation is observed between nitrogen free dimers and monomers. This finding is consistent with their common chemical origin: dimer formation is driven by

the recombination of RO_2 radicals derived from monomeric pathway, hence higher monomer concentrations will lead to higher dimers production.

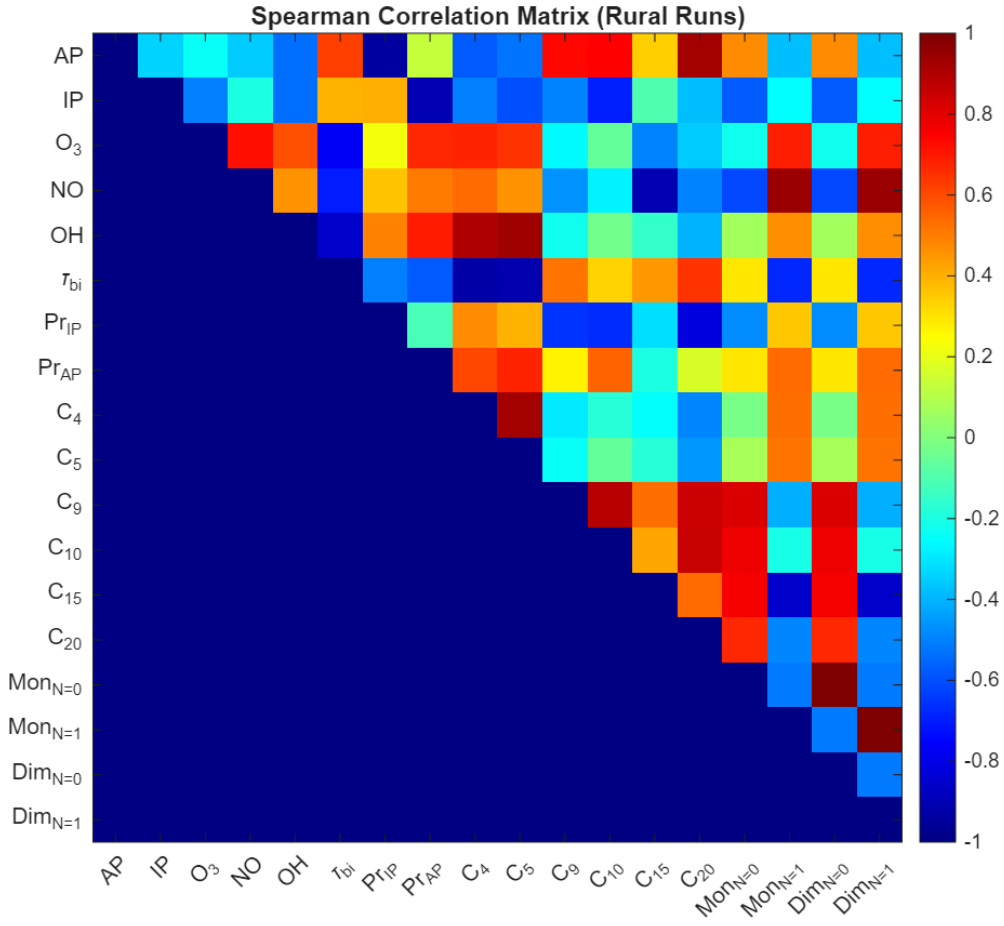

Figure 42: Spearman Correlation Matrix for the Rural runs under daylight conditions (lights On)

After this first investigation of the key variables affecting the resulting organic composition, more details about the dimers composition will be discussed in the next section zooming in into the contribution of each C_x molecule on the total dimers range.

Dimers Composition

Once the main trends in monomer composition were analysed, the analysis was extended to dimeric species. Dimers are primarily formed through the RO_2 combination and represent key precursors for NPF and SOA growth. Figure 43 reports the relative contribution of each class of dimers, i.e. molecules presenting carbon number greater than 10, over the total amount of dimers. For C_{11}-C_{13} dimers, the fractions are moderately low and tend to be slightly higher in experiments with greater isoprene content (runs from 8 to 14 with AP: IP=1.4:8 ppbv), suggesting that these smaller dimers are favoured when isoprene is abundant. The C_{14} fraction shows a moderate increase with isoprene species. C_{15} dimers are primarily cross products of IP-RO_2 and AP-RO_2, and they exhibit the strongest increase when isoprene concentrations are doubled. This highlights the importance of IP-RO_2 availability for cross-dimer formation. C_{16} and C_{17} represent a relatively minor contribution, showing no strong systematic trend with precursor ratio and, thus, a lower sensitivity to AP: IP ratio. C_{18} dimers generally decrease when isoprene increases, suggesting that these products are mainly associated with fragmentation of products from AP-RO_2 self-reactions and are partially suppressed in mixed systems. C_{19} dimers also decline with higher isoprene, reflecting a similar suppression effect on AP-dominated species. Finally, C_{20} dimers, which primarily arise from AP-RO_2 self-reactions, decrease substantially as isoprene

increases, from ~0.27 down to ~0.13, consistent with the competitive effect of IP-RO_2 on the availability of AP-RO_2 for self-reaction.

Overall, these trends indicate that increasing the isoprene fraction shifts the dimer distribution toward intermediate-sized dimers (C_{14}–C_{15}), primarily formed via cross-reactions, while larger dimers derived from α-pinene self-reactions (C_{18}–C_{20}) are suppressed. This behaviour underscores the role of radical competition in determining the volatility and molecular composition of dimeric products and their potential contribution to particle growth.

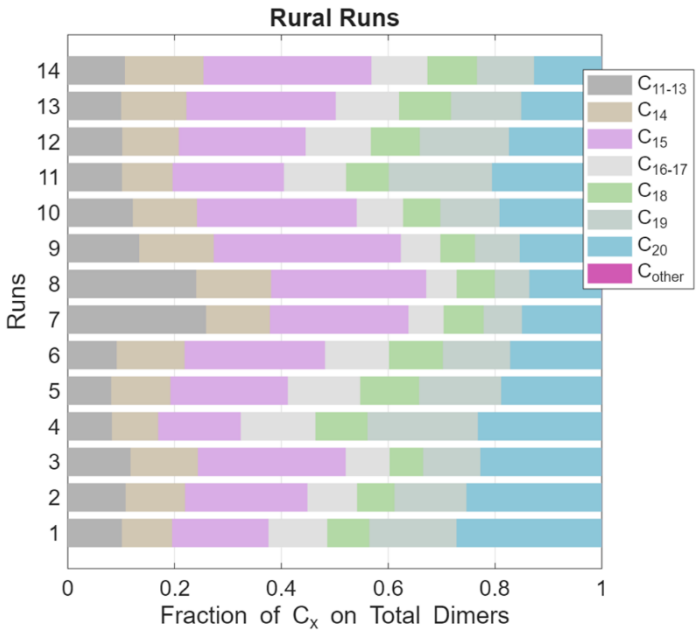

Figure 43: Fraction of dimers ($C_{>10}$) over the total amount of dimer molecules in the light runs. Run from 1 to 7 refer to AP: IP=2:4 ppbv whereas run from 8 to 14 present AP: IP=1.4:8 ppbv

As previously discussed, decodifying RO_2-RO_2 interactions is an extremely challenging procedure since the resulting products composition depends on the chemical structure of the parent RO_2 radicals.

A general overview of the key class of dimers formed in each scenario is reported in Figure 44. The isopleth-based plot estimates the relative efficiency of the interactions among the various RO_2 radicals. The dimers investigated, C_{15} and C_{20} clusters, are assumed to form by cross-reaction of AP-RO_2 and IP-RO_2 and self-reaction of AP-RO_2 respectively. Using total dimer concentrations offers a concise and preliminary way to compare the chemistry of the radical interactions towards other RO_2. The plot is based on the set of equation reported in section 4.4.2. For each dimer, the x-axis is defined as the product of the square of the bimolecular lifetime and the production rates of the two RO_2 precursors involved in its formation. Accordingly, for C_{20}, assumed to be formed via self-reactions of α-pinene derived RO_2 radicals, the x-axis is constructed using PR_1=PR_2, both equal to the total αpinene production rate. Conversely, considering C_{15} as the cross-product of AP-RO_2 and IP-RO_2, PR_1 and PR_2 correspond to the total production rates of isoprene and αpinene oxidation, respectively. The same procedure for the determination of PR_1 and PR_2 was performed for each plotted dimer. All the isopleths slopes are corrected for reaction rate constant k_{ROOR}, calculated in Section 4.4.3, and corresponding to loss rate 1/8 minutes.

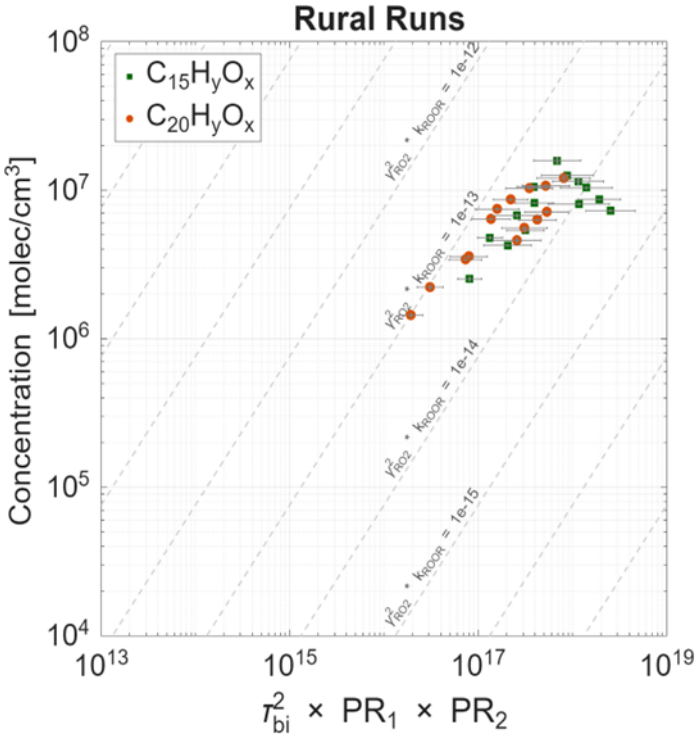

Figure 44: Isopleth plot correlating the concentrations of different dimers towards their correlated reaction rates and bimolecular lifetimes. On the isopleth the square product of the RO_2 branching ratio and the k_{ROOR} rate constant.

This investigation was not only performed for the general C_x contribution of key dimers but also for some tracer molecules expected to be formed in the system based on the injected precursors. In particular, for AP-RO_2 self-reaction leading to C_{20} compounds, the following compounds were investigated:

Table 11: C_{20} Tracer molecules and the corresponding parent RO_2

C_{20}-compound	**Parent RO_2 (1)**	**Parent RO_2 (2)**
$C_{20}H_{30}O_x$	$C_{10}H_{15}O_x$ as $RO_{2\text{-}\alpha p+O3}$	$C_{10}H_{15}O_x$ as $RO_{2\text{-}\alpha p+O3}$
$C_{20}H_{32}O_x$	$C_{10}H_{15}O_x$ as $RO_{2\text{-}\alpha p+O3}$	$C_{10}H_{17}O_x$ as $RO_{2\text{-}\alpha p+OH}$
$C_{20}H_{34}O_x$	$C_{10}H_{17}O_x$ as $RO_{2\text{-}\alpha p+OH}$	$C_{10}H_{17}O_x$ as $RO_{2\text{-}\alpha p+OH}$
$C_{20}H_{31}N_1O_x$	$C_{10}H_{15}O_x$ as $RO_{2\text{-}\alpha p+O3}$	$C_{10}H_{16}N_1O_x$ as $RO_{2\text{-}\alpha p+NO3}$
$C_{20}H_{32}N_2O_x$	$C_{10}H_{15}O_x$ as$RO_{2\text{-}\alpha p+NO3}$	$C_{10}H_{16}N_1O_x$ as $RO_{2\text{-}\alpha p+NO3}$

Analogously, for cross-reaction between AP-RO_2 and IP-RO_2 leading to C_{15}, the following compounds were analysed:

Table 12: C_{15} Tracer molecules and the corresponding parent RO_2

C_{15}-compound	**Parent RO_2 (1)**	**Parent RO_2 (2)**
$C_{15}H_{24}O_x$	$C_{10}H_{15}O_x$ as $RO_{2\text{-}\alpha p+O3}$	$C_5H_9O_x$ as $RO_{2\text{-ip}+O3}$
$C_{20}H_{25}O_xN_1$	$C_{10}H_{16}N_1O_x$ as $RO_{2\text{-}\alpha p+NO3}$	$C_5H_9O_x$ as $RO_{2\text{-ip}+OH}$
$C_{15}H_{26}O_x$	$C_{10}H_{17}O_x$ as $RO_{2\text{-}\alpha p+OH}$	$C_5H_9O_x$ $RO_{2\text{-ip}+OH}$

Among these compounds it is expected that nitrogen-containing species mainly contribute to the total dimers balance during nighttime chemistry, as a result of NO_3-oxidation pathways.

Based on the equation set reported in section 4.4.2, these tracer molecules have been reported in Figure 45. For each molecule, the PR values used to position the point on the plots are related to the parent VOC-O_x pathway leading to the formation of the molecule itself (see Tables 11 and 12). For example, for $C_{20}H_{30}O_x$ formed from self-reaction of two αpinene-ozonolysis RO_2, the PR rates reported are the PR for

ozonolysis. The isopleths represent the product of the square of the branching ratio γ_{RO2}^2 and the rate constant of the accretion reaction k_{ROOR}.

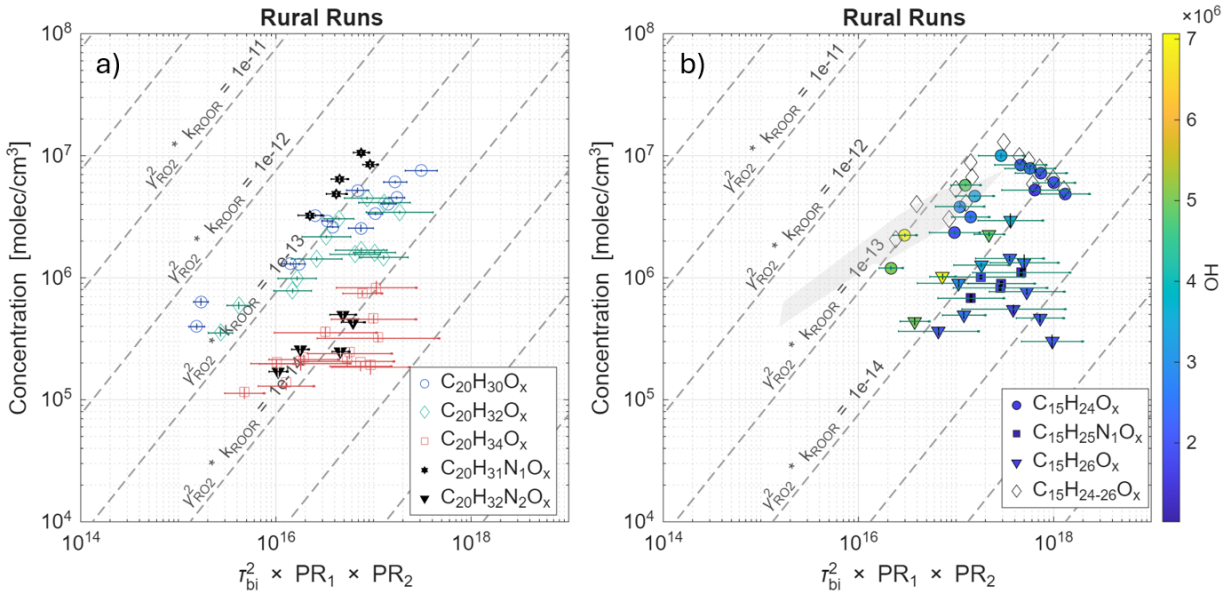

Figure 45: Isopleths Plot representing the formation rate of key dimeric molecules. Panel a) C_{20} species as result of AP-RO_2 self-reaction. Empty dots refer to daytime whereas black dots refer to nighttime runs (lights off). Panel b) representing C_{15} compounds resulting from AP-RO_2 and IP-RO_2 cross-reaction. The grey halo on the C_{15} plot corresponds to the total C_{20} concentration (without discriminating against H-number)

Due to the lack of additional information, it is not possible to discriminate the single contribution of the branching ratio and the ROOR rate constant but inferring this global value represents an initial step providing valuable information about the leading interaction mechanisms driving accretion reaction.

Figure 45a reports the C_{20} molecules for daytime runs (empty symbols) and nighttime chemistry (dark symbols). Considering $C_{20}H_{30\text{-}34}$, the positioning of the points on the different isopleths suggests a higher efficiency in the self-reaction of AP-RO_2 molecules, which exhibits a ($\gamma_{RO2}^2 k_{ROOR}$) around $1 \cdot 10^{-13}$[molec/cm³ s]. For the AP-RO_2 released by reaction of αpinene with OH, the results exhibit faster cross-reaction between ozonolysis-AP-RO_2 and OH-AP-RO_2 (($\gamma_{RO2}^2 k_{ROOR}$) between $1 \cdot 10^{-14}$and $1 \cdot 10^{-13}$ molec/cm³s) than self-reaction between OH-generated AP-RO_2 (($\gamma_{RO2}^2 k_{ROOR}$) around $1 \cdot 10^{-14}$ molec/cm³ s). Considering night chemistry, one order of magnitude of discrepancy is recorded for self-reaction of AP-RO_2 from NO_3 chemistry and cross reaction of the same with AP-RO_2 from ozonolysis. This finding suggests that the cross reaction is faster than self- RO_2-RO_2 interactions.

For the C_{15}, Figure 45b, less evidence in terms of molecular trends is registered. In general, $C_{15}H_{24}Ox$ tend to collocate on ($\gamma_{RO2}^2 k_{ROOR}$) around $1 \cdot 10^{-13}$molec/cm³s whereas $C_{15}H_{26}Ox$ on the isopleth representing ($\gamma_{RO2}^2 k_{ROOR}$) around $1 \cdot 10^{-14}$molec/cm³s]. A subgroup of the analysed runs presents a decreasing concentration trend of $C_{15}H_{24}Ox$ and $C_{15}H_{26}Ox$ by increasing the $\tau_{bi}{}^2 PR_1 PR_2$. This trend is actually correlated with a decreasing τ_{bi} coupled with increasing OH. More investigations will be devoted in understanding the cause-effect correlation between these variables and the registered results.

Additional investigations about the key C_{15} and C_{20} clusters were carried out in terms of oxidation state. This has been here calculated as (Kroll et al., 2011b):

$$OS_c = 2\frac{O}{C} - \frac{H}{C} - 3\frac{N}{C} \qquad \text{(Eq. 31)}$$

Where O, C, H and N are the number of oxygens, carbons, hydrogens and nitrogens, respectively, of the specific molecule. Figure 46a shows the evolution of the oxidation state for C_{15} and C_{20} dimers as a

function of lifetime τ_{bi}. In general, an increase in the OS_c is registered by incrementing τ_{bi}, showing a progressive oxidation of the various compounds during time. C_{20} dimers exhibit lower OS_c values compared to C_{15}, suggesting that C_{20} compounds may be less oxidized or may contain more reduced bonds. This is likely due to their formation primarily through self-reactions of α-pinene RO_2 radicals, which generally produce less oxidized products compared to the cross-reactions responsible for the formation of C_{15} dimers. The colorbar scale shows that higher $OH:O_3$ values correspond to lower OS_c especially for C_{20}. This result suggests that in scenarios with high O_3/OH oxidation activity, the generated dimers may require time to achieve higher oxidations exhibiting lower oxidation in short lifetimes.

Figure 46b reports the double bond equivalents (DBE) against the OH concentration in the system for C_{15} and C_{20} dimers. DBE provides insight into the structural complexity of the observed molecules, indicating the number of double bonds and rings present. By examining DBE as a function of OH concentration, we can assess how increasing oxidative conditions influence molecular saturation and chemical structure.

For both C_{15} and C_{20} classes of compounds, DBE values generally decrease slightly as OH concentration increases. This trend suggests that higher OH concentrations promote partial saturation of the molecules, likely through reactions that open double bonds or rings and introduce more saturated oxygen-containing functional groups.

Notably, C_{20} dimers consistently exhibit higher DBE values (around 5.5 to 6), indicating a higher level of unsaturation or more complex cyclic structures compared to C_{15} dimers, which show DBE around 4 to 4.5. This supports the idea that C_{20} dimers, mostly formed by αpinene RO_2 self-reactions, maintain more unsaturation and structural complexity, while C_{15} dimers, formed by cross reactions, are somewhat more saturated. The color gradient suggests that the highest combined oxidant levels ($OH:O_3$) correspond to slightly lower DBE values, reinforcing the notion that more intense oxidation conditions favor saturation and functionalization over maintaining unsaturated structures.

Overall, this graph complements the oxidation state analysis, showing that oxidative aging impacts not only the oxygen content (OS_C) but also the molecular backbone saturation (DBE), with distinct behaviors between C_{15} and C_{20} dimer classes.

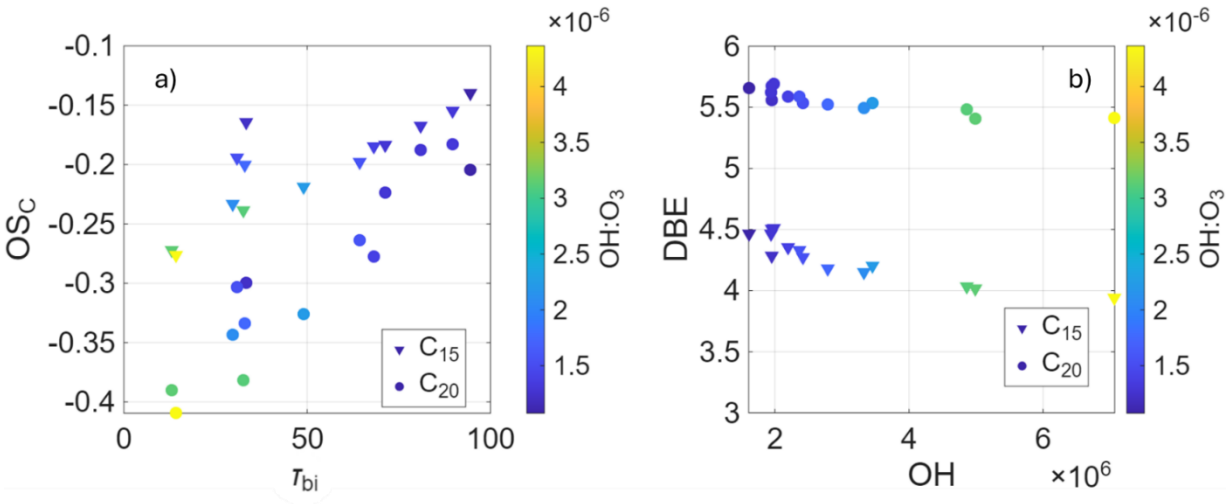

Figure 46: Details about the oxidation of the monitored dimers for daytime chemistry. Panel a) reports the oxidation state evolution against τ_{bi} for C_{15} and C_{20} coloured by the concentration ratio of the two key oxidants, O_3 and OH. Panel b) records the double bond equivalents (DBE) against OH concentration.

After investigating the composition of the compounds produced in our system, the subsequent results present the effects of these variables on NPF. Figure 47 reports the particle distribution for some AP: IP=2:4ppbv runs, having same τ_{bi} but different OH concentrations. The plot aims to highlight the effects

of varying hydroxyl radical concentrations on C_x products and, consequently, on NPF. Increased OH concentration does not only affect the concentration intensity registered by SMPS (Figure 47 Panels a and b) but its impact becomes more and more clear by monitoring the trend in particle concentration registered by the CPC. This result suggest that OH-driven oxidation is a determining factor in the formation of particles, confirming the importance of OH role in BVOC atmospheric chemistry.

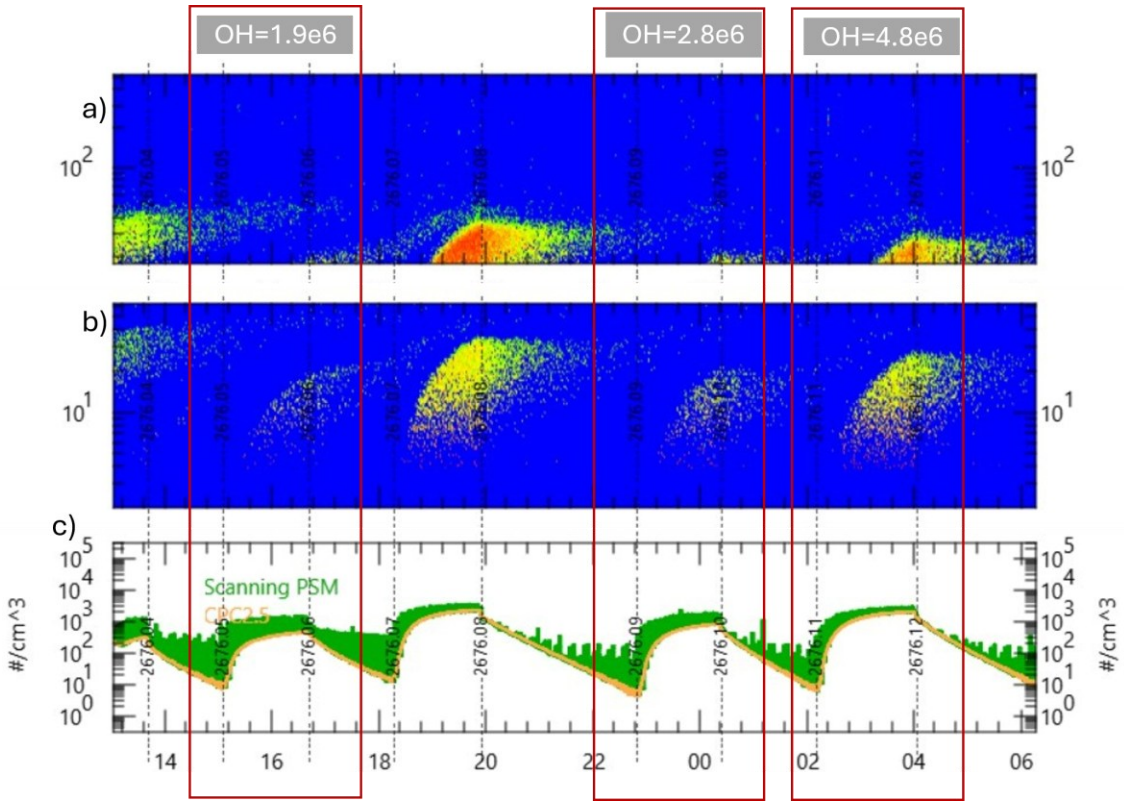

Figure 47: Panels a) and b) report the banana plots of new particle formation events showing particle diameter as a function of time, recorded by long- and nano-SMPS, respectively. The color scale represents particle number concentration. Panel c) CPC particle distribution, against time. In red three highlighted runs presenting OH concentrations equal to 1.9e6, 2.8e6 and 4.8e6 molec/cm^3

4.5.2 Suburban Scenario (AVOCs/BVOCs)

The second scenario investigates conditions mimicking a suburban environment. In this case, the complexity of the system increases due to the simultaneous presence of three precursors: isoprene, αpinene and 1,2,4-trimethylbenzene. In addition to biogenic peroxy radicals (IP-RO_2 and AP-RO_2), the oxidation of TMB introduces aromatic RO_2 species, which significantly alter the radical budget and reaction pathways. TMB-derived RO_2 radicals are generally characterized by a lower tendency toward extensive autoxidation compared to biogenic RO_2 species and are more efficiently terminated via bimolecular reactions, particularly under NO-influenced conditions. Furthermore, the introduction of TMB further enhances the competition for oxidants and RO_2 reaction partners already observed in the mixed isoprene–α-pinene system. In particular, the increased abundance of relatively short-lived aromatic RO_2 radicals shifts the balance away from self- and cross-reactions among biogenic RO_2 species, thereby affecting both monomer and dimer composition.

As for rural runs, αpinene and isoprene were injected in ratios 1.4:8 ppbv and 2:4 ppbv whereas 1,2,4-trimethylbenzene was added in concentrations ranging from 2.5 to 10 ppbv. As for the previous scenario, the temperature of the system was set equal to 25°C and NO concentration was kept lower than 1 ppb.

Monomeric Composition

The analysis of the key monomers associated with this environmental scenario is reported in Figure 48. As for rural runs, $C_{4\text{-}5}$ and C_{10} are mainly associated to isoprene and αpinene chemistry, respectively. C_9 species arise either from C_{10}-compound fragmentation or from direct TMB oxidation; the separation of these two contributions is particularly challenging.

C_4 and C_5 exhibit a lower contribution, probably due to the competition of OH reacting with either isoprene or TMB. The introduction of aromatic precursors like TMB affects the chemistry of C_9; Figure 48b shows that the greatest contributions of C_9 monomers occur in the runs 3,6 and 7, where the TMB-OH production rate is also higher. As for rural runs, C_{10} does not linearly vary with αpinene production rate, which may be explained considering that α-pinene chemistry may not be the unique reactive pathway leading to C_{10} species.

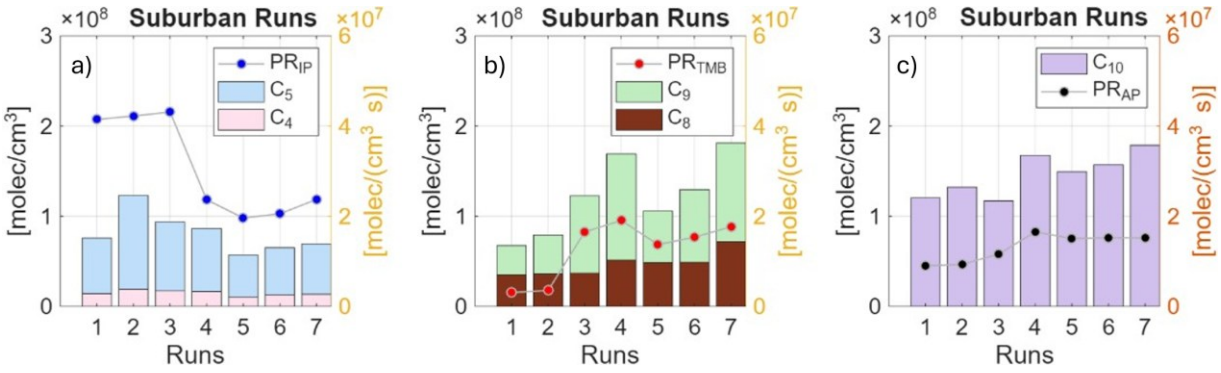

Figure 48: Concentration of some monomeric species for the suburban runs the correlated production rate. Panel a) reports the concentrations of $C_{4\text{-}5}$ against production rate of isoprene. Panel b) registers C_9 and C_8 contributions mainly associated with TMB chemistry and Panel c) correlates C_{10} concentration with AP production rate.

Different TMB concentrations were investigated, to explicit the effect of TMB addition on the composition of released compounds. Figure 49 reports the fractions of some key classes of compounds for two runs, presenting analogous OH concentrations (~$2 \cdot 10^6$ molec/cm^3), same AP:IP ratio but different TMB concentrations. The pie chart illustrates the composition of some classes of compounds over the total organic compounds with the numeric contributions summarized in Table 13. As expected, increasing TMB concentrations leads to a decrease in $C_{4\text{-}5}$ likely due to the competition between IP and TMB in reacting with OH radicals. Concurrently, C_9 increases whereas C_{10} decreases. Furthermore, a slight increase in total dimer content was also observed, resulting from enhanced cross-reactions involving TMB oxidation products.

By examining the stacked bars in Figure 49, the contributions of individual dimer species can be distinguished. All the C_9-associated species increase with higher TMB concentration, resulting in higher fractions of C_{14}, C_{18} and C_{19}, directly associated with self-and cross-TMB-C_9 reaction. Conversely, C_{20} and C_{15} exhibit a decreasing trend, reflecting the redistribution of RO_2 interactions under the influence of TMB.

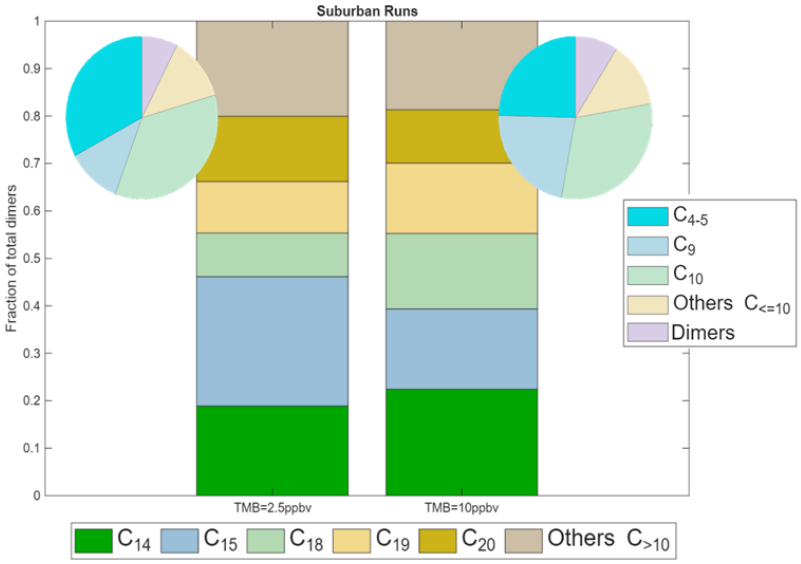

Figure 49: Effect of increasing TMB concentration on runs with same AP: IP and OH concentrations. The Pie charts report the concentration of some classes of compounds detected in the run divided by carbon atoms, whereas the bars represent the contributions of some key dimeric species to the total dimers signal

Table 13: Fractions of the Pie chart shown in Figure 49.

	TMB=2.5ppbv	**TMB=10ppbv**
C_{4-5}	32.8%	24.6%
C_9	11.5%	22.5%
C_{10}	35.2%	30.7%
Others $C_{<=10}$	12.9%	13.2%
Dimers	7.6%	9.0%

Figure 50 reports the contribution of some key C_x products over the total dimer composition. The stronger C_9 contribution for the suburban scenario associated with TMB introduction impacts the concentration of some TMB-RO_2 related dimers. In particular, a decrease of the C_{15} and C_{20} fractions over the total dimers is recorded, coupled with an increase of C_{14}, C_{18} and C_{19}. Indeed, C_{14} can be a product of cross-reactions of TMB-RO_2 and IP-RO_2, C_{18} is an accretion product of self-reaction of TMB-RO_2 and C_{19} is formed from cross-reaction of AP-RO_2 and TMB-RO_2.

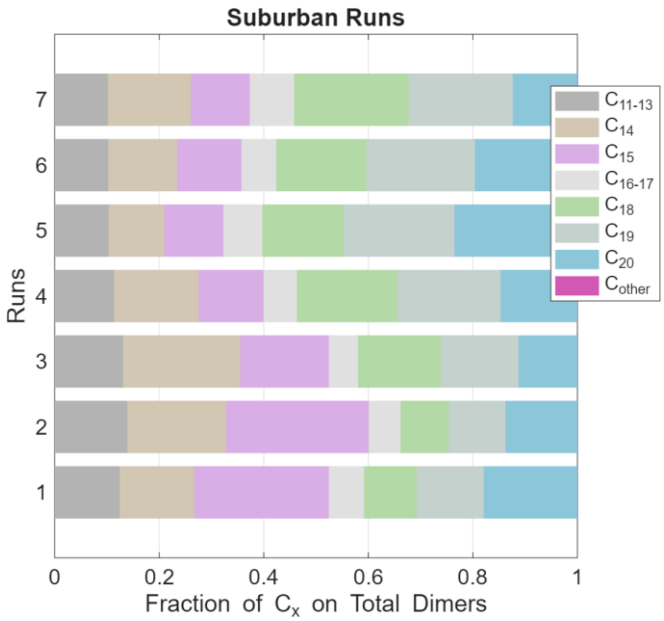

Figure 50: Fraction of C_x over total dimers in the suburban scenario

Similarly to pure BVOCs runs, the analysis of some key tracers associated with the interaction of the RO_2 present in the investigated system is proposed in Figure 51. The molecules and their reactive source are reported in Table 14.

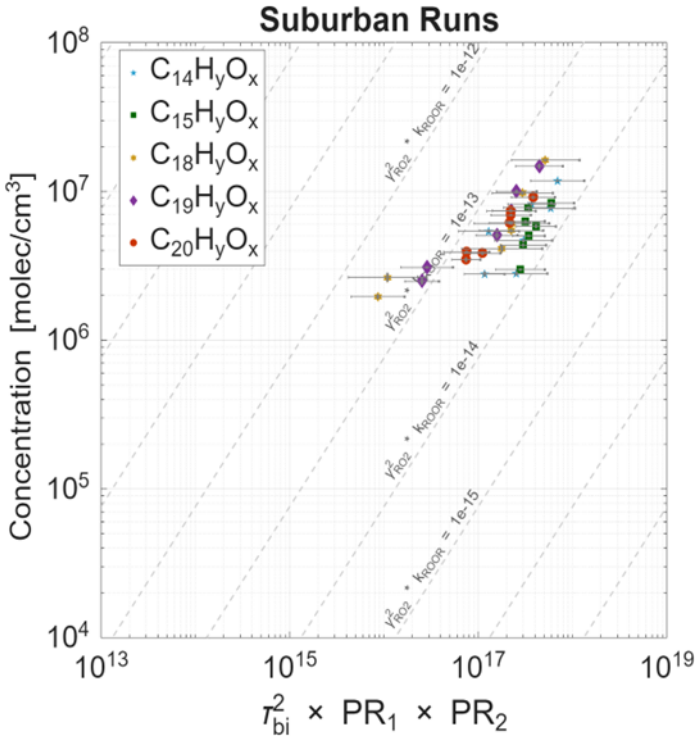

Figure 51: Isopleths plot for summed C_x contribution for dimers in suburban runs

The results highlight almost homogeneous concentrations among all the dimers, with some slight differences in the position of their contribution on the ($\gamma_{RO2}^2 k_{ROOR}$) isopleths. The dots exhibiting the lowest C_{18} and C_{19} concentrations correspond to the runs with 2.5 ppbv injected TMB, thus reflecting a limitation in precursor availability. The clustering of data points along similar isopleths may indicate that altered input variables, i.e., precursors concentrations, oxidants availability, bimolecular lifetime, primarily impact the overall concentrations rather than on the RO_2 recombination efficiency. Thus,

variations in the experimental conditions primarily affect the absolute dimer yields rather than altering the underlying formation regime.

In this case, the PRs for each C_x were calculated according to the parent molecule as reported in Table 14:

Table 14: Key C_x compounds for dimers and their parent RO_2 radical

C_x-compound	**Parent RO_2 (1)**	**Parent RO_2 (2)**
$C_{14}H_yO_x$	$C_5H_yO_x$ as IP-RO_2	$C_9H_yO_x$ as TMB-RO_2
$C_{15}H_yO_x$	$C_{10}H_yO_x$ as AP-RO_2	$C_5H_yO_x$ as IP-RO_2
$C_{18}H_yO_x$	$C_9H_yO_x$ as TMB-RO_2	$C_9H_yO_x$ as TMB-RO_2
$C_{19}H_yO_x$	$C_{10}H_yO_x$ as AP-RO_2	$C_9H_yO_x$ as TMB-RO_2
$C_{20}H_yO_x$	$C_{10}H_yO_x$ as AP-RO_2	$C_{10}H_yO_x$ as AP-RO_2

New Particle Formation

After analysing the key ROOR accretion products, the NPF tendency for each run was investigated to identify the key variables controlling atmospheric particle growth.

Figure 52 illustrates the NPF evolution derived from SMPS measurements (long and nano DMA, in Figure 52a and Figure 52b, respectively) together with the particle number concentrations registered by the CPC (Figure 52c). The three runs are characterized by progressively increasing OH concentrations, reported at the top of the panels in molecules·cm^{-3}. The pie charts (Figure 52d) associated with each run show that an increase in the OH concentration leads to pronounced changes in the chemical composition, particularly in the contribution of dimers. Specifically, the fraction of dimers to the total organic compounds systematically increases with increasing OH concentrations. Considering the monomeric species contribution, higher OH levels result in an enhanced contribution from C_4-C_5 compounds, consistent with the increased availability of hydroxy radicals coupled with the reduced competition between isoprene-OH driven chemistry and TMB-OH oxidation pathways. Furthermore, C_9-C_{10} fractions also increase primarily due to enhanced C_9 chemistry under high-OH conditions. Although not shown in this section, the contribution of individual carbon-number classes to the total dimers reveals an increase in cross-RO_2 reaction products (i.e., C_{14}, C_{18}, and C_{19}) with increasing OH, accompanied by a slight decrease in C_{20}. These compositional alterations are coherent with the observed NPF trend, indicating that enhanced OH concentrations promote more efficient oxidation and accretion processes, ultimately strengthening particle growth and new particle formation.

It is important to note that the relationship between dimer concentration and new particle formation (NPF) is not a straightforward direct correlation, as the volatility of the dimers plays a crucial mediating role in particle growth and stability. Therefore, a higher abundance of dimers does not necessarily imply increased NPF without considering their chemical composition and volatility. This initial analysis provides valuable insight into the evolving chemical landscape, but further detailed investigations are needed to fully elucidate the mechanistic links between dimer characteristics and NPF processes.

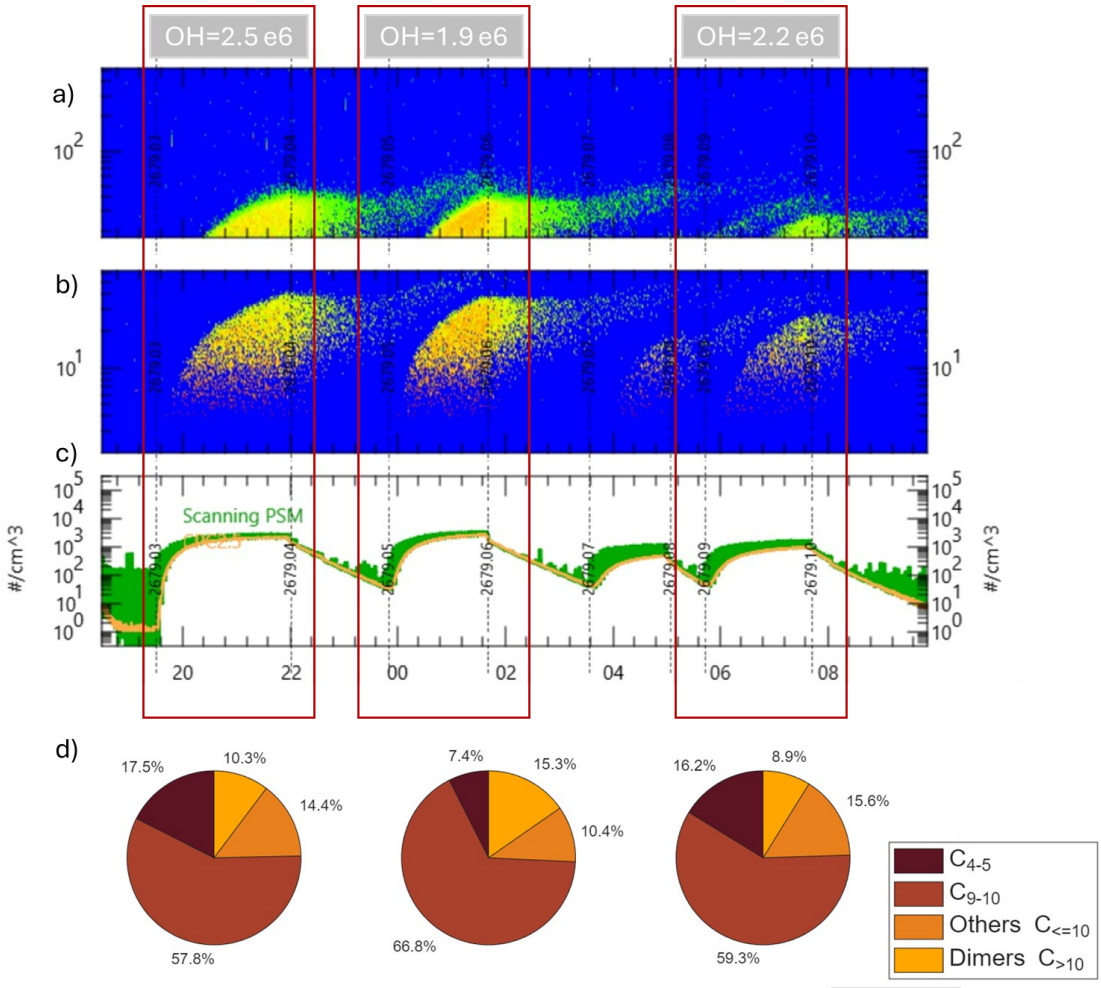

Figure 52: New Particle Formation plot for Suburban runs. Panel a) reports the banana plot registered by Long-SMPS, panel b) reports the plot recorded by nanoSMPS, panel c) particle counting by CPC and panel d) the corresponding key contribution to the composition of the selected runs, highlighted in red.

4.5.3 Urban Scenario

This last chapter focuses on the investigation of an urban-like scenario. In these experiments, naphthalene, toluene, and trimethylbenzene were injected into the CLOUD chambers in different concentrations, and the runs were carried out with a temperature of the system equal to 20°C.

The Spearman correlation matrix for these runs is reported in Figure 53. The shown matrix for the urban runs reveals a strongly oxidant-driven chemical regime, dominated by OH chemistry. OH radicals show a significantly positive correlation with most of carbon-number resolved C_x classes, particularly from C_9 to C_{20}, indicating that secondary formation and molecular growth are primarily controlled by oxidation intensity rather than precursor abundance alone. O_3 exhibits a similar, though slightly weaker, correlation pattern, consistent with a photochemically mature urban environment. The negative correlation of the chemical lifetime τ_{bi}, with OH, production rates and high-carbon-containing classes, highlight faster chemical processes under high-oxidant conditions. The production rates derived from different aromatic precursors are strongly intercorrelated but show subtle differences in their association with carbon-number classes: naphthalene-related production is more closely linked to $C_{14\text{-}20}$ species, while TOL and TMB contribute more broadly to intermediate carbon ranges (C_9 to C_{14}). Lower-carbon classes, up to C_9, exhibit weaker correlations with oxidants, indicative of fresher or less processed material, whereas higher-carbon classes C_{16}-C_{20} are tightly intercorrelated and strongly

associated with OH-driven chemistry, characteristic of advanced secondary processing in urban atmospheres.

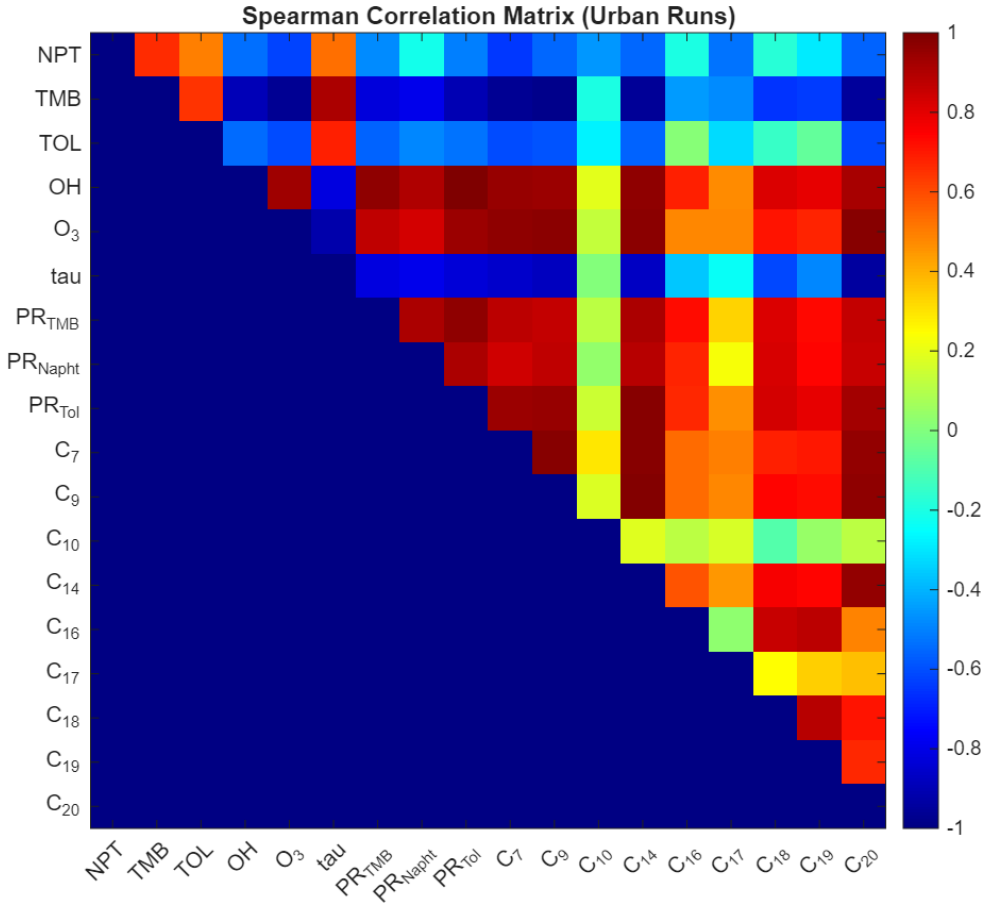

Figure 53: Spearman correlation coefficient matrix for Urban Runs

Figure 54 reports the positioning of the dimers C_x classes on the isopleth-defined plotting space. The source of each C_x contribution is reported in Table 15. The concentrations of the various investigated compounds show that, in general, C_{14} and C_{17} species exhibit higher concentrations. This may be related to the high reactivity of naphthalene toward OH radicals, which leads to increased production of NPT-RO_2 radicals. Once formed, these radicals may react with higher efficiency through self-reaction or cross-reaction with TOL-RO_2, explaining the higher concentrations and higher values of the branching ratio product with reaction constant ($\gamma_{RO2}^2 k_{ROOR}$). C_{20} cluster also exhibit high values of ($\gamma_{RO2}^2 k_{ROOR}$), which may confirm the fast reactivity of NPT-RO_2 radicals. TMB-related RO_2 exhibit instead lower ($\gamma_{RO2}^2 k_{ROOR}$) values, calculated around $1 \cdot 10^{-13}$ $cm^3 \cdot molec^{-1}$.

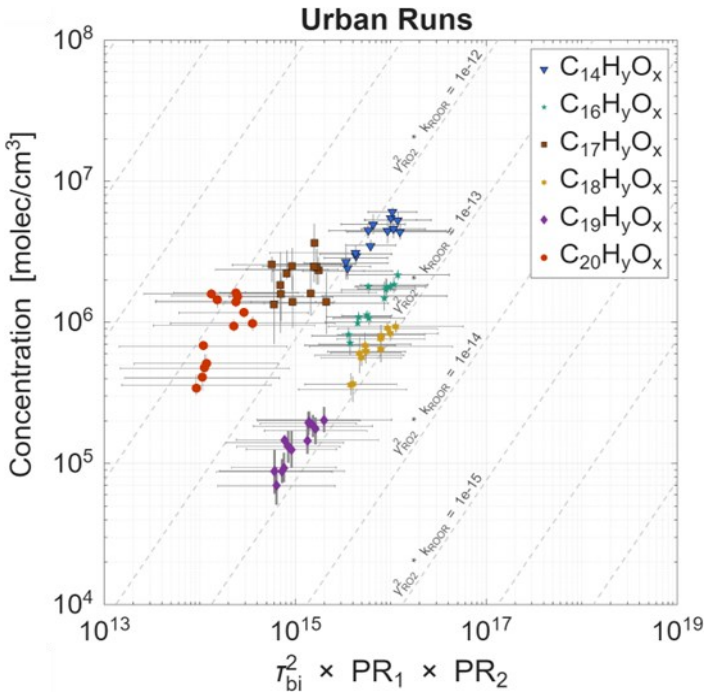

Figure 54: Isopleth plot reporting the various contribution of C_x dimers in urban runs.

Table 15 records the RO_2 source of each dimeric class reported in Figure 54. Further investigations will be conducted to monitor the atmospheric evolution of specific C_x compounds divided by hydrogen number so to infer the interaction tendencies among different RO_2 molecules.

Table 15: C_x contribution for the Urban runs and correlated C_x contribution

C_x-compound	**Parent RO_2 (1)**	**Parent RO_2 (2)**
$C_{14}H_yO_x$	$C_7H_yO_x$ as TOL-RO_2	$C_7H_yO_x$ as TOL-RO_2
$C_{16}H_yO_x$	$C_9H_yO_x$ as TMB-RO_2	$C_7H_yO_x$ as TOL-RO_2
$C_{17}H_yO_x$	$C_7H_yO_x$ as NPT-RO_2	$C_7H_yO_x$ as TOL-RO_2
$C_{18}H_yO_x$	$C_9H_yO_x$ as TMB-RO_2	$C_9H_yO_x$ as TMB-RO_2
$C_{19}H_yO_x$	$C_7H_yO_x$ as NPT-RO_2	$C_9H_yO_x$ as TMB-RO_2
$C_{20}H_yO_x$	$C_7H_yO_x$ as NPT-RO_2	$C_7H_yO_x$ as NPT-RO_2

NPF trends for urban runs are not reported in this section because they are currently under investigation.

By considering Figures 44, 51, and 54, it is possible to compare the results in terms of the chemical regimes dominating the different scenarios. In the rural runs, the investigated C_{15} and C_{20} dimers are mostly aligned along specific isopleths, indicating a chemistry dominated by autoxidation and efficient ROOR formation. The limited dispersion of the data suggests relatively uniform kinetic control.

In the suburban runs, the distribution becomes less homogeneous. The simultaneous presence of biogenic and anthropogenic precursors induces increased competition among reactive channels; however, the overall tendency remains consistent with the theoretical framework, confirming the combined parameter as a reliable predictor.

A systematic shift towards lower values of $\tau_{bi}^2 \times PR_1 \times PR_2$ observed in the urban runs reflects a reduced efficiency of molecular accretion and RO_2–RO_2 recombination leading to ROOR formation. This behavior may be attributed to RO_2 structures that are less prone to autoxidation and more likely to undergo competing reaction pathways.

4.6 Conclusions

In this chapter, the investigation of RO_2-RO_2 interactions in different atmospherically relevant scenarios is proposed. For each case study, the chemistry of the system correlated with monomers and dimers analysis, with further investigation on the ROOR formation, and, eventually, NPF is investigated. The study was performed using CLOUD Chamber at CERN, Geneva. This facility allowed the mimicking of extremely controlled, realistic scenarios, using a complex light system to replicate both daytime and nighttime chemistry. The calculation of some key parameters, τ_{bi}, β, and oxidation state, allowed us to study the variables driving RO_2-RO_2 interactions.

Rural runs were conducted by injecting αpinene and isoprene into CLOUD chamber, using biogenic ratios (AP:IP) ranging from 1.4:8 ppbv to 2:4 ppbv, coherently concentrations of pristine environments and remote forests. Across all experimental conditions, NO concentration was maintained below 1 ppbv. Preliminary investigations showed how even such low NO levels can influence RO_2 chemistry, generally affecting the monomer-to-dimer ratio.

Regarding precursors oxidation, results showed that isoprene rapidly consumes OH radicals, thereby limiting OH availability for αpinene oxidation and, consequently, altering radical chemistry of the system. $C_{4\text{-}5}$ and $C_{9\text{-}10}$ contributions to total organic compounds are estimated as key monomeric species linked to IP and AP oxidation, respectively. Through the formulation of a detailed balance equation mechanism, it was possible to constrain the range of branching ratio and accretion rate constants responsible for the formation of some key tracers dimers. After quantifying the contributions of various dimers to the system, particularly C_{15} and C_{20}, the attribution of some key dimers to specific oxidative pathways was examined, revealing distinct tendencies for each RO_2 to undergo either self- or cross-reactions with other radicals. Oxidative aging was found to increase the oxidation state, promoting molecular saturation, as indicated by lower values of double-bond equivalents. Finally, NPF trends were presented, highlighting OH concentration as a critical factor affecting particle formation from BVOCs.

Suburban experiments aim at replicating the atmospheric scenario that can be found in a suburban area of a big city, thus αpinene and isoprene injection was coupled with 1,2,4-trimethylbenzene introduction in concentrations spanning from 2.5 to 10 ppbv. The main effect induced by TMB addition is related to the presence of AVOC- RO_2 that compete with biogenic peroxy radials for oxidants and reaction partners, thus reducing self- and cross reactions among BVOCs. Looking at the monomer composition, the contribution C_9 in this case can not only be attributed to αpinene fragmentation but also from TMB oxidation and fragmentation, complicating source attribution. Results showed that increased TMB concentration decrease $C_{4\text{-}5}$ and C_{10} fractions due to competitive OH consumption. TMB addition also affects the dimers composition: C_{14}, C_{18} and C_{19} (derived by self- and cross- reactions of TMB-RO_2) exhibit increased concentrations whereas, C_{15} and C_{20} contribution results suppressed. Also in this case, higher OH concentrations enhance oxidation by increasing both monomers and dimers formation and supporting particle growth. The comparison of three experimental conditions shows that greater oxidation and accretion efficiency when OH increases. The relationship between dimers and NPF is mediated by volatility, thus further research to calculate the contribution of each C_x to volatility basis set is actually under investigation. In conclusion. TMB-RO_2 are short-lived, favour bimolecular termination, and alter the radical pool, highlighting the non-additive and competitive nature of mixed precursor systems in suburban-like atmospheres.

The last investigated scenario mimics a highly polluted urban environment, replicated by injecting naphthalene, trimethylbenzene and toluene within CLOUD chamber. These runs exhibit a chemical regime dominated by OH oxidation, with oxidative intensity driving new particle formation and molecular growth. In particular, the analysis of the dimers composition exhibits a strong correlation of molecules with a high carbon skeleton ($C_{16\text{-}20}$) and OH-driven chemistry. Although NPF data are still under investigation, these preliminary results suggest that interactions among different RO_2 radicals

play a key role in controlling secondary chemistry and particle formation pathways in urban-like atmospheres.

4.7 Further Steps

The next steps of this work will focus on estimating the volatility of the compounds formed in each experimental scenario, through the volatility basis set (VBS) framework. Since current VBS schemes are typically developed for either biogenic or anthropogenic precursors, this approach will help address the uncertainties associated with cross-RO_2 dimers formed after the interaction of AVOCs-RO_2 and BVOCs-RO_2. Furthermore, additional efforts will be devoted to the discrimination of the contributions of RO_2 branching ratio and the reaction rate constant, allowing a more quantitative assessment of the role of RO_2-RO_2 interactions in dimer formation and molecular growth.

4.8 References

Almeida T., Johansen S., Golin Almeida T., Martì C., Kurté T., Zà J. (2024). Theoretical Analysis of the OH-initiated atmospheric oxidation reactions of imidazole Theoretical analysis of the OH-initiated atmospheric oxidation reactions of imidazole. Physical Chemistry Chemical Physics, 26, 23570-23587, https://doi.org/10.1039/d4cp02103g

Andersen, S. T., Carpenter, L. J., Nelson, B. S., Neves, L., Read, K. A., Reed, C., Ward, M., Rowlinson, M. J., & Lee, J. D. (2021). Long-term NO x measurements in the remote marine tropical troposphere. Atmos. Meas. Tech, 14, 3071–3085. https://doi.org/10.5194/amt-14-3071-2021

Andreae, M. O., Acevedo, O. C., Araùjo, A., Artaxo, P., Barbosa, C. G. G., Barbosa, H. M. J., Brito, J., Carbone, S., Chi, X., Cintra, B. B. L., Da Silva, N. F., Dias, N. L., Dias-Júnior, C. Q., Ditas, F., Ditz, R., Godoi, A. F. L., Godoi, R. H. M., Heimann, M., Hoffmann, T., Yáñez-Serrano, A. M. (2015). The Amazon Tall Tower Observatory (ATTO): Overview of pilot measurements on ecosystem ecology, meteorology, trace gases, and aerosols. Atmospheric Chemistry and Physics, 15(18), 10723–10776. https://doi.org/10.5194/ACP-15-10723-2015

Atkinson, R. (2000). Atmospheric chemistry of VOCs and NOx. Atmospheric Environment, 34(12–14), 2063–2101. https://doi.org/10.1016/S1352-2310(99)00460-4

Atkinson, R., & Arey, J. (2003). Atmospheric Degradation of Volatile Organic Compounds. Chemical Reviews, 103(12), 4605–4638. https://doi.org/10.1021/CR0206420

Atkinson, R., Baulch, D. L., Cox, R. A., Crowley, J. N., Hampson, R. F., Hynes, R. G., Jenkin, M. E., Rossi, M. J., & Troe, J. (2006). Atmospheric Chemistry and Physics Evaluated kinetic and photochemical data for atmospheric chemistry: Volume II-gas phase reactions of organic species The IUPAC Subcommittee on Gas Kinetic Data Evaluation for Atmospheric Chemistry. In Atmos. Chem. Phys (Vol. 6). www.atmos-chem-phys.net/6/3625/2006/

Bates, K. H., Burke, G. J. P., Cope, J. D., & Nguyen, T. B. (2021). The nitrate radical (NO 3) oxidation of alpha-pinene is a significant source of secondary organic aerosol and organic nitrogen under simulated ambient nighttime conditions. https://doi.org/10.5194/ACP-2021-703

Bates, K. H., & Jacob, D. J. (2019). A new model mechanism for atmospheric oxidation of isoprene: Global effects on oxidants, nitrogen oxides, organic products, and secondary organic aerosol. Atmospheric Chemistry and Physics, 19(14), 9613–9640. https://doi.org/10.5194/ACP-19-9613-2019

Batterman, S. A., Peng, C. Y., & Braun, J. (2002). Levels and composition of volatile organic compounds on commuting routes in Detroit, Michigan. Atmospheric Environment, 36(39–40), 6015–6030. https://doi.org/10.1016/S1352-2310(02)00770-7

Beauregard, D. (1994). LOCATING AND ESTIMATING AIR EMISSIONS FROM SOURCES OF TOLUENE Final Report Prepared for Environmental Protection Agency, EPA-454/R-93-047.

Berndt, T., Hoffmann, E. H., Tilgner, A., & Herrmann, H. (2025). Highly oxidized products from the atmospheric reaction of hydroxyl radicals with isoprene. Nature Communications 2025 16:1, 16(1), 2068-. https://doi.org/10.1038/s41467-025-57336-1

Berndt, T., Richters, S., Jokinen, T., Hyttinen, N., Kurtén, T., Otkjær, R. V., Kjaergaard, H. G., Stratmann, F., Herrmann, H., Sipilä, M., Kulmala, M., & Ehn, M. (2016). Hydroxyl radical-induced formation of highly oxidized organic compounds. Nature Communications 2016 7:1, 7(1), 13677-. https://doi.org/10.1038/ncomms13677

Berndt, T., Richters, S., Kaethner, R., Voigtländer, J., Stratmann, F., Sipilä, M., Kulmala, M., & Herrmann, H. (2015). Gas-Phase Ozonolysis of Cycloalkenes: Formation of Highly Oxidized RO2 Radicals and Their Reactions with NO, NO2, SO2, and Other RO2 Radicals. Journal of Physical Chemistry A, 119(41), 10336–10348. https://doi.org/10.1021/ACS.JPCA.5B07295

Berndt, T., Scholz, W., Mentler, B., Fischer, L., Herrmann, H., Kulmala, M., & Hansel, A. (2018). Accretion Product Formation from Self- and Cross-Reactions of RO2 Radicals in the Atmosphere. Angewandte Chemie - International Edition, 57(14), 3820–3824. https://doi.org/10.1002/ANIE.201710989

Bianchi, F., Kurtén, T., Riva, M., Mohr, C., Rissanen, M. P., Roldin, P., Berndt, T., Crounse, J. D., Wennberg, P. O., Mentel, T. F., Wildt, J., Junninen, H., Jokinen, T., Kulmala, M., Worsnop, D. R., Thornton, J. A., Donahue, N., Kjaergaard, H. G., & Ehn, M. (2019). Highly Oxygenated Organic Molecules (HOM) from Gas-Phase Autoxidation Involving Peroxy Radicals: A Key Contributor to Atmospheric Aerosol. Chemical Reviews, 119(6), 3472–3509. https://doi.org/10.1021/ACS.CHEMREV.8B00395

Bloss, C., Wagner, V., Jenkin, M. E., Volkamer, R., Bloss, W. J., Lee, J. D., Heard, D. E., Wirtz, K., Martin-Reviejo, M., Rea, G., Wenger, J. C., & Pilling, M. J. (2005). Development of a detailed chemical mechanism (MCMv3.1) for the atmospheric oxidation of aromatic hydrocarbons. Atmos. Chem. Phys, 5, 641–664. www.atmos-chem-phys.org/acp/5/641/SRef-ID:1680-7324/acp/2005-5-641EuropeanGeosciencesUnion

Bohn, B., & Zetzsch, C. (2012). Kinetics and mechanism of the reaction of OH with the trimethylbenzenes – experimental evidence for the formation of adduct isomers. Physical Chemistry Chemical Physics, 14(40), 13933–13948. https://doi.org/10.1039/C2CP42434G

Calvert, J. G., Atkinson, R., Becker, K. H., Kamens, R. M., Seinfeld, J. H., Wallington, T. J., & Yarwood, G. (2002a). Reactions Of Ozone With Aromatic Compounds. The Mechanisms Of Atmospheric Oxidation Of Aromatic Hydrocarbons, 167–189. https://doi.org/10.1093/OSO/9780195146288.003.0004

Calvert, J. G., Atkinson, R., Becker, K. H., Kamens, R. M., Seinfeld, J. H., Wallington, T. J., & Yarwood, G. (2002b). Reactions Of Ozone With Aromatic Compounds. The Mechanisms Of Atmospheric Oxidation Of Aromatic Hydrocarbons, 167–189. https://doi.org/10.1093/OSO/9780195146288.003.0004

Calvert, J. G., Orlando, J. J., Stockwell, W. R., & Wallington, T. J. (2015). Mechanisms of Reactions of HO2 and RO2 Radicals. The Mechanisms of Reactions Influencing Atmospheric Ozone. https://doi.org/10.1093/OSO/9780190233020.003.0008

Carter, W. P. L., & Heo, G. (2012). DEVELOPMENT OF REVISED SAPRC AROMATICS MECHANISMS.

Chan, A. W. H., Kautzman, K. E., Chhabra, P. S., Surratt, J. D., Chan, M. N., Crounse, J. D., Kürten, A., Wennberg, P. O., Flagan, R. C., & Seinfeld, J. H. (2009). Secondary organic aerosol formation from photooxidation of naphthalene and alkylnaphthalenes: Implications for oxidation of intermediate volatility organic compounds (IVOCs). Atmospheric Chemistry and Physics, 9(9), 3049–3060. https://doi.org/10.5194/ACP-9-3049-2009

Chen, T., Zhang, P., Chu, B., & al., et. (2022). Secondary organic aerosol formation from mixed volatile organic compounds: Effect of RO2 chemistry and precursor concentration. Npj Climate and Atmospheric Science, 5, 95. https://doi.org/10.1038/s41612-022-00321-y

Crounse, J. D., Nielsen, L. B., Jørgensen, S., Kjaergaard, H. G., & Wennberg, P. O. (2013). Autoxidation of organic compounds in the atmosphere. Journal of Physical Chemistry Letters, 4(20), 3513–3520. https://doi.org/10.1021/JZ4019207

Crutzen, P. J., Lawrence, M. G., & Pöschl, U. (1999). On the background photochemistry of tropospheric ozone. Tellus B: Chemical and Physical Meteorology, 51(1), 123. https://doi.org/10.3402/TELLUSB.V51I1.16264

Dada, L., Lehtipalo, K., Kontkanen, J., Nieminen, T., Baalbaki, R., Ahonen, L., Duplissy, J., Yan, C., Chu, B., Petäjä, T., Lehtinen, K., Kerminen, V. M., Kulmala, M., & Kangasluoma, J. (2020). Formation and growth of sub-3-nm aerosol particles in experimental chambers. Nature Protocols, 15(3), 1013–1040. https://doi.org/10.1038/s41596-019-0274-z

Dada, L., Stolzenburg, D., Simon, M., Fischer, L., Heinritzi, M., Wang, M., Xiao, M., Vogel, A. L., Ahonen, L., Amorim, A., Baalbaki, R., Baccarini, A., Baltensperger, U., Bianchi, F., Daellenbach, K. R., DeVivo, J., Dias, A., Dommen, J., Duplissy, J., … Kulmala, M. (2023). Role of sesquiterpenes in biogenic new particle formation. Science Advances, 9(36). https://doi.org/10.1126/SCIADV.ADI5297

D'Ambro, E. L., Lee, B. H., Liu, J., Shilling, J. E., Gaston, C. J., Lopez-Hilfiker, F. D., Schobesberger, S., Zaveri, R. A., Mohr, C., Lutz, A., Zhang, Z., Gold, A., Surratt, J. D., Rivera-Rios, J. C., Keutsch, F. N., & Thornton, J. A. (2017). Molecular composition and volatility of isoprene photochemical oxidation secondary organic aerosol under low- and high-NOx conditions. Atmospheric Chemistry and Physics, 17(1), 159–174. https://doi.org/10.5194/ACP-17-159-2017

Dong, Z., Tang, R., Liu, H., Zhang, Q., Zong, W., Cheng, J., & Shi, X. (2023). The formation mechanism of highly oxygenated organic molecules produced by toluene in the urban atmosphere. Atmospheric Environment, 295, 119555. https://doi.org/10.1016/J.ATMOSENV.2022.119555

dos Santos, T. C., Dominutti, P., Pedrosa, G. S., Coelho, M. S., Nogueira, T., Borbon, A., Souza, S. R., & Fornaro, A. (2022). Isoprene in urban Atlantic forests: Variability, origin, and implications on the air quality of a subtropical megacity. Science of the Total Environment, 824. https://doi.org/10.1016/j.scitotenv.2022.153728

Dusanter, S., Vimal, D., Stevens, P. S., Volkamer, R., Molina, L. T., Baker, A., Meinardi, S., Blake, D., Sheehy, P., Merten, A., Zhang, R., Zheng, J., Fortner, E. C., Junkermann, W., Dubey, M., Rahn, T., Lewandowski, P., Prueger, J., & Holder, H. (2009). Atmospheric Chemistry and Physics Measurements of OH and HO 2 concentrations during the MCMA-2006 field campaign-Part 2: Model comparison and radical budget. Atmos. Chem. Phys, 9, 6655–6675. www.atmos-chem-phys.net/9/6655/2009/

Eddingsaas, N. C., Loza, C. L., Yee, L. D., Chan, M., Schilling, K. A., Chhabra, P. S., Seinfeld, J. H., & Wennberg, P. O. (2012). Atmospheric Chemistry and Physics α-pinene photooxidation under controlled chemical conditions-Part 2: SOA yield and composition in low-and high-NO x environments. Atmos. Chem. Phys, 12, 7413–7427. https://doi.org/10.5194/acp-12-7413-2012

Ehn, M., Thornton, J. A., Kleist, E., Sipilä, M., Junninen, H., Pullinen, I., Springer, M., Rubach, F., Tillmann, R., Lee, B., Lopez-Hilfiker, F., Andres, S., Acir, I. H., Rissanen, M., Jokinen, T., Schobesberger, S., Kangasluoma, J., Kontkanen, J., Nieminen, T., … Mentel, T. F. (2014). A large source of low-volatility secondary organic aerosol. Nature 2014 506:7489, 506(7489), 476–479. https://doi.org/10.1038/nature13032

El-Sayed, M. M., Ortiz-Montalvo, D. L., Hennigan, C. J., & H El-Sayed, M. M. (2018). The Effects of Isoprene and NOx on Secondary Organic Aerosols Formed Through Reversible and Irreversible Uptake to Aerosol Water. Atmospheric Chemistry and Physics, 18(2), 1171. https://doi.org/https://doi.org/10.5194/acp-18-1171-2018

Finlayson-Pitts, B. J., & Pitts, J. N. Jr. (2000). Chemistry of the Upper and Lower Atmosphere. Chemistry of the Upper and Lower Atmosphere. https://doi.org/10.1016/B978-0-12-257060-5.X5000-X

Friedrich, R., & Obermeier, A. (1999a). Anthropogenic Emissions of Volatile Organic Compounds. Reactive Hydrocarbons in the Atmosphere, 1–39. https://doi.org/10.1016/B978-012346240-4/50002-3

Garmash, O., Rissanen, M. P., Pullinen, I., Schmitt, S., Kausiala, O., Tillmann, R., Zhao, D., Percival, C., Bannan, T. J., Priestley, M., Hallquist, Å. M., Kleist, E., Kiendler-Scharr, A., Hallquist, M., Berndt, T., McFiggans, G., Wildt, J., Mentel, T. F., Ehn, M., & Garmash olgagarmash, O. (2020). Multi-generation OH oxidation as a source for highly oxygenated organic molecules from aromatics. Atmos. Chem. Phys, 20, 515–537. https://doi.org/10.5194/acp-20-515-2020

Gkatzelis, G. I., Coggon, M. M., McDonald, B. C., Peischl, J., Gilman, J. B., Aikin, K. C., Robinson, M. A., Canonaco, F., Prevot, A. S. H., Trainer, M., & Warneke, C. (2021). Observations Confirm that Volatile Chemical Products Are a Major Source of Petrochemical Emissions in U.S. Cities. Environmental Science & Technology, 55(8), 4332–4343. https://doi.org/10.1021/ACS.EST.0C05471

Glowacki, D. R., Wang, L., & Pilling, M. J. (2009). Evidence of Formation of Bicyclic Species in the Early Stages of Atmospheric Benzene Oxidation. Journal of Physical Chemistry A, 113(18), 5385–5396. https://doi.org/10.1021/JP9001466

Guenther, A. (1995). A global model of natural volatile organic compound emissions. Journal of Geophysical Research, 100(D5), 8873–8892. https://doi.org/10.1029/94JD02950;WGROUP:STRING:PUBLICATION

Hallquist, M., Wenger, J. C., Baltensperger, U., Rudich, Y., Simpson, D., Claeys, M., Dommen, J., Donahue, N. M., George, C., Goldstein, A. H., Hamilton, J. F., Herrmann, H., Hoffmann, T., Iinuma, Y., Jang, M., Jenkin, M. E., Jimenez, J. L., Kiendler-Scharr, A., Maenhaut, W., … Wildt, J. (2009). The formation, properties and impact of secondary organic aerosol: Current and emerging issues. Atmospheric Chemistry and Physics, 9(14), 5155–5236. https://doi.org/10.5194/ACP-9-5155-2009

Hantschke, L., Novelli, A., Bohn, B., Cho, C., Reimer, D., Rohrer, F., Tillmann, R., Glowania, M., Hofzumahaus, A., Kiendler-Scharr, A., Wahner, A., & Fuchs, H. (2021). Atmospheric photooxidation and ozonolysis of "3-carene and

3-caronaldehyde: Rate constants and product yields. Atmospheric Chemistry and Physics, 21(16), 12665–12685. https://doi.org/10.5194/ACP-21-12665-2021

Heald, C. L., Henze, D. K., Horowitz, L. W., Feddema, J., Lamarque, J. F., Guenther, A., Hess, P. G., Vitt, F., Seinfeld, J. H., Godstein, A. H., & Fung, I. (2008). Predicted change in global secondary organic aerosol concentrations in response to future climate, emissions, and land use change. Journal of Geophysical Research Atmospheres, 113(5), 5211. https://doi.org/10.1029/2007JD009092;REQUESTEDJOURNAL:JOURNAL:21562202D;PAGE:STRING:ARTICLE/CHAPTER

Henze, D. K., & Seinfeld, J. H. (2006). Global secondary organic aerosol from isoprene oxidation. Geophysical Research Letters, 33(9), 9812. https://doi.org/10.1029/2006GL025976;SUBPAGE:STRING:FULL

Huang, L., Zhao, B., Wang, S., Chang, X., Klimont, Z., Huang, G., Zheng, H., & Hao, J. (2023). Global Anthropogenic Emissions of Full-Volatility Organic Compounds. Environmental Science & Technology, 57(43), 16435–16445. https://doi.org/10.1021/ACS.EST.3C04106

Huang, W., Junninen, H., Garmash, O., Lehtipalo, K., Stolzenburg, D., Lampilahti, J. L. P., Ezhova, E., Schallhart, S., Rantala, P., Aliaga, D., Ahonen, L., Sulo, J., Quéléver, L. L. J., Cai, R., Alekseychik, P., Mazon, S. B., Yao, L., Blichner, S. M., Zha, Q., Bianchi, F. (2024). Potential pre-industrial-like new particle formation induced by pure biogenic organic vapors in Finnish peatland. Science Advances, 10(14), 9191. https://doi.org/10.1126/SCIADV.ADM9191

Heinritzi, M., Dada, L., Simon, M., Stolzenburg, D., Wagner, A. C., Fischer, L., Ahonen, L. R., Amanatidis, S., Baalbaki, R., Baccarini, A., Bauer, P. S., Baumgartner, B., Bianchi, F., Brilke, S., Chen, D., Chiu, R., Dias, A., Dommen, J., Duplissy, J., … Curtius, J. (2020). Molecular understanding of the suppression of new-particle formation by isoprene. Atmospheric Chemistry and Physics, 20(20), 11809–11821. https://doi.org/10.5194/ACP-20-11809-2020

Janyasuthiwong, S., Choomanee, P., Bualert, S., Maneejantra, S., Charoenpun, T., Chommon, W., & Jitjun, S. (2022). Biogenic volatile organic compound emission from tropical plants in relation to temperature changes. Environmental Challenges, 9, 100643. https://doi.org/10.1016/J.ENVC.2022.100643

Jenkin, M. E., Saunders, S. M., Wagner, V., & Pilling, M. J. (2003b). Atmospheric Chemistry and Physics Protocol for the development of the Master Chemical Mechanism, MCM v3 (Part B): tropospheric degradation of aromatic volatile organic compounds. Atmos. Chem. Phys, 3, 181–193. www.atmos-chem-phys.org/acp/3/181/

Jenkin, M. E., Valorso, R., Aumont, B., & Rickard, A. R. (2019). Estimation of rate coefficients and branching ratios for reactions of organic peroxy radicals for use in automated mechanism construction. Atmospheric Chemistry and Physics, 19(11), 7691–7717. https://doi.org/10.5194/ACP-19-7691-2019

Jenkin, M. E., Young, J. C., & Rickard, A. R. (2015). The MCM v3.3.1 degradation scheme for isoprene. Atmospheric Chemistry and Physics, 15(20), 11433–11459. https://doi.org/10.5194/ACP-15-11433-2015

Jia, C., Batterman, S., Jia, C., & Batterman, S. (2010). A Critical Review of Naphthalene Sources and Exposures Relevant to Indoor and Outdoor Air. International Journal of Environmental Research and Public Health 2010, Vol. 7, Pages 2903-2939, 7(7), 2903–2939. https://doi.org/10.3390/IJERPH7072903

Jones, C. E., Hopkins, J. R., & Lewis, A. C. (2011). Atmospheric Chemistry and Physics In situ measurements of isoprene and monoterpenes within a south-east Asian tropical rainforest. Atmos. Chem. Phys, 11, 6971–6984. https://doi.org/10.5194/acp-11-6971-2011

Kang, S., Wildt, J., Pullinen, I., Vereecken, L., Wu, C., Wahner, A., Zorn, S. R., & Mentel, T. F. (2025). Formation of highly oxygenated organic molecules from αpinene photooxidation: evidence for the importance of highly oxygenated alkoxy radicals. EGUsphere, 1–33. https://doi.org/10.5194/EGUSPHERE-2025-2772

Kautzman, K. E., Surratt, J. D., Chan, M. N., Chan, A. W. H., Hersey, S. P., Chhabra, P. S., Dalleska, N. F., Wennberg, P. O., Flagan, R. C., & Seinfeld, J. H. (2010). Chemical composition of gas- and aerosol-phase products from the photooxidation of naphthalene. The Journal of Physical Chemistry. A, 114(2), 913–934. https://doi.org/10.1021/JP908530S

Kenagy, H. S., Heald, C. L., Tahsini, N., Goss, M. B., & Kroll, J. H. (2024). Can we achieve atmospheric chemical environments in the laboratory? An integrated model-measurement approach to chamber SOA studies. Science Advances, 10(37), 1482. https://doi.org/10.1126/SCIADV.ADO1482

Kenseth, C. M., Huang, Y., Zhao, R., Dalleska, N. F., Caleb Hethcox, J., Stoltz, B. M., & Seinfeld, J. H. (2018). Synergistic O_3 + OH oxidation pathway to extremely low-volatility dimers revealed in β-pinene secondary organic aerosol. Proceedings of the National Academy of Sciences of the United States of America, 115(33), 8301–8306. https://doi.org/10.1073/PNAS.1804671115;ISSUE:ISSUE:DOI

Khan, M. A. H., Holland, R., Mould, C., Bacak, A., Percival, C. J., Shallcross, D. E., Khan, M. A. H., Holland, R., Mould, C., Bacak, A., Percival, C. J., & Shallcross, D. E. (2025). Isoprene Emissions, Oxidation Chemistry and Environmental Impacts. Atmosphere 2025, Vol. 16, 16(3). https://doi.org/10.3390/ATMOS16030259

Kirkby, J., Curtius, J., Almeida, J., Dunne, E., Duplissy, J., Ehrhart, S., Franchin, A., Gagné, S., Ickes, L., Kürten, A., Kupc, A., Metzger, A., Riccobono, F., Rondo, L., Schobesberger, S., Tsagkogeorgas, G., Wimmer, D., Amorim, A., Bianchi, F., Kulmala, M. (2011). Role of sulphuric acid, ammonia and galactic cosmic rays in atmospheric aerosol nucleation. Nature 2011 476:7361, 476(7361), 429–433. https://doi.org/10.1038/nature10343

Kirkby, J., Duplissy, J., Sengupta, K., Frege, C., Gordon, H., Williamson, C., Heinritzi, M., Simon, M., Yan, C., Almeida, J., Trostl, J., Nieminen, T., Ortega, I. K., Wagner, R., Adamov, A., Amorim, A., Bernhammer, A. K., Bianchi, F., Breitenlechner, M., … Curtius, J. (2016). Ion-induced nucleation of pure biogenic particles. Nature 2016 533:7604, 533(7604), 521–526. https://doi.org/10.1038/nature17953

Klippenstein, S. J., & Elliott, S. N. (2023). OH Roaming during the Ozonolysis of α-Pinene: A New Route to Highly Oxygenated Molecules? Journal of Physical Chemistry A, 127(50), 10647–10662. https://doi.org/10.1021/ACS.JPCA.3C05179/SUPPL_FILE/JP3C05179_SI_003.MP4

Kroll, J. H., Donahue, N. M., Jimenez, J. L., Kessler, S. H., Canagaratna, M. R., Wilson, K. R., Altieri, K. E., Mazzoleni, L. R., Wozniak, A. S., Bluhm, H., Mysak, E. R., Smith, J. D., Kolb, C. E., & Worsnop, D. R. (2011). Carbon oxidation state as a metric for describing the chemistry of atmospheric organic aerosol. Nature Chemistry 2010 3:2, 3(2), 133–139. https://doi.org/10.1038/nchem.948

Kumar, V., Slowik, J. G., Baltensperger, U., Prevot, A. S. H., & Bell, D. M. (2023). Time-Resolved Molecular Characterization of Secondary Organic Aerosol Formed from OH and NO3 Radical Initiated Oxidation of a Mixture of Aromatic Precursors. Environmental Science & Technology, 57(31), 11572–11582. https://doi.org/10.1021/ACS.EST.3C00225

Lannuque, V., & Sartelet, K. (2024). Development of a detailed gaseous oxidation scheme of naphthalene for secondary organic aerosol (SOA) formation and speciation. Atmospheric Chemistry and Physics, 24(15), 8589–8606. https://doi.org/10.5194/ACP-24-8589-2024

Laothawornkitkul, J., Taylor, J. E., Paul, N. D., & Hewitt, C. N. (2009). Biogenic volatile organic compounds in the Earth system: Tansley review. New Phytologist, 183(1), 27–51. https://doi.org/10.1111/J.1469-8137.2009.02859.X;PAGE:STRING:ARTICLE/CHAPTER

Lehtipalo, K., Yan, C., Dada, L., Bianchi, F., Xiao, M., Wagner, R., Stolzenburg, D., Ahonen, L. R., Amorim, A., Baccarini, A., Bauer, P. S., Baumgartner, B., Bergen, A., Bernhammer, A. K., Breitenlechner, M., Brilke, S., Buchholz, A., Mazon, S. B., Chen, D., … Worsnop, D. R. (2018). Multicomponent new particle formation from sulfuric acid, ammonia, and biogenic vapors. Science Advances, 4(12). https://doi.org/10.1126/SCIADV.AAU5363

Lelieveld, J., Gromov, S., Pozzer, A., & Taraborrelli, D. (2016). Global tropospheric hydroxyl distribution, budget and reactivity. Atmos. Chem. Phys, 16, 12477–12493. https://doi.org/10.5194/acp-16-12477-2016

Levy, H. (1971). Normal atmosphere: Large radical and formaldehyde concentrations predicted. Science, 173(3992), 141–143. https://doi.org/10.1126/SCIENCE.173.3992.141;WEBSITE:WEBSITE:AAAS-SITE;JOURNAL:JOURNAL:SCIENCE;ISSUE:ISSUE:DOI

Li, H., Canagaratna, M. R., Riva, M., Rantala, P., Zhang, Y., Thomas, S., Heikkinen, L., Flaud, P. M., Villenave, E., Perraudin, E., Worsnop, D., Kulmala, M., Ehn, M., & Bianchi, F. (2021). Atmospheric organic vapors in two European

pine forests measured by a Vocus PTR-TOF: Insights into monoterpene and sesquiterpene oxidation processes. Atmospheric Chemistry and Physics, 21(5), 4123–4147. https://doi.org/10.5194/ACP-21-4123-2021

Li, X. B., Yuan, B., Wang, S., Wang, C., Lan, J., Liu, Z., Song, Y., He, X., Huangfu, Y., Pei, C., Cheng, P., Yang, S., Qi, J., Wu, C., Huang, S., You, Y., Chang, M., Zheng, H., Yang, W., … Shao, M. (2022). Variations and sources of volatile organic compounds (VOCs) in urban region: insights from measurements on a tall tower. Atmospheric Chemistry and Physics, 22(16), 10567–10587. https://doi.org/10.5194/ACP-22-10567-2022

Li, Y., & Wang, L. (2014). The atmospheric oxidation mechanism of 1,2,4-trimethylbenzene initiated by OH radicals. Physical Chemistry Chemical Physics, 16(33), 17908–17917. https://doi.org/10.1039/C4CP02027H

Lin, C., Hu, R., Xie, P., Lou, S., Zhang, G., Tong, J., Liu, J., & Liu, W. (2022). Nocturnal atmospheric chemistry of NO3 and N2O5 over Changzhou in the Yangtze River Delta in China. Journal of Environmental Sciences, 114, 376–390. https://doi.org/10.1016/J.JES.2021.09.016

Liu, S. C., Kley, D., McFarland, M., Mahlman, J. D., & Levy, H. (1980). On the origin of tropospheric ozone. Journal of Geophysical Research: Oceans, 85(C12), 7546–7552. https://doi.org/10.1029/JC085IC12P07546

Liu, T., Hong, Y., Li, M., Xu, L., Chen, J., Bian, Y., Yang, C., Dan, Y., Zhang, Y., Xue, L., Zhao, M., Huang, Z., & Wang, H. (2022). Atmospheric oxidation capacity and ozone pollution mechanism in a coastal city of southeastern China: Analysis of a typical photochemical episode by an observation-based model. Atmospheric Chemistry and Physics, 22(3), 2173–2190. https://doi.org/10.5194/ACP-22-2173-2022

Liu, X., Huang, Y., Chen, Y., Feng, X., Li, J., Xu, Y., Chen, Y., Gu, D., Sun, H., Ning, Z., Yu, J., Chow, W. S., Lin, C., Xiang, Y., Zhang, T., Granier, C., Brasseur, G., Wang, Z., & Fung, J. C. H. (2025). Abundance of volatile organic compounds and their role in ozone pollution management: evidence from multi-platform observations and model representation during the 2021–2022 field campaign in Hong Kong. Atmospheric Chemistry and Physics, 25(23), 17629–17649. https://doi.org/10.5194/ACP-25-17629-2025

Liu, X., Ran, L., Lin, W., Xu, X., Ma, Z., Dong, F., He, D., Zhou, L., Shi, Q., & Wang, Y. (2022). Measurement report: Variations in surface SO2 and NOx mixing ratios from 2004 to 2016 at a background site in the North China Plain. Atmospheric Chemistry and Physics, 22(10), 7071–7085. https://doi.org/10.5194/ACP-22-7071-2022

Lu, K. D., Hofzumahaus, A., Holland, F., Bohn, B., Brauers, T., Fuchs, H., Hu, M., Häseler, R., Kita, K., Kondo, Y., Li, X., Lou, S. R., Oebel, A., Shao, M., Zeng, L. M., Wahner, A., Zhu, T., Zhang, Y. H., & Rohrer, F. (2013). Atmospheric Chemistry and Physics Missing OH source in a suburban environment near Beijing: observed and modelled OH and HO_2 concentrations in summer 2006. Atmos. Chem. Phys, 13, 1057–1080. https://doi.org/10.5194/acp-13-1057-2013

Mayhew, A. W., Franzon, L., Bates, K. H., Kurtén, T., Lopez-Hilfiker, F. D., Mohr, C., Rickard, A. R., Thornton, J. A., & Haskins, J. D. (2025). The global importance of gas-phase peroxy radical accretion reactions for secondary organic aerosol loading. Atmos. Chem. Phys., 25, 17027–17046. https://doi.org/10.5194/acp-25-17027-2025

McFiggans, G., Mentel, T. F., Wildt, J., Pullinen, I., Kang, S., Kleist, E., Schmitt, S., Springer, M., Tillmann, R., Wu, C., Zhao, D., Hallquist, M., Faxon, C., Le Breton, M., Hallquist, Å. M., Simpson, D., Bergström, R., Jenkin, M. E., Ehn, M., … Kiendler-Scharr, A. (2019). Secondary organic aerosol reduced by mixture of atmospheric vapours. Nature 2019 565:7741, 565(7741), 587–593. https://doi.org/10.1038/s41586-018-0871-y

Messina, P., Lathière, J., Sindelarova, K., Vuichard, N., Granier, C., Ghattas, J., Cozic, A., & Hauglustaine, D. A. (2016). Global biogenic volatile organic compound emissions in the ORCHIDEE and MEGAN models and sensitivity to key parameters. Atmospheric Chemistry and Physics, 16(22), 14169–14202. https://doi.org/10.5194/ACP-16-14169-2016

Mitchell, M. J., Landers, D. H., Berner, R. A., Cook, R. B., Schindler, D. W., Nriagu, J. O., Coker, R. D., & Limnol Oceanogr ; Bilonick, R. A. (1984). Toluene degradation products in simulated atmospheric conditions. Nature 1984 311:5983, 311(5983), 248–250. https://doi.org/10.1038/311248a0

Molteni, U., Bianchi, F., Klein, F., El Haddad, I., Frege, C., Rossi, M. J., Dommen, J., & Baltensperger, U. (2018). Formation of highly oxygenated organic molecules from aromatic compounds. Atmospheric Chemistry and Physics, 18(3), 1909–1921. https://doi.org/10.5194/ACP-18-1909-2018

Monks, P. S., Archibald, A. T., Colette, A., Cooper, O., Coyle, M., Derwent, R., Fowler, D., Granier, C., Law, K. S., Mills, G. E., Stevenson, D. S., Tarasova, O., Thouret, V., Von Schneidemesser, E., Sommariva, R., Wild, O., & Williams, M. L. (2015). Tropospheric ozone and its precursors from the urban to the global scale from air quality to short-lived climate forcer. Atmos. Chem. Phys, 15, 8889–8973. https://doi.org/10.5194/acp-15-8889-2015

Nozière, B. (2025). Trends in organic peroxide (ROOR) formation in the reactions of C1–C4 alkyl peroxy radicals (RO2) in gas. Chemical Science, 16(36), 16590–16596. https://doi.org/10.1039/D5SC03559G

Okuljar, M., Garmash, O., Olin, M., Kalliokoski, J., Timonen, H., Niemi, J. V, Paasonen, P., Kontkanen, J., Zhang, Y., Hellén, H., Kuuluvainen, H., Aurela, M., Manninen, H. E., Sipilä, M., Rönkkö, T., Petäjä, T., Kulmala, M., Dal Maso, M., & Ehn, M. (2023). Influence of anthropogenic emissions on the composition of highly oxygenated organic molecules in Helsinki: a street canyon and urban background station comparison. Atmos. Chem. Phys, 23, 12965–12983. https://doi.org/10.5194/acp-23-12965-2023

Orlando, J. J., & Tyndall, G. S. (2012). Laboratory studies of organic peroxy radical chemistry: an overview with emphasis on recent issues of atmospheric significance. Chemical Society Reviews, 41(19), 6294–6317. https://doi.org/10.1039/C2CS35166H

Peng, W., Le, C., Porter, W. C., & Cocker, D. R. (2022). Variability in Aromatic Aerosol Yields under Very Low NOx Conditions at Different HO2/RO2 Regimes. Environmental Science & Technology, 56(2), 750–760. https://doi.org/10.1021/ACS.EST.1C04392

Peng, Z., Lee-Taylor, J., Orlando, J. J., Tyndall, G. S., & Jimenez, J. L. (2019). Organic peroxy radical chemistry in oxidation flow reactors and environmental chambers and their atmospheric relevance. Atmospheric Chemistry and Physics, 19(2), 813–834. https://doi.org/10.5194/ACP-19-813-2019

Peñuelas, J., & Staudt, M. (2010). BVOCs and global change. Trends in Plant Science, 15(3), 133–144. https://doi.org/10.1016/j.tplants.2009.12.005

Phousongphouang, P. T., & Arey, J. (2002). Rate constants for the gas-phase reactions of a series of alkylnaphthalenes with the OH radical. Environmental Science & Technology, 36(9), 1947–1952. https://doi.org/10.1021/ES011434C

Ponnusamy, S., Sandhiya, L., & Senthilkumar, K. (2017). The atmospheric oxidation mechanism and kinetics of 1,3,5-trimethylbenzene initiated by OH radicals – a theoretical study. New Journal of Chemistry, 41(18), 10259–10271. https://doi.org/10.1039/C7NJ01285C

Presto, A. A., & Donahue, N. M. (2006). Investigation of α-Pinene + Ozone Secondary Organic Aerosol Formation at Low Total Aerosol Mass. Environmental Science and Technology, 40(11), 3536–3543. https://doi.org/10.1021/ES052203Z

Pye, H. O. T., Chan, A. W. H., Barkley, M. P., & Seinfeld, J. H. (2010a). Global modeling of organic aerosol: The importance of reactive nitrogen (NOx and NO3). Atmospheric Chemistry and Physics, 10(22), 11261–11276. https://doi.org/10.5194/ACP-10-11261-2010

Pye, H. O. T., Chan, A. W. H., Barkley, M. P., & Seinfeld, J. H. (2010b). Global modeling of organic aerosol: The importance of reactive nitrogen (NOx and NO3). Atmospheric Chemistry and Physics, 10(22), 11261–11276. https://doi.org/10.5194/ACP-10-11261-2010

Roelofs, G. J., & Lelieveld, J. (1997). Model study of the influence of cross-tropopause O3 transports on tropospheric O3 levels. Tellus, Series B: Chemical and Physical Meteorology, 49(1), 38–55. https://doi.org/10.3402/TELLUSB.V49I1.15949;WGROUP:STRING:PUBLICATION

Rolletter, M., Kaminski, M., Acir, I. H., Bohn, B., Dorn, H. P., Li, X., Lutz, A., Nehr, S., Rohrer, F., Tillmann, R., Wegener, R., Hofzumahaus, A., Kiendler-Scharr, A., Wahner, A., & Fuchs, H. (2019). Investigation of the α-pinene photooxidation by OH in the atmospheric simulation chamber SAPHIR. Atmospheric Chemistry and Physics, 19(18), 11635–11649. https://doi.org/10.5194/ACP-19-11635-2019

Schervish, M., Heinritzi, M., Stolzenburg, D., Dada, L., Wang, M., Ye, Q., Hofbauer, V., DeVivo, J., Bianchi, F., Brilke, S., Duplissy, J., El Haddad, I., Finkenzeller, H., He, X. C., Kvashnin, A., Kim, C., Kirkby, J., Kulmala, M., Lehtipalo, K., … Donahue, N. M. (2024). Interactions of peroxy radicals from monoterpene and isoprene oxidation simulated in the

radical volatility basis set. Environmental Science: Atmospheres, 4(7), 740–753. https://doi.org/10.1039/D4EA00056K

Schwantes, R. H., Teng, A. P., Nguyen, T. B., Coggon, M. M., Crounse, J. D., St. Clair, J. M., Zhang, X., Schilling, K. A., Seinfeld, J. H., & Wennberg, P. O. (2015). Isoprene NO3 Oxidation Products from the RO2 + HO2 Pathway. Journal of Physical Chemistry A, 119(40), 10158–10171. https://doi.org/10.1021/ACS.JPCA.5B06355

Seinfeld, J. H. ., & Pandis, S. N. . (2016). Atmospheric chemistry and physics : from air pollution to climate change. 1120.
https://books.google.com/books/about/Atmospheric_Chemistry_and_Physics.html?hl=it&id=n_RmCgAAQBAJ

Shen, J., Russell, D. M., DeVivo, J., Kunkler, F., Baalbaki, R., Mentler, B., Scholz, W., Yu, W., Caudillo-Plath, L., Sommer, E., Ahongshangbam, E., Alfaouri, D., Almeida, J., Amorim, A., Beck, L. J., Beckmann, H., Berntheusel, M., Bhattacharyya, N., Canagaratna, M. R., … He, X. C. (2024a). New particle formation from isoprene under upper-tropospheric conditions. Nature 2024 636:8041, 636(8041), 115–123. https://doi.org/10.1038/s41586-024-08196-0

Shen, J., Russell, D. M., DeVivo, J., Kunkler, F., Baalbaki, R., Mentler, B., Scholz, W., Yu, W., Caudillo-Plath, L., Sommer, E., Ahongshangbam, E., Alfaouri, D., Almeida, J., Amorim, A., Beck, L. J., Beckmann, H., Berntheusel, M., Bhattacharyya, N., Canagaratna, M. R., … He, X. C. (2024b). New particle formation from isoprene under upper-tropospheric conditions. Nature 2024 636:8041, 636(8041), 115–123. https://doi.org/10.1038/s41586-024-08196-0

Simon, M., Dada, L., Heinritzi, M., Scholz, W., Stolzenburg, D., Fischer, L., C. Wagner, A., Kürten, A., Rörup, B., He, X. C., Almeida, J., Baalbaki, R., Baccarini, A., S. Bauer, P., Beck, L., Bergen, A., Bianchi, F., Bräkling, S., Brilke, S., … Curtius, J. (2020). Molecular understanding of new-particle formation from α-pinene between -50 and +25 °C. Atmospheric Chemistry and Physics, 20(15), 9183–9207. https://doi.org/10.5194/ACP-20-9183-2020

Šimpraga, M., Takabayashi, J., & Holopainen, J. K. (2016). Language of plants: Where is the word? Journal of Integrative Plant Biology, 58(4), 343–349. https://doi.org/10.1111/JIPB.12447

Stanton, N. A., & Tandon, N. F. (2023). How does tropospheric VOC chemistry affect climate? An investigation of preindustrial control simulations using the Community Earth System Model version 2. Atmospheric Chemistry and Physics, 23(16), 9191–9216. https://doi.org/10.5194/ACP-23-9191-2023

Suh, I., Lei, W., & Zhang, R. (2001). Experimental and Theoretical Studies of Isoprene Reaction with NO3. Journal of Physical Chemistry A, 105(26), 6471–6478. https://doi.org/10.1021/JP0105950

Teng, A. P., Crounse, J. D., & Wennberg, P. O. (2017). Isoprene Peroxy Radical Dynamics. Journal of the American Chemical Society, 139(15), 5367–5377. https://doi.org/10.1021/JACS.6B12838

Tomaz, S., Wang, D., Zabalegui, N., Li, D., Lamkaddam, H., Bachmeier, F., Vogel, A., Monge, M. E., Perrier, S., Baltensperger, U., George, C., Rissanen, M., Ehn, M., El Haddad, I., & Riva, M. (2021). Structures and reactivity of peroxy radicals and dimeric products revealed by online tandem mass spectrometry. Nature Communications 2021 12:1, 12(1), 300-. https://doi.org/10.1038/s41467-020-20532-2

Tsiligiannis, E., Hammes, J., Salvador, C. M., Mentel, T. F., & Hallquist, M. (2019). Effect of NOx on 1,3,5-trimethylbenzene (TMB) oxidation product distribution and particle formation. Atmospheric Chemistry and Physics, 19(23), 15073–15086. https://doi.org/10.5194/ACP-19-15073-2019

Tyndall, G. S., Cox, R. A., Granier, C., Lesclaux, R., Moortgat, G. K., Pilling, M. J., Ravishankara, A. R., & Wallington, T. J. (2001). Atmospheric chemistry of small organic peroxy radicals. Journal of Geophysical Research Atmospheres, 106(D11), 12157–12182. https://doi.org/10.1029/2000JD900746;CTYPE:STRING:JOURNAL

Wagner, P., & Kuttler, W. (2014). Biogenic and anthropogenic isoprene in the near-surface urban atmosphere - A case study in Essen, Germany. Science of the Total Environment, 475, 104–115. https://doi.org/10.1016/j.scitotenv.2013.12.026

Wang, L., Lun, X., Wang, Q., & Wu, J. (2024). Biogenic volatile organic compounds emissions, atmospheric chemistry, and environmental implications: a review. Environmental Chemistry Letters 2024 22:6, 22(6), 3033–3058. https://doi.org/10.1007/S10311-024-01785-5

Wang, W., Yuan, B., Su, H., Cheng, Y., Qi, J., Wang, S., Song, W., Wang, X., Xue, C., Ma, C., Bao, F., Wang, H., Lou, S., & Shao, M. (2023). A large role of missing volatile organic compounds reactivity from anthropogenic emissions in ozone pollution regulation. https://doi.org/10.5194/EGUSPHERE-2023-2647

Wayne, R. P. . (2006). Chemistry of atmospheres : an introduction to the chemistry of the atmospheres of earth, the planets, and their satellites. 775. https://global.oup.com/academic/product/chemistry-of-atmospheres-9780198503750

Wayne, R. P., Barnes, I., Biggs, P., Burrows, J. P., Canosa-Mas, C. E., Hjorth, J., Le Bras, G., Moortgat, G. K., Perner, D., Poulet, G., Restelli, G., & Sidebottom, H. (1991). The nitrate radical: Physics, chemistry, and the atmosphere. Atmospheric Environment. Part A. General Topics, 25(1), 1–203. https://doi.org/10.1016/0960-1686(91)90192-A

Wennberg, P. O., Bates, K. H., Crounse, J. D., Dodson, L. G., McVay, R. C., Mertens, L. A., Nguyen, T. B., Praske, E., Schwantes, R. H., Smarte, M. D., St Clair, J. M., Teng, A. P., Zhang, X., & Seinfeld, J. H. (2018a). Gas-Phase Reactions of Isoprene and Its Major Oxidation Products. Chemical Reviews, 118(7), 3337–3390. https://doi.org/10.1021/ACS.CHEMREV.7B00439

Wennberg, P. O., Bates, K. H., Crounse, J. D., Dodson, L. G., McVay, R. C., Mertens, L. A., Nguyen, T. B., Praske, E., Schwantes, R. H., Smarte, M. D., St Clair, J. M., Teng, A. P., Zhang, X., & Seinfeld, J. H. (2018b). Gas-Phase Reactions of Isoprene and Its Major Oxidation Products. Chemical Reviews, 118(7), 3337–3390. https://doi.org/10.1021/ACS.CHEMREV.7B00439

Wolfe, G. M., Cantrell, C., Kim, S., Mauldin Iii, R. L., Karl, T., Harley, P., Turnipseed, A., Zheng, W., Flocke, F., Apel, E. C., Hornbrook, R. S., Hall, S. R., Ullmann, K., Henry, S. B., Digangi, J. P., Boyle, E. S., Kaser, L., Schnitzhofer, R., Hansel, A., … Keutsch, F. N. (2013). Missing peroxy radical sources Atmospheric Chemistry and Physics Missing peroxy radical sources within a rural forest canopy Missing peroxy radical sources. Atmos. Chem. Phys. Discuss, 13, 31713–31759. https://doi.org/10.5194/acpd-13-31713-2013

Wu, R., Pan, S., Li, Y., & Wang, L. (2014). Atmospheric Oxidation Mechanism of Toluene. Journal of Physical Chemistry A, 118(25), 4533–4547. https://doi.org/10.1021/JP500077F

Xiao, M., Wang, M., Mentler, B., Garmash, O., Lamkaddam, H., Molteni, U., Simon, M., Ahonen, L., Amorim, A., Baccarini, A., Bauer, P. S., Chen, D., Chiu, R., Dada, L., Duplissy, J., Finkenzeller, H., Fischer, L., He, X. C., Heinritzi, M., … El Haddad, I. (2025). Anthropogenic organic aerosol in Europe produced mainly through second-generation oxidation. Nature Geoscience 2025 18:3, 18(3), 239–245. https://doi.org/10.1038/s41561-025-01645-z

Xu, L., Møller, K. H., Crounse, J. D., Otkjær, R. V., Kjaergaard, H. G., & Wennberg, P. O. (2019a). Unimolecular Reactions of Peroxy Radicals Formed in the Oxidation of α-Pinene and β-Pinene by Hydroxyl Radicals. The Journal of Physical Chemistry A, 123(8), 1661–1674. https://doi.org/10.1021/ACS.JPCA.8B11726

Xu, L., Møller, K. H., Crounse, J. D., Otkjær, R. V., Kjaergaard, H. G., & Wennberg, P. O. (2019b). Unimolecular Reactions of Peroxy Radicals Formed in the Oxidation of α-Pinene and β-Pinene by Hydroxyl Radicals. The Journal of Physical Chemistry A, 123(8), 1661–1674. https://doi.org/10.1021/ACS.JPCA.8B11726

Xu, R., Thornton, J. A., Lee, B. H., Zhang, Y., Jaeglé, L., Lopez-Hilfiker, F. D., Rantala, P., & Petäjä, T. (2022). Global simulations of monoterpene-derived peroxy radical fates and the distributions of highly oxygenated organic molecules (HOMs) and accretion products. Atmospheric Chemistry and Physics, 22(8), 5477–5494. https://doi.org/10.5194/ACP-22-5477-2022

Yang, B., Wiser, F. C., Mcneill, V. F., Fiore, A. M., Tao, M., Henze, D. K., Sen, S., & Westervelt, D. M. (2023). Implementation and evaluation of the automated model reduction (AMORE) version 1.1 isoprene oxidation mechanism in GEOS-Chem †. https://doi.org/10.1039/d3ea00121k

Zang, H., Luo, Z., Li, C., Li, Z., Huang, D., & Zhao, Y. (2024). Nocturnal Atmospheric Synergistic Oxidation Reduces the Formation of Low-volatility Organic Compounds from Biogenic Emissions. https://doi.org/10.5194/EGUSPHERE-2024-1131

Zhang, J., Choi, M., Ji, Y., Zhang, R., Zhang, R., & Ying, Q. (2021). Assessing the Uncertainties in Ozone and SOA Predictions due to Different Branching Ratios of the Cresol Pathway in the Toluene-OH Oxidation Mechanism. ACS Earth and Space Chemistry, 5(8), 1958–1970. https://doi.org/10.1021/ACSEARTHSPACECHEM.1C00092

Zhang, J., Huff Hartz, K. E., Pandis, S. N., & Donahue, N. M. (2006). Secondary Organic Aerosol Formation from Limonene Ozonolysis: Homogeneous and Heterogeneous Influences as a Function of NOx. Journal of Physical Chemistry A, 110(38), 11053–11063. https://doi.org/10.1021/JP062836F

Zhang, X., Luo, J., Pan, W., Xue, Q., Liu, X., Fu, J., Zhang, A., & Jiang, G. (2025). Implications of VOC oxidation in atmospheric chemistry: development of a comprehensive AI model for predicting reaction rate constants. Atmospheric Chemistry and Physics, 25(20), 13379–13391. https://doi.org/10.5194/ACP-25-13379-2025

Zhao, Y., Thornton, J. A., & Pye, H. O. T. (2018). Quantitative constraints on autoxidation and dimer formation from direct probing of monoterpene-derived peroxy radical chemistry. Proceedings of the National Academy of Sciences of the United States of America, 115(48), 12142–12147. https://doi.org/10.1073/PNAS.1812147115;WGROUP:STRING:PUBLICATION

Zhi, Y., Jin, Z., Lu, L., Yang, T., Zhou, D., Pei, Z., Wu, D., Fu, D., Zhang, D., & Li, X. (2021). Improving atmospheric corrosion prediction through key environmental factor identification by random forest-based model. Corrosion Science, 178, 109084. https://doi.org/10.1016/J.CORSCI.2020.109084

Ziemann, P. J., & Atkinson, R. (2012). Kinetics, products, and mechanisms of secondary organic aerosol formation. Chemical Society Reviews, 41(19), 6582–6605. https://doi.org/10.1039/C2CS35122F

Zou, Z., Chen, T., Chen, Q., Sun, W., Han, S., Ren, Z., Li, X., Song, W., Ge, A., Wang, Q., Tian, X., Pei, C., Wang, X., Zhang, Y., & Wang, T. (2025). Observation and modeling of atmospheric OH and HO2* radicals at a subtropical rural site and implications for secondary pollutants. Atmospheric Chemistry and Physics, 25(14), 8147–8161. https://doi.org/10.5194/ACP-25-8147-2025

5. Conclusions

This study investigated atmospheric aerosols, with a particular focus on anthropogenic contributions, by combining different approaches ranging from combustion diagnostic to atmospheric simulation studies. The study focused on three key points:

- ❖ The characterization of both gaseous precursors and aerosol particles released by different combustion systems.
- ❖ The alteration of the produced compounds through source manipulation.
- ❖ The chemical and physical evolution of gas- and particle-phase species in complex atmospheric environments.

More specifically, the research was structured in three Work Packages, each designed to address a specific scientific question.

- Question 1: Can anthropogenic emissions from combustion systems, including gaseous precursors (like AVOCs) as well as particulate matter such as soot, be reduced? Is it possible to alter the chemistry of combustion through the use of strategic solutions, such as dopant molecules, to develop cleaner technologies?

WP1 tries to answer this question by investigating the effects of ozone addition on a partially premixed laminar methane flame, operated at two equivalence ratios, Φ=11.9 and Φ=7.6, representative of two different sooting tendencies. This flame configuration is commonly observed in premixed burners for laboratory or industrial applications. The analysis was conducted through particle size distribution measurements coupled with physical and chemical investigations on the produced soot, involving Raman spectroscopy and atomic force microscopy. Results showed that ozone introduction impacts on resonantly stabilized radicals, by removing them, and thus altering the chemistry of the system. A reduction in terms on soot number and size (down to few-PAHs layers) was recorded after the introduction of the dopant. Particles formed from ozonized flames were registered to be flatter, indicating a lower cross-linking in the aromatic network coupled with a reduced 3D growth. Moreover, the presence of larger aromatic constituents was inferred from the Raman spectra results, due to the higher I(D)/I(G) ratio. Globally, ozone seems to alter the formation of aromatic crosslinks by decreasing them and thus altering HACA mechanism. The soot samples were collected at different positions over the burner (Z) and higher Z positions, corresponding to oxidative flame region, presented minor ozone-induced alterations with only a slight increase in the intervalley region of the Raman spectra, corresponding to amorphous carbon. This final conclusion is consistent with enhanced oxidation of mature soot in the presence of ozone molecules.

Further investigations may be oriented towards understanding the effect of different ozone concentrations or different equivalence ratios. Moreover, this study is related to the characterization of primary particles, directly released by the combustion system. It may be of interest for future studies to monitor also the effects of the dopant on secondary aerosols particles.

- Question 2: How does atmospheric aging impact and drive AVOCs transformations? Is it possible to extract some key reactive pathways and variables driving the formation of primary and secondary aerosols from gas-phase precursors?

WP2 focused on the characterization of primary and secondary emissions released by a premixed laminar ethylene–air-rich flame, selected as a representative combustion system due to the relevance of ethylene as a key combustion intermediate. Flame products were extracted at different heights above the burner (Z) and characterized before and after OH-induced aging oxidation. The aging process was simulated in an oxidation flow reactor (DOFR™) equipped with internal UV-lights able to induce O_3

photolysis and achieve an OH concentration corresponding to two days of oxidation. Particle size distribution analysis revealed the formation of larger particles due to photo-oxidation, confirmed by the presence of new modes. High resolution mass spectrometry showed a clear transformation from POA to SOA with reduced hydrocarbon-like (CH) species coupled with an increase in oxygenated carbon compounds, confirmed by Van Krevelen diagrams. Collecting exhausts at different Zs, allowed to monitor the evolution of POA and SOA from a wider range of precursors, formed at different residence times. Within this context, higher Zs are associated with increased concentrations of fullerenes. Overall, these results demonstrated that gas-phase precursors released by this system can easily undergo oxidation reactions, leading to the chemical transformation of POA and the generation of SOA, closely resembling ambient compositions.

- Question 3: How do AVOCs evolve in the presence of pre-emitted compounds? Do BVOCs or other pre-released species affect their atmospheric evolution?

WP3 experiments were conducted in the CLOUD chamber facility, a 26.1 m^3 reactor equipped with mixing fans and a complex light system to accurately simulate atmospheric conditions. Within this context, not solely AVOCs but also BVOCs atmospheric evolution was investigated. In particular, three scenarios were analysed, mimicking a pristine remote environment, a suburban area, and a highly polluted city. αpinene and isoprene were selected as representative BVOC compounds, whereas trimethylbenzene, naphthalene, and toluene were injected as AVOCs. The analysis focused on VOCs oxidation and more specifically on the driving mechanisms leading to dimers formation.

In rural scenarios, the monomers composition was dominated by the contributions of C_5 and C_{10} species, associated with isoprene and αpinene chemistry, respectively. Dimers formation revealed distinct tendencies for self- and cross-RO_2 reactions, particularly monitored though the monitoring of C_{15} and C_{20} clusters. In suburban conditions, the addition of 1,2,4-trimethylbenzene translated into the introduction of an anthropogenic RO_2 radical competing with biogenic RO_2. The interactions among these radicals released by different sources revealed a suppression of BVOC-derived dimers formation and a shifted dimer composition towards anthropogenic products. Finally urban conditions, simulated with the injection of a mixture of anthropogenic VOCs, were dominated by OH-driven chemistry, promoting the formation of high-carbon number dimers ($C_{16\text{-}20}$) and molecular growth. Overall, the results showed that RO_2-RO_2 interactions critically control secondary chemistry and particle formation across different atmospheric environments.